ABSTRACT

Title of Dissertation:	DESIGN AND ASSEMBLY OF BLOCK COPOLYMER-MODIFIED NANOPARTICLES INTO SUPRACOLLOIDAL, MOLECULAR MIMICS
	Kyle Thomas Webb, Doctor of Philosophy, 2023
Dissertation directed by:	Professor Zhihong Nie Professor John Fourkas Department of Chemistry and Biochemistry

Large strides have been achieved in nanoparticle self-assembly, using various strategies to achieve ordered, supracolloidal structures, ranging from dimers to chains and vesicles to 3-D lattices. However, these methods, while expanding the scope and accessibility of design, face inherent limitations in targeting complex structures with high yields, particularly when using isotropic building blocks (e.g. gold nanoparticles and polystyrene nanoparticles). Additionally, research studying the reversibility of nanoparticle assemblies is mostly limited to small-ligand-modified particles rather than polymer-modified nanoparticles. Polymers are particularly advantageous as they provide a higher degree of functionality to the nanoparticle surface and allow for increased control in directing particle interactions. This control is necessary to continue furthering the advancement of gold nanoparticles in plasmonics, sensors, and catalysts.

Here, we introduce two strategies to assemble gold nanoparticles into supracolloidal nanostructures. Gold nanoparticles are modified with complementary, functionalized-block-

copolymers that drive the assembly of the nanoparticles. The first strategy uses a diblock copolymer composed of a hydrophilic outer block and an acid or base-functionalized inner block. Upon mixing, particles are assembled due to the acid–base neutralization between the complementary block copolymers. The resultant supracolloids consist of nanoparticles precisely arranged in space, which mimic the geometries of small molecules. The particle interactions are fine tuned by varying the size and feeding ratio of the nanoparticles, along with the length and composition of the block copolymers. Careful tuning of these parameters yields nanostructures with different valences that were produced in high yield. Additionally, the implementation of a long outer, hydrophilic polymer block provided the assembled nanostructures stability when transferred from THF to water. Colloidal stability in an aqueous medium could allow for expanded use of these nanostructures in cellular uptake studies and biomedical applications.

The second strategy uses a diblock copolymer composed of a hydrophilic outer block and an inner block containing either complementary host or guest moieties. Particularly, we take advantage of the well-established interactions between β-cyclodextrin and adamantane as the host and guest molecules. Upon the slow addition of water, particles assemble due to the host–guest interactions between the complementary block copolymers, as the hydrophobic adamantane moieties are driven within the β-cyclodextrin macrocycles. Fine tuning of the nanoparticle sizes and feeding ratios and the block copolymer lengths and compositions results in high yields of targeted supracolloids that also mimic the geometries of molecules. Interestingly, the size difference between the host and guest-modified particles led to different types of nanostructures.

In addition, due to the reversibility of the host–guest interactions, we demonstrate the ability of our system to reorder in response to competitive host moieties. Upon addition of free β-

cyclodextrin, the host–guest interactions are disrupted, resulting in disassembly of the nanostructures, which we could reassemble upon removal of the free cyclodextrin. Finally, due to the strength of the nanoparticle interactions, we also tested the selectivity of the nanoparticle interactions by assembling the host building block with different guest building blocks. We showed that when assembled with competing guest building blocks, the β-cyclodextrin building blocks preferentially interact the adamantane building blocks due to the stronger particle interactions. This reversibility and selectivity make our system a potential candidate for use in biosensors.

DESIGN AND ASSEMBLY OF BLOCK COPOLYMER-MODIFIED NANOPARTICLES INTO SUPRACOLLOIDAL, MOLECULAR MIMICS

by

Kyle Thomas Webb

Dissertation submitted to the Faculty of the Graduate School of the
University of Maryland, College Park, in partial fulfillment
of the requirements for the degree of
Doctor of Philosophy
2023

Advisory Committee:
Professor John T. Fourkas, Chair
Professor Zhihong Nie
Professor Lyle Isaacs
Professor Efrain Rodriguez
Professor Robert M. Briber, Dean's Representative

Dedication

To my beloved parents, brother, and partner, thank you for your unwavering support throughout this journey.

Acknowledgements

For those that have followed me through my graduate school journey, they know that my path here has not been the smoothest and that I have faced a lot of unique obstacles. I owe it to the many people who have helped me through those tough times for allowing me to become the chemist and the person I am today. First, I want to thank my two advisors, Dr. Zhihong Nie and Dr. John Fourkas. I still remember my first meeting with Dr Nie my first semester in graduate school. He started explaining his work and showed me his ideas that would one day turn into this thesis. I remember seeing the images on his screen and was struck by the whimsy and fun of the project. I remember leaving that meeting excited and quickly started to connect with the others in the lab. From that day forward, Dr. Nie became a mentor to me and helped expand my knowledge and skills.

I then had the pleasure of working with and learning from Dr. Fourkas. When switching to a new advisor, I remember the uncertainty and not knowing whether I should continue with my studies. However, upon meeting with Dr. Fourkas, I was reassured that I could complete my degree. Through covid, changing lab spaces, and many failed experiments, Dr. Fourkas was there to provide advice and reassure me that I was on the right path. He helped me find the strength in myself to keep going, and for that, I am eternally grateful. I was also lucky to have amazing colleagues alongside me to help in that regard.

The first lab mates I want to thank are Dr. Marcus Carter, Dr. Qian Zhang, Dr. Chelsey Lamar, and Dr. Xiaoying Lin. The five of us were there to support each other

through everything. I could call any of them to vent or ask for help, and I knew they would be there and I for them. They became my rock during a very hard time, and we formed a close friendship that went beyond work. I also want to thank my mentors in the lab for training me along the way. Specifically, I want to thank Dr. Chenglin Yi, Dr. Shaoyi Zhang, and Dr. Xikuang Yao. The three of them showed me the skills I needed and also provided valuable advice. Their work was foundational for me, and I could not have asked for a better group of mentors. Furthermore, I want to thank a few of my other former Nie lab members Dr. Yang Yang, Dr. Maria Perez, Dr. Chuncai Kong, Dr. Hongyu Guo, and Dr. Yao Tang for their added support and advice throughout the years.

In addition to the Nie lab, it's also important for me to thank the former and current Fourkas lab members for their support and feedback throughout the years. I want to thank Dr. Nikos Liaros, Dr. Farah Dawood, Dr. Amanda Souna, Dr. Samuel Cohen, Dr. Sandra Guttierrez Razo, Matt Hourwitz, Siddharth Singh, Dr. Mona Abostate, Nick Fisher, Kishalay Mahato, Abhishek Srinivasan, Arman Hussain, Daniel Jovinelli, and Dawson Reed. I treasure the fact that I can call most of my lab members not only colleagues but also friends.

I also want to thank my committee members, who have been here with me on this journey. Thank you Dr. Lyle Isaacs, Dr. Efrain Rodriguez, and Dr. Robert Briber for your feedback and advice throughout this process. You all have been astounding mentors over the years, and I hope to emulate the things you have all taught me moving forward.

In grad school, I learned that mentors could come from both in and outside of the lab. Thus, I want to give a huge thank you to Dr. Steven Wolf, Dr. Matthew Thum, Dr. Steven Murkli, Dr. Andrea Zeppuhar. Coming into grad school, I did not have a strong synthetic chemistry background, and these four were always available to help whenever I needed advice or had questions. Particularly, Andrea always offered her time and friendship. Andrea became one of my first grad school friends, and I have been lucky enough to see her grow into the talented chemist and person she is today, so long as I do not bother her when the angry panda is on her desk.

I also want to thank the faculty and staff who I have had the pleasure of working with over the years. Thank you to Dr. Jiancun Rao and Dr. Sz-Chian Liou for training me on the various instruments I have used over the years. Thank you to Dr. Amanda Souna and Dr. Lee Friedman for your amazing mentorship. Teaching for the two of you turned something most graduate students dread into a part of grad school that I really enjoyed. Particularly, I will always remember Wednesday nights playing trivia with Dr. Friedman, Andrea, Steven, Darrin, and Devyn even through the arguments over Croatia and its beautiful seas.

This leads nicely to the many friends I have made in grad school throughout the years. There are too many to name and count, but I could not have made it through the years without them. From playing intramural sports, to department events, to weddings and parties, and finally to my yearly Friendsgiving dinners and barbeques, the time I have spent with you all is something I will always treasure and am eternally grateful for. However, I would like to highlight a few people. Specifically, I want to thank the “Adventure Club” members, Dr. Aravind

Chandrasekaran, Dr. Teodora Kljaic, Kevin Ramirez, Yehnara Ettinoffe, Medha Rath, and Joelle Fuchs. You all have become my core group of friends in Maryland through covid. Even if we may have almost lost one or two to falling off a boat in South Carolina and again in Puerto Rico, I know I can always depend on you all for anything. You all have touched my life in ways I will never forget, and I know that the bond we share is one that I will never forget.

Finally, I want to thank my family and partner. To my parents and brother, thank you for never losing faith in me and for always being there when I needed your support. To Danielle and Krista, my two closest friends who have become the sisters I never had, thank you for always supporting me through my good times and especially during my bad times. Lifelong friends are hard to come by, and I was lucky enough to find two. To Kevin, my loving partner, thank you for being my rock these past three years. You have been the one person that I truly let see me when I am at my lowest. You were the one reassuring me that I was good enough and that I was worthy of my position. You were the one that when I broke helped put me back together again, and I could not have made it through this without you. I love you all more than anything, and I cannot thank you all enough for the strength you have given me throughout the years. And to all those that have helped me throughout the years that I may not have mentioned by name, just know that you have all left an indelible mark on my life and that I owe where I am today just as much to you as I do myself. I see my thesis as a thank you to the people who have come before me, and I hope by the end of this paper and my presentation, that message stands clear and firm.

Table of Contents

List of Tables

List of Figures

List of Abbreviations

1D: one dimensional

2D: two dimensional

3D: three dimensional

AA: acrylic acid

AAO: anodic aluminum oxide

Ada: adamantyl

AdMA: adamantyl methacrylate

ADT: azobenzene dithiol

AIBN: azobis(isobutyronitrile)

ATRP: atom-transfer radical polymerization

BCP: block copolymer

BF: breath free

B-PgNP: block copolymer-grafted nanoparticle

CB[8]: cucurbit[8]uril

α-CD: alpha-cyclodextrin

β-CD: beta-cyclodextrin

β-CDMA: β-cyclodextrin methacrylate

γ-CD: gamma-cyclodextrin

CD: cyclodextrin

CNT: carbon nanotube

CPADB: 4-cyano-4-(phenylcarbonothiolythio)pentanoic acid

CPB: concentrated polymer brush

CTAB: cetyltrimethyl ammonium bromide

C_w: water content

CWC: critical water content

D_c: channel diameter

DCC: N,N'-dicylcohexylcarbodiimide

DMA: N,N'dimethylacrylamide

DMAEMA: N,N-dimethylaminoethyl methacrylate

DMAP: 4-(dimethylamino)pyridine

DMBMA: 3,3-dimethyl-1-butyl methacrylate

DMF: N,N-dimethylformamide

DMSO: dimethyl sulfoxide

D_p: particle diameter

DPD: dissipative particle dynamics

FEG: field-emission gun

GMA: glycidyl methacrylate

$HAuCl_4$: gold (III) chloride trihydrate

HCl: hydrochloric acid

H-PgNP: homopolymer-grafted nanoparticle

HPLC: high-performance liquid chromatography

JP: Janus particle

LAMP: lipoic acid 2-hydroxy-3-(methacryloyloxy)-propyl ester

LISA: light-induced self-assembly

LSPR: localized surface plasmon resonance

MHz: megahertz

M-PgNP mixed-polymer-grafted nanoparticle

MeO_2MA: 2-(2-methoxyethoxy)ethyl methacrylate

MWCNT: multiwall carbon nanotube

NC: nanocube

ND: nanodisc

NMR: nuclear magnetic resonance

NMRP: nitroxide-mediated radical polymerization

NP: nanoparticle

NR: nanorod

NT: nanotube

NV: nanovesicle

P2VP: poly(2-vinylpyridine)

P4VP: poly(4-vinylpyridine)

PAA: poly(acrylic acid)

PDMS: polydimethylsiloxane

PDP: pentadecylphenol

PEG: poly(ethylene glycol)

PEO: poly(ethylene oxide)

PgMA: propargyl methacrylate

PgNP: polymer-grafted nanoparticle

PMAA: poly(methacrylic acid)

PMMA: poly(methyl methacrylate)

PNIPAM: poly-*N*-isopropylacrylamide

PS: polystyrene

PtBA: poly(*tert*-butyl acrylate)

PVA: polyvinyl alcohol

PVP: polyvinyl pyrrolidone

R_0: root-mean-square end-to-end distance

RAFT: reversible addition-fragmentation chain-transfer

R_g: radius of gyration

Rpm: revolutions-per-minute

RT: room temperature

SAED: selected-area diffraction

SDPB: semi-dilute polymer brush

SEM: scanning electron microscope

SgNP: small-molecule/ligand-grafted nanoparticle

St: styrene

TEA: triethylamine

TEM: transmission electron microscope

TGA: thermogravimetric analysis

THF: tetrahydrofuran

UV: ultraviolet

Vis: visible

Chapter 1: Introduction

Nature has developed clever and intricate strategies to assemble simple building blocks into complex architectures, using functionalized materials that are responsive to environmental conditions. For example, the strong hydrogen bonding between complementary DNA base pairs forms the unique double helix structure of DNA, whereas the formation of cell membranes can be attributed to the assembly of phospholipid bilayers. These structures are the direct result of self-assembly, which is defined as the spontaneous arrangement of disordered moieties into ordered ensembles via local interactions between the individual components.[1] Further, the concept of self-assembly extends beyond the realm of biological systems and has been used by researchers on both the nano and micro scale to design and create functionalized materials with unique properties for targeted applications in various fields. This adaptability provides the unique advantage of being able to fine tune the specific building-block interactions to target desired structures and fabricate from the ground-up in contrast to costly, traditional top-down approaches.

One subclass of self-assembly, known as colloidal self-assembly, has garnered particular interest as nano and micro particles are able to be assembled into structures ranging from dimers and trimers to chains, vesicles, and larger 3D colloidal nanocrystals. Specifically, the use of small-molecule/ligand or polymer tethered nanoparticles (NPs) has been advantageous in various applications, including biosensors, bioimaging, catalysis, and nanomedicine. The combination of the unique optical properties of noble metals (*e.g.*, Au and Pt) with the optimizable functionality

of the surface ligands leads to unique chemical and physical properties, such as optical, magnetic, and stimulus-responsiveness, that neither component possesses on its own.[2-4] However, current methods, while expanding the scope and accessibility of design, face inherent limitations in targeting complex structures with high yields, particularly when using isotropic building blocks (*e.g.,* Au NPs and polystyrene (PS) NPs). Additionally, although work has been done to showcase the reversible self-assembly of these ensembles using different stimuli (*e.g.*, light,[5,6] pH,[7,8] temperature,[9] applied magnetic fields[10], and solvent conditions[11,12]), complete control at the nanoscale is limited.[13] Therefore, it is important to develop a strategy to address these issues to continue advancing applications in plasmonics,[14] catalysis,[15] and heavy metal detection.[16]

1.1 Introduction to Hybrid Nanomaterials

1.1.1 Different Classes of Hybrid Nanomaterials

Hybrid nanomaterials are particularly interesting for researchers, as those materials combine the properties of both the inorganic core and the organic molecules, ligands, and/or polymers that cap the surface. These properties can be further manipulated by assembling these structures together; however, the targeted self-assembly of particles on the nanoscale can be difficult to control, and thus, the functionalization of the ligands bound to the NP surface is crucial, as these ligands can drive the assembly in a desired direction based on specific molecular interactions. Thus, it is important to understand how changing the nature of these ligands impacts the resulting structures and assemblies. To address how these ligands impact self-assembly, we divide these hybrid nano building blocks into two different

subcategories: small-molecule/ligand-grafted NPs (SgNPs) and polymer-grafted NPs (PgNPs).[3] Following, we will examine their collective properties and highlight the differences between SgNPs and PgNPs.

1.1.2 Introduction to and Self-Assembly of SgNPs

SgNPs generally consist of NPs coated with small molecules and surfactants, and self-assembly of these NPs has led to the formation of various ordered structures through the modulation of nanoscale forces. For example, charge-mediated self-assembly, using oppositely charged surfactants,[17] small molecules,[18] and linker molecules,[19] has been used to form various structures, whereas azobenzene[5,10] and spiropyran[20] molecules have been used in the light-induced self-assembly (LISA) of Au NPs (Figure 1.1a).[5] As shown by Grzybowski and co-workers, reaction conditions, including solvent composition and ligand surface density, play a large role in determining the resultant structure.

Patchy particles can also be assembled into various structures depending on size, position, and number of patches, in addition to the driving force.[21-23] A representative example[23] is the formation of a colloidal Kagome lattice (Figure 1.1b). Here, triblock **ABA** Janus particles (JPs), in which the outer **A** blocks are hydrophobic and the inner **B** block is charged, are assembled via hydrophobic effects. Additionally, different interactions can be used to achieve a multi-stimulus responsive system. A representative system, demonstrated by Klajn and co-workers, was created by assembling Au core–shell NPs and Fe_3O_4 NPs that were modified with azobenzene.[10] As shown in Figures 1.1c1 and c3, under UV light, the Fe_3O_4 NPs

assemble due to isomerization of the azobenzene from *trans* to *cis*. Under an applied magnetic field, these aggregates assemble into a linear chain (Figures 1.1c2 and c4).

Although SgNPs have demonstrated a wide array of self-assembly motifs and structures through various driving forces, there are specific limitations in design complexity and tunability. For example, LISA is limited to a small catalogue of molecular triggers, and complex assembly products are still largely limited by the inherent isotropy of the starting SgNPs.[2-4] These problems can be overcome through implementation of patchy particles. However, the synthesis of patchy particles is complex and requires complicated and sophisticated designs. Thus, much research has focused on how polymers can overcome these limitations, as discussed below.

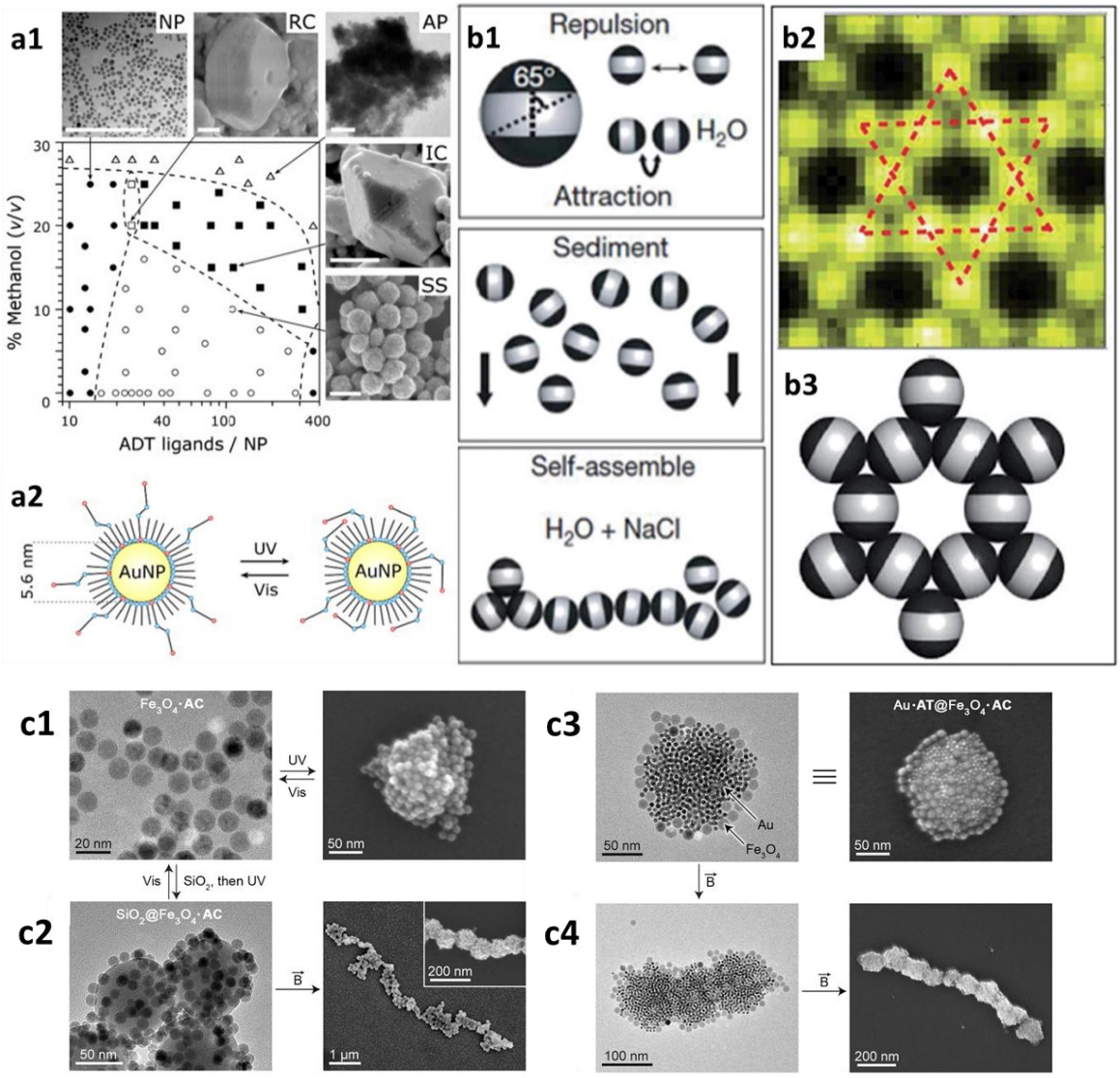

Figure 1.1 Representative assemblies of SgNPs. (a1) The phase diagram of different NP structures when Au NPs modified with azobenzene dithiol (ADT) are exposed to LISA based on the number of ADT ligands on the Au NP surface and the concentration of methanol in solution, and (a2) a schematic showing the isomerization of the ADT ligands.[5] (b1) The self-assembly of triblock JPs, in which the poles are hydrophobic, and the equator is charged, into a colloidal Kagome lattice. (b2) A fluorescence image and (b3) a representative cartoon of the assembled structure.[23] (c) TEM images showing the self-assembly and disassembly of azobenzene-coated magnetic Fe_3O_4 NPs and Au core–shell NPs when exposed to light and an applied magnetic field.[10]

1.1.3 Introduction to PgNPs

PgNPs offer several distinct advantages over SgNPs, including: 1) increased stability in solution; 2) a higher degree of functionality and tunability; and 3) increased biocompatibility.[3] For example, Yamamato and co-workers showcased the enhanced stability of Au NPs modified with cyclic poly(ethylene glycol) (PEG); these particles retained dispersibility through freezing and heating in addition to exhibiting prolonged blood circulation for use in biomedical applications.[24] Additionally, polymers are highly tunable and can be tailored to exhibit specific properties. Modifying NPs with tailored polymers provides precise control over particle interactions under different conditions, yielding thermodynamically stable structures. To control these interactions, polymer grafting density (σ), length (N), and composition, along with particle shape and size need to be considered.

1.2 PgNP Structural Parameters

1.2.1 Inorganic Cores

Inorganic NPs have properties that are dependent on their size, shape, and composition.[1-4] For example, Fe_3O_4 NPs are magnetic and can be manipulated by applied magnetic fields,[25] and Pt NPs have enhanced catalytic properties that have been used in applications ranging from cancer therapy[26-28] to fuel cells[29,30] to nanomotors.[31] Noble metals are particularly interesting, as they exhibit a strong localized surface plasmon resonance (LSPR).[3] LSPR occurs when the conduction-band electrons of the NP collectively oscillate when exposed to a specific frequency of light. This coupling of the plasmon with the incident light results in an enhancement of the electric field near the particle surface. The enhanced field rapidly

decays with distance from the particle. Furthermore, the composition, shape, and size of the particle directly influence the location and number of plasmon peaks, as defined by Mie theory. Here, the extinction cross-section of a spherical NP can be defined as:[32]

$$E(\lambda) = \frac{24\pi^2 N a^3 \varepsilon_m^{3/2}}{\lambda \ln(10)} \frac{\varepsilon_2(\lambda)}{(\varepsilon_1(\lambda)+2\varepsilon_m)^2+\varepsilon_2(\lambda)^2} \quad (1.1)$$

where λ is the wavelength of light, a is the radius of the particle, ε_1 and ε_2 are the real and imaginary parts of the metal dielectric function, ε_m is the dielectric function of the surrounding medium, and N represents the finite number of polarizable elements for the particle of interest. The extinction energy is proportional to the particle radius, resulting is a red-shift of the LSPR with increasing particle size. Additionally, particles with a more complex shape exhibit a greater number of plasmon peaks.[32] For example, nanorods (NRs) exhibit two primary plasmon peaks, corresponding to their longitudinal and transverse modes,[33] whereas nanotriangles exhibit three plasmon peaks, corresponding to the in-plane quadrupole, out-plane quadrupole, and the in-plane dipole.[34] The splitting and location of these peaks can be further manipulated by changing the aspect ratio of the particle. This tunability is incredibly useful and has enabled use of these particles in a wide array of applications, including sensing,[14,33,35] imaging,[36,37] catalysis,[15,31,38] photovoltaics,[39] and drug therapies (*e.g.*, photothermal, photoacoustic, and drug delivery).[4,25-28,38,40-43]

1.2.2. Polymer Brush Regimes

Polymers grafted onto a NP surface can be thought of as a polymer brush, which can exist in one of three regimes when the NP is spherical, as shown in Figure 1.2.[2,3,44] At low σ and N, the polymers adopt a loose coiled structure, where $\sigma < R_g^{-2}$

(R_g is the radius of gyration of the chains). This regime is denoted the mushroom regime, in which polymer chains do not interact with one another, as shown in the orange area. As σ and N increase beyond the threshold for chain entanglement, the polymer chains will begin to stretch out and enter the semi-dilute polymer brush (SDPB) regime (blue area). As σ continues to increase, the polymer chains enter the concentrated polymer brush (CPB) regime (green area). Interestingly, at high σ and high N, the brushes can initially exist in the CPB regime but transition to the SDPB regime once chains exceed a specific distance from the particle center (r_c) (yellow area). This phenomenon arises from the change in interchain spacing, which increases with respect to distance from the particle surface. The polymer brush height (h) scales as $h \propto N^{0.6}$ and $h \propto N^{0.8}$ for the SDPB and CPB regimes, respectively.

Additionally, PgNPs can be further subdivided based on the composition of the polymer brushes. These additional subcategories are homopolymer-PgNPs (H-PgNPs), mixed-polymer-PgNPs (M-PgNPs), and block copolymer (BCP) grafted NPs (B-PgNPs).

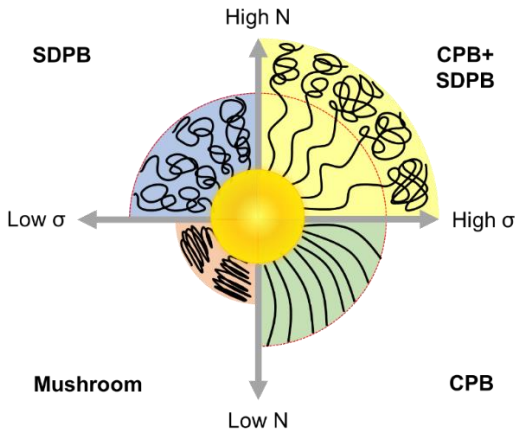

Figure 1.2 Schematic of polymer-brush regimes on a NP surface with respect to polymer length and grafting density.[3,44]

1.2.3 PgNP Surface Chemistry

Inorganic NPs are readily modified by grafting polymers to the NP surface or via a "grafting from" method, in which polymerization is initiated on the NP surface; however, this method usually leads to a uniform distribution of polymer across the particle surface, which limits the potential complexity of resulting assemblies.[3,45] Thus, to increase the range of assemblies that can be achieved, there have been many recent advances in regiospecific functionalization, including selective attachment of polymers to specific crystal facets of the NP surface and masking of regions on the NP surface with one polymer brush to direct the grafting of additional polymer to another region.[12,46,47] However, anisotropic functionalization of NPs remains difficult. Thus, a common method to overcome to overcome regiospecific functionalization is microphase separation,[48] in which different homopolymers[12,49-53] or BCP blocks[25,35,36,40,54,55] segregate into distinct regions, which can induce anisotropic interactions even though the surface chemistry is isotropic.

1.2.3.1 Surface Patterning of M-PgNPs

The design of M-PgNPs, in which polymers can phase segregate, is largely governed by the Flory and Huggins' theory of polymer mixing, which requires that both polymers be immiscible.[56,57] These systems are also governed by the σ, the grafting ratio, and the asymmetry of the polymer lengths, which can lead to vertical and/or lateral phase segregation. As shown in Figure 1.3a,[57] vertical phase segregation leads to layered nanostructures in which one polymer forms an inner core near the NP surface, while the other polymer stretches to form an outer shell. Conversely, lateral phase segregation leads to a rippled nanostructure in which

polymer regions alternate along the surface, yielding distinct patches. The last structure, which occurs when both vertical and lateral phase segregation are present, is the dimpled nanostructure. This structure occurs when one polymer region is surrounded by the other polymer region, yielding periodically distributed lattices on the NP surface.[56,57]

A representative system was reported by Zhao *et al.*, who used a "grafting from" method by attaching Y-shaped initiators on the surface of Si NPs.[56-61] Sequential surface-initiated polymerizations were then performed at these sites to grow poly(*tert*-butyl acrylate) (PtBA), using atom-transfer radical polymerization (ATRP), and PS, using nitroxide-mediated radical polymerization (NMRP); both polymer lengths and σ were kept roughly the same. Microphase separation was triggered, yielding rippled structures in which the size of the ripples increased with increasing molecular weight (M_w) (Figure 1.3b).[59]

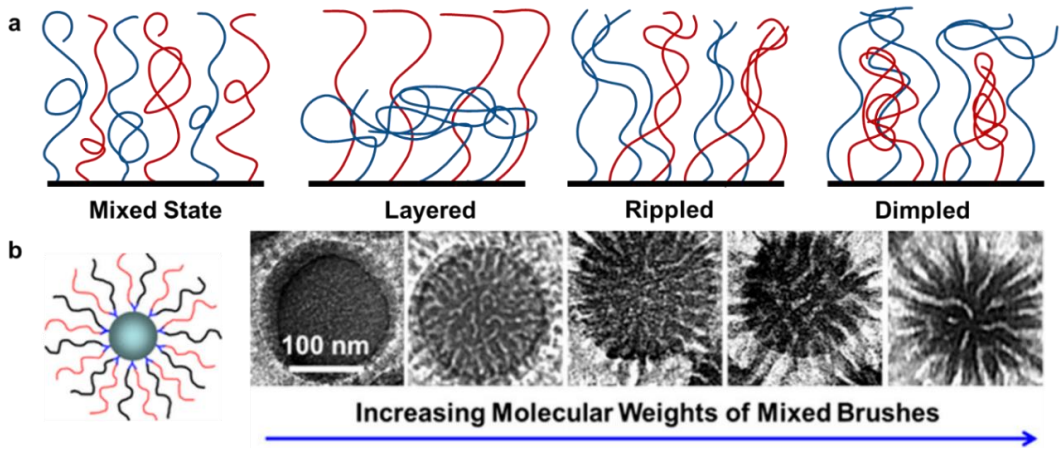

Figure 1.3 Microphase separation of mixed-polymer brushes when tethered to a NP surface. (a) A schematic of the different types of phase segregation of two immiscible polymers tethered to a NP surface.[57] (b) A schematic of an M-PgNP (left) and the phase segregation of PtBA and PS, tethered to a Si NP. This scheme yields rippled nanostructures, where the ripple size increases with polymer M_w (right).[59]

1.2.3.2 Surface Patterning of H-PgNPs

Similar to mixed brush systems, lateral phase separation can also be achieved with homopolymer systems through careful tuning of the solvent conditions and σ.[49,50,62] Kumacheva and co-workers demonstrated the formation of patchy particles by altering solvent conditions of PS-modified Au NPs. As the solvent quality is reduced, the polymer brush collapses, forming discrete patches on the particle surface (Figure 1.4a).[49] The number of patches is then controlled by the ratio between the particle diameter and the polymer length. At a constant σ, phase segregation was preferred for smaller particles, yielding patchy particles, whereas larger particles yielded core−shell structures when σ was not sufficiently small, highlighting the importance of a low σ value. Meanwhile, as the particle size was increased or the polymer length was decreased, the number of patches increased (Figures 1.4b and c).[49] Additionally, it was shown that patches preferentially formed at the tips of shaped particles due to the difference in surface energy. This behavior is summarized in a phase diagram (Figure 1.4d).[49]

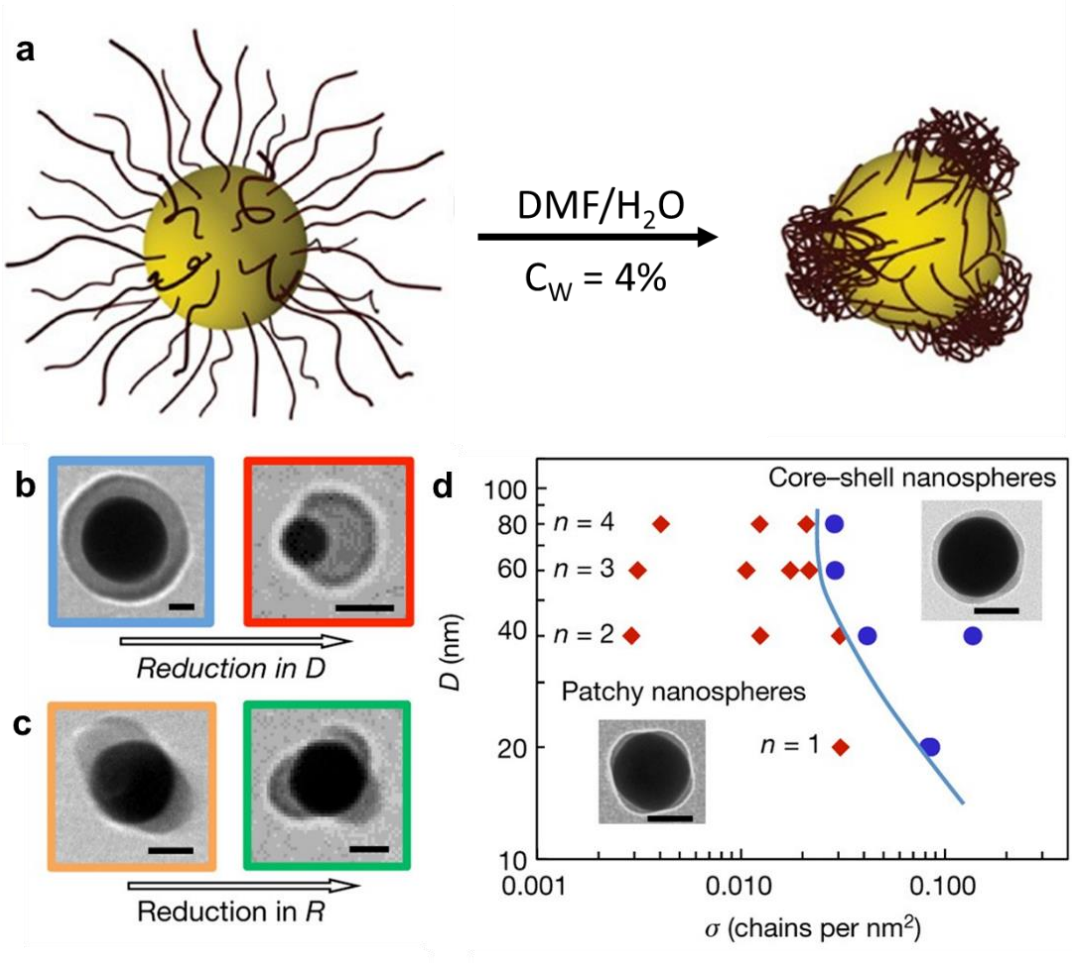

Figure 1.4 Microphase separation of H-PgNPs via selective solvents. (a) A schematic of the formation of patchy, PS-tethered Au NPs via solvent control. (b) The transition from core−shell to patchy particles via change in particle size. (c) Polymer-length effects on the number of patches on Au NPs. (d) A phase diagram showing how particle size and σ impact the morphology of PS-tethered Au NPs, where *n* represents the number of patches on patchy nanospheres.[49]

1.2.3.3 Surface Patterning of B-PgNPs

As shown above, H-PgNPs can form patchy particles; however, the solvent conditions used to achieve these patches can lead to particle instability, lowering product yields.[3] This effect can potentially be overcome using BCPs as opposed to

homopolymers, as one block of the BCP can stimulate the phase segregation while another block serves to stabilize the particle in solution. As reported by Kumacheva and co-workers, B-PgNPs, in which the inner BCP block is solvophobic, behave similarly to H-PgNPs, as described previously.[63] Simulation results show that BCP length and σ, along with solvent interactions with the solvophobic block, directly influence both the number and orientation of patches on the B-PgNP surface.[64] Additionally, the sequence of blocks within the BCP can also influence the surface patterning of B-PgNPs.[65] For example, when the solvophilicity of the blocks is inverted, meaning that the inner block (**A**) is solvophilic and the outer block (**B**) is solvophobic, large σ values induce greater phase segregation of the outer solvophobic block. Similarly, as the f_B value, defined as $N_B/(N_A+N_B)$, increases, there is also an increase in phase segregation. This effect leads to patchy particles with an increased number of patches, which is the reverse of what is expected from H-PgNPs[66] and B-PgNPs,[64] for which the inner BCP block is solvophobic (Figure 1.5a-b).[65] This observation is explained by the repulsion between the solvophilic inner BCP blocks as they swell under favorable solvent conditions.

Owing to the number and geometry of the patches, these patchy particles have been shown to assemble into a variety of structures (Figure 1.5c),[65] including small clusters, chains, and branched networks. This work shows that changes in the BCP structure, coupled with tailoring of NP surface and solvent interactions, can be used to control the directionality of the NP assembly.

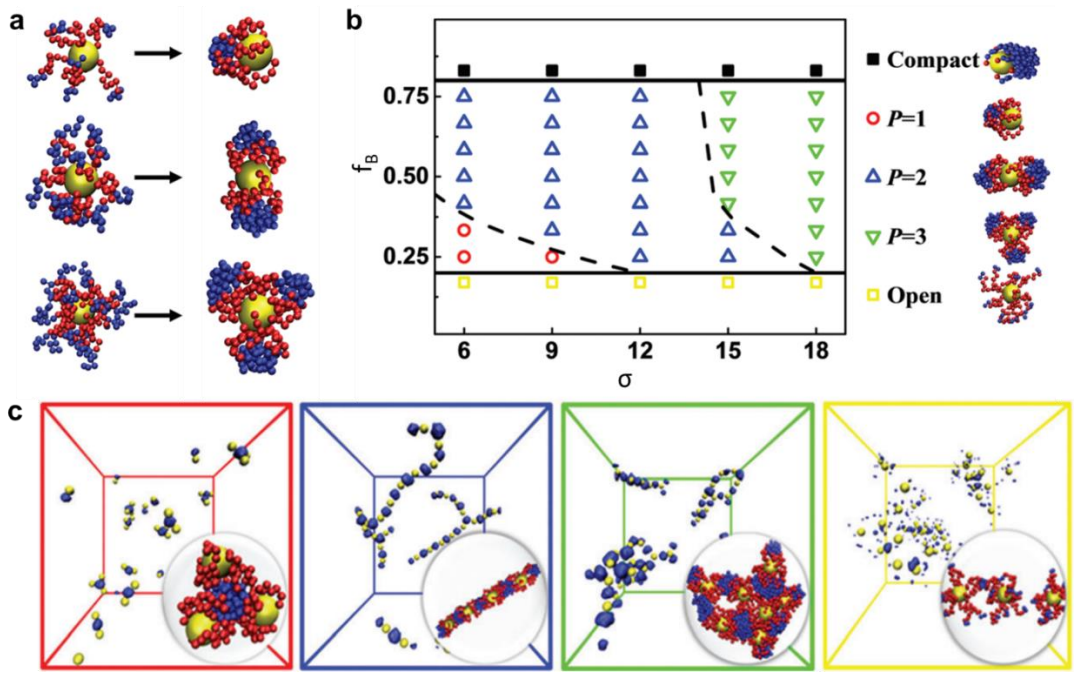

Figure 1.5 Microphase separation of B-PgNPs and their self-assembly. (a) Representative images of various nanoparticles modified with amphiphilic **AB** diblock copolymers, in which the inner block **A** is solvophilic and the outer block **B** is solvophobic, with different σ and f_B values. From top to bottom: (top) σ = 7 and f_B = 0.33, (middle) σ = 12 and f_B = 0.5, and (bottom) σ = 18 and f_B = 0.5; these conditions yielded 1-, 2-, and 3-patch particles, respectively. (b) A phase diagram relating the number of particle patches to σ and f_B of the tethered-diblock polymers. (c) Representative superstructures of the particle self-assembly when modified with the above described amphiphilic diblock polymers. From left to right: (far-left) σ = 7 and f_B = 0.33, (left-middle) σ = 12 and f_B = 0.5, (right-middle) σ = 18 and f_B = 0.5, and (far-right) σ = 9 and f_B = 0.17, which yield small clusters, chains, branched networks, and individual NPs, respectively. Here, it is noted that a sufficiently high f_B value is needed to facilitate polymer phase segregation, and thus particle self-assembly, as shown in the rightmost image.[65]

1.3 Templated Self-Assembly of PgNPs

NP self-assembly is advantageous, as the assembled structures can yield unique properties that differ from those of the individual building blocks. One of the more straightforward assembly techniques uses a template to guide the particles into position. In particular, the design and functionalization of these templates can dictate the location, orientation, and alignment of the assembling NPs, as particles are confined within the template through attractive interactions between the template and particle or via the formation of chemical bonds.[67,68] This strategy enabled the formation of a variety of nanostructures with high levels of complexity; these nanostructures have been used for a range of applications, with particular interest in sensors.[69] Here, assemblies will be categorized based on the types of templates used.

1.3.1 Hard Templates

Hard templates are rigid structures and can be traditional pressed devices, such as the polydimethylsiloxane (PDMS) microchannels used in microfluidic devices,[70,71] channels made through lithography,[72] and nanomaterial-based templates, such as the nanopores in anodic aluminum oxide (AAO)[73,74] or carbon nanotubes (CNTs).[75] The confinement dictates the orientation and alignment of the NPs as they enter. For example, Zhu and co-workers were able to control the packing and arrangement of PS-tethered Au NPs in AAO nanopores by controlling the ratio between particle diameter (D_p) and channel diameter (D_c), as shown in Figure 1.6A.[73] By tuning this ratio, they caused the particles to adopt linear arrays that were 1, 2, or 3 layers thick. This control over particle assembly was made possible because the polymer brush of the assembling PgNPs was flexible enough to allow for

confinement in spaces smaller than the overall diameter of the PgNPs. Similarly, Zhu and co-workers showed that this strategy works for Au NRs as well, in which PS-tethered Au NRs packed linearly or helically, dependent on an applied electric field.[74] Additionally, Liz-Marzan and co-workers used multiwall CNTs (MWCNTs) to assemble PS-sulfonate-modified Au NRs into nanostrings.[75]

1.3.2 Soft Templates

Soft templates are non-rigid structures that are generally either emulsions[76-80] or polymer matrices.[81-84] Only emulsions will be discussed in detail here, as polymer matrices will be discussed in depth later. Emulsion-based, liquid−liquid interfacial self-assembly will also be discussed in a later section.

The co-assembly of BCPs and PgNPs within microdroplets has enabled preparation of highly tunable, complex structures. Pioneering work was performed by Yang and co-workers. As shown in Figure 1.6B,[78] polystyrene-*b*-poly(4-vinylpyridine) (PS-*b*-P4VP) was assembled into colloidal structures, mirroring molecular geometries, via the membrane-extrusion emulsification of chloroform in a polyvinyl alcohol (PVA) solution. Afterwards, Au NPs were grown within the P4VP domains, which served as the outer domains. Jiang and co-workers later followed a similar process to expand upon these available structures, using both BCPs and polymer grafted Au NPs in their assembly.[79] They demonstrated pupae, pinecones, and acorn-shaped structures, with alternating PS and poly(2-vinylpyridine) P2VP layers, through careful manipulation of the volume percentage of PS-modified Au NPs when assembled with PS-*b*-P2VP (Figure 1.6C).[79] The assembly conditions were further refined to achieve other structures through tuning of the grafted PgNP

polymers (PS or a PS/P4VP mixture), BCP length and composition, and addition of surfactants. These approaches yielded analogous structures to those presented in Figure 1.6B,[78] with Au NPs oriented along the boundaries between the BCP domains.

Additionally, emulsion-based methods can be used to assemble binary PgNPs together, yielding larger 2D and 3D structures. For example, Zhu and co-workers assembled a binary mixture of PS-tethered Au NPs into core−shell nanospheres within nanodroplets (Figure 1.6D).[80] In this system, polymer length determined if the particle was located within the core or outer shell. Au NPs modified with shorter PS were preferentially located in the outer shell, due to the change in hydrophilicity.

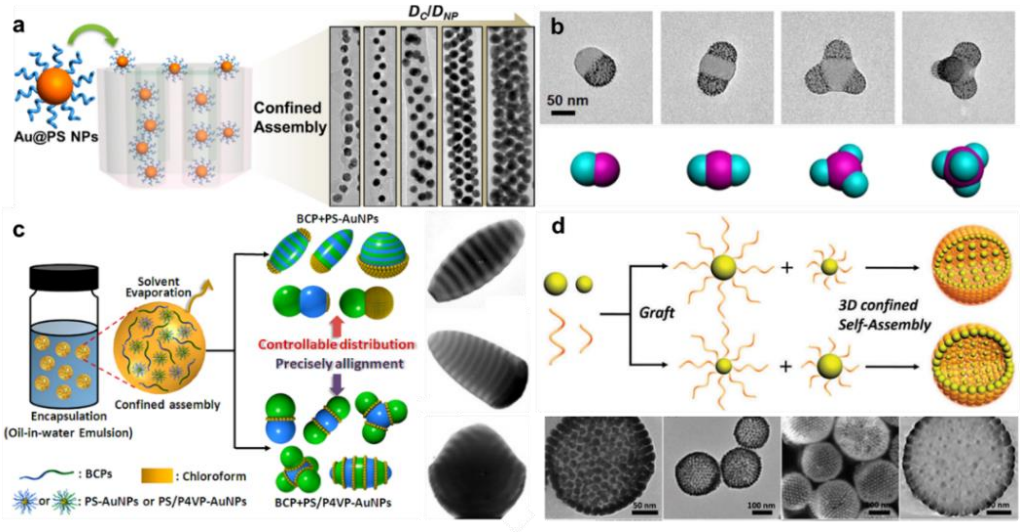

Figure 1.6 Template-based PgNP assembly. (a) The confinement and packing of PS-tethered Au NPs within AAO cylindrical nanopores, along with representative TEM images of the ensembles.[73] (b) Representative TEM images and cartoons of PS-*b*-P4VP colloidal molecules, with Au NPs embedded within the P4VP domains.[78] (c) The formation of hybrid nanostructures formed from the co-assembly of BCPs and polymer-tethered Au NPs in emulsion droplets along with representative iodine-stained TEM images of the pupa, pinecone, and acorn structures.[79] (d) The co-assembly of PS-tethered Au NPs of different sizes into core−shell nanostructures along with representative TEM and SEM images.[80]

1.4 Self-Assembly of PgNPs in Polymer Matrices

BCPs are known to phase separate in polymer matrices due to unfavorable enthalpic penalties between incompatible blocks, yielding well-defined nanostructures.[3,81] As an example, we will focus on an amphiphilic **AB** diblock copolymer of length *N*. As *N* increases, the incompatibility and resulting phase separation of the two polymer blocks increases due to the entropic mixing of the two blocks. Additionally, the enthalpic component is governed by the Flory-Huggins interaction parameter (χ_{AB}), which, when greater than 0, indicates that mixing of the two blocks is not favored. When $N\chi_{AB}$ is greater than 10.5, a periodic mesophase is formed, which is dependent on f_A; f_A is defined as N_A/N. As f_A is increased from 0 to 0.5, the ordered mesostructure changes from spheres, to cylinders, to the bicontinuous phase, to lamellae.[82]

These interesting phase properties have led researchers to incorporate NPs into BCP thin films to produce hybrid materials with unique electronic, optical, magnetic, and mechanical properties.[83,84] Traditionally, incorporation can be done in one of two ways: (1) via an *in situ* growth, in which the NPs are templated by the BCP assemblies,[85-87] or (2) via the co-assembly of BCPs and NPs.[88-90] This dissertation will focus on the later approach. The assembly technique relies on the phase separation of the NPs and BCPs to dictate the spatial arrangement of the NPs and overall morphology of the resultant structures.[91] The enthalpic contributions are controlled largely by the surface chemistries of both the NPs and BCPS, whereas the entropic contributions arise based on the NP size relative to that of the BCP domains.[92-94] These interactions can be further mitigated based on the NP capping

agents, and much such research has been performed using SgNPs;[95-98] however, only PgNPs will be discussed in detail here.

To gain control over particle orientation, it is important to consider the wettability of the PgNP polymer brush in the surrounding polymer matrix. The wettability can be controlled by tailoring the polymer composition and length, along with the polymer brush σ.[99,100] These interactions can then be manipulated to control the orientation and spatial arrangement of the PgNPs.[101] Thus, we can divide the interactions between the PgNPs and polymer matrix as being either incompatible or compatible.

1.4.1 Incompatible Interactions Between PgNPs and Polymer Matrices

As stated previously, phase separation occurs when the PgNP polymer brush is incompatible with the surrounding polymer matrix.[102-104] Additionally, spatial arrangement and particle orientation are governed by interparticle interactions, including dipole−dipole and van der Waals interactions. For example, Tao and co-workers reported the assembly of polymer grafted-silver nanocubes (Ag NCs), aligned face-to-face or edge-to-edge, within a thin polymer film, as shown in Figure 1.7.[102] Ag NCs were modified with either hydrophilic polyvinyl pyrrolidone (PVP) or PEG, and the polymer film is hydrophobic PS. The films were annealed, which triggered the particle assembly into chains, in which Ag NCs modified with PVP assembled edge-to-edge, and AgNCs modified with PEG assembled face-to-face. This strategy offers a facile way of manipulating particle orientations and interactions and can be expanded further by using particles with different shapes, such as NRs and NTs.[104]

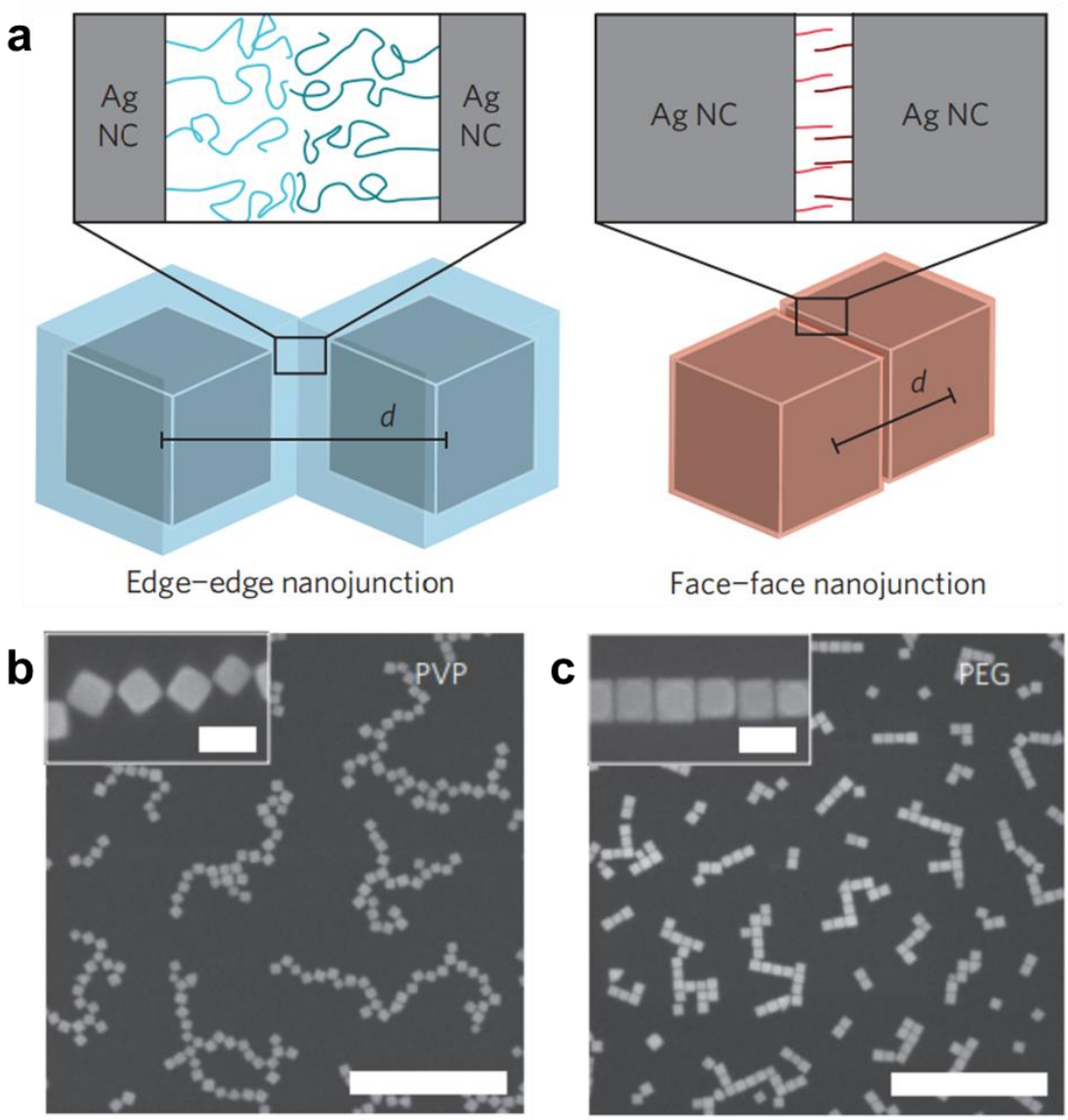

Figure 1.7 The self-assembly of polymer-modified Ag NCs in an incompatible thin polymer film. (a) Schematic of the assembly of polymer-modified Ag NCs in edge-to-edge and face-to-face orientations, which is dependent on the polymer length. (b,c) SEM images of the nanochains, comprised of hydrophilic, polymer-tethered Ag NCs in a PS thin film after annealing. Ag NCs are modified with (b) thiol-terminated PVP (M_W: 55 kg mol^{-1}) and (c) (11-mercaptoundecyl)tetra(ethylene glycol), which is thiol-terminated PEG with a chain length of 4. The scale bars for the large-area images are 1 μm, and the scale bars for the inset images are 100 nm.[102]

1.4.2 Compatible Interactions Between PgNPs and Homopolymer Matrices

In thin films, when the polymer brush of the PgNPs is compatible with the polymer matrix, unique assembly properties of the PgNPs can still arise. For example, in a homopolymer film, the polymer-brush density can influence the particle assembly due to the entropic penalty caused from the compression and extension of the polymer brush.[105] In the case of high σ (SDPB or CPB regimes), the PgNPs segregate to minimize the entropic penalty caused by the polymer shell compression. This behavior is known as autophobic dewetting, and it becomes more predominant as the particle surface curvature decreases.[106] When σ is low (SDPB or mushroom regimes), the polymer brush is more compressible, which can leave areas of the particle surface exposed to the polymer matrix. This situation leads to an interesting combination of forces. The enthalpy-increase leads to the phase segregation and aggregation of the PgNPs, which is counterbalanced by the steric repulsion between the polymer brushes on neighboring PgNPs. These conflicting effects can be controlled to yield various nanostructures, as demonstrated by Kumar *et al.*[107-109] In their work, PS-grafted Si NPs were assembled in a PS matrix in which the resulting structures were controlled by the interplay between the PgNPs ($\sigma N^{0.5}$) and the polymer matrix ($1/\alpha$). Here, α is defined as N/P, where N is the length of the polymer brush, and P is the length of the matrix polymer. Their assembly results can be seen in Figure 1.8,[107] which highlights the utility of this approach. Their results demonstrate how integral the polymer brush conformation change is in achieving the anisotropic assembly of PgNPs. Here, the authors use an isotropic building block,

which is significantly easier to synthesize compared to anisotropic PgNPs, which require regioselective modification.

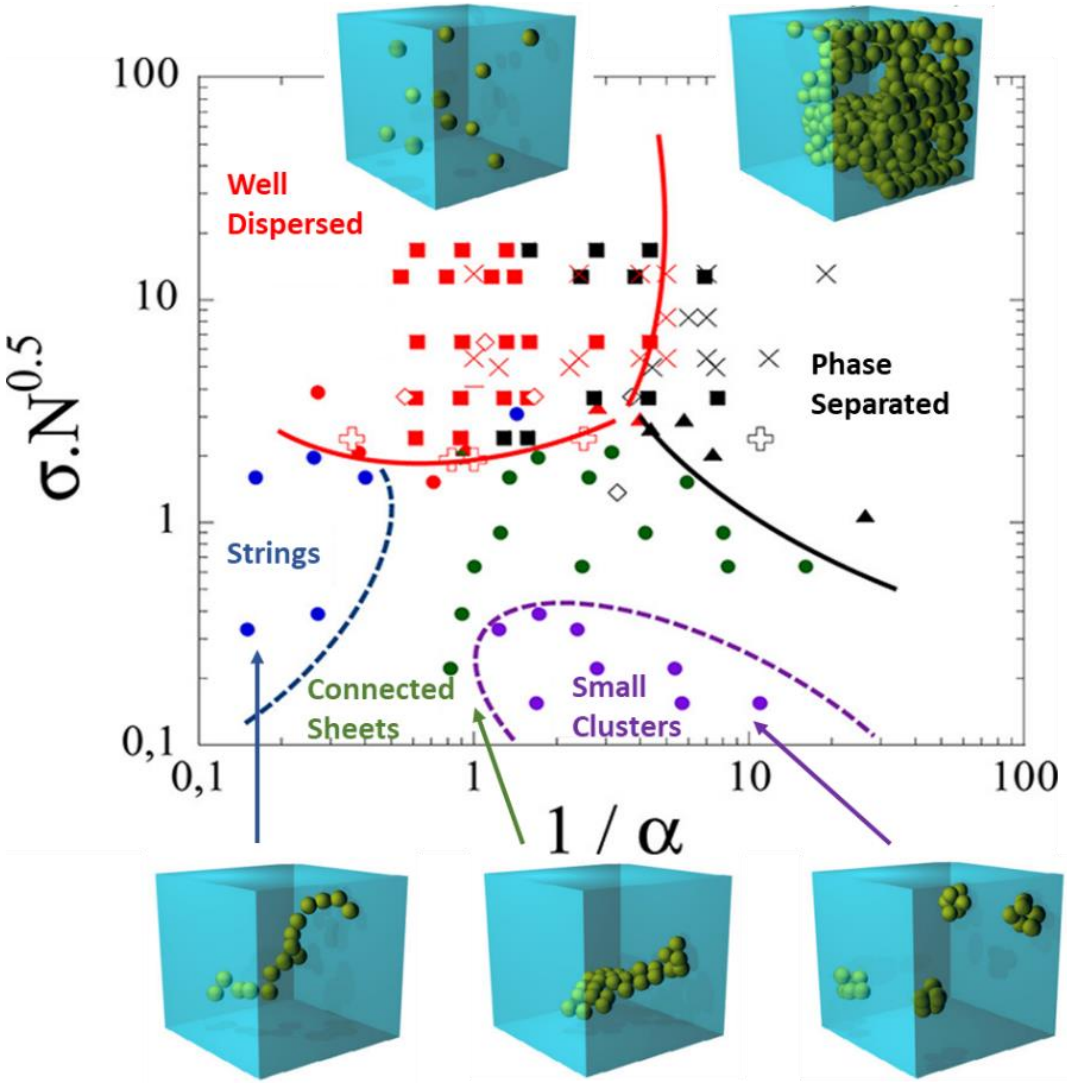

Figure 1.8 Phase diagram of the self-assembly of H-PgNPs in a compatible polymer matrix. The phase diagram is a function of $\sigma N^{0.5}$ and $1/\alpha$, where $\alpha = N/P$, N is the length of the polymer brush, and P is the length of the matrix polymer. Most experiments were performed at a loading of ~5 vol% with particles between 7 and 18 nm in diameter. The schematics represent the nanostructures formed. The red region represents well-dispersed particles, the black region represents phase-separated particles, the purple region represents small clusters, the green region represents connected sheets, and the blue region represents strings.[107]

1.4.3 Compatible Interactions Between PgNPs and BCP Matrices

In BCP matrices, the microphase domains tend to be comparable in size to the PgNPs, and thus, these domains can be used to encapsulate PgNPs with favorable polymer brush interactions with one block of the BCP matrix. This confinement controls the spatial arrangement and orientation of the PgNPs within the matrix. It is also noted that PgNPs with high σ are often used to avoid unfavorable interactions caused when the NP core becomes exposed at low σ.[3,106]

Different BCP phase domains, such as the cylindrical phase domain, can be tailored and used to encapsulate PgNPs; however, this approach remains challenging. In particular, the enthalpic penalty to confine NPs within cylindrical micelles is high, which causes a phase change of the cylindrical phase domains into spherical domains.[110] To overcome this problem, Zhu and co-workers reported the encapsulation of PgNPs within cylindrical micelles via a directed supramolecular assembly (Figure 1.9a).[111] PS-*b*-P4VP and pentadecylphenol (PDP) were added to chloroform to form PS-*b*-P4VP/PDP comb−coil supramolecules. Hierarchal structures were then achieved via the addition of PS-modified Au NPs to the BCP matrix. Upon annealing, the Au NPs assembled linearly within the centers of the PS cylindrical domains. The supramolecular matrix was then disassembled, yielding cylindrical micelles composed of PS-Au NP cores and P4VP outer shells.

This approach can also be used with other NP shapes, such as NRs, as shown in Figure 1.9b.[112] Of interest, NRs were found to assemble side-by-side into the ordered smectic B phase. This organization resulted from the high PgNP polymer brush σ, which weakened the interactions between the polymer matrix and the PgNP

polymer brush. Thus, the polymer brush was too dense to penetrate, leading to autophobic dewetting. To circumvent this phenomenon, NRs were modified with binary brushes of PS of different lengths, which improved the wettability and dispersion of the NRs within the PS domains. The NR and PS domain sizes also impacted the NR assembly and orientation, as longer NRs assembled parallel to the cylindrical micelles, whereas short NRs were ordered perpendicularly. When the micelle diameter was large, long NRs were hexagonally packed and twisted along the cylindrical axis to relieve the polymer conformation entropy and to accommodate the excluded volume of the polymer-capped ends of the NRs. In addition to cylindrical phases serving as templates, the above method can also be used with the lamellar phase domain to assemble different shaped NPs into extended 2D and 3D lattices, as shown in Figure 1.9c.[113]

Finally, high levels of nanostructure complexity can be achieved via the assembly of PgNPs in BCP matrices. As reported by Nandan and co-workers, PS-modified AgNPs were found to assemble into helices within the cylindrical PS domains of PS-*b*-P4VP films, as shown in Figure 1.9d.[114] These structures were theorized to exist, along with others such as zigzag ensembles. However, the conditions to achieve these structures are highly constrained, which makes the targeted assembly of these structures difficult.[115] Overall, controlling the interactions between the PgNP polymer brush and the polymer matrix is crucial in achieving the self-assembly of PgNPs in polymer matrices. Control can largely be accomplished through fine tuning the σ of the PgNP polymer brush, whereas the BCP phase domains can be used to direct the assembly of structures that are more complex.

However, control remains challenging, as mitigating the competing forces and interactions between the NPs and BCPs makes these techniques difficult to replicate.

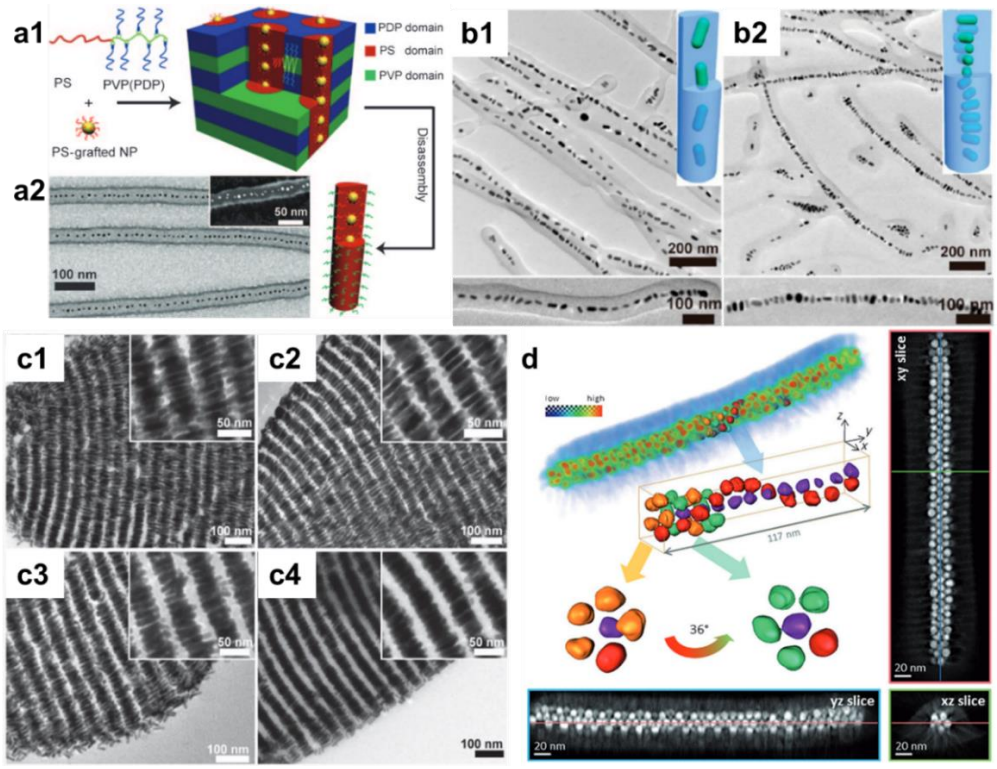

Figure 1.9 The self-assembly of PgNPs in BCP matrices. (a1) Schematic of the PS-*b*-P4VP/PDP comb–coil supramolecules. The PS block forms cylindrical phase domains in which the PS-tethered Au NPs then assemble linearly within the PS domains. The cylindrical micelles are then isolated upon disassembly. (a2) Bright-field TEM image of the isolated micelles encapsulated with the Au NPs; the inset is a dark-field TEM image.[111] (b) Bright-field TEM images of hybrid cylindrical micelles formed by the assembly of PS-tethered Au NRs within PS-*b*-P4VP/PDP supramolecules in which NRs are assembled (b1) end-to-end or (b2) side-by-side.[112] (c) Representative TEM images of PS-modified Au NR superlattices formed in P4VP(PDP) assemblies. Images show the end-to-end distance dependance caused by varying the length of PS, which are (c1) PS_{5K}, (c2) PS_{12K}, (c3) PS_{29K}, and (c4) PS_{50K}. Insets are magnified TEM images.[113] (d) 3D reconstruction obtained from the tomography of PS-tethered Ag NPs helically assembled within the PS domain of a nanofiber formed from a PS-*b*-P4VP matrix.[114]

1.5 Self-Assembly of PgNPs at Interfaces

Interfacial self-assembly is a widely used technique that can lead to the formation of various 2D and 3D structures. The reduction of interfacial energy drives the assembly as particles are transferred from one phase to another along the interface.[68] These phases can be tuned to control the assembly conditions, and the possible combinations of these phases are liquid–air and liquid–liquid.

1.5.1 Liquid–Air Interfaces

Liquid–air interfaces have shown great promise as templates to direct the self-assembly of nanomaterials into ordered structures. For instance, the formation of nanorings is well documented for polymers and other small molecules.[116] Similarly, small NPs have been used to achieve assembled nanorings following several different proposed mechanisms, including the Marangoni effect,[117] the hole-nucleation mechanism,[118] and the breath figure (BF) method.[116,119] The latter method is of particular interest due to its versatility as it take advantage of water droplets in the air to template the assembly. Zubarev and co-workers showcased this method via the self-assembly of PS-tethered Au NRs into nanorings, as shown in Figure 1.10a.[116] Here, Au NRs were suspended in a methylene chloride solution and were drop-casted onto carbon-coated grids. As the methylene chloride dried, water droplets from the air condensed onto the substrate, and the hydrophobic PS-tethered Au NRs then preferentially assembled around the water droplets, forming rings as the water droplets evaporated.

Larger ordered nanostructures can also be achieved as reported by Cheng and co-workers in which PS-tethered Au@Ag NCs were assembled into large 2D sheets

up to 3 mm in size.[120] These NCs were suspended in a chloroform solution and dropped onto a water droplet that had been cast onto a holey copper grid. The chloroform quickly evaporated, leaving a layer of NCs at the air−water interface. The water was then slowly evaporated, leading to the assembly of the NCs into hexagonal-tight-packed nanosheets with a high degree of uniformity. Furthermore, these large sheets showed enhanced mechanical properties and could be further shaped into nanoribbons and origami-type structures, as shown in Figure 1.10b.[120] This method can also be used to assemble different shaped particles into nanosheets and was implemented to form bilayers in which two different sized PgNPs comprised the respective layers.[121,122]

Larger, 3D extended superstructures can also be achieved through careful manipulation of the PgNP polymer brush. At sufficiently high σ, the outer polymer brush, which is in the SDPB regime, is relatively "soft", allowing for interpenetration of polymer brushes between adjacent NPs. The inner polymer brush, which is in the CPB regime, remains rigid and acts as a buffer to balance out the van der Waals interactions between particles. Thus, tuning of the polymer brush properties, such as σ and *N*, along with particle size and identity, can directly influence the packing structure and expand the properties of resulting superstructures.[123] This tunability was showcased by Alivisatos and co-workers, who reported the co-assembly of binary PS-tethered NPs (Au and Fe_3O_4) into 2D and 3D superstructures at the interface of diethylene glycol and air (Figure 1.10c).[124] The crystal structure was modulated by tuning the particle feeding ratio, NP core size, and polymer brush length, which greatly expanded the number of targeted structures that could be achieved through

minimal fine tuning of the PgNP building blocks. Additionally, Alivisatos and co-workers showed that the mechanical properties of these superlattices are largely governed by the composition of the polymer brush, which creates a viable pathway to synthesize high-strength, ultrathin films.[125]

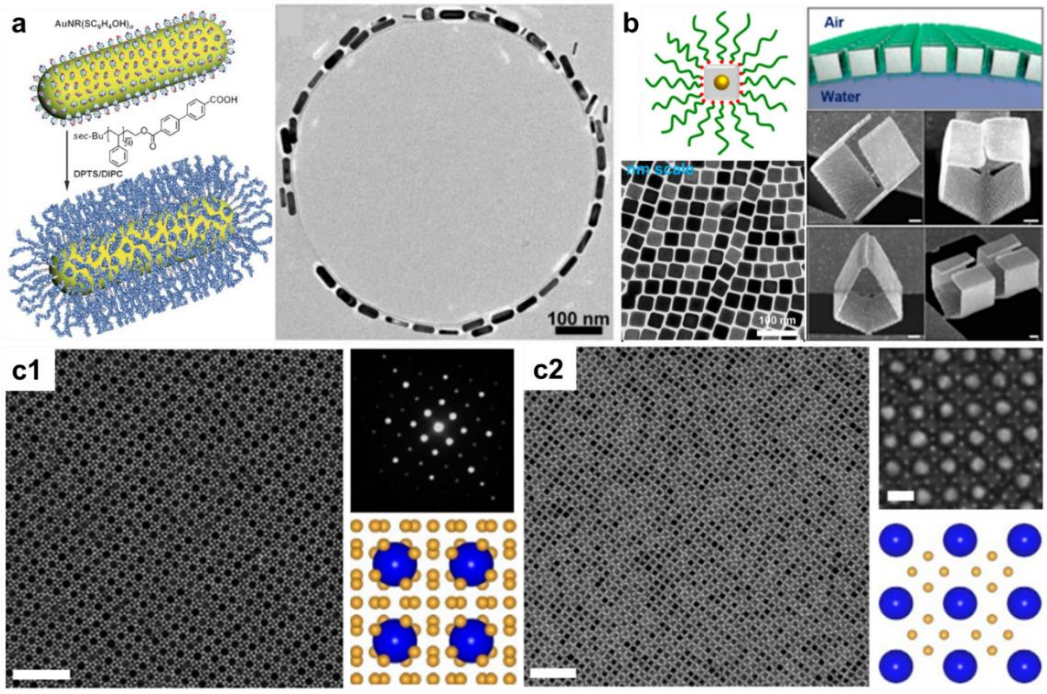

Figure 1.10 The self-assembly of PgNPs at liquid–air interfaces. (a) The interfacial self-assembly of PS-tethered Au NRs into nanorings at the air–water interface. The left is a cartoon representation of the PS-modified Au NRs, and the right is a TEM image of the assembled ring structure.[116] (b) The interfacial self-assembly of PS-tethered Au@Ag NCs at the air–water interface. From left to right: a TEM image of a Au@Ag NC sheet, followed by four images of plasmonic origami structures made from the NC sheet.[120] (c) The interfacial self-assembly of PS-tethered 3.8 nm Au and 14.3 nm Fe_3O_4 NPs into extended 2D and 3D superstructures at the air–diethylene glycol interface. (c1) The NaZ_{13} and (c2) $C_{60}K_6$ crystal structures. The left is a low magnification TEM image, the lower right is a structural model of the [001] crystal facet of the structure, and the top right is the corresponding (c1) selected-area diffraction (SAED) pattern or (c2) SEM image of the superstructure.[124]

1.5.2 Liquid–Liquid Interfaces

Liquid–liquid interfacial self-assembly has long been investigated since the early 1900s, as showcased by the work of Pickering and Ramsden, who demonstrated the formation of resistant films, composed of micron-sized particles, such as Fe_3O_4 and Si, at the interface of immiscible liquids.[126-128] Later, Pieranski derived a theoretical model in which the assembly of spherical particles with radius (r), at an oil–water interface is driven by the overall decrease in free energy, E_0 to E_1, yielding ΔE_1:[129]

$$E_0 - E_1 = \Delta E_1 = -\frac{\pi r^2}{\gamma_{OW}}[\gamma_{OW} - (\gamma_{PW} - \gamma_{PO})]^2 \quad (1.2)$$

Here, γ_{OW}, γ_{PW}, and γ_{PO} are the surface tensions of the oil–water, particle–water, and particle–oil interfaces. As shown in Eqn. 1.2, in an emulsion, for which γ_{OW}, γ_{PW}, and γ_{PO} are fixed, the stability of the assembly is based on the size of the particle. Larger particles are more stable, whereas smaller particles are not as effectively trapped, as the thermal energy is comparable to the interfacial free energy. However, the wettability of the particle, which is defined by the contact angle between the particle and oil–water interface, can also dictate the stability of the emulsion, and thus the assembly. Thus, small particles can still be used to stabilize microdroplets in solution, as was shown by Russell and co-workers, who used 2.8 nm CdSe NPs to stabilize droplets at a toluene–water interface, yielding CdSe nanocapsules.[130]

Furthermore, the use of PgNPs to create these assemblies is particularly attractive as this system addresses inherent drawbacks that arise from SgNPs, such as tunability of the interparticle distance within these films.[131,132] As an example, Baumberg and co-workers used Au NPs and Ag NPs modified with the

thermoresponsive polymer, poly-*N*-isopropylacrylamide (PNIPAM), to form thin sheets at the interface of water and hexadecane. The PNIPAM reduced the surface tension of the water, lowering the interfacial energy and allowing for formation of the thin sheet. Additionally, cycling the temperature past the PNIPAM phase temperature, T_C, drove contraction and expansion of the PNIPAM, which stimulated a plasmonic response. These transitions were further evidenced via bright-field microscopy, which showed a change in interparticle distance from 1.7 nm to 1.1 nm, and then back to 1.7 nm upon cooling.[132] This work expands upon traditional interfacial self-assembly. However, newer techniques, such as microfluidics, allow for more precise control.

1.5.3 Microfluidic–Based Liquid-Liquid Interfaces

Microfluidic techniques are unique in using a flow field to direct particle self-assembly. The shear force aligns the particles in the direction of flow, which is combined with the confinement of the narrow microfluidic channels. However, the stability of the resultant structures is limited, as the assemblies are prone to decay once the flow is removed. Thus, many microfluidic templates use chemically patterned surfaces during self-assembly to promote adhesion after the flow is removed.[133,134]

The formatting of the microfluidic device can also allow for multiple streams to combine, as shown by Abell and co-workers. They used a T-junction to form microdroplets in which the oil phase was directed perpendicular to the aqueous phase. The aqueous phase consisted of three streams: Au NPs modified with methylviologen moieties, napthol containing copolymers, and cucurbit[8]uril (CB[8]) moieties. These

streams were combined with the oil phase at the T-junction, where the Au NPs directed the supramolecular self-assembly to the oil–water interface, forming microcapsules. This assembly was driven by the host–guest interactions between the CB[8] and the methylviologen and napthol groups. The microcapsules stabilized the water droplets, yielding stable structures in high yield that could be isolated once the water droplets were evaporated.[135] Furthermore, this approach can be modified to create supracolloidal structures composed of different building blocks and other stimulus-responsive properties.[136]

Microfluidics is a powerful tool that allows for precise mixing and formation of desired nanodroplet templates to dictate self-assembly. Microfluidics can also be used in solution-based assemblies, which will be discussed in detail below. Overall, although this approach is powerful, careful formatting of the microfluidic channels can be challenging, and the directionality of the flow can limit the complexity of nanostructures that can be created.

1.6 Self-Assembly of PqNPs in Solution

Self-assembly in solution has proven to be an attractive method compared to previous methods, as solution-based self-assembly is generally a flexible strategy that does not rely on the use of templates to confine particles. Self-assembly is also easier to control from a thermodynamic perspective, especially when compared to methods involving polymer films, as the low mobility of larger particles is not an issue during the assembly.[137] Self-assembly also tends to be performed under less harsh conditions, avoiding stability issues incurred from processes such as annealing, which can break the polymer–NP bonds. Furthermore, the polymer brush σ can be tuned

over a wider range in solution, as low σ values can stabilize the particles' surfaces.[49] Conversely, in thin films, a high σ is required to shield the NP cores, which both mitigates van der Waals forces between the core and surrounding media and prevents interactions between the core and polymer domains that can weaken particle confinement within the desired domain.[94] Much research has been performed to determine how PgNPs assemble in solution, with results showing that the formation of patches on the particles' surfaces is crucial in controlling the desired product.[138-140] Patchiness on the particles' surfaces can be achieved through development of inherently anisotropic surfaces[12,141,142] or though phase separation of the polymer brushes.[49,51,54] Solution-based PgNP self-assembly can be classified based on the nature of the polymer brush as outlined earlier: M-PgNPs, H-PgNPs, and B-PgNPs.

1.6.1 M-PgNP Self-Assembly

As mentioned above, mixed polymer brushes can exhibit phase separation if the polymers are immiscible, yielding patches that can be used to drive self-assembly.[56-61] Specifically, the size ratio between the polymer brush and particle, $2R_g/d$, can influence the arrangement of the NPs. For example, in a binary brush system in which $2R_g/d >>> 1$, the lateral phase separation of the two polymers will yield an amphiphilic, **AB**-like structure with the NP at the center of the two polymer brushes. Thus, when assembled, the NPs tend to stay at the interface between the two polymer regimes, yielding bilayer-type supracolloids, such as the cylindrical core–shell structures reported by Zubarev *et al.*[143] In this system, Au NPs were modified with v-shaped PEO_{50}-*b*-PS_{40}, and assembly was triggered via the hydrophobic effect by slow addition of water, which is a poor solvent for the PS block.

Manipulation of the hydrophobicity and the hydrophilicity of the two polymer brushes can also yield different structures when assembled, as demonstrated by Moffitt and co-workers (Figure 1.11a).[144] This work demonstrated the synthesis and assembly of CdS quantum dots, which was achieved using the micellization of the triblock copolymer, polystyrene-*block*-poly(acrylic acid)-*block*-poly(methyl methacrylate) (PS-*b*-PAA-*b*-PMMA) via the assembly of Cd^{2+}-complexed PAA blocks followed by reaction with hydrogen sulfide to produce the CdS particles. This procedure yielded particles with a mixed polymer brush of PS and PMMA, which were rendered amphiphilic by crosslinking the PAA, followed by base-catalyzed hydrolysis of the PMMA, yielding poly(methacrylic acid) (PMAA). Here, the PS is hydrophobic and the PMAA is hydrophilic. The addition of water yielded Janus-type structures, triggering assembly in systems above the critical water content (CWC). The assembly structures were determined by controlling the concentration of the particles and the salinity of the solution.[144,145] These structures included vesicles, micelles, and segmented wormlike ensembles in which the NPs formed hexagonally packed disks separated by PS blocks.

Selective modification to form mixed polymer brushes in which the dispersity of the two different polymers is statistically averaged has proven quite versatile and has been used with other inorganic NPs.[52,146] For example, Liu and co-workers demonstrated a similar method using Au NPs instead of CdS. They employed the triblock copolymer, poly(ethylene oxide)-*block*-poly(lipoic acid 2-hydroxy-3-(methacryloyloxy)-propyl ester-*co*-glycidyl methacrylate)-*block*-polystyrene (PEO-*b*-P(LAMP-*co*-GMA)-*b*-PS. The center block is wrapped around the Au NPs, forming

Au-thiol bonds, yielding PgNPs with a mixed polymer block of hydrophobic PS and hydrophilic PEO. Assembly could then be triggered via addition of water, yielding micelles, rods, and vesicles, with the structure dependent on the volume ratio of the two polymers.[52]

When the value of $2R_g/d$ is about equal to 1, the NPs can stimulate phase separation of the two polymer blocks. The phase separation produces particles with layered polymer brush phases in which the solvophilic polymer serves as the outer layer and the solvophobic polymer serves as the inner layer, yielding NP monolayers when assembled.[35,51,53,147] As an example, Duan and co-workers demonstrated that Au NPs modified with PEO and PMMA assemble into vesicles in which the particles are encapsulated within the PMMA regime.[51] Furthermore, this strategy has been used to design stimulus-responsive vesicles by exchanging the PMMA for other polymers that have stimulus-responsive properties. For example, Duan and co-workers showed similar results using a copolymer of MMA and 4VP; however, 4VP is pH-responsive and becomes protonated at a pH of 5.4, thus making the copolymer hydrophilic instead of hydrophobic. This change in hydrophobicity results in the disassembly of the vesicles, which makes the vesicles useful applicants in drug delivery.[35,53] Other stimuli, such as light, can be used to similar effect.[147]

Finally, when $2R_g/d <<< 1$, the amphiphilic particles struggle to assemble into the vesicles observed at higher $2R_g/d$ values, due to the lower flexibility of the polymer brush. Thus, particles tend to assemble into dimers and other small multimers, such as in the work reported by Duan and co-workers. Here, upon addition of water, 40 nm Au NPs modified with PEO and PMMA assembled into dimers with

yields of about 60%; the dimers could then be disassembled upon addition of the more favorable solvent, DMF.[148]

1.6.2 H-PgNP Self-Assembly

Anisotropic H-PgNPs are inherently trickier to create due to the isotropic matter of polymers grafting to the NP surfaces; thus, researchers need to use inherent differences in surface chemistry to achieve anisotropy. A common method is targeting specific crystal facets for modification, as the binding energy is dependent on the facet.[12,149-156] This idea was pioneered by Kumacheva and co-workers, who selectively modified cetyltrimethyl ammonium bromide (CTAB)-stabilized AuNRs with PS at the poles. As shown in Figure 1.11b,[12] these **ABA** type NRs could be assembled into various structures by tuning the solvent conditions. In THF/water, the NRs preferred to stack side-by-side, yielding bundles, spheres, or vesicles, whereas when in DMF/water, the NRs preferred to assemble end-to-end, yielding rings or chains. In THF/DMF/water mixtures, bundled chains were achieved, combining aspects of both the THF/water and DMF/water assemblies. The resulting structures were achieved due to the interactions between the PS brush and the NR core with the surrounding medium. The interparticle distance could be controlled by changing the PS length, incubation time, and water content (C_w), in the assembly medium.

Kumacheva and co-workers further investigated this assembly process through the lens of polymerization in which the NR building blocks serve as "nano" monomers.[152-156] The PS-end capped AuNRs are bifunctional monomers that can polymerize via noncovalent interactions between the PS brushes on adjacent NRs. The reactivities of the PS brushes are independent of the "nano" polymer length,

which follows Flory's assumption of monomers in polycondensation polymerizations. Thus, the polymerization of these nanochains can be fit to a first order kinetic process as defined by:

$$X_n = 2[M]_0 kt + 1 \quad (1.3)$$

where X_n is the degree of polymerization, k is the rate constant, $[M]_0$ is the initial concentration of active end groups, and t is the assembly time. The kinetics of these nanochains can be further studied via the addition of chain stoppers, which are comprised of Au/Fe_3O_4 JPs that are modified with PS on the Au surface. Upon addition, the JPs block the active polymerization sites, and thus, terminate the growing chains.[156] This step-growth polymerization model is unique in providing insight into the kinetics of these assembly mechanisms that are independent of particle shape, composition, and driving force. A similar model was used to define the formation of nanochains from PS-modified ferromagnetic NPs, even though the driving force was addition of a magnetic field.[157,158]

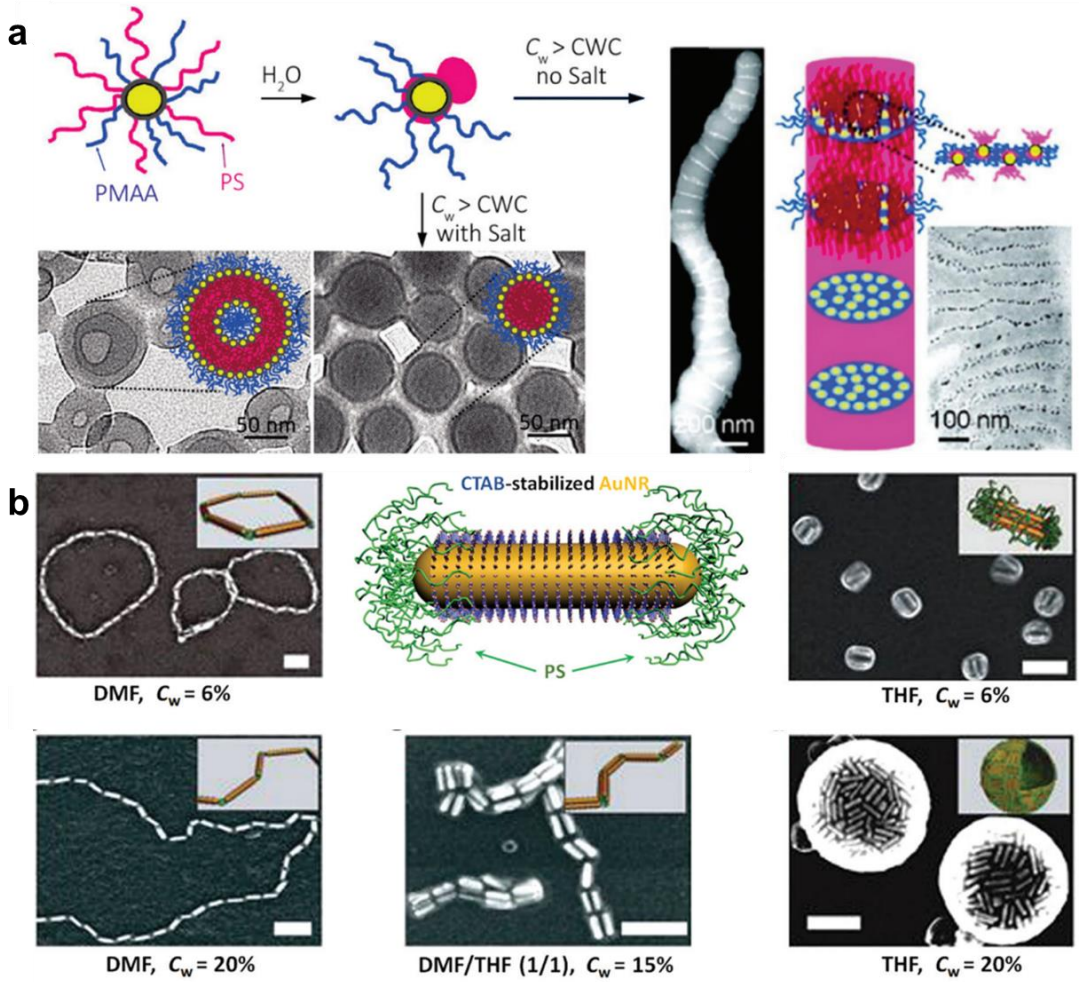

Figure 1.11 The self-assembly of M-PgNPs and H-PgNPs in selective solvents. (a) The self-assembly of CdS NPs modified with a polymer brush of PMAA and PS into various structures when the C_w > CWC. The effect of NaCl was also studied, with vesicles and micelles forming under the presence of salt, and segmented wormlike structures formed without salt.[144] (b) The self-assembly of CTAB-modified Au NRs that are end-capped with PS into various structures dependent on the solvent conditions. Samples assembled in DMF/water yielded ring and chain structures, whereas samples assembled in THF/water yielded bundles and spheres/vesicles. Samples assembled in DMF/THF/water, when the DMF:THF ratio was 1:1, yielded bundled chains.[12]

1.6.3 B-PgNP Self-Assembly

Compared to H-PgNPs, the anisotropy of B-PgNPs arises more easily due to conformational changes of the BCP brush, creating areas of high and low polymer density that can be used to drive the self-assembly of these particles.[65] Nie and co-workers have pioneered the use of this technique to trigger the assembly of B-PgNPs into various nanostructures, using different driving forces to achieve desired architectures.[25,31,35-37,43,54,55,159] This diversity in usage stems from the inherent advantages of B-PgNPs over both H-PgNPs and M-PgNPs, which include: i) fewer limitations regarding the size regimes of the NP core with respect to the polymer brush size and flexibility; ii) more precise control over chemical functionality and surface chemistry; and iii) greater control over targeted structure complexity and yield.[3] The high degree of functionality and tunability of the BCPs is paramount, making these materials ideal candidates for expanding both the scope of available architectures and facilitating the ease in achieving these ensembles through directed self-assembly of B-PgNPs.

1.6.3.1 Film Rehydration

Nie and co-workers demonstrated the self-assembly of thiol-terminated PS-*b*-PEO-modified Au NPs (Figure 1.12a)[54,55] into nanovesicles (NVs) and NTs composed of a monolayer of Au NPs using the film rehydration technique. Self-assembly was triggered via sonication or heating of the thin films in water, which is a poor solvent for PS. This process caused the outer layer of Au NPs to peel off the surface into the desired structures by minimizing the interactions between the water and the hydrophobic PS, as shown in Figure 1.12b.[54] The type of structure was

largely dependent on the hydrophilicity of the particles, which is determined by the ratio of the average root-mean-square end-to-end distance (R_0) of the PS block to the Au NP size (d_{Au}). NV formation is preferential when $R_0/d_{Au} < 0.5$, and NT formation is preferential when $R_0/d_{Au} \approx 0.5$. It is also noted that the film cannot be adequately rehydrated when $R_0/d_{Au} > 0.5$. This morphological transition is attributed to the change in hydrophilicity of the particles, which is determined by the σ of PEO on the particle surface. This density is defined as:

$$d = \sigma/[4\left(0.5 + \frac{R_0}{d_{Au}}\right)^2] \quad (1.4)$$

where σ is the BCP grafting density. Thus, when $R_0/d_{Au} \leq 0.5$, the PEO density is high enough to allow for film hydration and subsequent self-assembly of the Au NPs. The interparticle spacing can also be fine tuned by adjusting the length of the PS block. It was demonstrated that as the PS M_n was increased from 11.9 to 47.3 kDa, the interparticle distance increased from 5.7 ± 0.9 to 10.9 ± 2.9 nm, which is particularly useful, as interparticle spacing is closely linked to the emergent optical properties of noble metal NP assemblies.

Although promising, control over particle self-assembly using the film rehydration method can be difficult to control, as the resulting structures are mainly controlled via kinetics during film rehydration. Consequently, the size, size distribution, and morphology of the assembled structures can be affected by small changes in experimental conditions for which it is difficult to account.[3,54] Thus, Nie and co-workers explored the thermodynamically-controlled self-assembly of thiol-terminated PS-*b*-PEO-modified Au NPs in selective solvents to gain a better understanding and better control over assembly conditions.[55]

1.6.3.2 Self-Assembly in Selective Solvents

As mentioned above, thiol-terminated, PS-*b*-PEO-modified Au NPs can also be assembled in selective solvents (*ie.* THF/water), yielding structures including unimolecular micelles, clusters, and vesicles, as shown in Figure 1.12c.[55] Self-assembly is triggered via the collapse of the hydrophobic PS block when exposed to water, which minimizes the overall free energy of the system. Similar to what happens in the film rehydration method, the dimensions and morphologies of the resultant assembled nanostructures are dependent on the interplay between the NP size and PS length.[54] A morphological transition from vesicles to clusters to unimolecular micelles is observed as the PS length is decreased and the NP size is increased. This morphological transition was further clarified through dissipative particle dynamics (DPD) simulations, which suggest that the change in structure is controlled largely by the reorganization of the polymer brushes and the ability of the polymer shell to compress and deform. When the polymer brushes are too short, the polymer shell is unable to deform adequately, resulting in a lack of induced anisotropy. This phenomenon results in particles preferentially aggregating into unimolecular micelles and small clusters. Once the PS brush is sufficiently long, the polymers can adequately stretch and redistribute on the particle surface, yielding PgNPs that serve as analogues to **ABA** triblock copolymers in which the middle sections are hydrophobic, and the outer blocks are hydrophilic. These phase-separated B-PgNPs are able to assemble into NVs.[55]

The σ of the polymer brush is also crucial in dictating the path of assembly into the final nanostructure. As shown by Nie and co-workers, NVs can be formed via

a chain-growth method in which Au NPs assemble into chains that then collapse to form vesicles, or vesicles can also be formed via the collapse of assembled nanosheets, as shown in Figure 1.12d.[36] These vesicles will be referred to as chain vesicles and non-chain vesicles respectively. Chain vesicles form as the result of the redistribution of BCPs on the particles' surfaces during the first stage of assembly when σ is low (~0.3 chains/nm^2). As two B-PgNPs interact, the polymer brushes of both particles redistribute, yielding an area of higher polymer density at the interface between the two particles, along with areas of lower polymer density at opposite ends. Thus, future particles preferentially add to areas of lower polymer density due to attractive van der Waals interactions, rather than assuming a more ordered packing structure due to the increased steric interactions near the particle–particle interface established previously. These assembled strings then fold into vesicles to limit unfavorable solvent interactions. Meanwhile, when σ is high (≥ 0.5 chains/nm^2), particle interactions are mediated by solvophobic forces, leading to the formation of a monolayer in which PS domains are better shielded from the surrounding medium. These monolayers behave similarly to those previously described in studies using the film rehydration technique in which the monolayer folds in on itself, forming the final NV.[36,54,55]

Although both approaches form vesicles, the assembly pathway directly influences the packing of the particles within the vesicle wall, and thus, influences the optical properties of the nanostructures. Chain-vesicle formation results in an uneven packing of the particles within the vesicle wall, as particles within chains are packed more tightly than the chains are packed relative to one another. This packing structure

yields an average interparticle distance within the chains of 0.8 ± 0.1 nm and an average distance between nanochains of 12.3 ± 2.2 nm. Meanwhile, non-chain vesicle formation results in an even spacing of the particles within the vesicle wall and an average interparticle distance of 9.0 ± 1.5 nm. This difference in average interparticle distance results in drastically different optical absorption properties, as non-chain vesicles show a single large absorption peak between 590 nm and 620 nm, whereas comparably sized chain vesicles exhibit two absorption peaks, one at ~540 nm and another red-shifted peak at ~780 nm. Although both vesicles demonstrate red-shifting compared to individual Au NPs, the small interparticle distance in chain vesicles results in stronger plasmonic coupling, and thus, a more red-shifted peak.[36]

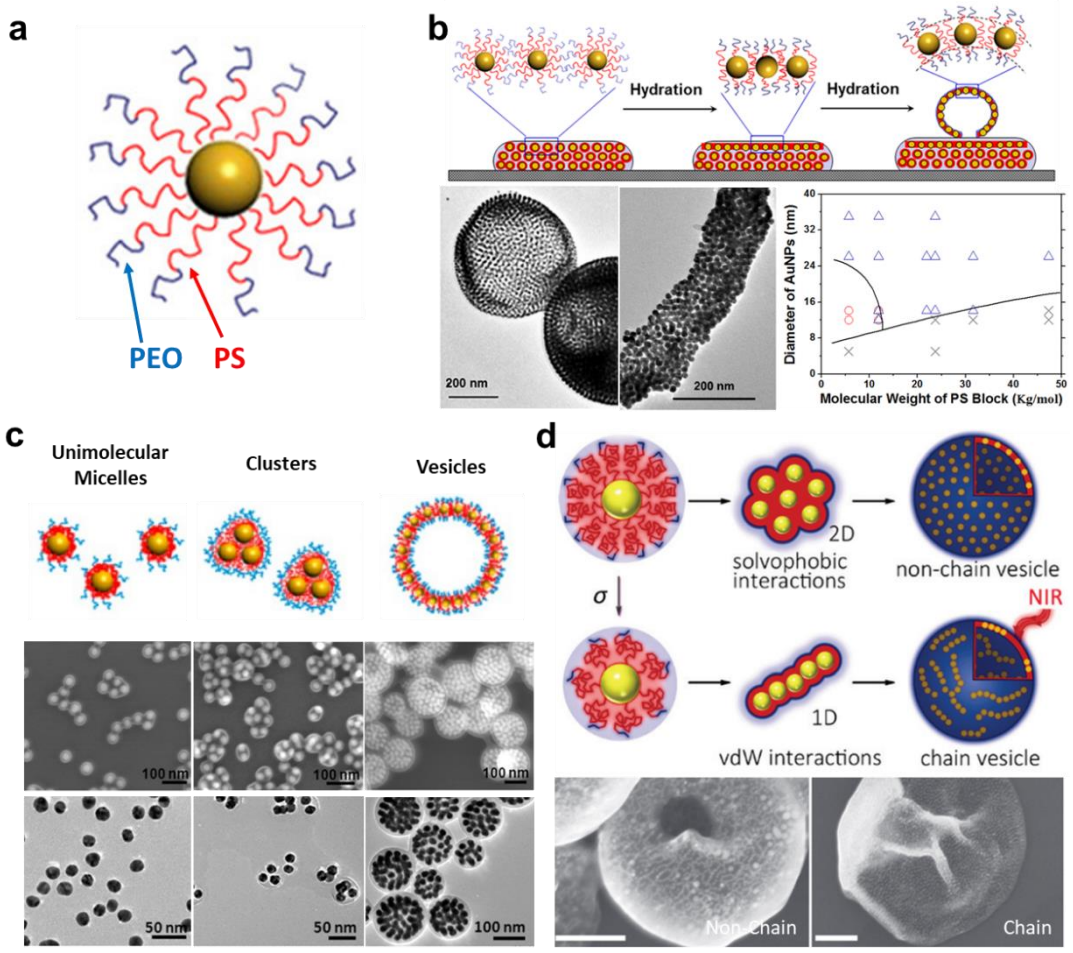

Figure 1.12 The self-assembly of thiol-terminated PS-*b*-PEO-modified Au NPs. (a) Model of the thiol-terminated PS-*b*-PEO modified Au NPs.[54,55] (b) Self-assembly of B-PgNPs via film rehydration. Top: Schematic of the polymer-brush conformation change during film rehydration. Bottom: Representative SEM image of the assembled NVs (left), representative TEM image of the assembled NTs (center), and a phase diagram of B-PgNP assembly structures as a function of particle size and PS length.[54] (c) Self-assembly of B-PgNPs via selective solvents (THF/water). Top: Illustration of the various assembled nanostructures. Middle: Representative SEM images of the assembled nanostructures. Bottom: Representative TEM images of the assembled nanostructures.[55] (d) Investigating the effect of σ on the self-assembly of B-PgNPs via selective solvents (THF/water). Top: Schematic showing the assembly of B-PgNPs into non-chain and chain vesicles based on σ. Bottom: Representative SEM images of the non-chain and chain vesicles.[36]

1.6.3.3 Self-Assembly in Microfluidics

As the particle size increases, the mobility of the assembling particles becomes significantly slower, which makes gaining control over the assembly kinetics particularly important. Consequently, microfluidics-based techniques offer a unique way to gain precise control and reproducibility over assembly kinetics that can be difficult to control in traditional solvent-based assemblies.[160] As discussed in Section 1.5.3, particle assembly can be triggered by mixing streams of disparate solutions; however, microfluidics is unique in the control that can be achieved over this mixing process, as the flow rate of each stream, the timing of mixing, and the particle concentration can all be easily fine tuned.[133-136] This ease of tunability allows for the formation of both kinetic products and various nonequilibrium structures, as demonstrated by Nie and co-workers.[31,161,162]

Using thiol-terminated, PS-*b*-PEO-modified Au NPs as building blocks, self-assembly was triggered by forcing a THF solution of NPs between two water streams in a microfluidic channel, creating a laminar flow of the three streams. This process created a solvent gradient that could be manipulated easily by adjusting the solvent flow rate, triggering self-assembly. NV formation was achieved under various flow rates of THF to water (Q_{THF}:Q_{H_2O}). As this ratio was increased, the NV size increased from 248.8 ± 71.5 to 592.3 ± 161.8 nm.[161] Furthermore, when the Au NPs were substituted with Au NRs, different nanostructure morphologies were achieved, including spherical micelles, giant vesicles, and raft-like disks, depending on the laminar flow rate. The morphological transition from spherical micelles to giant vesicles to raftlike disks could similarly be controlled by increasing Q_{THF}:Q_{H_2O}.[162]

1.6.3.4 Self-Assembly of Complementary B-PgNPs

Although promising, prior solution-based self-assembly methods lack specificity in particle interactions, which limits the complexity and reproducibility of the resultant nanostructures. Consequently, much progress has been made using complementary, DNA-based self-assembly methods to circumvent this problem[163-171]. However, self-assembly using complementary B-PgNPs offers a more flexible path to target unique, complex nanostructures.[172-175] This flexibility stems from targeting of the BCPs by precisely tailoring the BCP length, the reacting functional groups, and the density/location of the functional groups within the BCP chains.[2,3]

Nie and co-workers proposed a model system in which Au NPs were modified with either thiol-terminated polystyrene-*block*-poly(acrylic acid-*r*-styrene) (PS-*b*-P(AA-*r*-St)-SH) or thiol-terminated polystyrene-*block*-poly(N,N-dimethylaminoethyl methacrylate-*r*-styrene) (PS-*b*-P(DMAEMA-*r*-St)-SH), as shown in Figure 1.13a.[172] The particles were then assembled in THF though acid–base neutralization reactions of the carboxylic acid groups of the AA moieties and the amine groups of the DMAEMA moieties. This scheme enabled the formation of **AB** dimers that further assembled into alternating $\mathbf{(AB)_n}$ chains whose assembly kinetics mirrored the polycondensation of adipic acid and hexamethylenediamine into Nylon 66.

Nie and co-workers used a similar system to achieve molecular analogues in which particles could be treated like atoms. Similar BCPs were used here, but the outer PS block was replaced with PEO. Upon self-assembly in THF, various $\mathbf{AB_n}$ structures were created in which *n* could be equal to 1 through 6 with yields of up to 86.4% (Figure 1.13b).[173] This control was achieved through carefully tuning both the

BCP structural parameters and the particle-feeding ratios. Additionally, the inorganic NP core could be varied, with **AB$_2$** formation observed using Fe_3O_4 and Ag, which can yield different ferromagnetic and optical properties, respectively. This assembly method was further expanded to use differently shaped particles, with particle **A** being replaced with Ag nanodiscs (NDs) and nanotriangles (Figure 1.13c1).[174] The resultant self-assembly was influenced directly by the outer BCP block length on the ND or nanotriangle. Edge-type self-assembly between the NDs/nanotriangles and the Au NPs was preferred when the ND/nanotriangle BCP length was longer (PEO_{113}) (Figure 1.13c2), whereas face-type self-assembly was preferred when the BCP length was shorter (PEO_{45}) (Figure 1.13c3).

By changing the outer BCP block, the hydrophobicity of the B-PgNP can be greatly affected. Nie and co-workers used this concept to explore hierarchal self-assembly in which **AB** and **AB$_2$** nanostructures were further assembled into nanoflowers and nanoribbons, as shown in Figure 1.13d.[173] Hierarchal assembly was achieved by assembling **A** particles, which were modified using PS-*b*-P(AA-*r*-St)-SH, with **B** particles, which were modified using PEO-*b*-P(DMAEMA-*r*-St)-SH. Once assembled into **AB** or **AB$_2$** structures, samples, suspended in THF, were dropped onto a saturated aqueous solution of NaCl. As the THF evaporated, the **AB** dimers assembled into flower-type structures (Figure 1.13d1), with the **A** particles in the center and **B** particles on the outside, shielding the more hydrophobic **A** particles. This shielding is similarly observed with the **AB$_2$** structures, with the **A** particles forming the center of the ribbon and the **B** particles forming the edges (Figure 1.13d2).

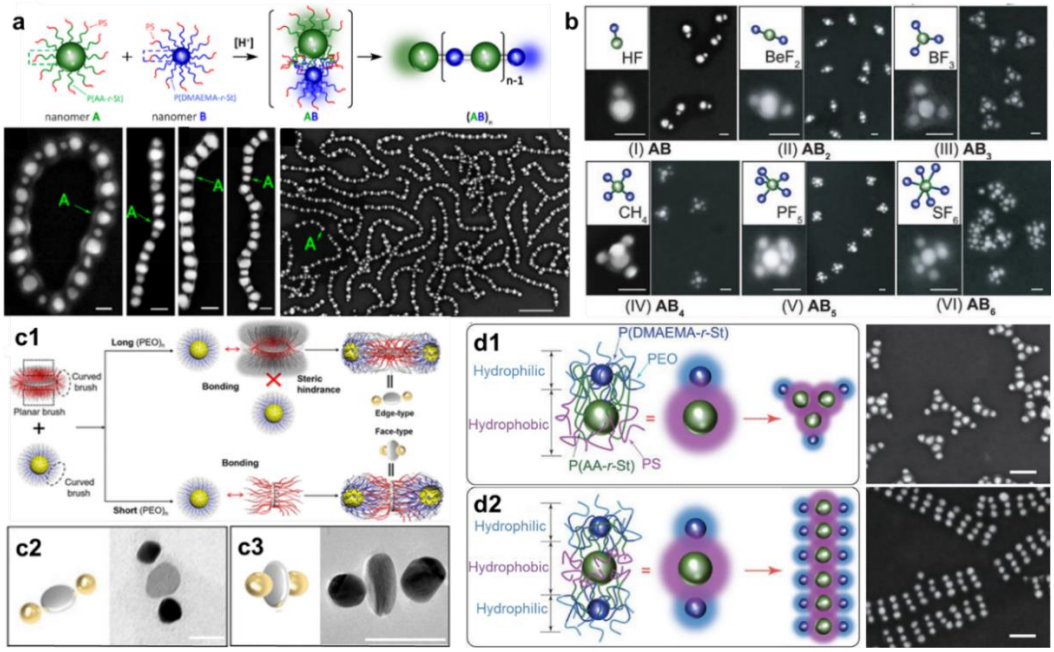

Figure 1.13 The self-assembly of Au NPs modified with complementary BCPs via acid–base neutralization. (a) Above: Schematic of the binary PgNPs, composed of Au NPs modified with BCPs, and their copolymerization into repeating chains via acid–base neutralization of the complementary BCPs. Below: Representative SEM images of the repeating chains with increasing size of particle **B** from left to right; particle **A** remains the same size. The rightmost image is a larger-area view of the leftmost image.[172] (b) Cartoons and SEMs of $\mathbf{AB_n}$ structures (x = 1 to 6) in which **A** particles are 36 nm and **B** particles are 20 nm in diameter.[173] (c) Self-assembly of complementary BCP-grafted Ag NDs and Au NPs. (c1) Schematic showing the self-assembly into either edge-type or face-type structures. (c2) Cartoon and representative TEM image of an $\mathbf{AB_2}$ edge-type structure. (c3) Cartoon and representative TEM image of an $\mathbf{AB_2}$ face-type structure.[174] (d) Hierarchal self-assembly of **AB** and $\mathbf{AB_2}$ nanostructures via the hydrophobic effect. (d1) Schematic and representative SEM image of the self-assembly of **AB** nanostructures into nanoflowers in which the hydrophobic particles form the center of the flower and the hydrophilic particles form the petals. (d2) Schematic and representative SEM image of the self-assembly of $\mathbf{AB_2}$ nanostructures into nanoribbons in which the hydrophobic particles form the center of the ribbon and the hydrophilic particles form the edges.[173]

1.7 Scope of this Dissertation

As discussed above, the use of PgNPs as nano building blocks is an attractive means of assembling a wide array of unique colloidal structures with selective properties that can be exploited for numerous applications. The use of B-PgNPs in recent years has greatly expanded the tunability and directionality of NP interactions, which can be achieved using isotropic building blocks in solution. However, current systems still largely require the use of non-aqueous assembly conditions, which can limit applicability. Furthermore, there has been renewed interest in intelligent, stimulus-responsive, and reversible design, which remains a challenge, as most systems lack reversibility. The goal of this thesis will be to address these concerns using intelligent BCP design.

Chapter 2 will focus on the design and self-assembly of B-PgNPs into colloidal nanostructures that mimic the bond structure of small molecules. The acid–base-containing blocks of these BCPs drive the assembly of the NPs via acid–base neutralization, whereas the long hydrophilic outer blocks provide stability in assembled structures when suspended in water. Chapter 3 will focus on a new, complementary pair of B-PgNPs, which are assembled via host–guest interactions into similar molecular mimics. The inner BCP block contains either the host or guest moieties, whereas the outer block remains hydrophilic to stabilize the assembled structures, as the addition of water is the driving force of the self-assembly. Careful fine tuning of the polymer lengths and NP sizes provides insight into the assembly mechanism. The reversible nature of these host–guest interactions allows us to study the disassembly mechanism of these structures upon addition of a competitive host.

Chapter 4 will focus on the competitive self-assembly of B-PgNPs when different guest-functionalized particles are introduced. We show assembly selectivity by assembling our ‘host’ B-PgNPs in solution with multiple types of ‘guest’ B-PgNP. Selectivity favors host–guest interactions in which the binding affinity between host and guest is the greatest. Thus, we show that our building blocks can self-sort based on the BCPs tethered to the NPs. Finally, Chapter 5 will give an overall summary of the work presented and will provide an outlook for future work.

Chapter 2: Self-Assembly of Water-Soluble Hairy Inorganic Nanoparticles (HINPs) via Acid–Base Neutralization

Overview. I report the design and assembly of block copolymer-tethered gold nanoparticles into colloidal suprastructures with defined valence. This self-assembly is achieved through an acid–base neutralization in which the block copolymers modified to the particle surface contain either the active acid or base moiety. The reactions between the acid and base moieties on complementary particles drive the particle assembly, forming a variety of AB_n structures that mimic the geometries of molecules such as HCl, CO_2, BH_3, and XeF_4. Additionally, due to the hydrophilic nature of the outer, polymer brush on both particles, the assembled nanostructures can be transferred and stored in aqueous media without loss of structure and stability. The stability of these structures in water and plasmonic properties may make these structures suitable candidates for cellular uptake studies and for use as biosensors.

2.1 Introduction

Throughout history, scientists have looked towards the natural world for inspiration, yet some of our earliest references stem from childhood. Although the self-assembly of DNA and proteins is often cited as inspiration, we can also look towards more simplistic models, such as the LEGO® sets many used in childhood. The LEGO® pieces represent our building blocks, which we can manipulate to form larger structures. Although somewhat pedantic, looking at self-assembly through this lens does offer a more whimsical view into the field and shows that through intelligent design, we can transform simple materials into stimulus-responsive

building blocks. However, the ability to implement, manipulate, and assemble particles on the nanoscale remains challenging.

In this study, our building blocks are hybrid PgNPs in which we take advantage of a variety of unique physical and chemical properties.[2,3] These properties arise from both the inorganic NP core and the polymer brush. As mentioned in Chapter 1, once PgNPs are assembled into larger colloidal structures, their collective properties can differ from those of the individual building blocks, due to the unique particle–particle interactions. The new properties make these assemblies particularly attractive for use in plasmonic devices,[14] drug delivery,[4,25-28,38,40-43] imaging,[36,37] and energy storage.[39]

A variety of different building blocks can be used and controlled through fine tuning of not only the building block structural parameters, but also the stimulus that drives the assembly.[2,3] As mentioned in Chapter 1, a wide array of assembly methods has been introduced, including the use of polymer matrices, interfaces, templates, and selective solvents. However, control over the directionality of the NP interactions remains challenging, which can limit the complexity and the yields of the resultant nanostructures. To circumvent this problem, a common assembly method uses complementary DNA strands to drive the assembly of nanomaterials in which NPs are modified with specific strands of DNA that will hybridize with complementary DNA strands.[163-171] This degree of specificity gives researchers a large amount of control in targeting specific structures, as highlighted by the works of Edwardson *et al.*, who were able to target small colloidal clusters with yields approaching 90%.[170] Furthermore, the use of DNA-based self-assembly can be implemented to create 3D-

suprastructures, as shown by Gang and co-workers, who assembled Au NPs and Au NCs together into ordered, 3D nanocrystals with periodicity.[171]

Although DNA-assisted assembly has greatly expanded the range of possible structures, there are inherent limitations that need to be addressed. The purification process can be quite difficult, resulting in relatively low yields, and the mechanical properties of larger 3D arrays have yet to be studied in detail. Thus, it is important to establish a simple, yet versatile strategy to assemble PgNPs into targeted nanostructures with high yields and tunability. Additionally, the stability of the resultant structures is equally important, particularly when in aqueous media. Many PgNP assemblies rely on hydrophobic polymer brushes, which can collapse and destabilize the assembled nanostructures in water.[36,54,55] Improved stability could allow for these assembled structures to find more uses in biological applications, including cell imaging,[36,37] biosensing,[33,35] and cancer therapies.[40-43]

In this Chapter, I expand upon our group's method for the self-assembly of B-PgNPs into higher-order colloidal nanostructures.[172-174] In this approach, different-sized Au NPs were modified with one of two complementary di-block BCPs, as shown in Figure 2.1. The two BCPs were PEO-*b*-P(AA-*r*-St)-SH and PEO-*b*-P(DMAEMA-*r*-St)-SH. The BCP-modified Au NPs are referred to as building blocks **A** and **B**, respectively. The inner block of the BCPs is a random copolymer of St, which serves as a steric buffer, and either a proton donor (the carboxylic acid of AA) or a proton acceptor (the tertiary amine of DMAEMA). The outer block is the hydrophilic homopolymer, PEO. The polymerization allows for fine tuning of the inner BCP block length and the ratio of the two monomers. This tunability allows for

better control over the number of interactions between the reacting building blocks. Additionally, the long, hydrophilic outer block provides enhanced stability to the assembled structures once they are transferred to water.

Self-assembly was initiated by mixing the two building blocks in a favorable solvent for the BCPs, such as THF. The particles were assembled via an acid–base neutralization between the complementary particles, yielding colloidal nanostructures with defined valence in high yields. Valence is the number of **B** particles bound to each **A** particle, in analogy to how we treat atoms in a molecule. A variety of assembly structures were formed by fine tuning the polymer length and composition along with the feeding ratio of the two building blocks. These structures include dimers **(AB)**, trimers **(AB_2)**, tetramers **(AB_3)**, pentamers **(AB_4)**, and other **AB_n** structures, along with alternating chains **$(AB)_n$**. Interestingly, regardless of the particle size, particle **A** served as the central 'atom' in the resultant structures, whereas the **B** particles surrounded the **A** particles. These results match those previously reported by Yi *et al.,* with comparable yields. Once assembled, the supracolloids were transferred to water. Imaging revealed that the resulting structures were mostly unchanged after solvent transfer; however, the interparticle distance between particle **A** and **B** was found to decrease, which resulted in a red-shift in the absorbance spectra of the samples.

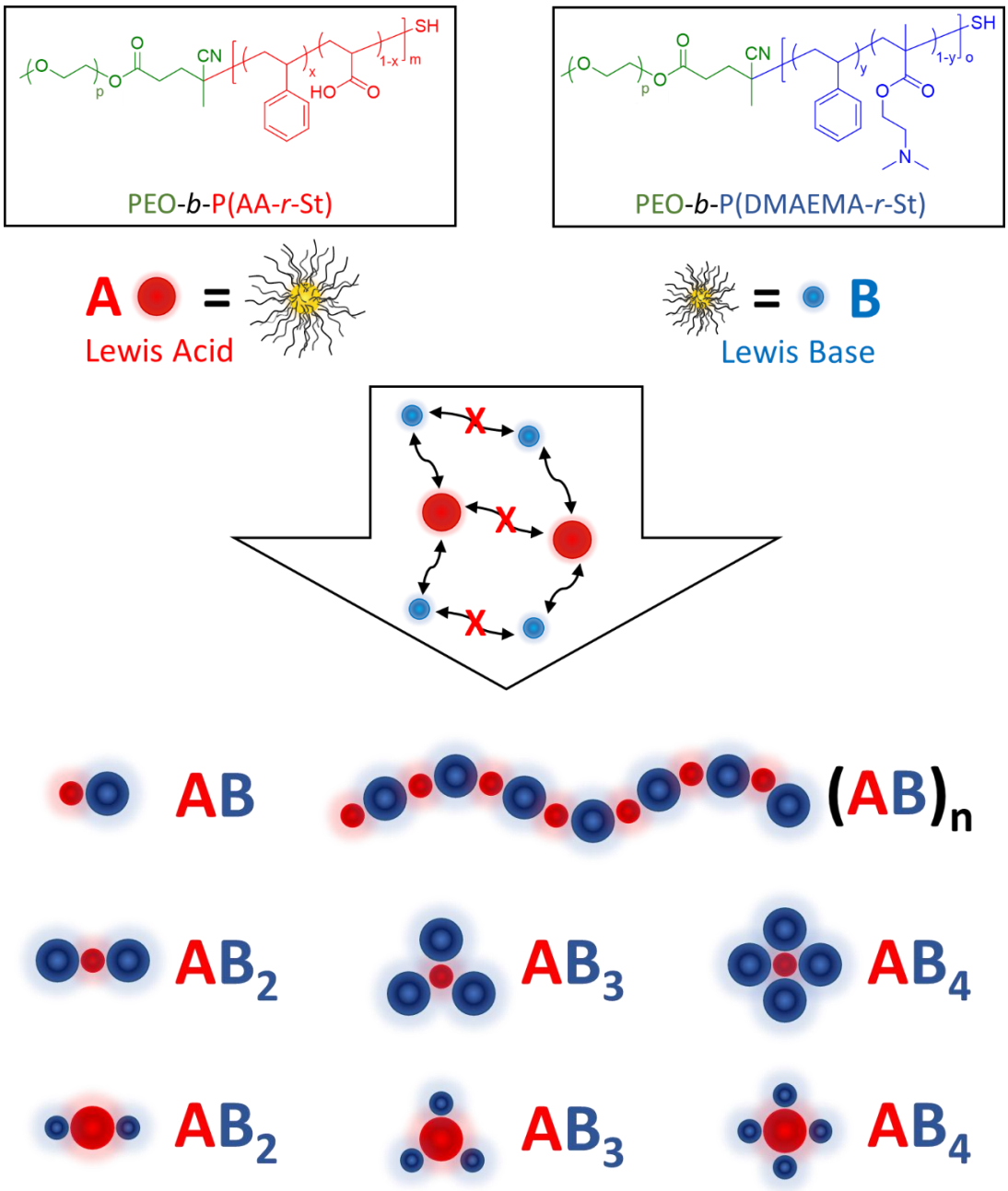

Figure 2.1 Schematic showing the assembly of complementary colloidal BCP-tethered Au NPs into various nanostructures with controlled valence via an acid–base neutralization reaction.

2.2 Materials and Experimental Methods

2.2.1 Materials

Gold (III) chloride trihydrate ($HAuCl_4$, ≥ 99.9% trace metals basis), sodium citrate tribasic dihydrate (≥ 99%), 4-cyano-4-(phenylcarbonothiolythio)pentanoic acid (CPADB), poly(ethylene glycol) methyl ether (PEG_{113}-OH; M_n: 5,000 $g \cdot mol^{-1}$ and PEG_{227}-OH; M_n: 10,000 $g \cdot mol^{-1}$), N,N'-dicyclohexylcarbodiimide (DCC, 99%), 4-(dimethylamino)pyridine (DMAP), *n*-butylamine (99.5%), dichloromethane (anhydrous, ≥ 99.8%), hydrochloric acid (HCl, ACS Reagent 37%), and dioxane (anhydrous, 99.8%) were purchased from Sigma Aldrich, and were all used as received. THF, DMF, petroleum ether, hexanes, and water (HPLC grade) were purchased from Fisher Scientific and were all used as received. Styrene (St, > 99%) and N,N-dimethylaminoethyl methacrylate (DMAEMA, 98%) were purchased from Sigma Aldrich and passed through a basic Al_2O_3 column to remove inhibitors. Acrylic acid (AA, 99%) was purchased from Sigma Aldrich and was distilled under vacuum before use. The monomers were stored in a freezer after removal of the inhibitors. Azobis(isobutyronitrile) (AIBN, 98%) was purchased from Sigma Aldrich and was recrystallized from ethanol before use. Deionized water (Millipore Milli-Q grade) with a resistivity of 18.0 MΩ or HPLC-grade water were used in all the experiments. Regenerated Cellulose membrane dry dialysis tubing (6-8 kD MWCO Standard Grade) was purchased from Fisher Scientific and was hydrated before use.

2.2.2 Synthesis of PEG-modified CPADB

PEG_{113}-OH and PEG_{227}-OH were modified with the reversible addition-fragmentation chain-transfer (RAFT) agent CPADB through a standard DCC/DMAP-

coupled esterification as follows. PEG (500 mg/1000 mg, 1.0 mmol) and CPADB (420 mg, 1.5 mmol) were added to a roundbottom flask with DCC (310 mg, 1.5 mmol), DMAP (31 mg, 0.25 mmol), and anhydrous dichloromethane (25.0 mL). The solution was purged with argon and stirred at RT for 48 h. The product was precipitated with cold petroleum ether (~90 mL, 10 ℃) and centrifuged at 5,000 rpm for 10 min. The solid was then dissolved in THF (~10 mL) and precipitated with petroleum ether (~90 mL). The solid was collected via centrifugation at 5,000 rpm for 10 min. This process was repeated two more times, and the final product was dried under vacuum for at least 24 h. The CPADB-modified PEG was stored in a freezer until needed.

2.2.3 Synthesis of Thiol-Terminated BCPs

The thiol-terminated BCPs, PEO-*b*-P(AA-*r*-St)-SH and PEO-*b*-P(DMAEMA-*r*-St)-SH were synthesized via RAFT polymerization. The synthetic procedure is shown in Figure 2.2.[173]

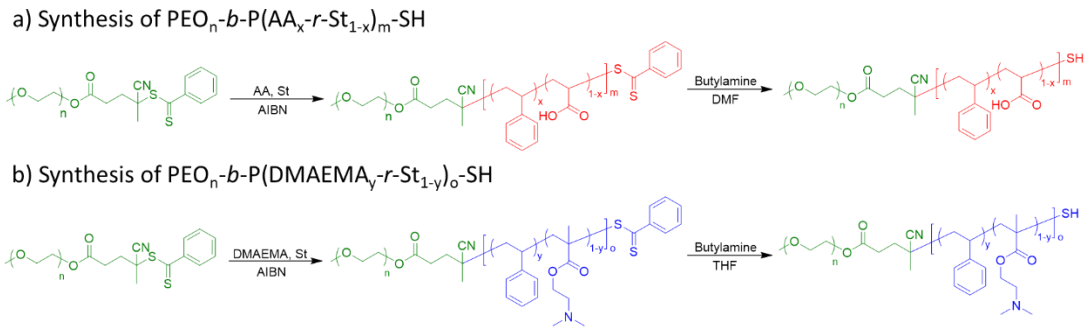

Figure 2.2 The synthesis of thiol-terminated BCPs: (a) PEO-*b*-P(AA-*r*-St)-SH and (b) PEO-*b*-P(DMAEMA-*r*-St)-SH.

2.2.3.1 Synthesis of PEO-b-P(AA-r-St)-SH

RAFT polymerization was used to synthesize PEO-*b*-P(AA-*r*-St)-SH BCPs of various lengths, as follows. PEG_{227}-CPADB (100 mg, 0.01 mmol) or PEG_{113}-CPADB (50 mg, 0.01 mmol) was added to a roundbottom flask with St (729 mg, 7 mmol) and AA (216 mg, 3 mmol). Anhydrous dioxane (5.00 mL) was added along with AIBN (10.0 µL of a 0.1 mM AIBN solution in dioxane). The AIBN served as a thermo-initiator. Solutions were then purged with argon for 30 min and stirred in a 75 °C oil bath for 6 to 12 h. The polymers were precipitated with cold hexanes (~90 mL, 10 °C) and centrifuged at 5,000 rpm for 10 min. The polymers were then dissolved in THF (~10 mL) and precipitated with hexanes (~90 mL). The solid was collected via centrifugation at 5,000 rpm for 10 min. This process was repeated two more times, and the final product was dried under vacuum for at least 24 h.

To reduce the dithiobenzoate into a thiol, the dried polymer PEO-*b*-P(AA-*r*-St) was dissolved in DMF (5.00 mL). Subsequently, *n*-butylamine (0.50 mL, 0.5 mmol) was added to DMF (10.00 mL), and this solution was added dropwise to the polymer solution. After 2 h of stirring at RT under argon, the solution was neutralized and precipitated with HCl (1.0 M) in an ice bath. The solids were vacuum-filtered and washed with cold water to remove any excess acid or salt. The polymers were then dissolved in THF (~10 mL) and precipitated with hexanes (~90 mL). The solid was collected via centrifugation at 5,000 rpm for 10 min. The polymers were then dissolved in THF (~10 mL) and precipitated with hexanes (~90 mL). The solid was collected via centrifugation at 5,000 rpm for 10 min. This process was repeated two

more times, and the final product was dried under vacuum for at least 24 h, yielding PEO-*b*-P(AA-*r*-St)-SH.

As a representative polymer, the following analysis was performed on BCP **A3** (see Table 2.1). From the ^{1}H NMR spectrum (in DMSO-*d6*, see Figure 6.1), the ^{1}H NMR-based molecular weight M_n is 41.0 Kg·mol^{-1}. The analysis was performed by comparing the integrals of the aromatic ring hydrogens of PS (6.4-7.3 ppm) and the carboxylic acid group hydrogens of AA (11.5-12.5 ppm) to the methylene group hydrogens of PEO (3.62-3.66 ppm). The length of the PEO block was known and was used as a standard to determine the amounts of PS and AA present in the final polymer. PEO-*b*-P(AA-*r*-St)-SH BCPs of different lengths and charge-ratios were synthesized by varying the reaction time, and they are listed in Table 2.1.

2.2.3.2 Synthesis of PEO-b-P(DMAEMA-r-St)-SH

RAFT polymerization was used to synthesize PEO-*b*-P(DMAEMA-*r*-St)-SH BCPs of various lengths, as follows. PEG_{227}-CPADB (100 mg, 0.01 mmol) or PEG_{113}-CPADB (50 mg, 0.01 mmol) was added to a roundbottom flask with St (729 mg, 7 mmol) and DMAEMA (430 mg, 3 mmol). Anhydrous dioxane (5.00 mL) was added along with AIBN (10.0 µL of a 0.1 mM AIBN solution in dioxane). The AIBN served as a thermo-initiator. Solutions were then purged with argon for 30 min and stirred in a 75 °C oil bath for 12 to 24 h. The polymers were precipitated with cold hexanes (~90 mL, 10 °C) and centrifuged at 5,000 rpm for 10 min. The polymers were then dissolved in THF (~10 mL) and precipitated with hexanes (~90 mL). The solid was collected via centrifugation at 5,000 rpm for 10 min. This process was

repeated two more times, and the final product was dried under vacuum for at least 24 h.

To reduce the dithiobenzoate into a thiol, we performed a modified version of the reduction outlined in Section 2.2.3.1. The dried polymer PEO-*b*-P(DMAEMA-*r*-St) was dissolved in THF (5.00 mL). Subsequently, *n*-butylamine (0.50 mL, 0.5 mmol) was added to the polymer solution. After 2 h of stirring at RT under argon, the solution was precipitated with cold hexanes (~90 mL, 10 °C) and centrifuged at 5,000 rpm for 10 min. The polymers were then dissolved in THF (~10 mL) and precipitated with hexanes (~90 mL). The solid was collected via centrifugation at 5,000 rpm for 10 min. This process was repeated two more times, and the final product was dried under vacuum for at least 24 h, yielding PEO-*b*-P(DMAEMA-*r*-St)-SH.

As a representative polymer, the following analysis was performed on BCP **D1** (see Table 2.1). From the ^{1}H NMR spectrum (in $CDCl_3$, see Figure 6.2), the ^{1}H NMR-based molecular weight M_n is 18.4 Kg·mol^{-1}. The analysis was performed by comparing the integrals of the aromatic ring hydrogens of PS (6.4-7.3 ppm) and the methyl group hydrogens of DMAEMA (0.1-0.8 ppm) to the methylene group hydrogens of PEO (3.62-3.66 ppm). The length of the PEO block was known and was used as a standard to determine the amounts of PS and DMAEMA present in the final polymer. PEO-*b*-P(DMAEMA-*r*-St)-SH BCPs of different lengths and charge-ratios were synthesized by varying the reaction time, and they are listed in Table 2.1.

Table 2.1 Characterization of Acid/Base-functionalized BCPs

BCP	Formula	Charge Ratio	M_n (^{1}H NMR) (Kg·mol^{-1})	R_0 (nm)
A1	PEO_{113}-*b*-P(AA_{55}-*r*-St_{180})$_{235}$-SH	0.24	27.7	10.1
A2	PEO_{113}-*b*-P(AA_{66}-*r*-St_{206})$_{272}$-SH	0.24	31.2	10.9
A3	PEO_{113}-*b*-P(AA_{102}-*r*-St_{275})$_{377}$-SH	0.27	41.0	12.7
A4	PEO_{227}-*b*-P(AA_{54}-*r*-St_{200})$_{254}$-SH	0.21	34.7	10.5
D1	PEO_{113}-*b*-P(DMAEMA$_{25}$-*r*-St_{91})$_{116}$-SH	0.22	18.4	7.8
D2	PEO_{113}-*b*-P(DMAEMA$_{41}$-*r*-St_{146})$_{187}$-SH	0.22	26.7	9.9
D3	PEO_{227}-*b*-P(DMAEMA$_{33}$-*r*-St_{84})$_{117}$-SH	0.28	23.9	7.9
D4	PEO_{227}-*b*-P(DMAEMA$_{47}$-*r*-St_{132})$_{179}$-SH	0.26	31.1	9.8

*R_0 for the inner BCP block is calculated from $R_0=bN^{0.5}$, whereas *b* is the Kuhn length (1.8 nm for PS) and *N* is the number of Kuhn segments. For simplicity, the Kuhn length for PS was used for the AA and DMAEMA moieties, as the inner block is mostly composed of PS.[124]

2.2.4 Au NP Synthesis

Au NPs of various sizes (20-40 nm) were synthesized using a previously reported method.[54,173,176] 1.00 mL of an aqueous $HAuCl_4$ solution (50 mg·mL^{-1}) was added to a roundbottom flask with 500 mL of HPLC water. The solution was brought to a boil under intense stirring. Once the solution was boiling, 20 mL of an aqueous 1% wt. sodium citrate solution were added, and the solution was allowed to reflux for an additional 30 min. During this time, the solution turned from a light yellow color to a dark purple color. Afterwards, the solution was cooled to 90 °C, while maintaining intense stirring. 20 mL of the citrate solution were then added, followed immediately by 1.00 mL of the $HAuCl_4$ solution. The solution was stirred at temperature for 15 min and was then removed from heat, yielding Au NPs of approximately 20 nm in diameter. Larger diameters were achieved by repeating the addition of sodium citrate and $HAuCl_4$, followed by stirring. Each cycle increased the

particle diameter by roughly 5 nm. Average diameters were measured using SEM images (Figure 6.3).

2.2.5 Au NP Polymer Modification

Au NPs were modified with the thiol-terminated BCPs via a ligand exchange process. 10.00 mL of Au NP solution were initially centrifuged and redispersed in 2.00 mL of DMF. Simultaneously, 8 mg of BCP were dissolved in 2.00 mL of DMF. To the polymer solution, the Au NP solution was added under sonication. The NP and BCP solutions were sonicated for 1 h and then incubated at RT overnight. The solutions were then centrifuged, and the supernatant was carefully removed. The particles were then redispersed in DMF (~2 mL). This process was repeated ten times before the final centrifuged solution was added to 5.00 mL of THF under sonication. The modified-NP solutions were stored at RT in glass vials.

2.2.6 Self-Assembly of HINPs

HINP self-assembly was triggered by mixing particles **A** and **B** together in a favorable solvent, such as THF. Initially, 100 µL of particle **A** were pipetted into 1.00 mL of THF in a 4 mL glass vial. This solution was added carefully to form a bottom layer with minimal mixing of the HINP solution and THF. Afterwards, varying amounts (20-500 µL) of the particle **B** solution were added under sonication to ensure an even particle distribution. The assembly solutions were allowed to sonicate for at least 10 s to ensure complete self-assembly. Afterwards, the solutions were imaged using SEM and TEM to determine the structure and yields of the resultant supracolloids.

2.2.7 Transfer of HINP Assemblies into Aqueous Media

To transfer the samples from DMF to water, 500 µL of the assembly solutions were pipetted into a 4 mL glass vial. 500 µL of water were added to the solutions over the course of 1 h using a syringe pump, under stirring. Afterwards, the solutions were incubated at RT for at least 1 h. The solutions were then added into hydrated dialysis tubing, and dialysis was performed against water for at least 12 h. Afterwards, the solutions were transferred into 4 mL glass vials and reimaged using SEM and TEM to study any changes that occurred after solvent transfer. UV-vis absorption spectroscopy was also performed on the samples.

2.2.8 Morphological and Structural Characterization

^{1}H NMR. ^{1}H NMR spectra were recorded using a Bruker AV-400 MHz high resolution NMR spectrometer.

UV-vis Absorption Spectroscopy. Absorbance measurements were performed using a Shimadzu UV-2501PC UV-vis recording spectrophotometer.

Thermogravimetric Analysis (TGA). TGA was used to characterize the BCP grafting-density on the NP surfaces. A 10.00 mL stock solution of building blocks was centrifuged to remove the supernatant. Hexane was then added, and the sample was centrifuged. The hexane was removed, and the solid pellet was collected. The pellets were then dried under vacuum for 24 h to remove any residual solvent. The measurements were performed under argon with a scan rate of 25 °C·min^{-1} from 25 °C to 800 °C. During the scan, the temperature was maintained at 100 °C for 30 min to further remove any remaining moisture. The weight fraction of the polymer ligands, f, was determined and was used to determine σ based on the polymer M_n.

SEM and TEM Imaging. SEM images were taken using a Hitachi SU-70 Schottky field-emission gun Scanning Electron Microscope (FEG-SEM) operated at 10.0 kV, and TEM images were taken using a JEOL LaB6 FEG Transmission Electron Microscope (FEG-TEM) operated at 200 kV. Samples for SEM or TEM were prepared by drying 5.0 μL of solution on a silicon wafer or a 300-mesh copper grid covered with carbon film, respectively.

2.3 Results and Discussion

2.3.1 BCP-Tethered NPs

As described above, Figure 2.1 shows the structures of the two complementary hybrid building blocks. Au NPs are modified with BCPs in which the inner block contains PS, which serves as a steric buffer that does not interact with the particle surface, and either an acid (AA) or a base (DMAEMA). Under favorable solvent conditions, this acid–base neutralization can drive the assembly of these particles as the acids and bases react in a stoichiometric manner. Meanwhile, the outer block is hydrophilic PEO, which serves as both a steric buffer and a protective shell to stabilize the final assembled products in an aqueous environment, as the inner BCP block is hydrophobic.

For simplicity, particles modified with the acid BCPs are denoted **A** particles, whereas particles modified with the base BCPs are denoted **B** particles. The number following the letter represents the polymer, and the subscript following the letter is the NP size (*e.g.*, $\mathbf{A1}_{\mathbf{20}}$ represents 20-nm particles modified with BCP **A1**, whereas $\mathbf{B1}_{\mathbf{35}}$ represents 35-nm particles modified with BCP **D1**). UV-vis absorption spectroscopy was used to characterize the Au NPs before and after surface

modification. The following analysis will use **A1**$_{40}$ and **B3**$_{20}$ particles as an example. After grafting the BCPs on the NP surfaces, a slight red-shift (~2-6 nm) was observed for both the **A1**$_{40}$ and **B3**$_{20}$ particles. This shift may be indicative of an increase in particle size due to the polymer brush on the surface of the Au NPs, or it may be caused by the change in the refractive index of the surrounding solution, as the unmodified particles are in water and the modified particles are in THF (Figure 2.3).

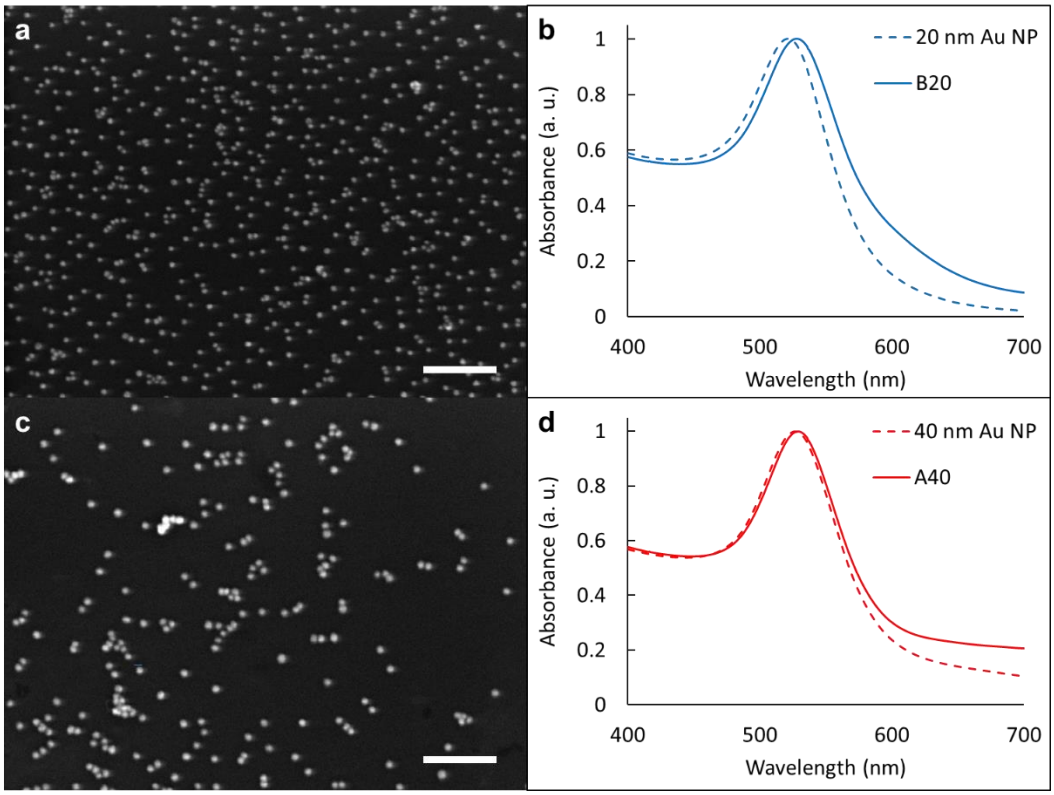

Figure 2.3 SEM images and UV-vis spectra of BCP-modified Au NPs. (a, c) SEM images of BCP-modified (a) 20-nm and (c) 40-nm Au NPs. (b, d). UV-vis spectra of (b) 20-nm Au NPs in aqueous solution and **A1**$_{40}$ particles in THF, and (b) 40-nm Au NPs in aqueous solution and **B3**$_{20}$ particles in THF. The scale bars are 400 nm.

TGA was used to determine the amount of grafted-BCPs on the surfaces of the NPs (Figure 2.4). Weight loss was observed at temperatures above 200 °C and

resulted from the thermal degradation of the BCPs into volatile products. Based on the masses of the tethered BCPs, σ values were estimated using:[124]

$$\sigma = \frac{f N_A \rho d}{6 M_n (1-f)} \quad (2.1)$$

where *f* is the weight fraction of the BCP determined by TGA, N_A is Avogadro's number, ρ is the density of the NP core (19.32 g·mL^{-1} for Au), *d* is the diameter of NP core, and M_n is the molecular weight of the BCP determined by ^{1}H NMR. We assume that the density of the NP core is the same as that of bulk Au and that there is no free polymer present in the system. From the TGA measurements, **A2$_{30}$** and **B2$_{30}$** showed weight losses of 8.0% and 8.9%, respectively. Using Eq. 2.1, we determined that the σ of **A2$_{30}$** and **B2$_{30}$** were 0.16 and 0.18 chains/nm^2, respectively.

Grafting density is known to play an important role in the conformation of the polymer brush, and it is assumed that the polymers are grafted uniformly on the particle surface. Based on the σ values, the average distance (d_l) between adjacent polymer anchor points can be estimated by assuming that the effective footprint for each individual BCP chain is a circular area whose radius is equal to half of the distance between adjacent chains. The average distances were estimated using:[124]

$$d_l = \frac{2}{\sqrt{\pi\sigma}} \approx \frac{1.1}{\sqrt{\sigma}} \quad (2.2)$$

Based on Eq. 2.2, the d_l values for **A2$_{30}$** and **B2$_{30}$** were 2.75 and 2.57 nm, respectively. The R_g for each of the BCPs can be calculated using:[124]

$$R_g = (R_0^2/6)^{1/2} \quad (2.3)$$

R_0 can be found in Table 2.1. The ratio R_g/d_l is estimated to be in the range of 1.5 to 1.7, which suggests that the grafted-BCPs adopt a mostly flexible polymer-brush conformation.[44] The polymer chains preferentially extend away from the NP surface

to avoid steric overcrowding. Near the particle surface, the polymer brushes adopt a more stretched conformation, entering the CPB regime. As the polymers extend further from the particle surface, the polymer chains relax and enter the SDPB regime. This conformation allows for the interpenetration of the complementary BCP brushes from neighboring Au NPs as the particles interact. The polymer brush flexibility also allows for polymer-brush deformation, which further benefits the particle interactions, allowing for redistribution of the particles, depending on resultant nanostructure assemblies. For example, particles can adjust position to make space for additional particles, as *n* increases in $\mathbf{AB_n}$ nanostructures.[173]

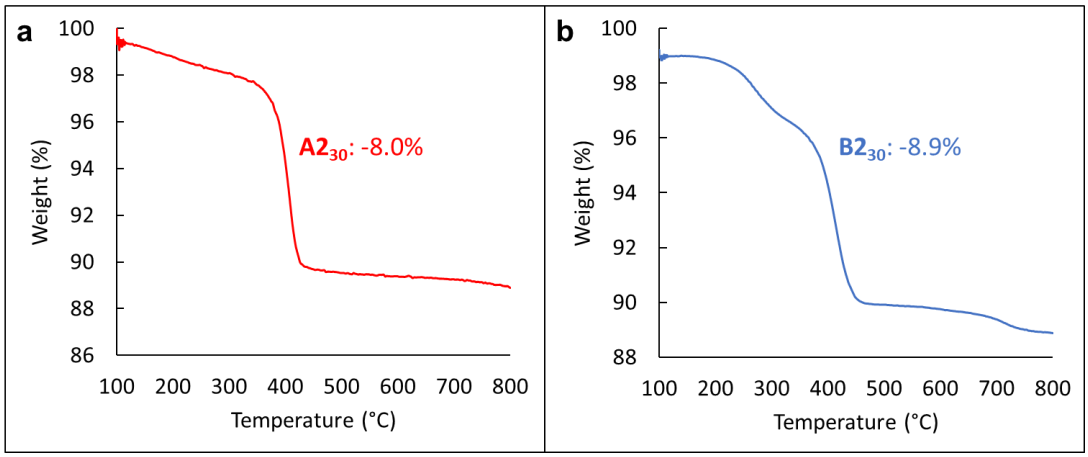

Figure 2.4 TGA curves of $\mathbf{A2_{30}}$ and $\mathbf{B2_{30}}$ particles.

2.3.2 HINP Self-Assembly

The self-assembly of particles **A** and **B** yielded a variety of different structures. The ultimate structures were largely governed by the particle feeding ratio and diameter along with the BCP lengths on the complementary building blocks. Particle **A** tended to be surrounded by particle **B** regardless of particle size. This behavior is likely due to the stability of the BCPs in the assembly solvent, THF, with

the acid BCP being less stable. As an example, when **A1**$_{20}$ and **B2**$_{35}$ particles were assembled in a feeding ratio that was roughly 1:1, **AB** dimers preferentially formed in yields of 79% (Figure 2.5). These yields were calculated by averaging over 500 assembly structures, which were counted by eye. These results match the outcomes of similar experiments by Nie and co-workers in which the outer PEO block was kept comparably short at PEO_{45}.[173]

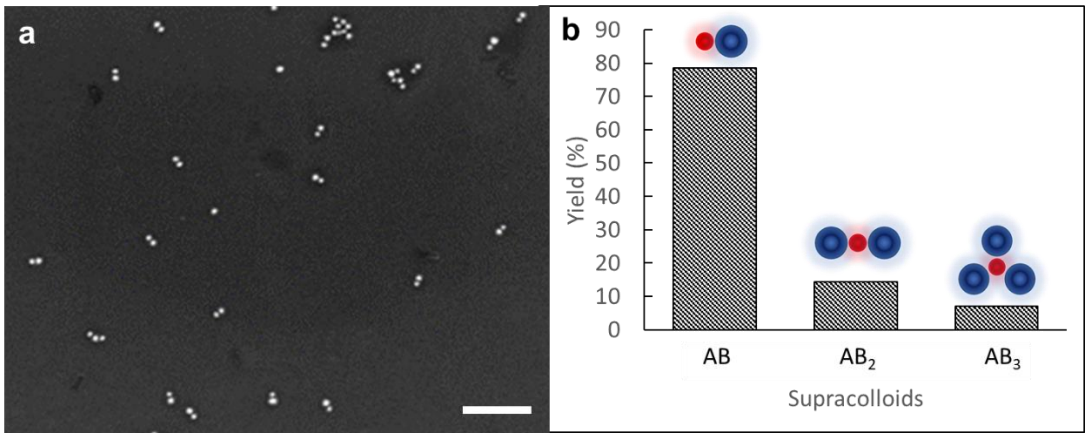

Figure 2.5 Supracolloidal **AB** dimers formed from the self-assembly of **A1**$_{20}$ and **B2**$_{35}$ in THF. (a) A representative SEM image of the dimers. (b) Population statistics of the assembly results showing the overall yields. The scale bar is 300 nm.

The interparticle distance was calculated from TEM images, which will be further discussed later, and was found to be 2.4 nm. This interparticle distance results in a slight red-shift (~ 3 nm) in the absorption spectrum when compared to that of the individual building blocks. This red-shifting suggests that supracolloids are forming in solution rather than during SEM and TEM sample preparation.

This method can be used to create additional structures by tuning different parameters. Using the above particle diameters as an example, the feeding ratio was further varied with increasing amounts of Particle **B**. As shown in Figure 2.6, as the

feeding ratio of **B**:**A** was increased from 1:1 to 2:1, we saw a shift from **AB** structures to $\mathbf{AB_2}$ structures, with yields of 80%. In the $\mathbf{AB_2}$ structures, particles preferentially adopted a linear geometry with two outer **B** particles and a center **A** particle. This geometry limits unfavorable interactions between the two **B** particles. As the feeding ratio was further increased to 3:1, we observed a shift from $\mathbf{AB_2}$ structures to $\mathbf{AB_3}$ structures, with yields of 68%. These structures follow a similar trend to that observed with $\mathbf{AB_2}$ structures in which the center **A** particle is surrounded by three **B** particles. The particles adopted a trigonal-planar geometry to limit interactions among the **B** particles. Particles adopt this geometry to limit the electrostatic repulsion of the similarly charged **B** particles. These results are confirmed by previous studies, which show that the **BAB** bond angles are roughly 120°.[173] Furthermore, when the feeding ratio was slightly less than 1:1, chainlike structures were formed, as shown in Figure 6.4. Chains are achieved when dimers initially form and then interact in solution via dipole interactions. These dipole interactions cause dimers to preferentially orient head-to-tail, with defects or branch points occurring due to the formation of trimers and other larger clusters.[172] Additional larger-area SEM images of assembled $\mathbf{AB_n}$ structures are in Figure 6.5.

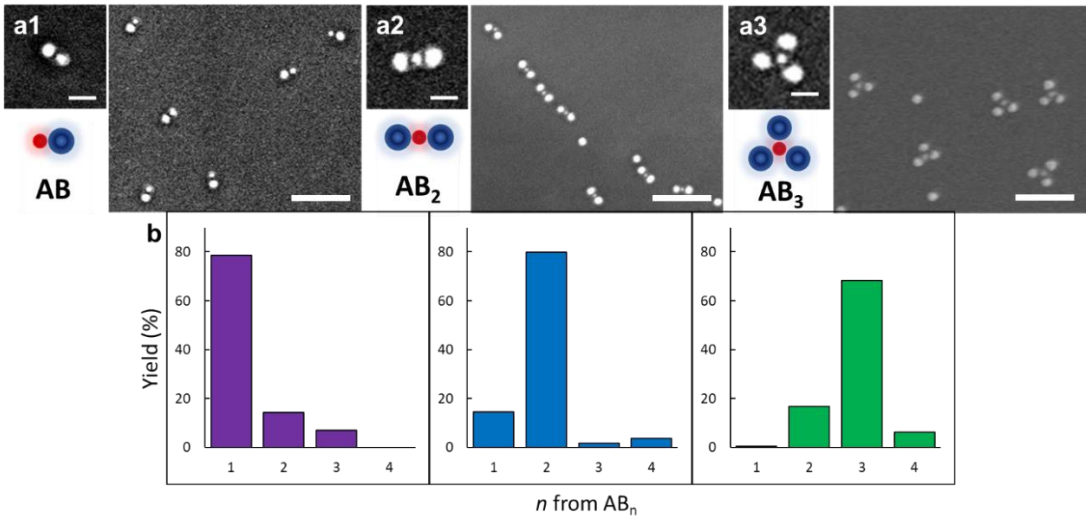

Figure 2.6 Representative supracolloidal structures formed from the self-assembly of **A**$_{20}$ and **B**$_{35}$. (a1-3) SEM images of the **AB**$_n$ structures. Small insets are zoomed in SEM images and cartoon representations of the resultant structures. (a1) **AB**, (a2) **AB**$_2$, and (a3) **AB**$_3$. (b) Population statistics plots corresponding to (a1-3) from left to right. BCP combinations were (a1) **A1**:**D2**, (a2) **A1**:**D1**, and (a3) **A4**:**D3**. The scale bars are 200 nm for the larger images and 50 nm for the inset images.

We also studied the effects of changing the particle sizes. The particle sizes were flipped, using **A1**$_{35}$ and **B1**$_{20}$ particles, which resulted in similar structures to those in Figure 2.6. As the feeding ratio of **B**:**A** was increased from 1:1 to 6:1, we observed a shift from **AB** to **AB**$_6$ structures. Yields for structures from **AB** to **AB**$_6$ were 76%, 82%, 77%, 68%, 50%, and 67%, respectively. SEM images of the structures and population statistics are shown in Figure 2.7, and larger-area SEM images are shown in Figure 6.6.

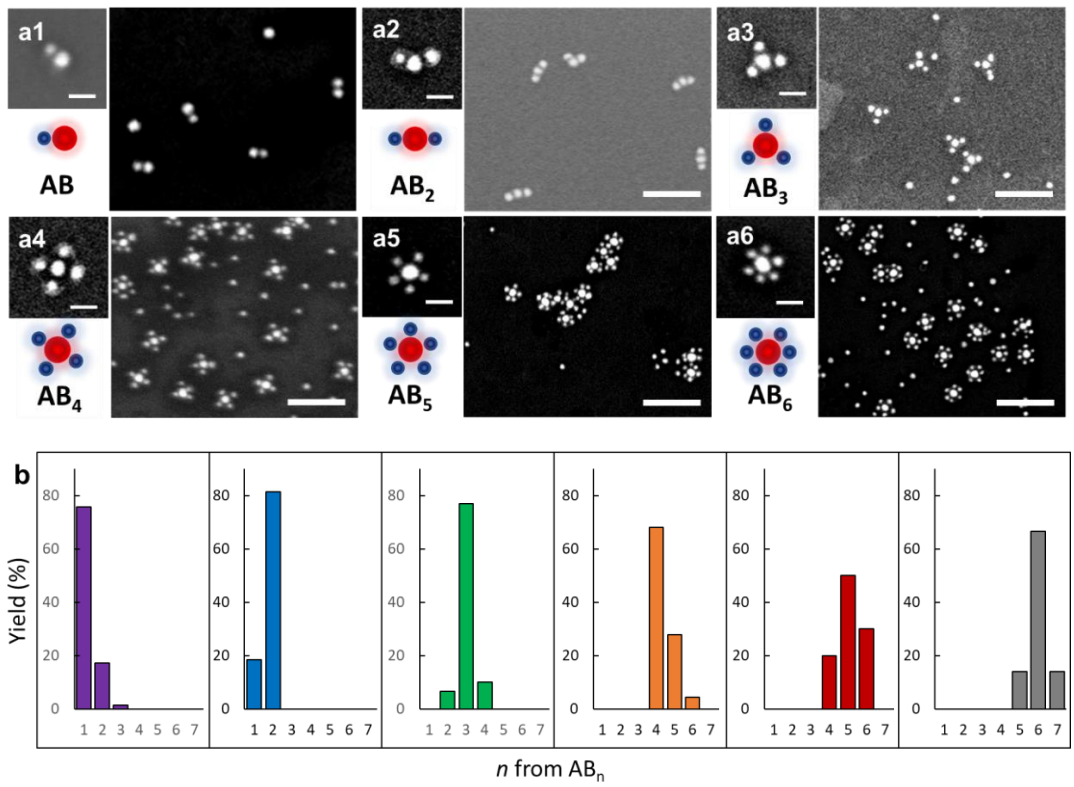

Figure 2.7 Representative supracolloidal structures formed from the self-assembly of **A35** and **B20**. (a1-6) SEM images of the **AB$_n$** structures. Small insets are zoomed in SEM images and cartoon representations of the resultant structures. (a1) **AB**, (a2) **AB2**, (a3) **AB3**, (a4) **AB4**, (a5) **AB5**, and (a6) **AB6** structures. (b) Population statistics plots corresponding to (a1-6) from left to right. BCP combinations were (a1) **A1**:**D2**, (a2) **A1**:**D1**, (a3) **A1**:**D1**, (a4) **A1**:**D2**, (a5) **A2**:**D2**, and (a6) **A2**:**D2**. The scale bars are 200 nm for the larger images and 50 nm for the inset images.

Similar to the assemblies in Figure 2.6, **AB2** and **AB3** structures in Figure 2.7 tended to adopt ideal angles for their geometries. Meanwhile, **AB4**, **AB5**, and **AB6** structures adopted non-ideal geometries. This phenomenon is likely a biproduct of the drying process for preparing SEM samples. Similar results presented by Yi *et al*. showed **AB4**, **AB5**, and **AB6** ensembles in their ideal geometries, as tetrahedral, trigonal bipyramidal, and octahedral, respectively.[173] These defined, directional

interactions are unique, as the nanostructures mirror the defined geometries of molecular analogues such as CO_2, BH_3, and XeF_4. This control is likely the result of both electrostatic repulsion but also anisotropy achieved via particle interactions. As shown in Figure 2.8, as particle **A** interacts with particle **B**, the polymer brushes must interact and entangle, allowing the acid and base moieties in the inner blocks to interact. This process leads to areas of high polymer density at the interface between the two particles, which creates an unfavorable environment for additional particles to interact due to the repulsive steric interactions. The high polymer density is coupled with the remaining charges on particle **B**, which further repel the additional positively charged **B** particles as they approach. Thus, the **B** particles are forced to interact preferentially with the polymer brush on the opposite side of the initially bound particle **B**, yielding **AB_2** trimers that have **BAB** bond angles of roughly 180°.

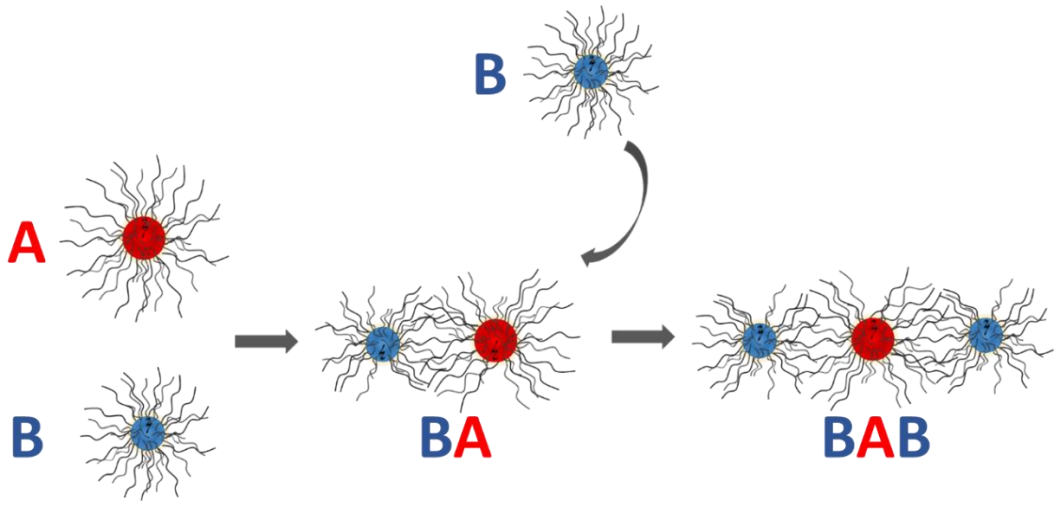

Figure 2.8 Schematic representation of **AB_2** trimer formation.

2.3.3 Transfer of HINP Assemblies into Water

Once assembled, the supracolloids were transferred into water via the slow addition of water into the assembly solutions until a 1:1 mixture of water:THF was achieved. Samples were then allowed to equilibrate for at least 1-2 h before dialysis was performed against water to remove the THF. Samples were imaged using SEM and TEM, and absorbance spectra were recorded and compared to spectra taken prior to the transfer. Results of $\mathbf{A_{20}}$–$\mathbf{B_{35}}$ particle assemblies are shown in Figure 2.9**.**

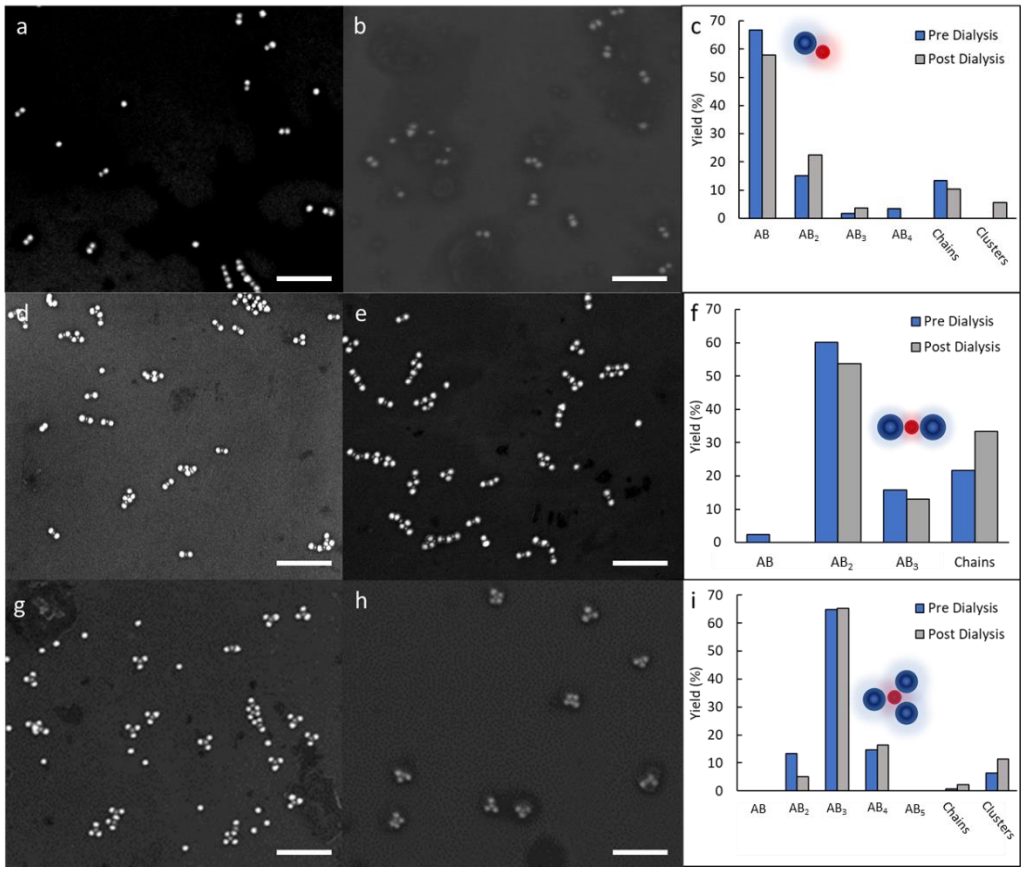

Figure 2.9 The self-assembly of $\mathbf{A_{20}}$ and $\mathbf{B_{35}}$ in THF followed by transfer to an aqueous medium. The major products are (a, b) **AB** dimers, (d, e) $\mathbf{AB_2}$ trimers, and (g, h) $\mathbf{AB_3}$ tetramers. SEM images of the representative nanostructures (a, d, g) prior to dialysis and (b, e, h) after dialysis. (c, f, i) Population statistics showing the change in nanostructure populations before and after dialysis. The BCP combinations were (a, b) **A4**:**D4**, (d, e) **A4**:**D3**, and (g, h) **A4**:**D3**. The scale bars are 300 nm.

As shown in Figure 2.9, the relative structures and population statistics of the assembled nanostructures remain largely unchanged after dialysis. However, there is a slight increase in the yields of higher valence structures. For example, as shown in Figure 2.9b, the yield of **AB** dimers decreased from 67% to 58%, whereas the yields of $\mathbf{AB_2}$ and $\mathbf{AB_3}$ structures increased from 15% to 22% and 2% to 4%, respectively. Similarly, we see a decrease in the yield of $\mathbf{AB_2}$ and $\mathbf{AB_3}$ structures from 60% to 54% and from 16% to 13%, respectively (Figure 2.9e). Meanwhile, there is an increase in chains from 22% to 33%. In Figure 2.9h we see a noticeable decrease in the prevalence of $\mathbf{AB_2}$ structures (13% to 5%), whereas there is a noted increase in the prevalence of $\mathbf{AB_4}$ structures (15% to 16%) and an increase in cluster formation (6% to 11%). This phenomenon is likely due to free particles interacting with existing structures during dialysis, yielding clusters and other higher-valence structures. Although both particles contain hydrophobic inner polymer brushes, the polymer brush of **A** is less stable in solution compared to the polymer brush of **B**, leading to a slight preference of higher valence structures in which the **A** particles are better shielded by the **B** particles. Furthermore, the stability of the nanostructures after transfer into water was enhanced when the outer PEO block was longer (PEO_{227}). This enhanced stability is likely due to the greater hydrophilicity and shielding effect of a longer outer BCP block. This trend is then further demonstrated when the particle sizes are flipped, using $\mathbf{A1_{35}}$–$\mathbf{B1_{20}}$ particle assemblies, as shown in Figures 2.10 and 6.7.

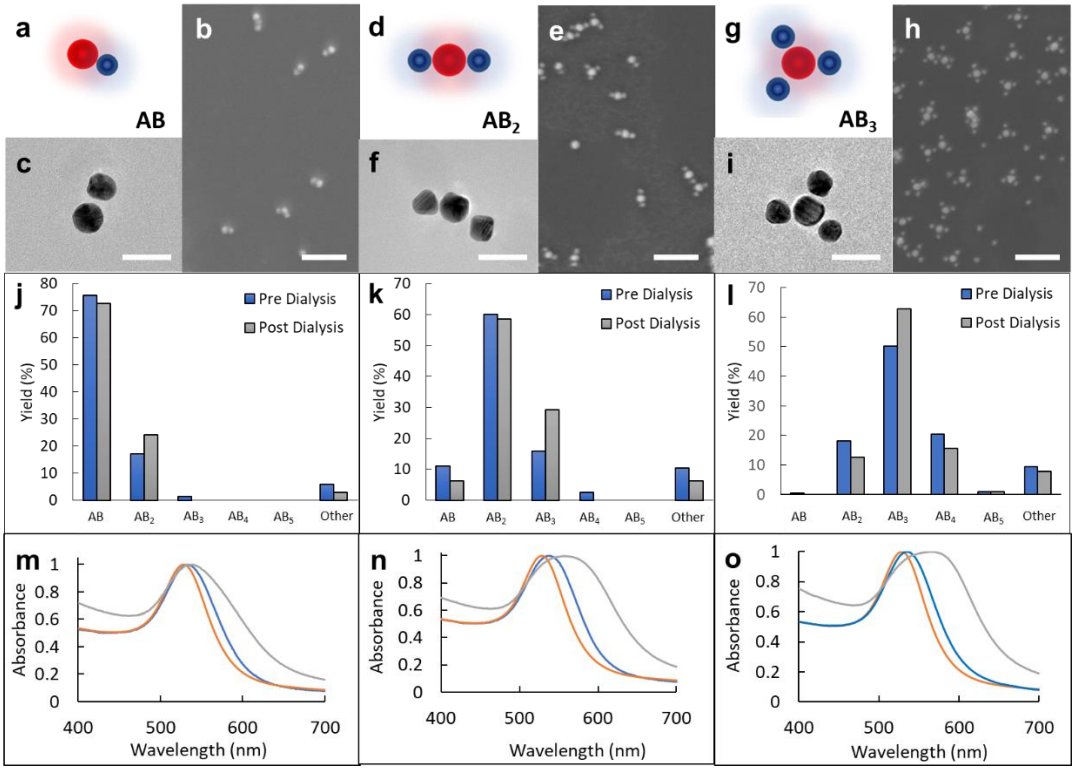

Figure 2.10 The self-assembly of **A1**$_{35}$ and **B1**$_{20}$ in THF followed by transfer to an aqueous medium. Assembled structures are (a-c, j, m) **AB** dimers, (d-f, k, n) **AB**$_2$ trimers, and (g-i, l, o) **AB**$_3$ tetramers. (a, d, g) Representative cartoons of the nanostructures. (b, e, h) SEM images and (c, f, i) TEM images of the representative nanostructures after dialysis. (j-l) Population statistics showing the change in nanostructure populations before and after dialysis. (m-o) UV-vis spectra showing the change in absorbance before (blue) and after (grey) dialysis compared to the spectra of **A1**$_{35}$ (orange). The SEM scale bars are 200 nm, and the TEM scale bars are 50 nm.

As shown in Figure 2.10, the relative structures and population statistics of the assembled nanostructures remain largely unchanged after dialysis. However, there is still a noticeable shift to higher-valence structures similar to the results shown in Figure 2.9. For example, as shown in Figure 2.10j, there is a slight decrease in **AB** dimers from 76% to 73% and an increase in **AB**$_2$ trimers from 17% to 24%. In Figure 2.10k, we see a decrease in **AB** and **AB**$_2$ structures from 11% to 6% and 60% to 59%,

respectively and an increase in **AB$_3$** tetramers from 16% to 29%. Finally, in Figure 2.7l, we see a decrease in **AB$_2$** trimers from 18% to 13% and an increase in **AB$_3$** tetramers from 50% to 63%. This trend is also observed in Figure 6.7, where there is a noticeable change in the amount of **AB$_3$** and **AB$_4$** structures before and after transfer into water. The percentage of **AB$_3$** structures drops from 46% to 28%, whereas the percentage of **AB$_4$** structures rises from 41% to 54%.

Additionally, there is a noticeable red-shift and broadening of the absorption peaks for all three structures. This shift increased with increasing number of **B** particles (Figure 2.10m-o). For **AB**, **AB$_2$**, and **AB$_3$** structures the absorbance peak red-shifted by 5, 20, and 26 nm, respectively. This phenomenon may be indicative of aggregation. However, we noticed that dialysis led to a change in interparticle distance between **A** and **B**. We further investigated the change in interparticle distance via TEM before and after dialysis, as shown in Figure 2.11.

2.3.4 Analysis of Interparticle Distance

Upon dialysis, the polymer brushes on both particles contract, as the inner BCP block is hydrophobic. This contraction of the polymer brush resulted in a decrease in interparticle distance between the central **A** and outer **B** particles, as shown in Figure 2.11. However, the change in interparticle distance is significantly more pronounced for higher-(valence structures compared to **AB** dimers. This is likely the result of crowding around the central particle and mitigation of steric and electrostatic interactions between adjacent **B** particles.

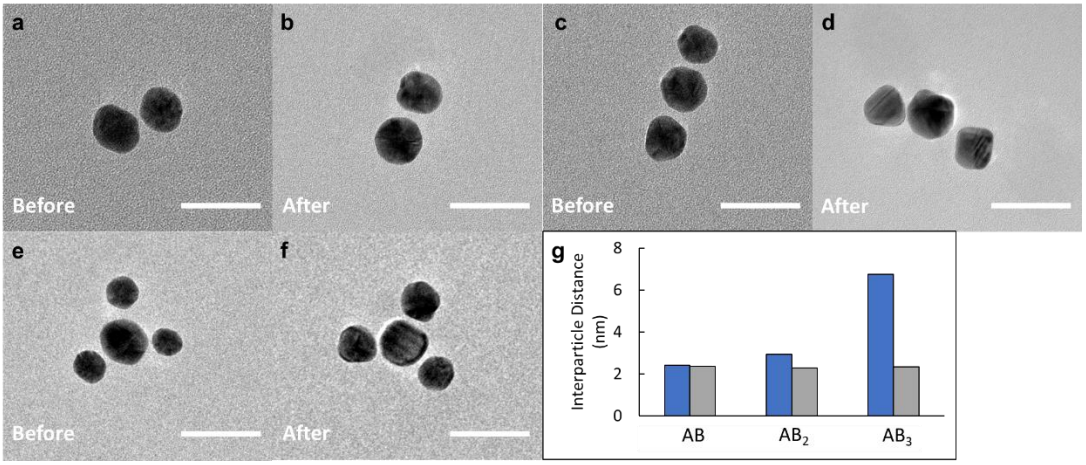

Figure 2.11 TEM images of representative $\mathbf{AB_n}$ nanostructures before and after dialysis. (a-b) **AB** dimers, (c-d) $\mathbf{AB_2}$ trimers, and (e-f) $\mathbf{AB_3}$ tetramers in which (a, c, e) are pre-dialysis, and (b, d, f) are post-dialysis. (g) Plot showing the change in interparticle distance between the central **A** particle and outer **B** particles before (blue) and after (grey) dialysis. The scale bars are 50 nm.

As demonstrated in Figure 2.8, **A** and **B** particles initially form **AB** dimers, breaking the isotropy of the polymer brush on particle **A**. This interaction results in an area of high polymer density and a minimal amount of unreacted acidic moieties at the **AB** particle interface. Meanwhile, the opposite face of particle **A** has mostly unreacted acidic moieties and a lower polymer density. Incoming **B** particles preferentially associate with the more reactive face of the **A** particle to form $\mathbf{AB_2}$ trimers. The **B** particles also align with a bond angle of roughly 180° to minimize Coulombic repulsion, leading to a slightly increased interparticle distance between **A** and **B**. $\mathbf{AB_3}$ structures are formed as the incoming **B** particle approaches from the top or bottom face of the central **A** particle. Particle **B** bonds to one of these faces, as they contain the most active acidic moieties. As the third **B** particle interacts with the **A** particle, the other two **B** particles are pushed from their ideal geometries to make

space for the new particle and minimize Coulombic repulsion. This particle rearrangement causes a further increase in interparticle distance between **A** and **B**, as shown in Figure 2.11g. The interparticle distance is shown to increase from 2.4 nm to 2.9 nm to 6.7 nm from **AB** to **AB$_2$** to **AB$_3$** structures, respectively. This increase in interparticle distance leads to a more extended polymer brush for the **AB$_3$** structures, which results in the inner hydrophobic polymer brush being more exposed to the solvent.

Upon dialysis with water, the polymer brushes for the **AB$_3$** structures collapse to shield the hydrophobic inner core, resulting in a decrease in the interparticle distance from 6.7 to 2.4 nm. This decrease in interparticle distance is also observed for **AB** and **AB$_2$** structures. However, the effect is not as pronounced, as the polymer brushes for both structures are not as extended due to decreased steric interactions. The change in interparticle distance is ~0.6 nm for **AB$_2$** trimers and is negligible for **AB** dimers. This minimal change in interparticle distance for **AB** dimers results in minimal red-shifting (~5 nm) compared to the sample prior to dialysis. Conversely, the decrease in interparticle distance for both **AB$_2$** and **AB$_3$** structures can explain the large red-shifts and broadening in both absorption spectra compared to the samples prior to dialysis.

2.4 Conclusion

In this Chapter, I demonstrated the formation of supracolloids with defined valences by modifying Au NPs with complementary, reactive BCPs. Defined nanostructures were achieved via fine tuning of the particle feeding ratio, particle sizes, and BCP lengths. The obtained supracolloids were all produced in high yields,

mirroring previous results. Importantly, the use of a longer outer, hydrophilic PEO block for our polymer brush proved pivotal in providing stability of our nanostructures when transferred to water. However, it must be noted that the use of PS as a steric buffer within the inner BCP block, resulted in an overall, hydrophobic inner block. Thus, when the assembled nanostructures were transferred to water, we observed a significant decrease in interparticle distance between particles **A** and **B**, as the polymer shell collapsed to shield the hydrophobic BCP domains. This decrease in interparticle distance resulted in significant red-shifting and broadening of the absorption spectra in most samples, while the structural integrity and yield remained mostly unchanged. The ability to control the directional interactions between particles, yielding desired colloidal nanostructures with defined valences, will be useful in applications, such as sensing and optoelectronics. Additionally, colloidal stability in an aqueous medium allows for expanded use in cellular uptake and biomedical applications such as biosensing and bioimaging.

Chapter 3: Self-Assembly of Block Copolymer-tethered Gold Nanoparticles into Supracolloidal Ensembles *via* Host–Guest Interactions

Overview. I report the design and self-assembly of block copolymer-tethered gold nanoparticles into colloidal suprastructures. This self-assembly is a host–guest driven process in which the block copolymers tethered to the particle surface contain either the hydrophilic host or the hydrophobic guest moiety. Under aqueous conditions, the guest moieties are destabilized and are therefore driven to form complexes with the host moieties. These interactions drive the particle assembly, enabling the formation of a variety of different structures. It is found that the particle size greatly impacts the geometry of resultant ensembles; the particle size mismatch yielded either chains and $\mathbf{AB_n}$ structures or branched chains and sunflower ($\mathbf{AB_x}$) structures. The effect of polymer length was also explored, and it was discovered that the number of sunflower structure petals increased with increasing length of the guest-functionalized polymer.

3.1 Introduction

The design of water-stable, colloidal ensembles, with unique structures and geometries, provides new avenues for applications in biosensing,[177] drug delivery,[178] and cancer therapies (photothermal and photodynamic),[179,180] as aqueous environments better mimic *in vivo* conditions than do organic solvents. As demonstrated in Chapter 2, we achieved the formation of defined colloidal nanostructures that were water-stable; however, this method does have inherent limitations. The acid–base-driven self-assembly requires multiple steps, as the initial self-assembly is performed in THF, and can be sensitive to small changes in the

environment, yielding undesired products and/or causing aggregation. Additionally, once assembled, the colloidal ensembles cannot be separated.[172-174] This lack of reversibility limits functionality in certain applications, such as plasmonics[14] and catalysis,[15] in which the ability to change the optical and chemical properties via reversible assembly is particularly advantageous.

Consequently, we took inspiration from the hydrogel-based self-assembly methods established by Harada *et al.*[181,182] In their approach, complementary hydrogel cubes were synthesized that contained various host or guest moieties. For simplicity, these hydrogel cubes will be referred to as either host or guest cubes. The host cubes contained cyclodextrin (CD, α or β) moieties and the guest cubes contained adamantyl (Ada), t-butyl, or n-butyl groups. When the complementary host and guest gels were agitated in an aqueous solution, linear chains of alternating host and guest blocks were formed. This assembly is caused by the high binding affinities of the hydrophobic guest moieties within the amphiphilic host macrocycles in aqueous environments. These binding affinities were calculated to be 1.5×10^{3} M^{-1} for β-CD–Ada, 1.7×10^{2} M^{-1} for β-CD–t-butyl, and 5.7×10^{1} M^{-1} for α-CD–n-butyl. Additionally, their system showed enhanced selectivity based on these binding affinities, as α-CD gels only formed chains with n-butyl gels, whereas β-CD gels only formed chains with t-butyl and Ada gels. Furthermore, the bond strength was so high for β-CD–Ada gels that they could only be separated at temperatures greater than 90 °C. At lower temperatures, the gels ruptured internally rather than at the gel–gel interface. This gel–gel self-assembly can also be driven through additional stimuli, such as photoirradiation,[183] reduction/oxidation,[184] pH,[185] and temperature.[186]

Although promising, extending this type of self-assembly to NPs remains challenging. Common stimuli include light,[5,6] pH,[7,8] temperature,[9] applied magnetic fields,[10] and solvent conditions;[11] however, most current assemblies use SgNPs, which limits the complexity and tunability of the resultant structures.[2-4] One approach to using PgNPs as building blocks is the use of tectons, as established by Macfarlane and co-workers.[187-194] Tectons are composed of inorganic NPs grafted with a dense polymer brush that are capped with hydrogen-bond acceptors. In Macfarlane's system, Au NPs are modified with thiol-terminated PS that is capped with complementary hydrogen-bonding moieties. Assembly is then initiated by mixing the complementary building blocks in an unfavorable solvent, such as n-decane, which triggers the hydrogen bonding. Disassembly can be initiated by adding a more favorable solvent, such as toluene. Furthermore, ordered assembly can be achieved through annealing at higher temperatures, yielding 3D arrays of different sizes with defined, repeating crystallinity.[191-194]

Although promising, Macfarlane's system requires high σ values and annealing to achieve targeted structures. To achieve increased ensemble complexity, it is advantageous to break the particle isotropy, as described previously using B-PgNPs as building blocks.[172-175] An example established by Nie and co-workers used reversible halogen interactions to drive particle assembly and disassembly, which was monitored using UV-vis and SEM imaging.[175] Complementary particles were assembled under favorable solvent conditions via halogen interactions, in which the halogen serves as a donor, and a Lewis base serves as the halogen acceptor. This self-assembly of the two building blocks resulted in various $\mathbf{AB_n}$ (n = 1-6) structures, with

yields greater than 75%, that could be tuned by controlling the building-block feeding ratio and BCP lengths. Structures were disassembled via the addition of a competitive Lewis base, yielding mostly single particles that could be reassembled upon removal of the competitive Lewis base. Although these results are exemplary, with yields and structures on par with those achieved using acid–base neutralization, this system still requires the self-assembly to be performed in non-aqueous conditions, with disassembly occurring upon addition of competing small molecules. To induce reassembly following particle disassembly, the small molecules need to be removed via dialysis, a requirement that we would like to avoid.

In this chapter, I expand upon our novel method for the self-assembly of hybrid NPs by using a new driving force in host–guest interactions. In this system, different-sized Au NPs were modified with one of two complementary diblock BCPs, as shown in Figure 3.1. These two BCPs were thiol-terminated poly(ethylene oxide)-*block*-poly(adamantyl methacrylate-*r*-dimethyl acrylamide) (*Abbrev*: PEO-*b*-P(AdMA-*r*-DMA)-SH) and poly(ethylene oxide)-*block*-poly(β-cyclodextrin methacrylate-*r*-dimethyl acrylamide) (*Abbrev*: PEO-*b*-P(β-CDMA-*r*-DMA)-SH). The BCP-modified Au NPs are referred to as building blocks **A** and **B**, respectively. The inner block is a random copolymer of DMA, which serves as a steric buffer, and either a guest moiety (AdMA) or a host macrocycle (β-CD). The outer block is the hydrophilic homopolymer, PEO. Ada and β-CD were chosen as a model host–guest system, as their interactions have been well studied and used in various self-assembly studies.[195-199] Ada groups are hydrophobic, and thus are driven within the β-CD cavities when exposed to water. Due to the flexibility of the β-CD macrocycle, the β-

CD moieties conform around the Ada groups, forming strong noncovalent interactions, leading to an intrinsic binding affinity of 6×10^4 M^{-1}.[195,196] However, due to the multivalency of this system, the binding affinity is likely much higher, as demonstrated by the work of Reinhoudt and co-workers.[196,197] Careful fine tuning of the inner BCP block length and ratio of the two monomers allows for better control over the number of interactions among the reacting building blocks, whereas the long, hydrophilic outer block allows for greater stability of the assembled structures in water.

The assembly process was initiated by slowly adding water to a mixture of both building blocks suspended in a more favorable solvent, DMF. The addition was performed under stirring to ensure even distribution of solvents. Subsequently, the solutions were dialyzed against water for at least 12 h to remove the DMF and drive the self-assembly. This process yielded a variety of colloidal nanostructures with defined valences in high yields. Different structures were formed by fine tuning the polymer length and composition, along with the feeding ratio of the two building blocks. These structures include dimers **(AB)**, trimers **(AB_2)**, tetramers **(AB_3)**, pentamers **(AB_4)**, and alternating chains **$(AB)_n$**, as demonstrated with our previous system. However, we found that when the guest particle size was larger than that of the host particle, we formed branched chains and sunflower structures **(AB_x)**. Regardless of particle size, particle **A** served as the central "atom" in the resultant structures, with the **B** particles surrounding particle **A**. This particle organization was rationalized as the host particles shielding the hydrophobic guest particles. These results mirror those reported in Chapter 2; however, the yields are not as high as in

our previous system, likely due to the strong hydrophobic effect imposed by our guest particles. The host–guest system also lacks the charge-based interactions that directed the growth of the nanostructures in the acid–base driven system.[172-174]

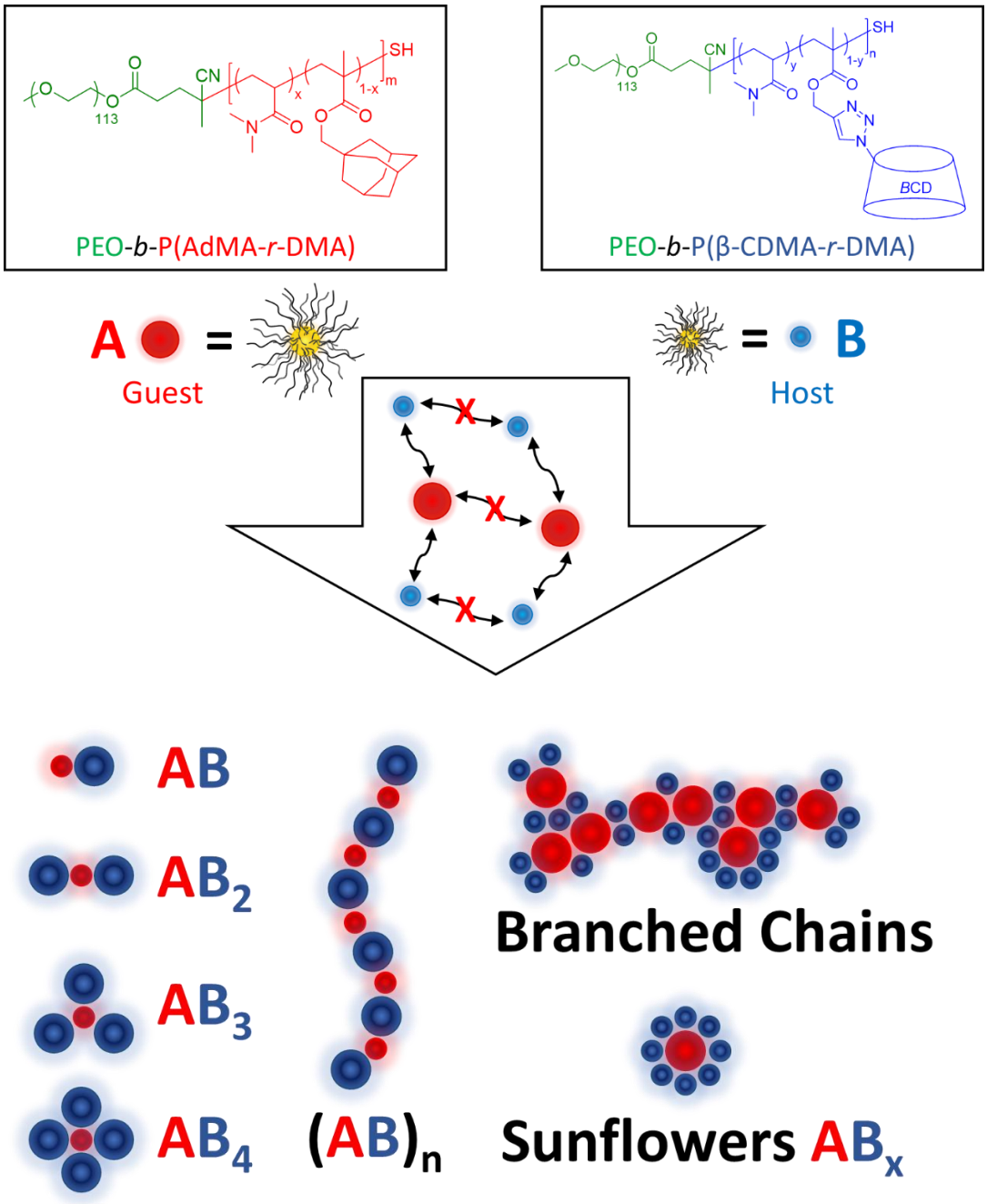

Figure 3.1 Schematic showing the assembly of complementary colloidal BCP-tethered Au NPs into various nanostructures via selective host–guest interactions.

3.2 Materials and Experimental Methods

3.2.1 Materials

1-(*p*-toluenesulfonyl)imidazole (99%), triethylamine (TEA, ≥ 99.5%), magnesium sulfate (anhydrous, ≥ 97%), β-cyclodextrin (β-CD, ≥ 97%), sodium hydroxide (≥ 98%), ammonium chloride (≥ 99.5%), sodium azide (≥ 99.5%), 1,1,2,2-tetrachloroethane (97%), dichloromethane (anhydrous, ≥ 99.8%), and dioxane (anhydrous, 99.8%) were purchased from Sigma Aldrich and were used as received. 1-adamantanemethanol (99%), THF, DMF, hexanes, ethyl acetate, and water (HPLC grade) were purchased from Fisher Scientific and were used as received. N,N-dimethylacrylamide (DMA, 99%) and propargyl methacrylate (PgMA, ≥ 98.0%) were purchased from Sigma Aldrich and passed through a basic Al_2O_3 column to remove inhibitors. The monomers were stored in a freezer after removal of the inhibitors. Azobis(isobutyronitrile) (AIBN, 98%) was purchased from Sigma Aldrich and was recrystallized from ethanol. Deionized water (Millipore Milli-Q grade) with a resistivity of 18.0 MΩ or HPLC-grade water were used in all the experiments. Regenerated Cellulose membrane dry dialysis tubing (6-8 kD MWCO Standard Grade) was purchased from Fisher Scientific and was hydrated before use.

3.2.2 Synthesis of Thiol-Terminated BCPs

The thiol-terminated BCPs, PEO-*b*-P(AdMA-*r*-DMA)-SH and PEO-*b*-P(β-CDMA-*r*-DMA)-SH were synthesized via RAFT polymerization. The synthetic procedure is shown in Figure 3.2. Syntheses and ^{1}H NMRs (Figure 6.8-10) of the precursors, AdMA, tosyl-β-CD, and N_3-β-CD are found in Chapter 6.

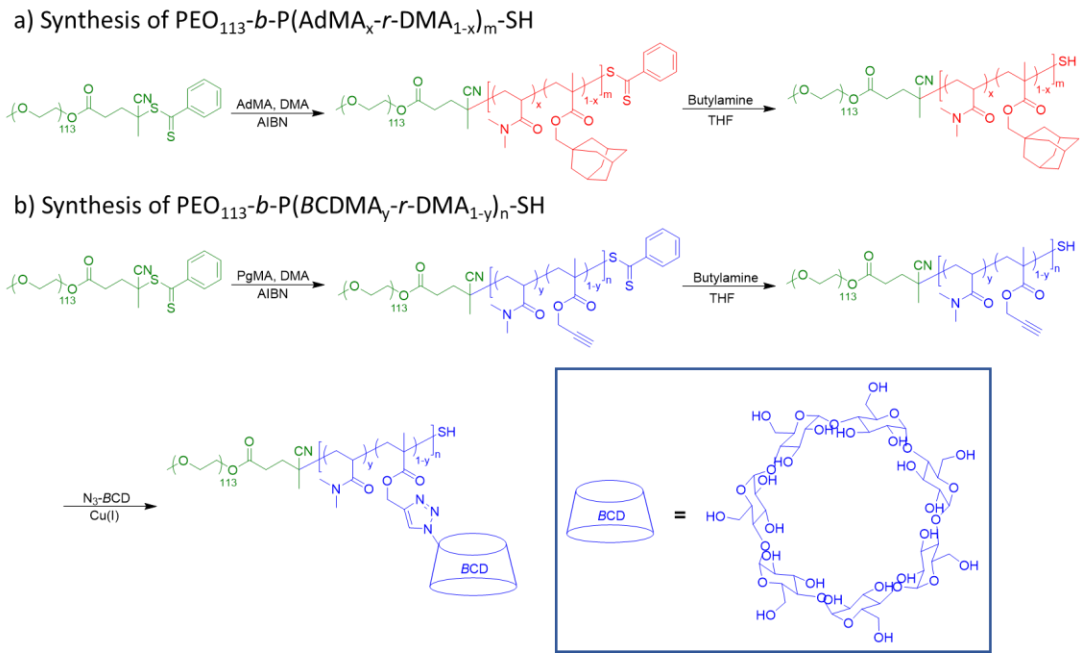

Figure 3.2 The synthesis of thiol-terminated BCPs: a) PEO-*b*-P(AdMA-*r*-DMA)-SH and b) PEO-*b*-P(β-CDMA-*r*-DMA)-SH.

3.2.2.1 Synthesis of PEO-b-P(AdMA-r-DMA)-SH

RAFT polymerization was used to synthesize PEO-*b*-P(AdMA-*r*-DMA)-SH BCPs of various lengths, as follows. PEG_{113}-CPADB (50 mg, 0.01 mmol) was added to a roundbottom flask with DMA (694 mg, 7 mmol) and AdMA (703 mg, 3 mmol). (The synthesis of AdMA is outlined in section 6.3.) Subsequently, anhydrous dioxane (5.00 mL) was added along with AIBN (10.0 µL of a 0.1 mM AIBN solution in dioxane). The AIBN served as a thermo-initiator. Solutions were then purged with argon for 30 min and then stirred in a 70 °C oil bath for 12-24 h. The polymers were precipitated with cold hexanes (~90 mL, 10 °C) and centrifuged at 5,000 rpm for 10 min. The polymers were then dissolved in THF (~10 mL) and precipitated with hexanes (~90 mL). The solid was collected via centrifugation at 5,000 rpm for 10 min. This process was repeated two more times, and the final product was dried under

vacuum for at least 24 h. The dithiobenzoate was then reduced following the procedure outlined in Section 2.2.3.2.

The following analysis was performed on BCP **AD2** as a representative polymer (see Table 3.1). From the ^{1}H NMR spectrum (in $CDCl_3$, see Figure 6.11), the ^{1}H NMR-based molecular weight M_n is 55.3 Kg·mol^{-1}. The analysis was done by comparing the integrals of the methyl group hydrogens of AdMA (0.6-1.1 ppm) and the N-methyl group hydrogens of DMA (2.3-3.4 ppm) to the methylene group hydrogens of PEO (3.62-3.66 ppm). The length of the PEO block was known and was used as a standard to determine the amounts of DMA and AdMA present in the final polymer. However, the methylene peak of PEO does slightly overlap with the ester group peak of AdMA, resulting in some error in the final M_n values. PEO-*b*-P(AdMA-*r*-DMA)-SH BCPs of different lengths and charge-ratios were synthesized by varying the reaction time (Table 3.1).

3.2.2.2 Synthesis of PEO-b-P(PgMA-r-DMA)-SH

RAFT polymerization was used to synthesize PEO-*b*-P(PgMA-*r*-DMA)-SH BCPs of various lengths, as follows. PEG_{113}-CTA (50 mg, 0.01 mmol) was added to a roundbottom flask with DMA (694 mg, 7 mmol) and PgMA (372 mg, 3 mmol). Anhydrous dioxane (5.00 mL) was added along with AIBN (10.0 µL of a 0.1 mM AIBN solution in dioxane). The AIBN served as a thermo-initiator. The solutions were then purged with argon for 30 min and then stirred in a 70 °C oil bath for 8-24 h. The polymers were precipitated with cold hexanes (~90 mL, 10 °C) and centrifuged at 5,000 rpm for 10 min. The polymers were then dissolved in THF (~10 mL) and precipitated with hexanes (~90 mL). The solid was collected via

centrifugation at 5,000 rpm for 10 min. This process was repeated two more times, and the final product was dried under vacuum for at least 24 h. The dithiobenzoate was then reduced following the procedure outlined in Section 2.2.3.2.

The following analysis was performed on BCP **P4**, as a representative polymer (see Table 3.1). From the ^{1}H NMR spectrum (in $CDCl_3$, see Figure 6.12), the ^{1}H NMR-based molecular weight M_n is 21.5 Kg·mol^{-1}. The analysis was done by comparing the integrals of the ester group hydrogens of PgMA (4.3-5.0 ppm) and the N-methyl group hydrogens of DMA (2.3-3.4 ppm) to the methylene group hydrogens of PEO (3.62-3.66 ppm). The length of the PEO block was known and was used as a standard to determine the amounts of DMA and PgMA present in the final polymer. PEO-*b*-P(PgMA-*r*-DMA)-SH BCPs of different lengths and charge-ratios were synthesized by varying the reaction time (Table 3.1).

3.2.2.3 Synthesis of PEO-*b*-P(β-CDMA-*r*-DMA)-SH

Copper-catalyzed, azide-alkyne cycloaddition was used to synthesize PEO-*b*-P(DMA-*r*-β-CDMA)-SH of various lengths following a previously reported procedure.[200] PEO_{113}-*b*-P(DMA-*r*-PgMA)-SH (0.01 mmol) and N_3-β-CD (1 eq. per PgMA) were added to a 25 mL roundbottom flask and dissolved in DMF (10.00 mL). (The synthesis of N_3-β-CD is outlined in Chapter 6.3). Copper sulfate (5 mol%) and sodium ascorbate (10 mol%) were added under stirring and flow of nitrogen. The solutions were purged for 30 min and were run overnight at 90 °C. The solutions were then cooled and precipitated in acetone (~90 mL) and collected via centrifugation at 5,000 rpm for 10 min. Afterwards, the polymers were dissolved in DMF (~10 mL) and precipitated with acetone (~90 mL). The solid was collected via

centrifugation at 5,000 rpm for 10 min. This process was repeated two more times, and the final product was dried under vacuum for at least 24 h, yielding PEO_{113}-*b*-P(β-CDMA-*r*-DMA)-SH.

The following analysis was performed on BCP **B4**, as a representative polymer (see Table 3.1). From the ^{1}H NMR spectrum (in DMSO-d6, see Figure 6.13), the ^{1}H NMR-based molecular weight M_n is 65.6 Kg·mol^{-1}. The analysis was done by comparing the integral of the triazole hydrogen (8.1-8.3 ppm) to the integral of the methyl hydrogens of β-CDMA (0.5-1.0 ppm). The ratio of the triazole groups to PgMA was used to determine the conversion rate of PgMA to β-CDMA. PEO-*b*-P(β-CDMA-*r*-DMA)-SH BCPs of different lengths and charge-ratios were synthesized (Table 3.1).

Table 3.1 Characterization of Host/Guest-functionalized BCPs

BCP	Formula	Monomer Ratio	M_n (^{1}H NMR) (Kg·mol^{-1})	R_0 (nm)
AD1	PEO_{113}-*b*-P(DMA_{183}-*r*-$AdMA_{80}$)$_{263}$-SH	0.30	41.9	8.44
AD2	PEO_{113}-*b*-P(DMA_{120}-*r*-$AdMA_{224}$)$_{344}$-SH	0.35	55.3	9.85
P1	PEO_{113}-*b*-P(DMA_{100}-*r*-$PgMA_{22}$)$_{122}$-SH	0.18	17.6	4.94
P2	PEO_{113}-*b*-P(DMA_{197}-*r*-$PgMA_{32}$)$_{229}$-SH	0.14	28.5	6.73
P3	PEO_{113}-*b*-P(DMA_{86}-*r*-$PgMA_{29}$)$_{115}$-SH	0.25	17.1	4.84
P4	PEO_{113}-*b*-P(DMA_{119}-*r*-$PgMA_{38}$)$_{157}$-SH	0.24	21.5	5.65
B1	PEO_{113}-*b*-P(DMA_{100}-*r*-β-$CDMA_{22}$)$_{132}$-SH	0.18	43.2	4.94
B2	PEO_{113}-*b*-P(DMA_{197}-*r*-β-$CDMA_{32}$)$_{229}$-SH	0.14	65.6	6.73
B3	PEO_{113}-*b*-P(DMA_{86}-*r*-β-$CDMA_{29}$)$_{115}$-SH	0.29	50.8	4.84
B4	PEO_{113}-*b*-P(DMA_{119}-*r*-β-$CDMA_{38}$)$_{157}$-SH	0.28	65.6	5.65

*R_0 for the inner BCP block is calculated using $R_0=bN^{0.5}$, whereas *b* is the Kuhn length (1.3 nm for PDMA) and *N* is the number of Kuhn segments. For simplicity, the Kuhn length for DMA was used for the AdMA and PgMA moieties, as the inner block is mostly composed of DMA. R_0 values for the **P** BCPs were assumed to stay constant after modifying with β-CD.[201]

As M_0, the mass of a Kuhn segment, has not been reported for PDMA, M_0 was calculated using:[202]

$$R_{Max} = nl\cos\left(\frac{\theta}{2}\right) \quad (3.1)$$

$$R_{Max} = Nb \quad (3.2)$$

$$M_0 = \frac{M_n}{N} \quad (3.3)$$

where R_{Max} is the fully extended polymer chain length, n is the number of monomers/polymer chain, l is the average bond length of a C-C bond in the polymer backbone, θ is the bond angle assuming the polymer is in the total *trans* conformation, and N is the number of Kuhn segments per polymer chain. The value of nl is 0.255 nm,[203] and calculations were based on BCP **P1**, assuming the inner BCP block only consisted of DMA. The calculated M_0 value is 875.7 g·mol^{-1}.

3.2.3 Au NP Polymer Modification

Au NPs were modified with the thiol-terminated BCPs via a ligand-exchange process. 10.00 mL of the Au NP solution were centrifuged down, and the supernatant was removed. Simultaneously, 8 mg of BCP were dissolved in 4.00 mL of DMF. The Au NP solution was added dropwise to the polymer solution under sonication, and the resultant solution was then further sonicated for 1 h. Afterwards, the solution was incubated at RT overnight. The solution was then centrifuged and washed ten times with DMF. The modified-NP solution was stored at RT in a glass vial.

3.2.4 Self-Assembly of HINPs

HINP self-assembly was triggered by mixing particles **A** and **B** together in a favorable solvent, such as DMF. Initially, 100 µL of particle **A** were pipetted into 1.00 mL of DMF in a 4 mL glass vial. Afterwards, varying amounts (100-400 µL) of

particle **B** were added under sonication to ensure even distribution. Subsequently, 1.00 mL of water was added, using a mechanical syringe pump, to 1.00 mL of the NP solution over the course of 1 h under stirring. The solutions were then allowed to equilibrate for at least 1 h before being dialyzed against water for at least 12 h. Prior to use, the dialysis tubing was hydrated for 10 min. The solutions were imaged using SEM and TEM to determine the structure and yields of the resultant supracolloids.

3.2.5 Morphological and Structural Characterization

^{1}H NMR. ^{1}H NMR spectra were recorded using Bruker AV-400 MHz high resolution NMR spectrometer.

UV-vis Absorption Spectroscopy. Absorbance measurements were performed using a Shimadzu UV-2501PC UV-Vis recording spectrophotometer.

Thermogravimetric Analysis (TGA). TGA was used to characterize the BCP grafting density on the NP surfaces. A 10.00 mL stock solution of building blocks was centrifuged to remove the supernatant. Hexane was then added, and the sample was centrifuged. The hexane was removed, and the solid pellet was collected. The pellet was dried in a vacuum oven for 24 h to remove any residual solvent. The measurements were performed under argon, with a scan rate of 25 °C·min^{-1}, from 25 °C to 800 °C. During the scan process, the temperature was maintained at 100 °C for 30 min to remove any moisture. The weight fraction of the polymer ligands, *f*, was then determined and used to determine σ based on the polymer M_n.

SEM and TEM Imaging. SEM images were taken using either a Hitachi SU-70 Schottky field-emission gun Scanning Electron Microsccope (FEG-SEM) operated at 10.0 kV, and TEM images were taken using a JEOL LaB6 FEG Transmission

Electron Microscope (FEG-TEM) operated at 200 kV. Samples for SEM or TEM were prepared by drying 5.0 μL of solution on a silicon wafer or a 300-mesh copper grid covered with carbon film, respectively.

3.3 Results and Discussion

3.3.1 BCP-Tethered NPs

As described previously, Figure 3.1 shows the structures of the two complementary hybrid building blocks. Au NPs are modified with BCPs in which the inner block contains DMA, which serves as a hydrophilic, steric buffer that should not interact strongly with the particle surface, and either a guest (AdMA) or host (β-CDMA) functionalized monomer. When slowly exposed to water, the hydrophobic guest moieties are driven within the amphiphilic host macrocycles, yielding host–guest complexes that drive the self-assembly of the respective particles. Meanwhile, the outer block is hydrophilic PEO, which serves both as a steric buffer and as protective shell to stabilize the final assembled products in aqueous environments.

For simplicity, particles modified with the guest-functionalized BCPs are denoted as **A** particles, whereas particles modified with the host-functionalized BCPs are denoted as **B** particles. The number following the letter represents the polymer, and the subscript following the letter is the NP size (*e.g.*, **A1$_{20}$** represents 20-nm particles modified with BCP **AD1**, whereas **B1$_{35}$** represents 35-nm particles modified with BCP **B1**). UV-vis absorption spectroscopy was used to characterize the Au NPs before and after the surface modification. After grafting the BCPs on the NP surfaces, a slight red-shift (~8 nm) was observed, as demonstrated for the **B2$_{20}$** and **A2$_{30}$** particles in Figure 3.3. This shift may be indicative of an increase in the particle size

due to the polymer brush on the surface of the Au NPs, or may be caused by the change in the refractive index of the surrounding solution, as the unmodified particles are in water and the modified particles are in DMF. The particle concentrations were calculated to be between 1.1×10^{-9} and 3.4×10^{-9} M based on the amount of Au in solution. The free polymer concentration in solution was estimated to be below 10^{-16} M and was not expected to interfere with the assembly results.[204]

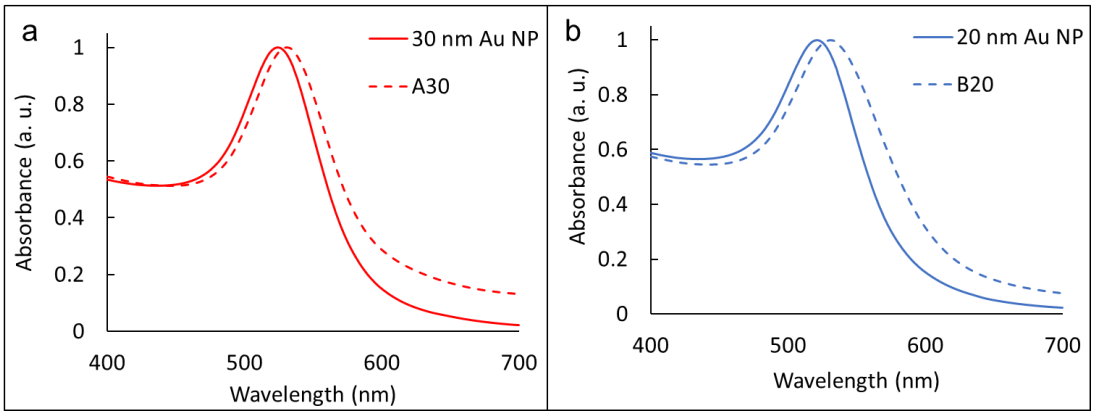

Figure 3.3 UV-vis spectra of BCP-modified Au NPs. (a) 30-nm Au NPs in aqueous solution and **A2$_{30}$** particles in DMF, and (b) 20-nm Au NPs in aqueous solution and **B2$_{20}$** particles in DMF.

TGA was performed to determine the amount of grafted-BCPs on the surfaces of the NPs (Figure 3.4). Using **A2$_{20}$** and **B2$_{30}$** as an example, weight loss was observed at temperatures above 200 °C, resulting from the thermal degradation of the BCPs into volatile products. From the TGA measurement, **A2$_{20}$** and **B2$_{30}$** showed weight losses of 30.5% and 3.1%, respectively. Using Eq. 2.1, we determined that the σ of **A2$_{20}$** and **B2$_{30}$** were 0.31 and 0.03 chains/nm^2, respectively. From Eq. 2.2, we then solved for the d_l values for **A2$_{20}$** and **B2$_{30}$**, which were 1.98 nm and 6.53 nm, respectively. The R_g for each of the BCPs could be calculated using Eq. 2.3. The ratio

of R_g/d_l is estimated to be in the range of 0.4 to 2.0, which suggests that the grafted-BCPs adopt a mostly flexible polymer-brush conformation, as discussed in detail previously.[44]

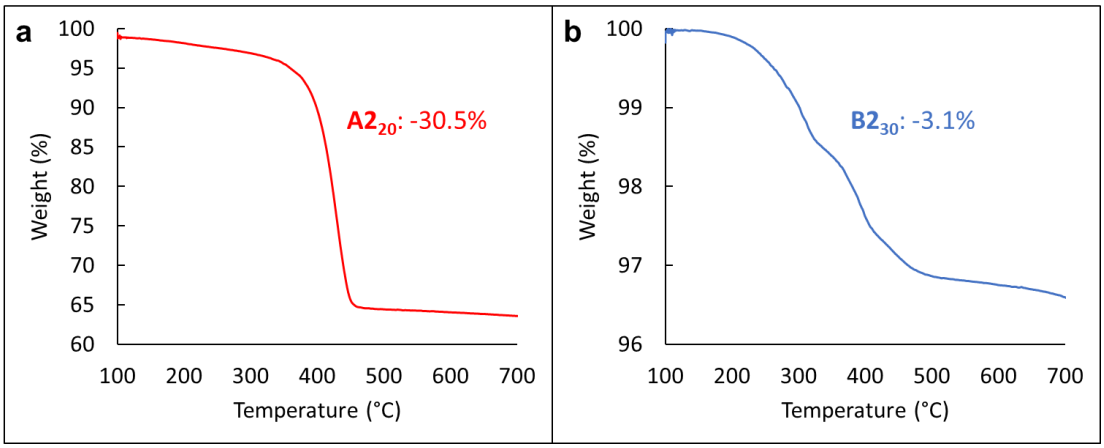

Figure 3.4 TGA curves of **A2$_{20}$** and **B2$_{30}$** particles.

3.3.2 HINP Self-Assembly

The assembly of particles **A** and **B** yielded a variety of different structures, which were largely governed by the particle feeding ratio and size, as particle **A** tended to be shielded by particle **B** regardless of particle size. This particle orientation is likely due to the BCP stability in the assembly solvent, water, as the **A** particles are destabilized when exposed to aqueous conditions due to the BCP being hydrophobic. This phenomenon is clearly noted in Figure 3.5, where the polymer shell on the **A** particles is clearly visible compared to that on the **B** particles. Initially, the building blocks are modified, stored, and mixed in DMF. Water is then slowly introduced over the course of 1 h under vigorous stirring, and particle solutions are then allowed to further equilibrate for at least 1 h prior to dialysis against water for at least 12 h to remove the DMF.

As an example, when the particle feeding ratio between **B1**$_{35}$:**A1**$_{20}$ was less than 1:1, chainlike structures were prevalent (Figure 3.5). The hydrophobic **A** particles are largely shielded by the more hydrophilic **B** particles, yielding **AB** and **AB**$_2$ structures that then further assemble into chains. The lack of linearity can be explained by the formation of larger clusters that can serve as branching points. Additionally, this system lacks the strong dipole observed in the **AB**$_n$ nanostructures previously discussed. Thus, we observe some like-particle interactions in addition to complementary-particle interactions. Furthermore, we observed evidence of self-assembly by comparing the absorption spectrum of our chainlike structures to that of our **B**$_{35}$ particles. We see a shift in the peak absorption of ~4 nm, which is indicative of self-assembly.

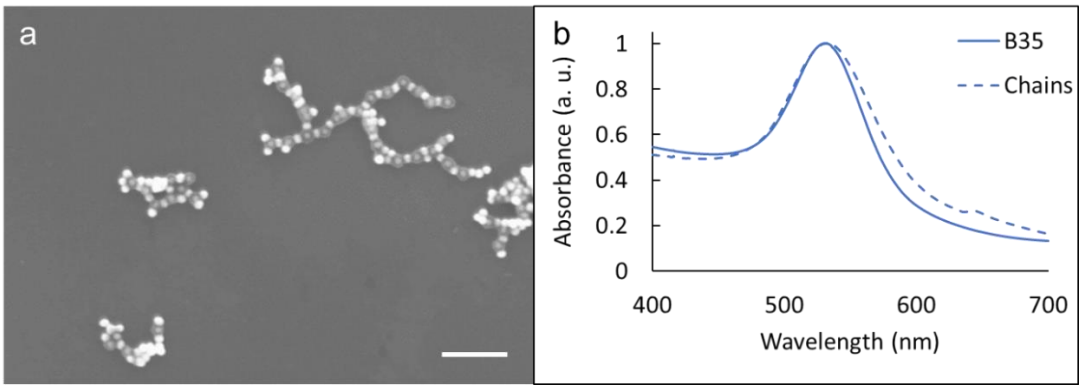

Figure 3.5 The self-assembly of **A1**$_{20}$ and **B1**$_{35}$ into nanochains. (a) A representative SEM image of the nanochains formed from the self-assembly of **A1**$_{20}$ and **B1**$_{35}$ in water when the particle feeding ratio of **B**:**A** was slightly less than 1:1. (b) The absorption spectra of the assembled nanochains compared to the **B1**$_{35}$ particles. The scale bar is 200 nm.

This method can be used to achieve additional structures by tuning parameters, including the particle feeding ratio and the particle sizes. Using the above

particle sizes and BCP combination as an example, the feeding ratio was further varied with increasing amounts of Particle **B**. As shown in Figure 3.6, as the feeding ratio of **B**:**A** was increased from 1:1 to 4:1, we saw a shift from **AB** structures to higher-order $\mathbf{AB_n}$ structures and clusters; however, control over the desired structure was limited when comparing population statistics to those presented in Chapter 2. This reduction in yield is likely caused by the hydrophobic effect, which is induced by the hydrophobic polymer brush surrounding the central **A** particles. Thus, it is beneficial for the central particles to be shielded by the more hydrophilic **B** particles, which creates a more polydisperse population of nanostructures that are not as limited by the unfavorable charge interactions that we observed in our acid–base system. These yields were calculated by averaging over 500 assembly structures, which were counted by eye. Additionally, non-assembled particles were neglected when determining the average nanostructure yields.

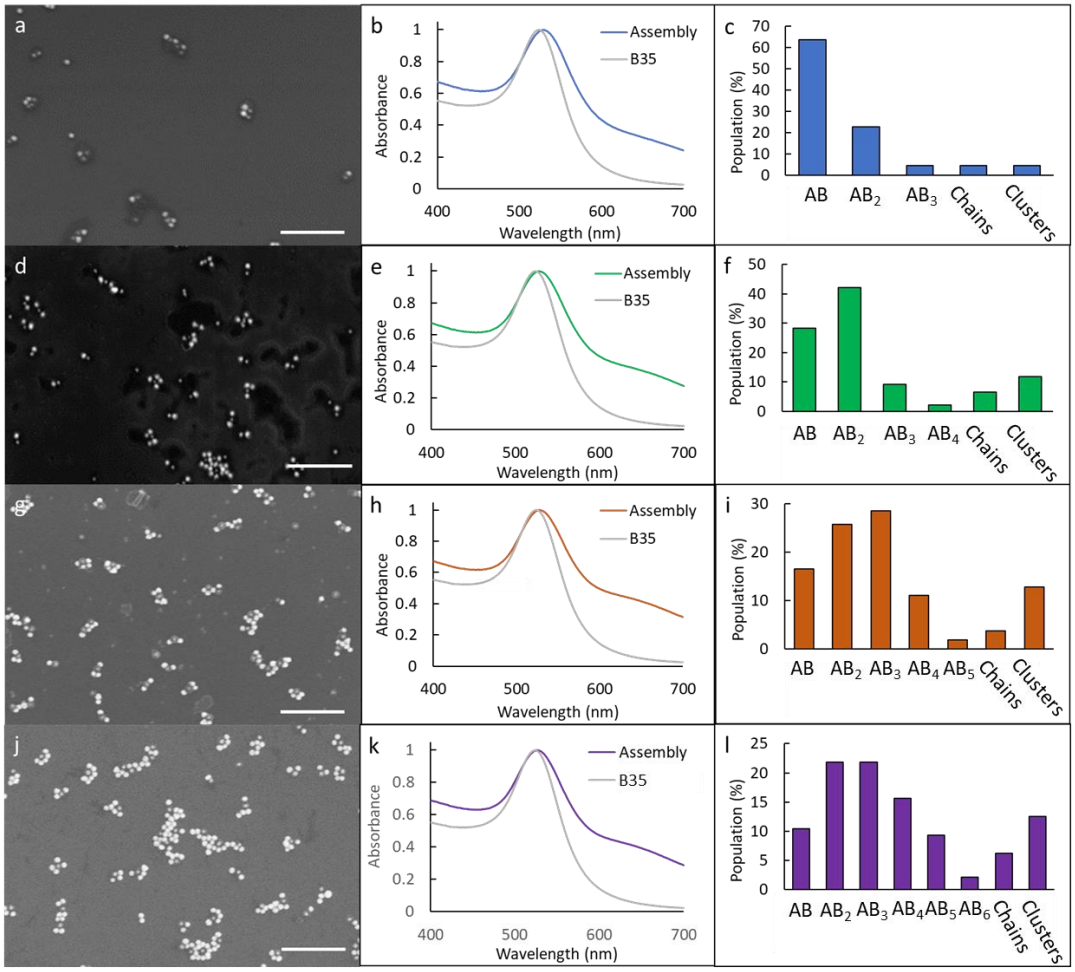

Figure 3.6 The self-assembly of **A1$_{20}$** and **B3$_{35}$** into various **AB$_n$** nanostructures. (a-c, d-f, g-i, j-l) Assembled nanostructures with an increasing feeding ratio of **B**:**A**. The feeding ratios are roughly 1:1, 2:1, 3:1, and 4:1. (a, d, g, j) Representative SEM images. (b, e, h, k) UV-vis absorption plots showing the change in the absorbance peak compared to the **B$_{35}$** particles. (c, f, i, l) Population statistics plots showing the yields of the different nanostructures. The scale bars are 200 nm.

As we increased the particle feeding ratio of **B**:**A**, the number of higher-order **AB$_n$** structures increased, and the number of dimers and trimers decreased. For example, we observed that 64% of nanostructures in Figure 3.6a are **AB** dimers. This percentage then decreased with the increasing feeding ratio of particle **B** from 1:1 to

4:1, as shown in Figure 3.7. The population percentage dropped from 64% to 28% to 17% to 10% respectively. We observed a similar trend with the formation of $\mathbf{AB_2}$ trimers as we saw an initial increase from 23% to 42% followed by a decrease to 26% and 22%. $\mathbf{AB_3}$ structures similarly started at low yields, reaching a peak yield of 29% at a feeding ratio of 3:1 before decreasing in population. Meanwhile, $\mathbf{AB_4}$ and $\mathbf{AB_5}$ structures that were not observed at low feeding ratios did increase in population with increasing feeding ratio though the peak yields remained low at 16% and 9%, respectively at a feeding ratio of 4:1.

The assembly results were further confirmed when analyzing the UV-vis absorption results, as shown in Figure 3.6b,e,h,k. In all four plots, there is a clear red-shift of the peak absorption of the assemblies when compared to the unassembled particles. These red-shifts range from 4 to 6 nm for all four samples. Additionally, there is a slight shoulder that appears and grows at around 650 nm. Interestingly, this peak grows with increasing particle feeding ratio. This observation is indicative of potential slight aggregation, which could account for the increase in cluster formation observed as the feeding ratio increased. It is also possible that the hydrophobic **A** particles can self-associate or aggregate due to hydrophobic effects. Thus, we chose to study this self-assembly behavior further by systematically varying the particle size and the polymer length.

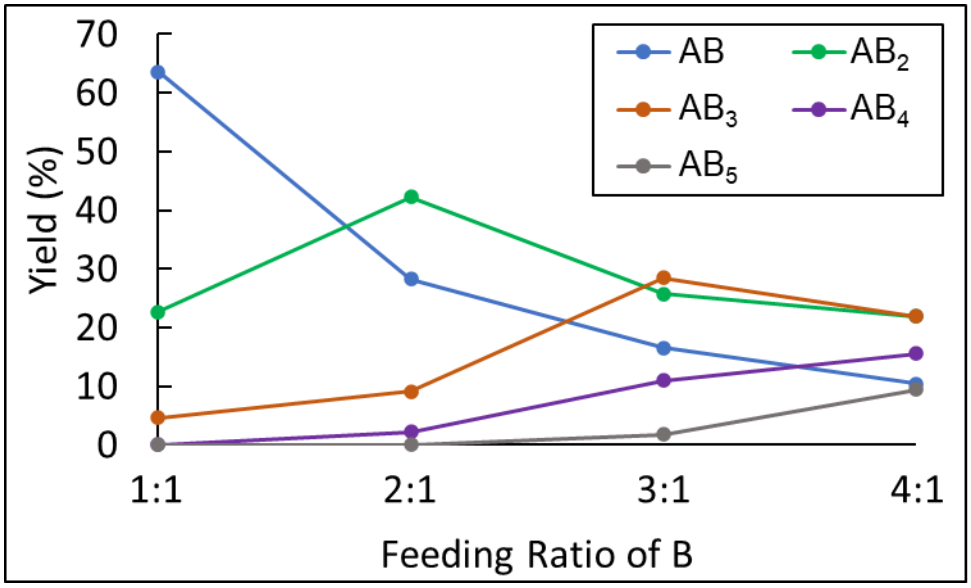

Figure 3.7 The change in nanostructure populations as a function of the feeding ratio of **B3**$_{35}$:**A1**$_{20}$.

3.3.3 Particle Size Effects on the Self-Assembly

We prepared assemblies using different particle sizes to gain further insight into the self-assembly mechanism. As shown in Figure 3.8, **A1**$_{20}$ particles were assembled with 20, 35, and 40 nm **B3** particles; the feeding ratio was 2:1. Regardless of the size of particle **B**, all three assemblies resulted in similar population distributions of assembled nanostructures, with a slight exception for **B3**$_{20}$:**A1**$_{20}$. As shown in Figure 3.8a, the population of **AB**$_2$ structures is only marginally greater than the populations of **AB**, **AB**$_3$, and **AB**$_4$ structures. This product distribution is likely caused by the decrease in host moieties on the smaller **B** particles. Thus, to shield and stabilize the assembled nanostructures effectively, more **B** particles are needed to bind to the central **A** particle, leading to a lower overall yield of the expected **AB**$_2$ product and a broader distribution of additional products.

This study was expanded upon by assembling **A1**$_{20}$ with **B3**$_{20}$ and **B3**$_{40}$ at different feeding ratios of **B** (Figures 6.14 and 6.15). The results for the **B3**$_{20}$ assemblies follow the trend observed in Figure 3.8a. Although there is a preference for dimer formation when the feeding ratio of **B**:**A** is ~ 1:1, structure specificity is limited as the feeding ratio is increased. Feeding ratios greater than 2:1 lead mostly to cluster formation. **B3**$_{20}$ results are contrasted with **B3**$_{40}$ results, as **B3**$_{40}$ assemblies follow a similar trend to the assemblies with **B3**$_{35}$. For the **B3**$_{40}$ system, **AB** dimers form preferentially when the feeding ratio of **B**:**A** ≈ 1:1. There is then a shift to **AB**$_2$ and **AB**$_3$ structures as the particle feeding ratio is increased to 2:1 and 3:1 (Figure 6.16). These results matched the trend observed based on particle size mismatch, as a greater control over **AB**$_n$ structure assembly is observed when the size of **A** is smaller than that of **B**.

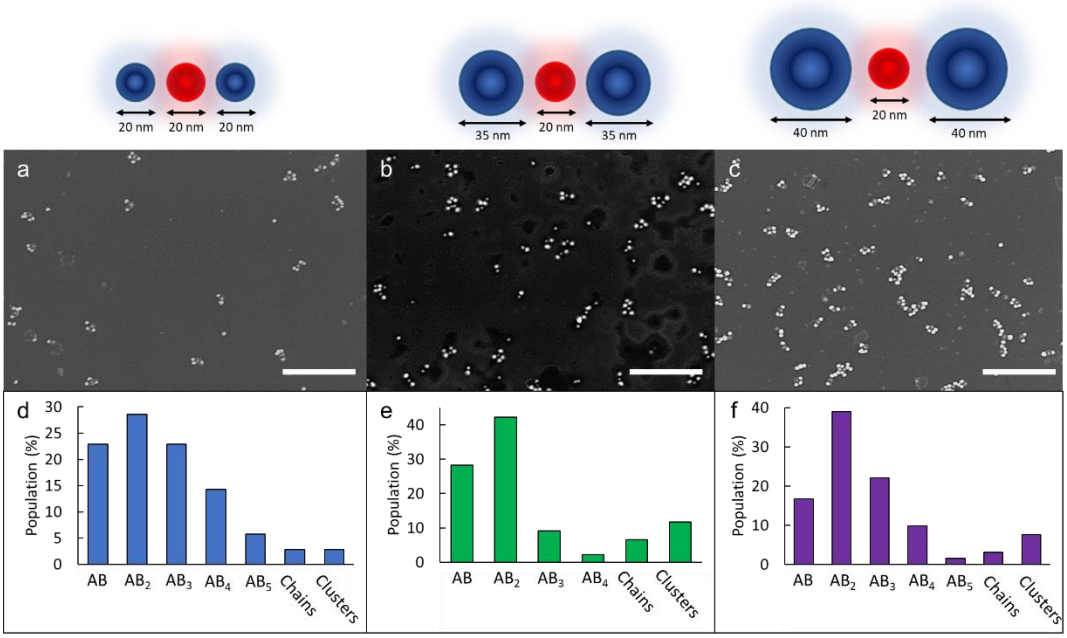

Figure 3.8 The self-assembly of **A1$_{20}$** and **B3** particles of increasing diameter. **B3** particles are (a,d) 20 nm, (b,e) 35 nm, and (c,f) 40 nm in diameter. The feeding ratio of the **B**:**A** was 2:1. (a-c) Representative SEM images of the assemblies. (d-f) Population statistics plots showing the yields of the different nanostructures. The scale bars are 400 nm.

We further explored the effect of particle size using **A1$_{35}$** particles, which were assembled with 20-, 35-, and 40-nm **B3** particles at a feeding ratio of 1:1. As shown in Figure 3.9a-c, we see a noticeable shift in nanostructures as the size of **B** changes. When **B** is larger than **A**, results match the trend observed in Figure 3.6a, in which **AB** dimers represent the major structure with a yield greater than 50%, whereas **AB$_2$**, **AB$_3$**, and small clusters make up the majority of the other obtained structures. We saw this trend continue when **A** and **B** are the same size for which **AB** structures represent the majority product with a yield greater than 60%. Conversely, when **B** was smaller than **A**, we saw the formation of higher-valence structures in

substantial yields compared to the expected **AB** structure, for which the yield was notably low. This phenomenon is likely caused by hydrophobic effects, as the central **A** particle is destabilized in water. As the **A** and **B** particles interact, the polymer brushes bend towards one another, exposing the hydrophobic inner polymer brush of the **A** particle. When the **B** particle is larger, and thus coated in more BCPs containing the active β-CD moiety, the polymer brush of the **A** particle is better shielded, as the Ada groups bind within the β-CD cavities. However, when particle **B** is smaller, more of the inner polymer brush of particle **A** is exposed, due to the decrease in available β-CD groups on the smaller **B** particle. This situation leads to instability of particle **A**, which is alleviated either through further interactions with additional **B** particles or via aggregation of the particles into non-uniform structures, which can account for the increase in cluster formation we observed. Thus, although **AB** structures are still the major product, we also observe $\mathbf{AB_2}$ and $\mathbf{AB_3}$ structures with yields near 20% compared to the 28% yield for **AB** dimers. These trends were further confirmed as particle feeding ratios were varied (Figures 3.10, 6.17, and 6.18).

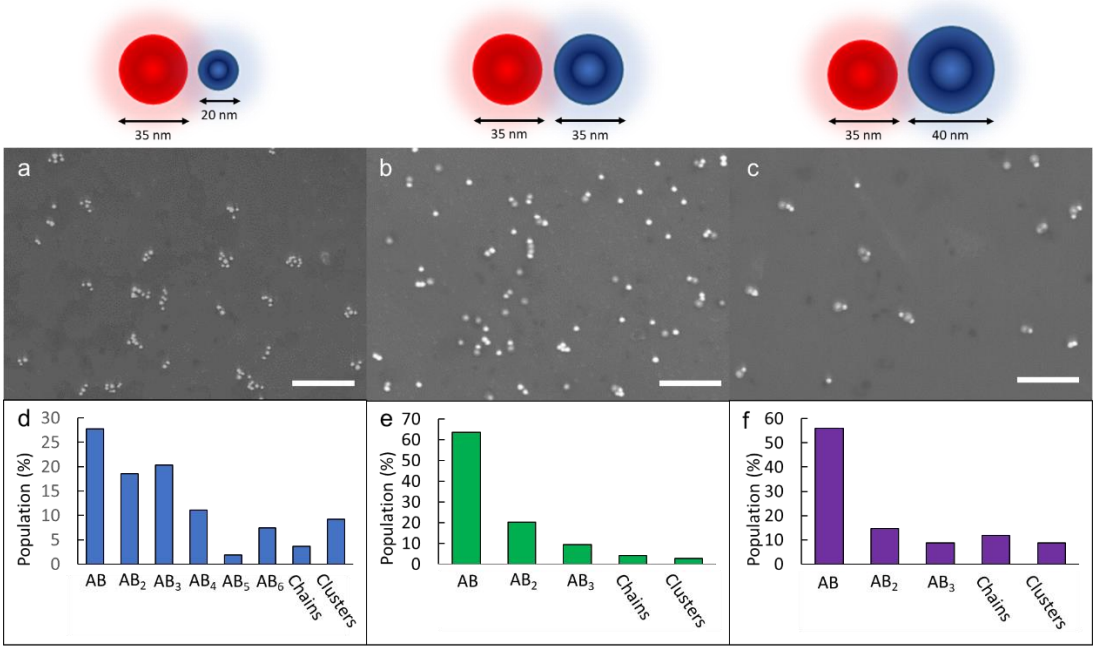

Figure 3.9 The self-assembly of **A1**$_{35}$ and **B3** particles of increasing diameter. **B3** particles are (a,d) 20 nm, (b,e) 35 nm, and (c,f) 40 nm in diameter. The feeding ratio of the **B**:**A** was 1:1. (a-c) Representative SEM images of the assemblies. (d-f) Population statistics plots showing the yields of the different nanostructures. The scale bars are 400 nm.

3.3.4 The Self-Assembly of Branched chains and Sunflower Type Structures

This section will explore the unique structures that arise from the mismatch in particle size in which particle **A** is significantly larger than particle **B**. This phenomenon is demonstrated in Figure 3.10, in which we examine how the feeding ratio of **B**$_{20}$:**A1**$_{35}$ affects the resulting nanostructures.

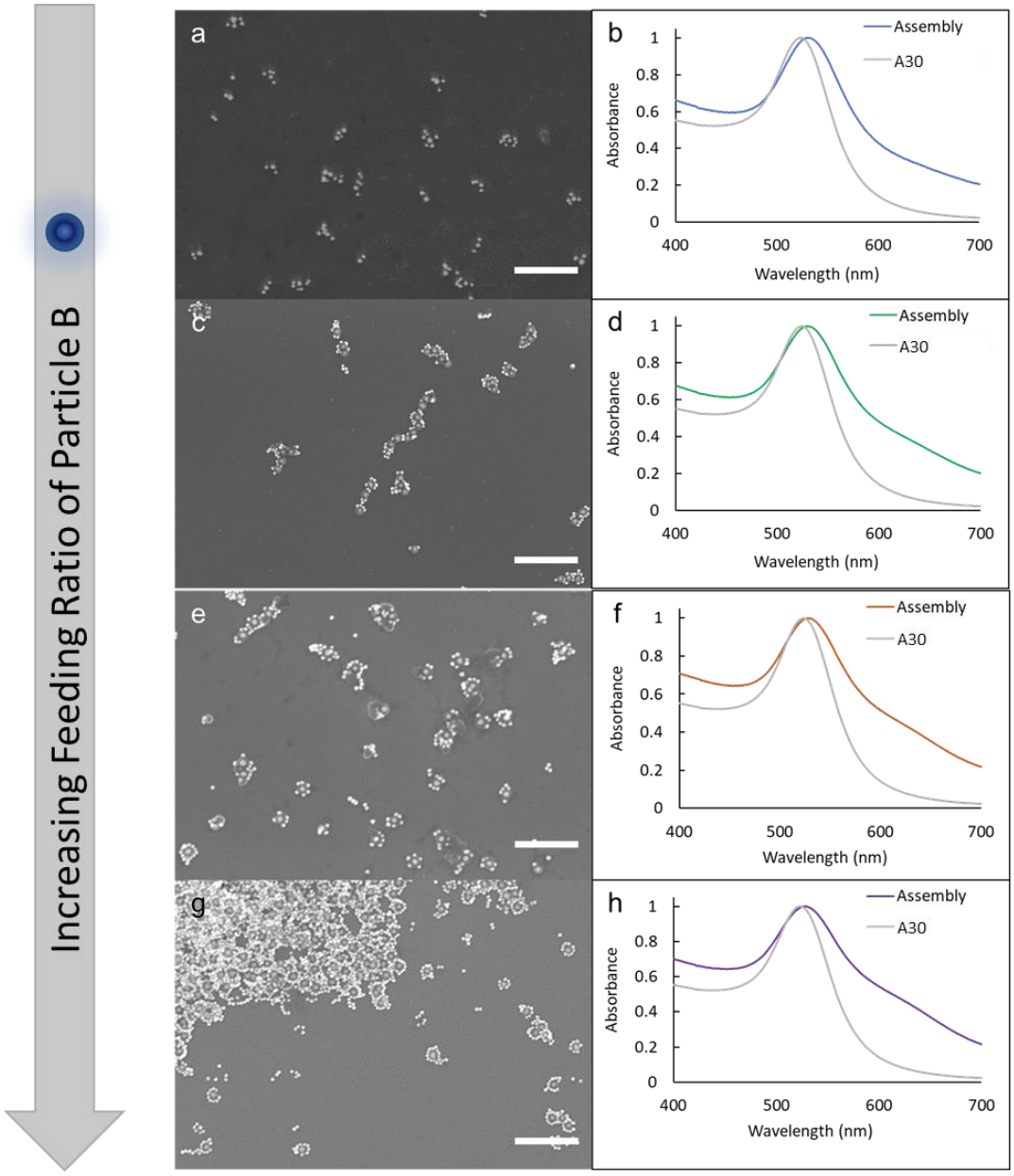

Figure 3.10 The self-assembly of **A1**$_{35}$ and **B**$_{20}$ particles into various nanostructures. (a-b, c-d, e-f, g-h) represent assembled nanostructures with an increasing feeding ratio of **B**:**A**. The feeding ratios are roughly 1:1, 2:1, 3:1, and 4:1. (a, c, e, g) Representative SEM images. (b, d, f, h) UV-vis absorption plots showing the change in the absorbance peak compared to **A**$_{35}$ particles. **B** BCPs are (a) **B3**, (c) **B3**, (e) **B4**, and (g) **B4**. The scale bars are 400 nm.

As the feeding ratio of **B**:**A** was increased from 1:1 to roughly 4:1, we observed a noticeable shift in the assembled structures. As the feeding ratio was increased from 1:1 to 2:1, we stopped seeing the formation of discrete $\mathbf{AB_n}$ nanostructures and rather observed the formation of branched chains in which the **A** particles appear to be assembling both with the **B** particles and themselves. As shown in Figure 3.10B, these chainlike structures show the **A** particles mostly interacting with **B** particles, which serve as linkers between **A** particles in the chain. However, we also see clear indication of adjacent **A** particles whose polymer shells are merged, which suggests some interaction is occurring between these particles. These interactions are likely due to the hydrophobic effect, causing the **A** particles to interact with one another to lower the unfavorable interfacial energy between the particles and the surrounding solvent.[49] As the feeding ratio was further increased to ~3:1, the concentration of **B** particles became sufficient to fully encapsulate the **A** particles, yielding $\mathbf{AB_x}$, sunflower-type structures in addition to branched chains. These structures were formed due to the stabilizing effect of the host–guest interactions between the β-CD and Ada moieties, which are stronger than hydrophobic effects driving the **A** particles to interact with one another. Furthermore, we can quantify the number of 'petals' in each sunflower structure in addition to the number of sunflower structures versus branched chains as shown in Figure 3.11.

Here, the yield of the sunflower structures is 74% and the yield of branched chains is 12%, which shows the preference for sunflower structures at this feeding ratio. Meanwhile, the remaining structures are small aggregates and clusters. Additionally, the average number of petals per sunflower was found to be 6 (± 2),

suggesting a preference for a hexagonal packing array. However, it must be noted that the percentage of sunflower structures with 6 petals is still relatively low, at 30%, with a wide spread of different petal amounts ranging from 3 to 11.

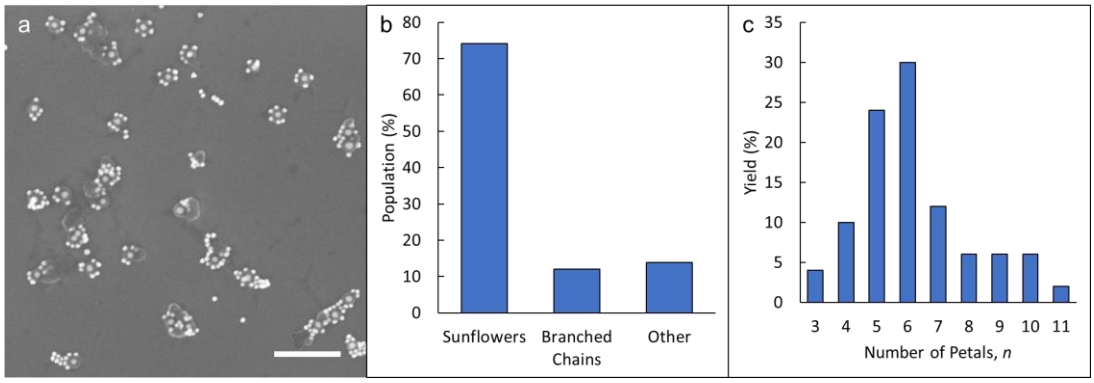

Figure 3.11 The self-assembly of **A1**$_{35}$ and **B4**$_{20}$ particles into sunflower structures. (a) SEM image of the **AB**$_x$ sunflower structures. (b) Plot showing the population statistics of the different assembly structures. (c) Plot showing the distribution of the number of petals per sunflower structure, in which the number of petals is representative of the number of **B** particles per **A** particle. The scale bar is 400 nm.

As the feeding ratio between **B**:**A** was further increased to 4:1, we began seeing the formation of a disordered 'honeycomb' monolayer. As shown in Figure 3.11g, it appears that the sunflower structures began packing in a hexagonally, close-packed array. This observation was further confirmed in Figure 3.12, in which the central **A** particles are denoted as red spheres. Upon labeling the particles, a repeating honeycomb pattern appears, denoted by red lines connecting the spheres. The average particle distance between the central particles was 144 (± 23) nm, and the average particle distance between the central particle and the corner particles was 88 (± 21) nm with an average bond angle of 60 (± 18)°.

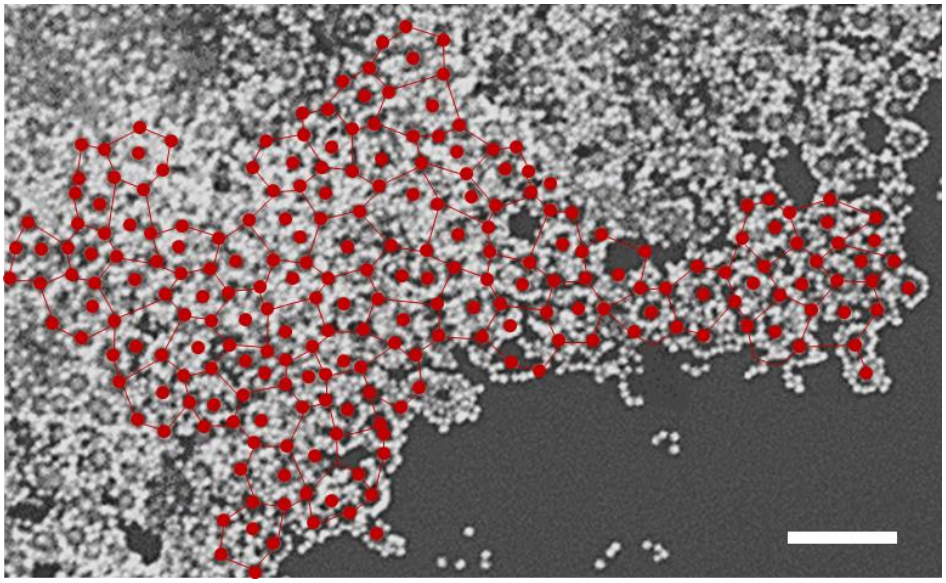

Figure 3.12 The self-assembly of $\mathbf{A1}_{35}$ and $\mathbf{B4}_{20}$ particles into a honeycomb array. Representative SEM image in which red spheres are **A** particles. The scale bar is 500 nm.

We next increased the size of the **A** particles to 40 nm, which were assembled with 20-, 35-, and 40-nm **B1** particles at a **B**:**A** feeding ratio of 2:1. As shown in Figure 3.13, we observed that the type of nanostructures formed generally agreed with previous results. Thus, when particle **A** is significantly larger than particle **B**, we see a larger spread of assembly structures. Meanwhile, when particle **A** is roughly the same size as particle **B**, we see more discrete $\mathbf{AB}_n$ structures formed. Studies changing the feeding ratio of $\mathbf{B}_n$:$\mathbf{A}_{40}$ (n = 20, 35, and 40 nm) are shown in Figures 6.19-21.

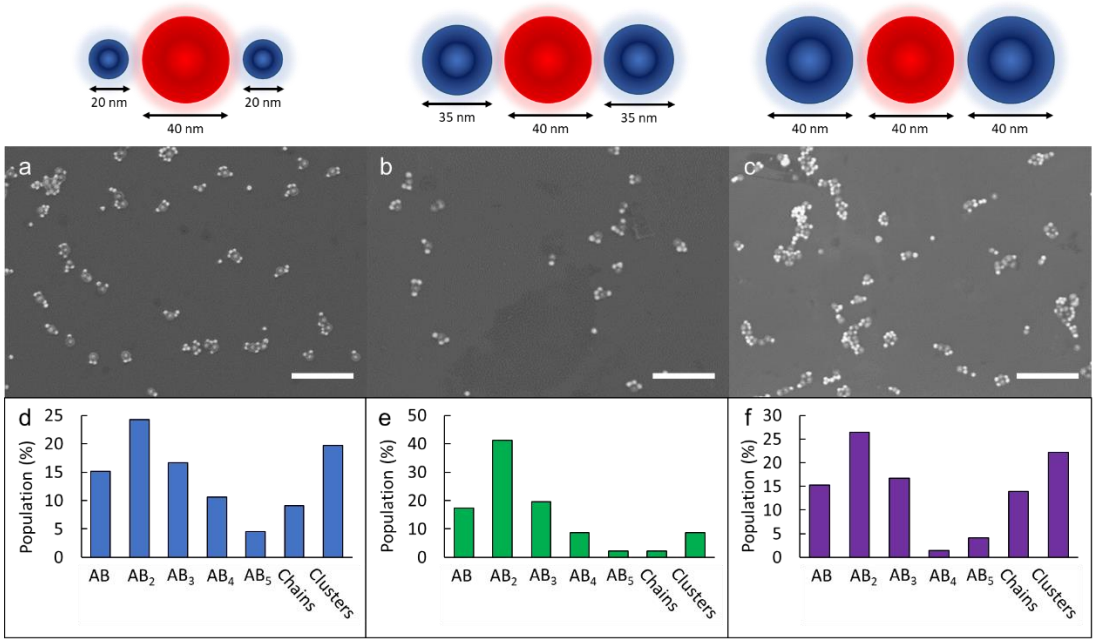

Figure 3.13 The self-assembly of **A1$_{40}$** and **B1** particles of increasing diameter. **B1** particles are (a,d) 20 nm, (b,e) 35 nm, and (c,f) 40 nm in diameter. The feeding ratio of the **B**:**A** particles was 2:1. (a-c) Representative SEM images of the assemblies. (d-f) Population statistics plots showing the yields of the different nanostructures. The scale bars are 400 nm.

3.3.5 Polymer Length Effects

We further investigated this system by comparing the self-assembly results when different polymer lengths were used. For example, we can directly compare the assemblies of **A1$_{20}$**:**B3$_{35}$** and **A1$_{20}$**:**B4$_{35}$** (Figure 3.14). As demonstrated, the polymer length of the host polymer had little effect on the nanostructure populations. This lack of change is likely the result of both polymers being roughly the same composition, as the shorter **B3** polymer has 29 β-CD moieties/chain, whereas the longer **B4** polymer has 38 β-CD moieties/chain. Thus, yields for the resultant structures are comparable (64% and 70% for **AB** dimers, and 42% and 42% for **AB$_2$** trimers).

Similarly, we can also examine the effect of the **B** polymer length on the sunflower structures (Figure 6.22). Comparing assembly results of **A1**$_{35}$:**B3**$_{20}$ and **A1**$_{35}$:**B4**$_{20}$, we see that both result in the formation of sunflower structures in which the average number of petals, *n*, is the same (6 ± 2 and 6 ± 2).

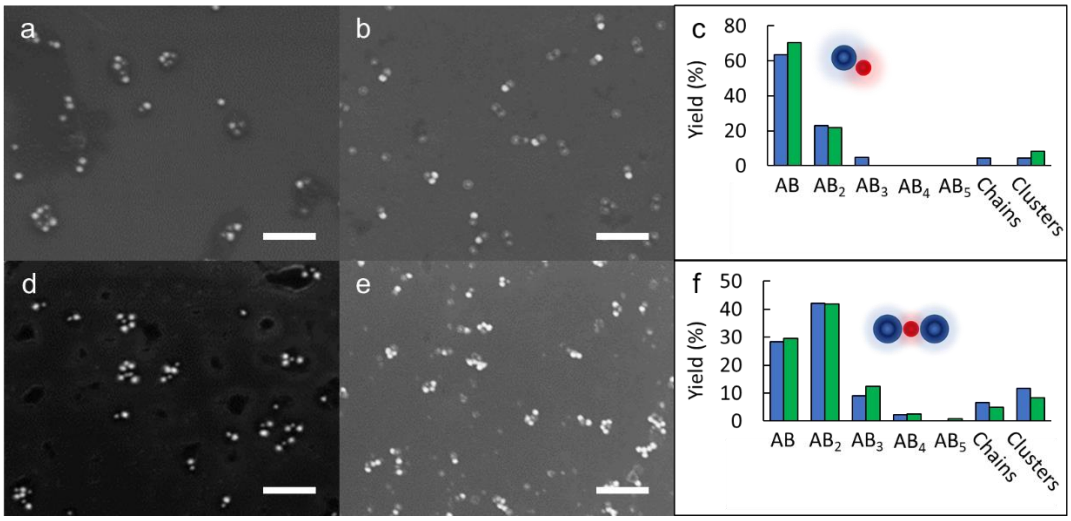

Figure 3.14 Host polymer-length effect on the self-assembly of **A1**$_{20}$ and **B**$_{35}$. (a,b,d,e) Representative SEM images in which the host particles were (a,d) **B3**$_{35}$ and (b,e) **B4**$_{35}$. (c,f) Population statistics plots showing the yields of the different assembled nanostructures in which the major products were (c) dimers and (f) trimers. The scale bars are 200 nm.

We also ran self-assembly studies using different lengths of our guest polymer (Figure 3.15). In this study, we compared the assemblies of **A1**$_{35}$:**B3**$_{20}$ and **A2**$_{35}$:**B3**$_{20}$. Both **A1**$_{35}$ and **A2**$_{35}$ assemblies yielded sunflower nanostructures; however, the polymer shell of the **A2**$_{35}$ is thicker than that of **A1**$_{35}$. The increased polymer brush height results in a higher average number of petals at 8 (± 2) compared to 6 (± 2) for **A1**$_{35}$ assemblies. This result is caused by the increase in hydrophobic guest moieties surrounding the **A** particles that can interact with more **B** particles to passivate the

hydrophobic effects between the polymer brush and surrounding medium. These results were further confirmed through TEM imaging (Figure 6.23).

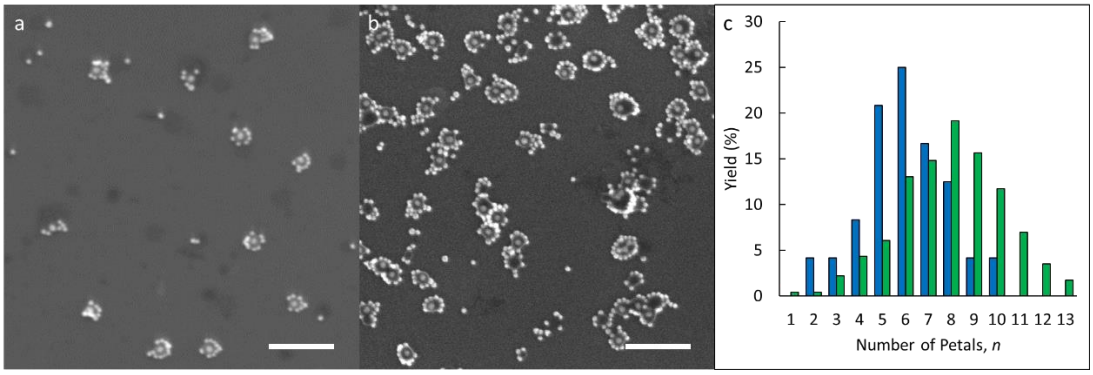

Figure 3.15 Guest polymer-length effect on the self-assembly of $\mathbf{A}_{35}$ and $\mathbf{B3}_{20}$ into sunflower nanostructures. (a,b) Representative SEM images in which the guest particles were (a) $\mathbf{A1}_{35}$ and (b) $\mathbf{A2}_{35}$. (c) Plot showing the distribution of the number of petals per sunflower structure in which the number of petals is representative of the number of **B** particles per **A** particle. The scale bars are 400 nm.

3.4 Conclusion

In this Chapter, I demonstrated the formation of supracolloids with defined valences by modifying Au NPs with complementary reactive BCPs. Self-assembly was driven by host–guest interactions between the complementary polymer brushes, as the guest moieties were destabilized under aqueous conditions. These interactions resulted in defined nanostructures that were achieved via fine tuning of the particle feeding ratio, particle sizes, and BCP lengths. The obtained supracolloids followed similar trends to those observed in our acid–base driven assembly; however, the particle size-ratio between the two building blocks largely determined the types of assembly structures we achieved along with their yields. When particle **A** was smaller than particle **B**, we saw mostly $\mathbf{AB}_n$ structures in which *n* increased with **B**:**A**. When

particle **A** was the same size as particle **B**, we still saw the formation of $\mathbf{AB_n}$ structures; however, we observed lower overall yields due to fewer available host moieties to stabilize the guest moieties. When particle **A** was larger than particle **B**, we observed $\mathbf{AB_n}$ formation at lower **B**:**A** feeding ratios, followed by a structural transition as the particle feeding ratio was increased in which we observed the formation of branched chains and sunflower type structures. Furthermore, at high feeding ratios, we observed the formation of hexagonally packed honeycomb sheets. Thus, we showed that we could target different structure-types through small changes to our building blocks. The ability to control the directional interactions between particles, yielding desired colloidal nanostructures, allows for use in various applications, such as sensing and optoelectronics. Furthermore, because this assembly is driven by host–guest interactions, which are both reversible and selective, these assemblies could serve as potential candidates for studying reversibility and competitive self-assembly, which we will examine in Chapter 4.

Chapter 4: Reversible Self-Assembly of Supracolloidal Nanostructures and the Selectivity of the Assembly

Overview. Reversible self-assembly of inorganic nanoparticles is an emerging field. The ability to disassemble and reassemble nanostructures is advantageous, expanding the potential uses of these assemblies in applications such as sensing devices and catalysis. However, the ability to reassemble particles once disassembled remains challenging. I report the reversibility of assembled, colloidal nanostructures, as discussed in Chapter 3. Under aqueous conditions, the forward assembly is triggered, whereas disassembly is triggered via the addition of a competing host. Furthermore, competitive self-assembly was explored in which particles modified with BCPs containing the host moieties were assembled with particles modified with BCPs containing different guest moieties. In this study, we showed that the "host" particles preferentially interacted with "guest" particles based on the strength of the association constants between the host and guest moieties, demonstrating assembly selectivity.

4.1 Introduction

Reversible NP self-assembly is a developing field that has garnered attention recently, as the technique provides new avenues for controlling particle–particle interactions. As described previously, there have been many studies highlighting the reversible self-assembly of SgNPs; however, control over particle interactions and interparticle spacing is limited due to the rigidity and small size of the surface ligands.[5-11] Studies using PgNPs remain limited, as most systems result in large-scale aggregates that can be disassembled upon exposure to light,[205] a change in pH,[206,207]

and a change in temperature.[208] It is therefore important to develop a means targeting complex nanostructures that can be disassembled and reassembled.

As described in Chapter 3, we have designed a system that uses host–guest interactions to assemble B-PgNPs into supracolloidal nanostructures. In this chapter, I demonstrate the reversibility of these assemblies, in addition to the selectivity of these particle–particle interactions. Reversibility was achieved via the addition of free β-CD, which serves as a competitive host that forms a more stable host–guest inclusion complex with the guest moieties in the polymer brush of particle **A**. This complexation disrupts the interactions between particles **A** and **B**, resulting in disassembly. Particles could then be reassembled upon dialysis against water, as the free host moieties were washed away due to the concentration difference.

We also studied the strength of the interactions between particles **A** and **B** by assembling particle **B** with particles modified with different guest-functionalized BCPs. We chose two additional guest-functionalized BCPs, which were thiol-terminated poly(ethylene oxide)-*block*-poly(3,3-dimethyl-1-butyl methacrylate-*r*-dimethyl acrylamide) (*Abbrev*: PEO-*b*-P(DMBMA-*r*-DMA)-SH) and poly(ethylene oxide)-*block*-poly(2-(2-methoxyethoxy)ethyl methacrylate-*r*-dimethyl acrylamide) (*Abbrev*: PEO-*b*-P(MeO_2MA-*r*-DMA)-SH). The BCP-modified Au NPs are referred to as building blocks **D** and **M** respectively. Similar to the **AD** BCPs detailed in Chapter 3, the inner block of **D** and **M** is a random copolymer of DMA, which serves as a steric buffer, and a guest moiety (the *tert*-butyl group of DMBMA or the diethylene glycol chain of MeO_2MA), whereas the outer block is the hydrophilic homopolymer, PEO. We chose to study these two functional groups because they

represent guest moieties with different binding affinities to β-CD compared to Ada groups. As reported by Harada and co-workers, the K_a value for a β-CD–*tert*-butyl complex is 3.40×10^2 M^{-1},[181,209] whereas β-CD is not known to form complexes with PEG of any molecular weight.[210,211]

Self-assembly was triggered by slowly adding water to solutions containing particles **A**, **B**, and **D**/**M**, which were initially mixed in DMF. The solutions were subsequently dialyzed against water for at least 12 h to remove DMF and drive the self-assembly. This process yielded a variety of colloidal nanostructures, which we analyzed to determine the frequency and nature of the particle–particle interactions (Figure 4.1). We demonstrated that particle **B** preferentially interacts with particle **A** regardless of particle concentration or identity of the competing guest-functionalized particle. Furthermore, the assembly results agree with the results in Chapter 3, as we observed branched chains and sunflower structures when particle **A** was larger than particle **B**, and we observed a greater fraction of $\mathbf{AB_n}$ structures when particle **B** was larger than particle **A**. However, the overall yields of these structures were reduced due to competition from particles **D** and **M**. This system provides new insight into the formation of supracolloidal nanostructures when particles are assembled in complex environments containing different types of modified particles.

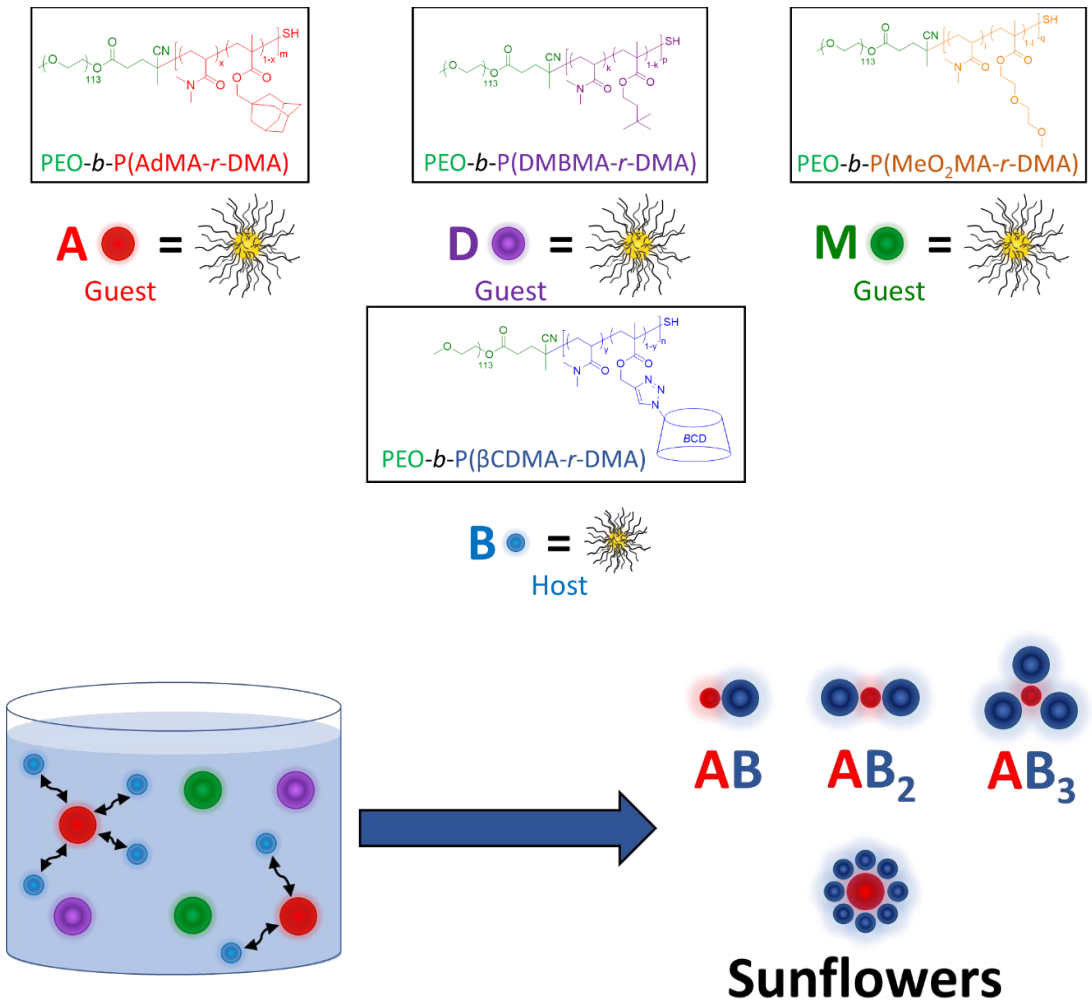

Figure 4.1 Schematic showing the selective assembly of complementary colloidal BCP-tethered Au NPs into various nanostructures via selective host–guest interactions when multiple guest-functionalized NP species are in solution. The double-headed arrows signify that particles **A** and **B** preferentially interact to form $\mathbf{AB_n}$ or sunflower structures, depending on the NP size mismatch.

4.2 Materials and Experimental Methods

4.2.1 Materials

Dichloromethane (anhydrous, ≥ 99.8%), and dioxane (anhydrous, 99.8%) were purchased from Sigma Aldrich and were used as received. THF, DMF, hexanes,

ethyl acetate, and water (HPLC grade) were purchased from Fisher Scientific and were used as received. 3,3-dimethyl-1-butanol and β-cyclodextrin (β-CD, > 99% HPLC grade) were purchased from TCI America and were used as is. N,N-dimethylacrylamide (DMA, 99%) and 2-(2-methoxyethoxy)ethyl methacrylate (MeO_2MA) were purchased from Sigma Aldrich and passed through a basic Al_2O_3 column to remove inhibitors. The monomers were stored in a freezer after removal of the inhibitors. Azobis(isobutyronitrile) (AIBN, 98%) was purchased from Sigma Aldrich and was recrystallized from ethanol. Deionized water (Millipore Milli-Q grade) with a resistivity of 18.0 MΩ or HPLC-grade water were used in all the experiments. Regenerated Cellulose membrane dry dialysis tubing (6-8 kD MWCO Standard Grade) was purchased from Fisher Scientific and was hydrated before use.

4.2.2 Synthesis of Thiol-Terminated BCPs

The thiol-terminated BCPs, PEO-*b*-P(DMBMA-*r*-DMA)-SH and PEO-*b*-P(MeO_2MA-*r*-DMA)-SH, were synthesized via RAFT polymerization. The synthetic procedure is shown in Figure 4.2. The **AD** and **B** BCPs synthesized in Chapter 3 were also used in the experiments described in this Chapter. Further information pertaining to the synthesis and characterization of the **AD** and **B** BCPs can be found in Section 3.2.2.

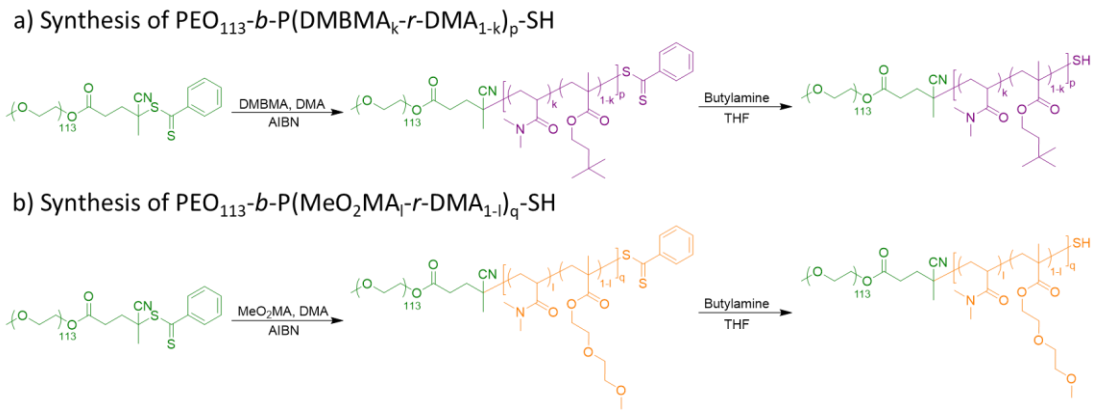

Figure 4.2 The synthesis of thiol-terminated BCPs: a) PEO-*b*-P(DMBMA-*r*-DMA)-SH, and b) PEO-*b*-P(MeO_2MA-*r*-DMA)-SH.

4.2.2.1 Synthesis of PEO-b-P(DMBMA-r-DMA)-SH

RAFT polymerization was used to synthesize PEO-*b*-P(DMBMA-*r*-DMA)-SH, as follows. PEG_{113}-CPADB (50 mg, 0.01 mmol) was added to a roundbottom flask with DMA (694 mg, 7 mmol) and DMBMA (307 mg, 3 mmol). (The synthesis of DMBMA is outlined in the Section 6.4, and the ^{1}H NMR is shown in Figure 6.24) Anhydrous dioxane (5.00 mL) was added along with AIBN (10.0 µL of a 0.1 mM AIBN solution in dioxane). The AIBN served as a thermo-initiator. Solutions were then purged with argon for 30 min and stirred in a 70 °C oil bath for 18 h. The polymer was precipitated with cold hexanes (~90 mL, 10 °C) and centrifuged at 5,000 rpm for 10 min. The polymer was then dissolved in THF (~10 mL) and precipitated with hexanes (~90 mL). The solid was collected via centrifugation at 5,000 rpm for 10 min. This process was repeated two more times, and the final product was dried under vacuum for at least 24 h. The dithiobenzoate was then reduced following the procedure outlined in Section 2.2.3.2.

The following analysis was performed on BCP **DB1** (see Table 4.1). From the ^{1}H NMR spectrum (in $CDCl_3$, see Figure 6.25), the ^{1}H NMR-based molecular weight M_n is 46.8 Kg·mol^{-1}. The analysis was performed by comparing the integrals of the ester group hydrogens of DMBMA (3.9-4.4 ppm) and the N-methyl group hydrogens of DMA (2.3-3.4 ppm) to the methylene group hydrogens of PEO (3.62-3.66 ppm). The length of the PEO block was known and was used as a standard to determine the amounts of DMA and DMBMA present in the final polymer.

4.2.2.2 Synthesis of PEO-b-P(MeO$_2$MA-r-DMA)-SH

RAFT polymerization was used to synthesize PEO-*b*-P(MeO$_2$MA-*r*-DMA)-SH, as follows. PEG$_{113}$-CPADB (50 mg, 0.01 mmol) was added to a roundbottom flask with DMA (694 mg, 7 mmol) and MeO$_2$MA (565 mg, 3 mmol). Anhydrous dioxane (5.00 mL) was added along with AIBN (10.0 µL of a 0.1 mM AIBN solution in dioxane). The AIBN served as a thermo-initiator. Solutions were then purged with argon for 30 min and stirred in a 70 °C oil bath for 12 h. The polymer was precipitated with cold hexanes (~90 mL, 10 °C) and centrifuged at 5,000 rpm for 10 min. The polymer was then dissolved in THF (~10 mL) and precipitated with hexanes (~90 mL). The solid was collected via centrifugation at 5,000 rpm for 10 min. This process was repeated two more times, and the final product was dried under vacuum for at least 24 h. The dithiobenzoate was then reduced following the procedure outlined in Section 2.2.3.2.

The following analysis was performed on BCP **M1** (see Table 4.1). From the ^{1}H NMR spectrum (in $CDCl_3$, see Figure 6.26), the ^{1}H NMR-based molecular weight M_n is 41.4 Kg·mol^{-1}. The analysis was performed by comparing the integrals of the

ester group hydrogens of MeO_2MA (3.9-4.4 ppm) and the N-methyl group hydrogens of DMA (2.3-3.4 ppm) to the methylene group hydrogens of PEO (3.62-3.66 ppm). The length of the PEO block was known and was used as a standard to determine the amounts of DMA and MeO_2MA present in the final polymer.

Table 4.1 Characterization of Guest-functionalized BCPs

BCP	Formula	Monomer Ratio	M_n (^{1}H NMR) (Kg·mol^{-1})	R_0 (nm)
DB1	PEO_{113}-*b*-P($DMBMA_{117}$-*r*-DMA_{221})$_{338}$-SH	0.35	46.8	8.98
M1	PEO_{113}-*b*-P(MeO_2MA_{107}-*r*-DMA_{164})$_{271}$-SH	0.39	41.4	8.38

*R_0 for the inner BCP block is calculated from $R_0=bN^{0.5}$, whereas *b* is the Kuhn length (1.3 nm for PDMA) and *N* is the number of Kuhn segments. For simplicity, the Kuhn length for DMA was used for the DMBMA and MeO_2MA moieties, as the inner block is mostly composed of DMA.[198]

4.2.3 Nanostructure Reversibility

To test the reversibility of the assembled structures, we first assembled **A** and **B** particles together, as outlined in Section 3.2.4. Once assembled, 1.00 mL of the assembly solution was added to a glass vial with an aqueous β-CD solution (100 μL, 0.01 M). The solutions were sonicated for 10 s and then stirred gently for 2 h. Afterwards, UV-vis absorption spectra were measured. Samples were reassembled through dialysis against water for at least 12 h to remove the free β-CD from solution. UV-Vis spectra and SEM images were taken after reassembly. This process was repeated to test the cyclability of the particle assembly and disassembly.

4.2.4 Competitive Self-Assembly

HINP self-assembly was triggered by mixing particles **A**, **B,** and **D** or **M** together in a favorable solvent, such as DMF. Initially, the particle **A** solution was

pipetted into 1.00 mL of DMF in a 4 mL glass vial. Different amounts of the particles **B** and **D**/**M** solutions were then added under sonication to ensure even distribution. Subsequently, 1.00 mL of water was added, using a mechanical syringe pump, to 1.00 mL of the NP solution over the course of 1 hr. The solutions were then allowed to equilibrate for at least 1 h before being dialyzed against water for at least 12 h. Prior to use, the dialysis tubing was hydrated for 10 min. The solutions were imaged using SEM to determine the structure and yields of the resultant supracolloids.

We similarly tested the addition of competitive guest-modified particles to samples that were already assembled. 100 μL of the particle **B** and particle **M** solutions were added to 1.00 mL of DMF. These solutions were then assembled following the procedure outlined above. Once assembled, 100 μL of the particle **A** solution were added. The solution was allowed to equilibrate for 1 h prior to dialysis against water to remove the residual DMF that was added. The samples were then reimaged using SEM to assess any changes.

4.2.5 Morphological and Structural Characterization

^{1}H NMR. ^{1}H NMR spectra were recorded using Bruker AV-400 MHz high resolution NMR spectrometer.

UV-vis Absorption Spectroscopy. Absorbance measurements were performed using a Shimadzu UV-2501PC UV-Vis recording spectrophotometer.

Thermogravimetric Analysis (TGA). TGA was used to characterize the BCP grafting density on the NP surfaces. A 10.00 mL stock solution of building blocks was centrifuged to remove the supernatant. Hexane was then added, and the sample was centrifuged. The hexane was removed, and the solid pellet was collected. The pellets

were then dried in a vacuum oven for 24 h to remove any residual solvent. The measurements were performed under argon, with a scan rate of 25 °C·min^{-1} from 25 °C to 800 °C. During the scan process, the temperature was maintained at 100 °C for 30 min to further remove any remaining moisture. The weight fraction of the polymer ligands, *f*, was then determined and used to determine σ based on the polymer M_n.

SEM Imaging. SEM images were taken using a Hitachi SU-70 Schottky field-emission gun Scanning Electron Microsccope (FEG-SEM) operated at 10.0 kV. Samples were prepared by drying 5.0 μL of solution on a silicon wafer.

4.3 Results and Discussion

4.3.1 BCP-Tethered NPs

Au NPs are modified with BCPs in which the inner block contains DMA, which serves as a hydrophilic, steric buffer that does not interact with the particle surface, and either a guest (AdMA, MeO_2MA, DMBMA) or host (β-CDMA). When slowly exposed to water, the hydrophobic guest moieties are driven within the amphiphilic host macrocycles, yielding host–guest complexes that drive the self-assembly of the respective particles. Meanwhile, the outer block is hydrophilic PEO, which serves both as a steric buffer and as protective shell to stabilize the final assembled products in aqueous environments.

For simplicity, the particles modified with AdMA BCPs are denoted **A** particles, the particles modified with MeO_2MA BCPs are denoted **M** particles, the particles modified with DMBMA BCPs are denoted **D** particles, and the particles modified with β-CDMA BCPs are denoted **B** particles. The number following the letter represents the polymer, and the subscript following the letter is the NP size

(*e.g.*, **M1**$_{20}$ represents 20-nm particles modified with BCP **M1**, whereas **D1**$_{30}$ represents 30-nm particles modified with BCP **DB1**). UV-vis absorption spectroscopy was used to characterize the Au NPs before and after surface modification. After grafting the BCPs on the NP surfaces, a slight red-shift (~6 nm) was observed for all particles, which indicates an increase of particle size due to the polymer brush on the surface of the Au NPs, or it may be caused by the change in the refractive index of the surrounding solution, as the unmodified particles are in water and the modified particles are in DMF (Figure 4.3).

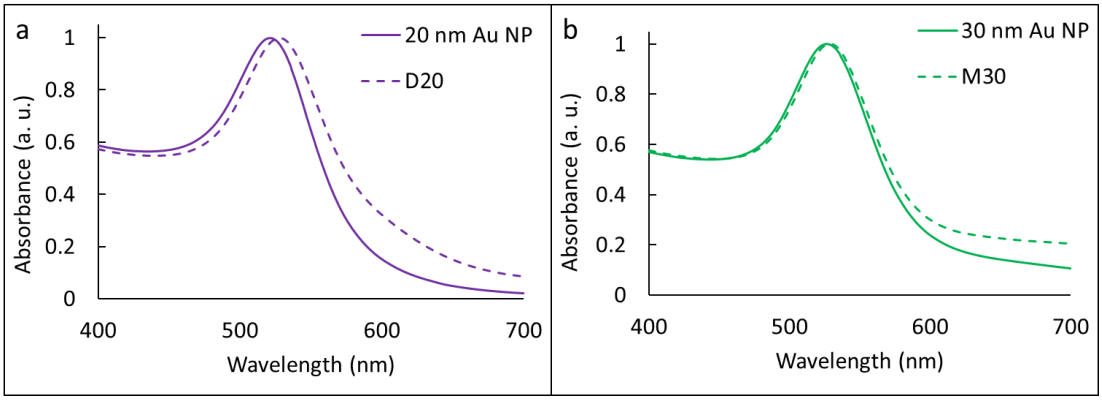

Figure 4.3 UV-vis spectra of the BCP-modified Au NPs. (a) 20-nm Au NPs in aqueous solution and **D1**$_{20}$ particles in DMF, and (b) 30-nm Au NPs in aqueous solution and **M1**$_{30}$ particles in DMF.

TGA was used to determine the amount of grafted-BCPs on the surfaces of the NPs (Figure 4.4). Using **D1**$_{30}$ and **M1**$_{30}$ as an example, weight loss was observed at temperatures above 200 °C, resulting from the thermal degradation of the BCPs into volatile products. From the TGA measurement, **D1**$_{30}$ and **M1**$_{30}$ showed weight losses of 6.5% and 8.3%, respectively. Using Eq. 2.1, we determined that the σ of **D1**$_{30}$ and **M1**$_{30}$ were 0.09 and 0.13 chains/nm^2, respectively. From Eq. 2.2, we then

solved for the d_l values for **D1$_{30}$** and **M1$_{30}$**, which were 3.74 and 3.08 nm, respectively. The R_g values for each of the BCPs were calculated using Eq. 2.3. The ratio of R_g/d_l is estimated to be in the range of 1.0 to 1.1, which suggests that the grafted-BCPs adopt a mostly flexible polymer-brush conformation[44]. The polymer chains preferentially extend away from the NP surface to avoid steric overcrowding, as discussed in detail previously.

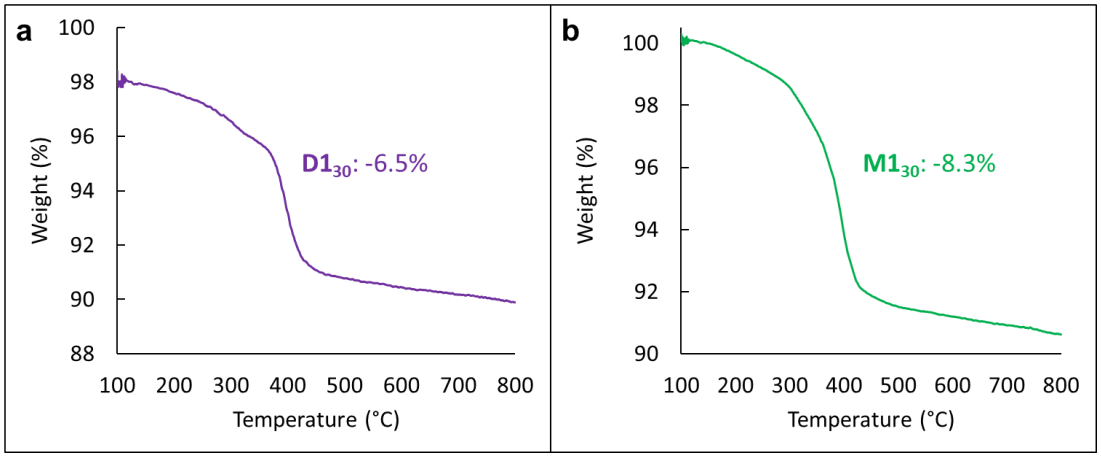

Figure 4.4 TGA curves of **D1$_{30}$** and **M1$_{30}$** particles.

4.3.2 Studying Reversibility

To study the reversibility of the particle assembly, we added free β-CD to solutions of our assembled particles and allowed the solutions to equilibrate. We measured the change in absorbance of the samples and imaged the samples using SEM after reassembling the particles to determine if there was any change in structure. A representative assembly and reassembly cycle using an **A2$_{20}$**–**B2$_{30}$** assembly is shown below in Figure 4.5.

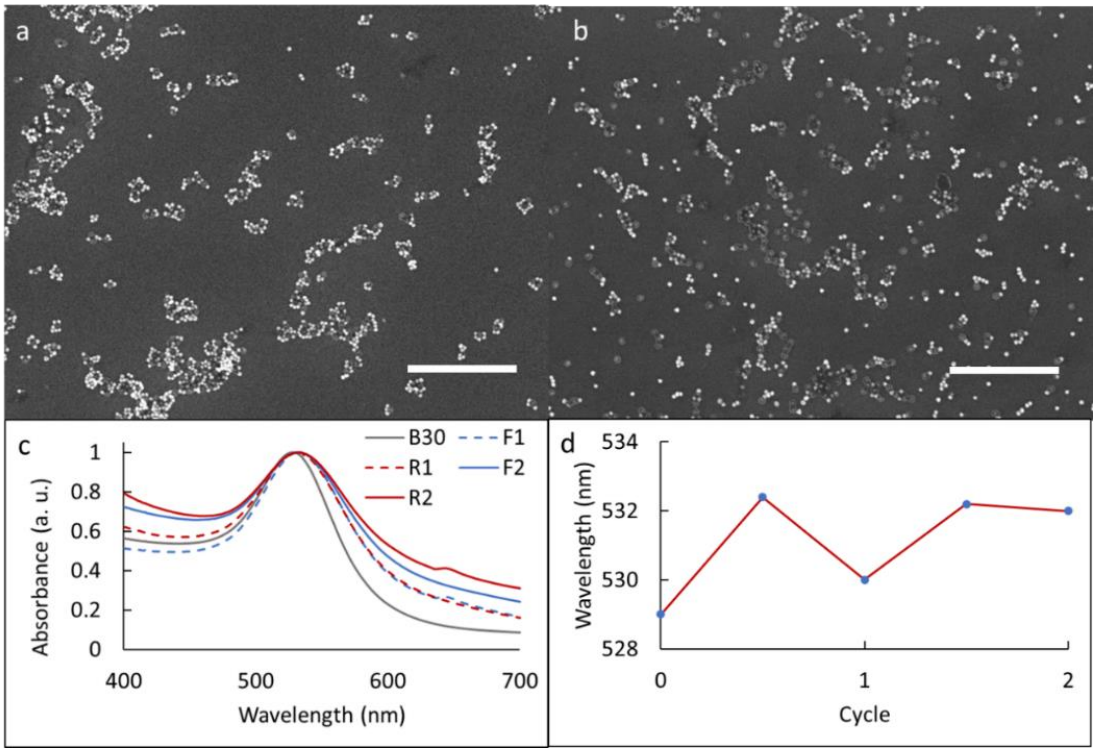

Figure 4.5 The self-assembly and disassembly of **A2$_{20}$** and **B2$_{30}$**. (a,b) Representative SEM images of the particle self-assembly in which (a) is the initial assembly, and (b) is the reassembly upon removal of the free β-CD from solution. (c) UV-vis absorption spectra showing the change in peak absorbance upon particle assembly and disassembly compared to **B$_{30}$** particles. **F1** and **F2** represent the forward assemblies, and **R1** and **R2** represent the reverse assemblies. (d) Plot showing the change in the peak absorption wavelength as the particles are assembled and disassembled. Each cycle represents a forward self-assembly followed by disassembly. The scale bars are 1 μm.

As shown in Figure 4.5a, we observed clear signs of particle self-assembly, which was further confirmed by the red-shift of the absorption peak from 529.0 to 532.4 nm. Upon addition of free β-CD, we observed a slight blue-shift of the peak from 532.4 to 530.2 nm. This blue-shift is indicative of some particle disassembly; however, it is important to note that the absorption spectrum of the assembly after

addition of the free β-CD does not entirely align with the absorption spectrum of the unassembled **B_{30}** particles. This observation suggests that the particles are not fully disassembled.

Following particle disassembly, we tested whether the particles could be reassembled by removing the free β-CD from solution, which we achieved through dialysis against water. After 12 h of dialysis, the samples were reimaged, as shown in Figure 4.5b. Comparing Figures 4.5a and 4.5b, we observe that there is a slight loss of structure. However, the SEM images show that the structures remain mostly unchanged, which is further confirmed by the UV-vis absorption results. Upon reassembly, we observed a slight red-shift to 532.2 nm, which is similar to the peak shift observed upon initial particle assembly. Finally, we tested the disassembly of the assemblies again via the addition of free β-CD, which did not result in a clear change in the UV-vis spectrum. This observation implies that the particles did not disassemble, and that the assembly/disassembly process cannot be cycled repeatedly. The lack of cyclability may be the result of the strong hydrophobic effect that drives the forward assembly, which can destabilize the system, resulting in particle aggregation. These results were further confirmed when assembling **$A2_{30}$** and **$B2_{20}$** particles (Figure 4.6). Although not the ideal result, the initial disassembly and reassembly of these **AB_n** nanostructures is promising.

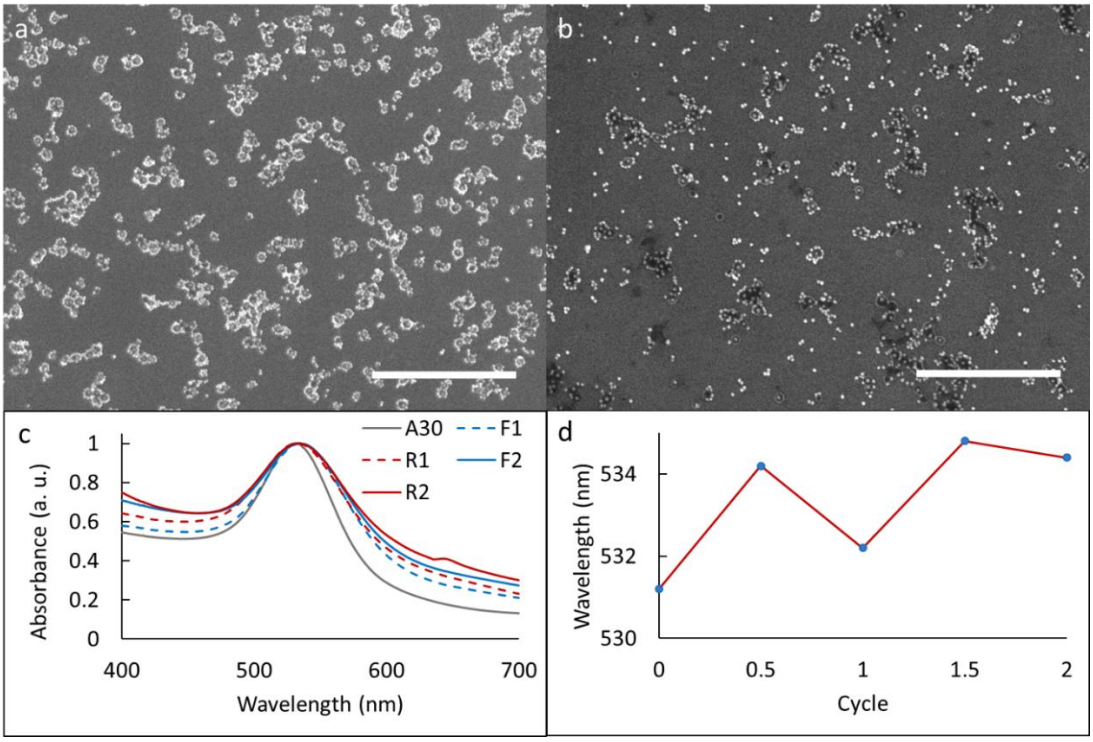

Figure 4.6 The self-assembly and disassembly of **A2$_{30}$** and **B2$_{20}$**. (a,b) Representative SEM images of the particle self-assembly in which (a) is the initial assembly, and (b) is the reassembly upon removal of the free β-CD from solution. (c) UV-vis absorption spectra showing the change in peak absorbance upon particle assembly and disassembly compared to **A$_{30}$** particles. **F1** and **F2** represent the forward assemblies, and **R1** and **R2** represent the reverse assemblies. (d) Plot showing the change in the peak absorption wavelength as the particles are assembled and disassembled. Each cycle represents a forward self-assembly followed by disassembly. The scale bars are 1 μm.

4.3.3 Competitive Self-Assembly

To demonstrate the selectivity of our particle interactions, initial self-assembly was performed using **B1$_{20}$** and either **D1$_{40}$** or **M1$_{40}$** particles. The particles were assembled using the same strategy outlined in Chapter 3, and the resultant structures were analyzed using SEM (Figure 4.7). As shown below, neither assembly resulted in

the formation of defined structures. This result was expected for the **M** particles, as β-CD is not known to form stable complexes with PEG. However, we expected to see stronger interactions between the **B** and **D** particles. There are some signs of **B1**$_{20}$–**D1**$_{40}$ interactions, as there are small clusters in Figure 4.7a; however, the particle ordering appears random. This result may indicate that the hydrophobicity of the **A** particles helps drive the interactions between the **A** and **B** particles, as the **A** particles are much more hydrophobic than the **D** particles. These results suggest that the **B** particles may show selectivity towards the **A** particles when assembled in solutions containing both **A** and **D**/**M** particles.

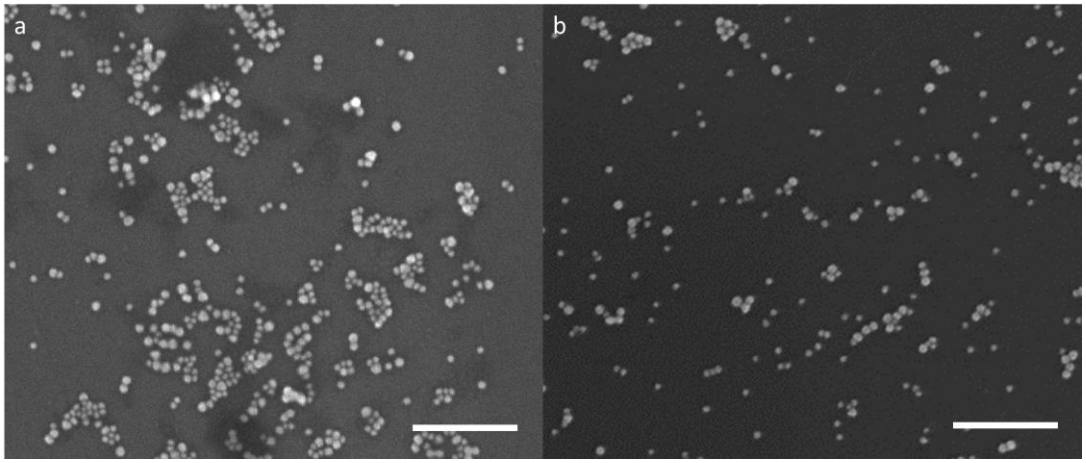

Figure 4.7 The self-assembly of **B2**$_{20}$ with **D1**$_{40}$ and **M1**$_{40}$. Representative SEM images of the assemblies, in which the guest-modified particles are (a) **D1**$_{40}$ and (b) **M1**$_{40}$. The scale bars are 400 nm.

Following the assembly results of **B1**$_{20}$ and **D1**$_{40}$ or **M1**$_{40}$, we tested the selectivity of the particle–particle interactions. Samples were prepared by mixing **B2**$_{20}$ and **A2**$_{30}$ particles together with 40-nm particles modified with either **M1** or **DM1**. The feeding ratios of the three particles were 2:1:1. The samples were imaged using SEM, and the particle–particle interactions were quantified (Figure 4.8). As

shown below, the **B2$_{20}$** particles are preferentially associated with the **A2$_{30}$** particles instead of the **M1$_{40}$** and **D1$_{40}$** particles. In Figure 4.8a, 78% of host–guest particle interactions occurred between the **B2$_{20}$** and **A2$_{30}$** particles, and in Figure 4.8d, 87% of host–guest particle interactions occurred between the **B2$_{20}$** and **A2$_{30}$** particles. Interactions were calculated by eye and were averaged from over 1000 particle–particle interactions. Additionally, we observed the formation of sunflower-type structures in both assemblies, with yields of 66% and 72%, respectively. Zoomed-in SEM images are shown in Figure 4.8a,b for better visualization of the particle interactions. The assembly was further confirmed through UV-vis absorption, in which there is a clear red-shift of the absorption peaks after self-assembly (Figure 4.9c,d).

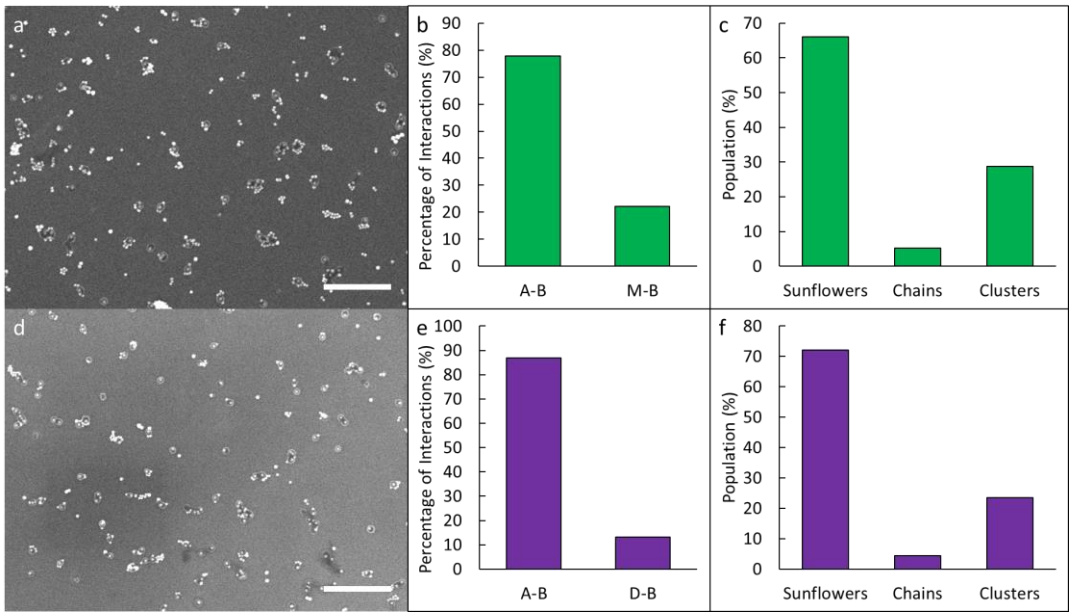

Figure 4.8 The self-assembly of **B2$_{20}$** and **A2$_{30}$** with either **M1$_{40}$** or **D1$_{40}$**. Large-area SEM images in which the secondary guest particle is (a) **M1$_{40}$** and (d) **D1$_{40}$**. (b, e) Plots showing the particle–particle interactions between the **B2$_{20}$** particles and the guest BCP-modified particles. (c, f) Population statistics plots showing the nanostructure populations. The scale bars are 500 nm.

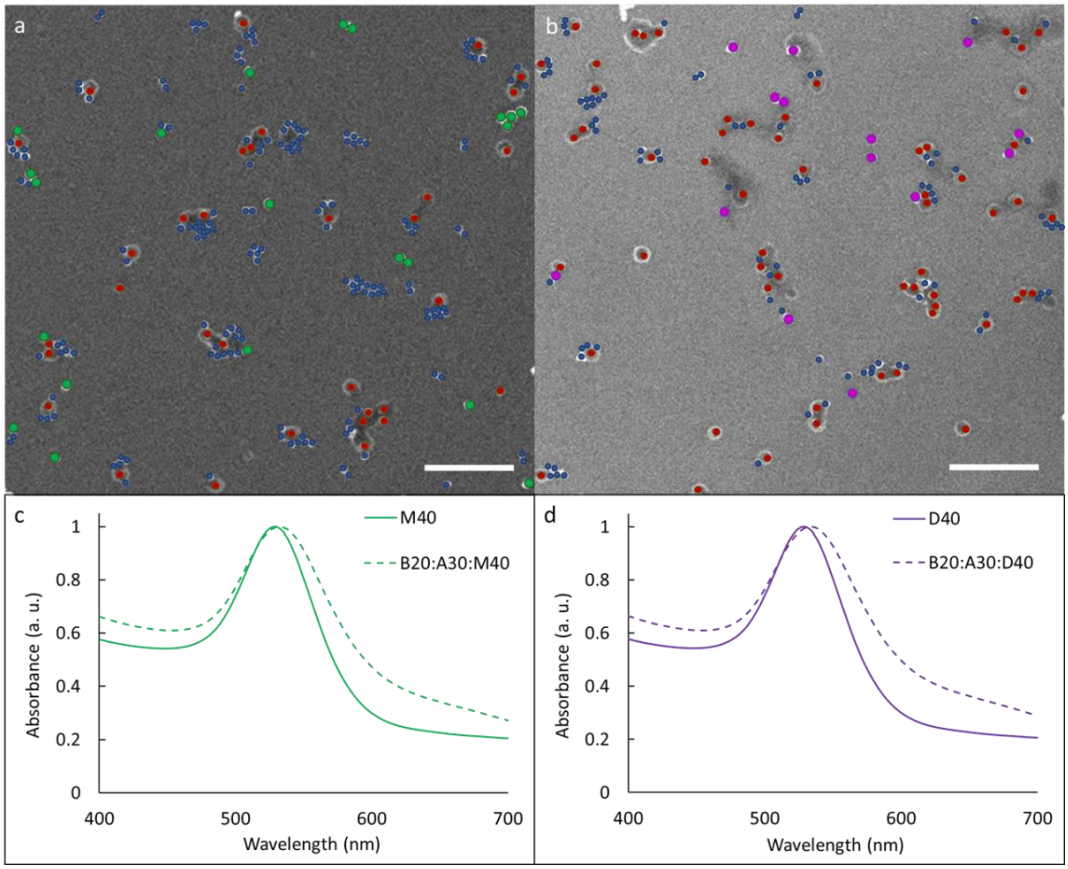

Figure 4.9 The self-assembly of **B2$_{20}$** and **A2$_{30}$** with either **M1$_{40}$** or **D1$_{40}$**. Labeled SEM images in which the secondary guest particle was (a) **M1$_{40}$** and (d) **D1$_{40}$**. The labeled particles are **B2$_{20}$** (blue), **A2$_{30}$** (red), **M1$_{40}$** (green), and **D1$_{40}$** (purple). UV-vis absorption of the modified, 40-nm particles (solid) and the assemblies (dashed), in which (c) **M1$_{40}$** and (d) **D1$_{40}$**. The scale bars are 400 nm.

The nanostructure yields were calculated by averaging over 500 assembly structures, which were counted by eye. Additionally, non-assembled particles were neglected when determining the average nanostructure yields. We can adjust the particle concentrations and feeding ratios between the different species in solution to achieve results similar to those reported in Chapter 3. For example, we assembled **B2$_{20}$**, **A2$_{30}$**, and **M1$_{40}$** particles together at a feeding ratio of 2:2:1 and quantified the results (Figure 4.10). We observed the formation of sunflower structures, which

matches the results established in Chapter 3 in which sunflower structures were obtained when particle **A** was larger than particle **B**. Roughly 80% of assembled structures were sunflower structures with an average number of petals equal to 6 (± 2). Additionally, we observed that our **B** particles preferentially assembled with the **A** particles rather than with the **M** particles, confirming the results shown in Figure 4.8a. Here, 86% of host–guest particle interactions occurred between **A** and **B** particles, whereas 14% of host–guest particle-interactions occurred between **M** and **B** particles.

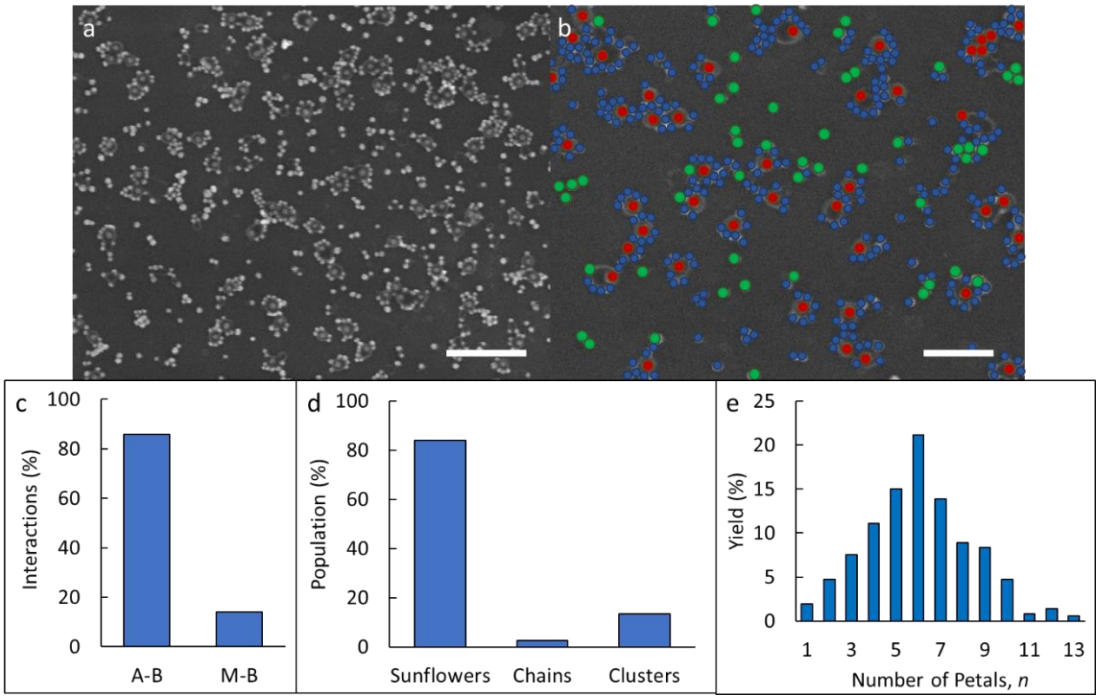

Figure 4.10 The self-assembly of **B2$_{20}$**, **A2$_{30}$**, and **M1$_{40}$** at a feeding ratio of 2:2:1. (a) SEM image of the assembly structures. (b) Labeled zoomed-in SEM image. The labeled particles are **B2$_{20}$** (blue), **A2$_{30}$** (red), and **M1$_{40}$** (green). (c) Plot showing the particle–particle interactions between the **B2$_{20}$** particles and the **A2$_{30}$** and **M1$_{40}$** particles. (d) Population statistics of the nanostructures. (e) Plot showing the distribution of the number of petals per sunflower structure in which the number of petals is representative of the number of **B** particles per **A** particle. The scales bars are 400 nm in (a) and 200 nm in (b).

We also assembled **B2**$_{20}$, **A2**$_{30}$, and **M1**$_{40}$ particles together at a feeding ratio of 2:1:2 and quantified the results (Figure 4.11). We observed the formation of sunflower structures, and the results matched those obtained in Figure 4.10. Roughly 86% of assembled structures were sunflower structures, with an average number of petals equal to 4 (± 2). The remaining structures were mostly small clusters and yolk-type clusters in which the center was composed of multiple **A** particles. Additionally, the **B** particles preferentially assembled with the **A** particles rather than the **M** particles; however, the number of **M**–**B** interactions increased as compared to Figure 4.10. 76% of host–guest particle interactions occurred between **A** and **B** particles, whereas 24% of host–guest particle interactions occurred between **M** and **B** particles. This result suggests that particle concentration does have an impact on the particle interactions.

We can also achieve sunflower-type structures when assembling **A2**$_{40}$ particles with smaller **D** and **B** particles (20 and 30 nm). The results of these experiments are shown in Figures 6.27 and 6.28. More than 80% of host–guest particle-interactions occurred between **A** and **B** particles. Additionally, we observed the formation of sunflower structures in which the average number of petals were 4 (± 2) and 3 (± 1), respectively, when particles **A** and **B** interacted. When particles **D** and **B** interacted, we observed **AB**$_{n}$ structures. These results were further confirmed through UV-vis absorption in which there was a red-shift of the peak of roughly 5-6 nm.

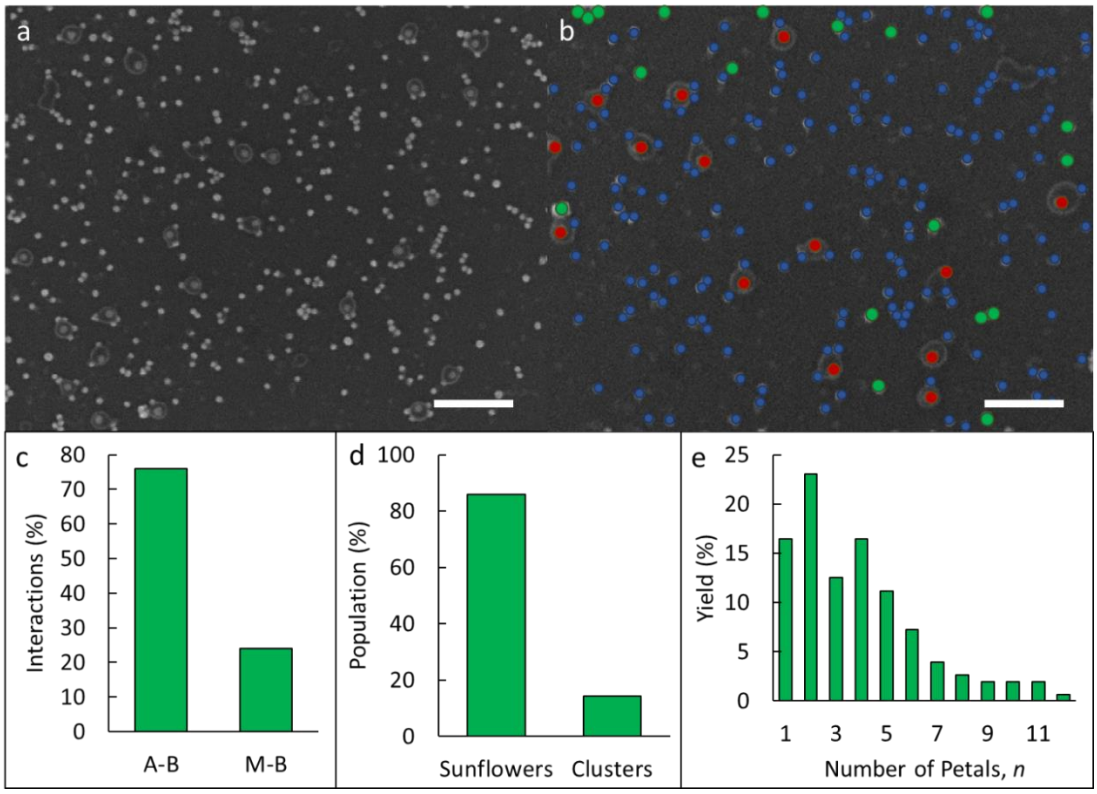

Figure 4.11 The self-assembly of **B2**$_{20}$, **A2**$_{30}$, and **M1**$_{40}$ at a feeding ratio of 2:1:2. (a) SEM image of the assembly structures. (b) Labeled zoomed-in SEM image. The labeled particles are **B2**$_{20}$ (blue), **A2**$_{30}$ (red), and **M1**$_{40}$ (green). (c) Plot showing the particle–particle interactions between the **B2**$_{20}$ particles and the **A2**$_{30}$ and **M1**$_{40}$ particles. (d) Population statistics of the nanostructures. (e) Plot showing the distribution of the number of petals per sunflower structure in which the number of petals is representative of the number of **B** particles per **A** particle. The scale bars are 400 nm in (a) and 200 nm in (b).

4.3.4 Particle Size Effects

To study competitive self-assembly further, we investigated particle size effects. Samples were prepared by mixing **B2**$_{40}$ and **A2**$_{30}$ particles together with 20-nm particles modified with either **M1** or **DM1**. The feeding ratios of the three particles were 2:1:1. Samples were then imaged using SEM, and the particle–particle

interactions were quantified (Figure 4.12). The results followed the trend established in Figures 4.8-4.11, in which the majority of host–guest particle-interactions occurred between **A** and **B** particles, regardless of whether **M** or **D** particles were introduced.

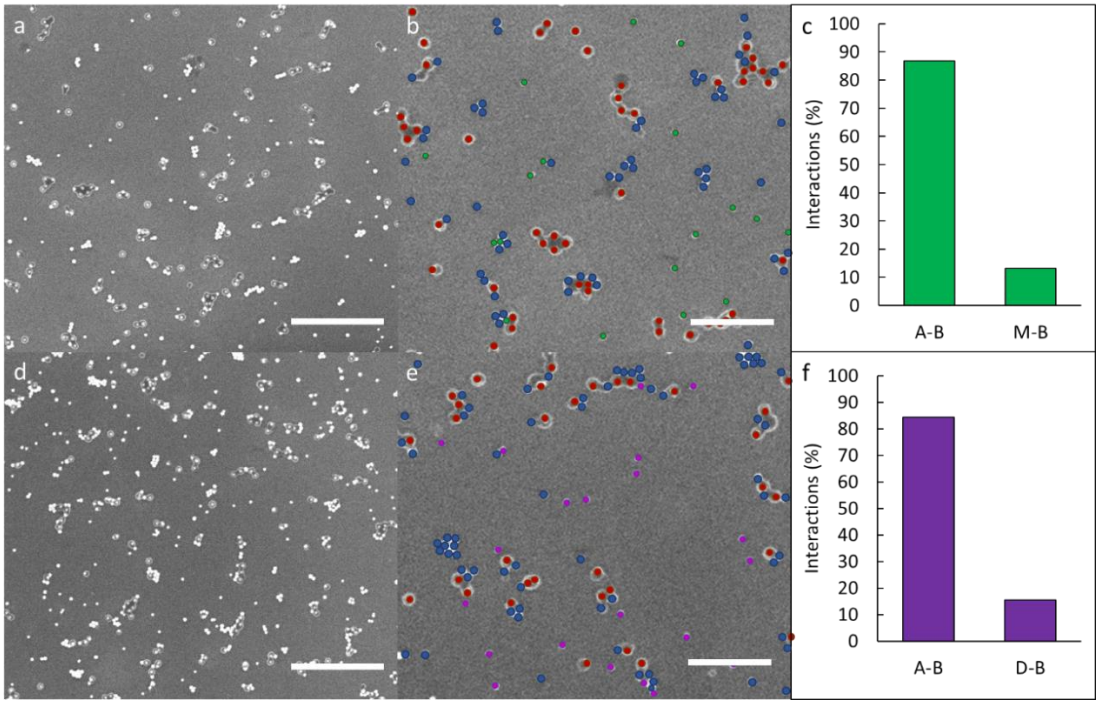

Figure 4.12 The self-assembly of **B2$_{40}$** and **A2$_{30}$** with either **M1$_{20}$** or **D1$_{20}$** at a feeding ratio of 2:1:1. Large-area SEM images in which the secondary guest particle was (a) **M1$_{40}$** and (d) **D1$_{40}$**. (b, e) Labeled zoomed-in SEM images. The labeled particles are **B2$_{40}$** (blue), **A2$_{30}$** (red), **M1$_{20}$** (green), and **D1$_{20}$** (purple). (c, f) Plots showing the particle–particle interactions between the **B2$_{20}$** particles and the guest BCP-modified particles. The scale bars are 800 nm in (a, d) and 400 nm (b, e).

These trends are further supported by studies in which we changed the particle sizes, as shown in Figures 4.13. As shown in Figure 4.13, the assembly results match those observed in Chapter 3 when particle **A** is smaller than particle **B**. We largely observed **AB** and **AB$_2$** structures, along with smaller amounts of higher-valence **AB$_n$** structures, regardless of whether particle **B** was 30 or 40 nm in diameter. The

respective yields of the **AB** structures were 34% and 42%, and the respective yields of **AB$_2$** structures were 29% and 26%. We also observed that most host–guest particle interactions occurred between the **A** and **B** particles, as both assemblies showed **A**–**B** interactions accounting for over 80% of all host–guest particle interactions.

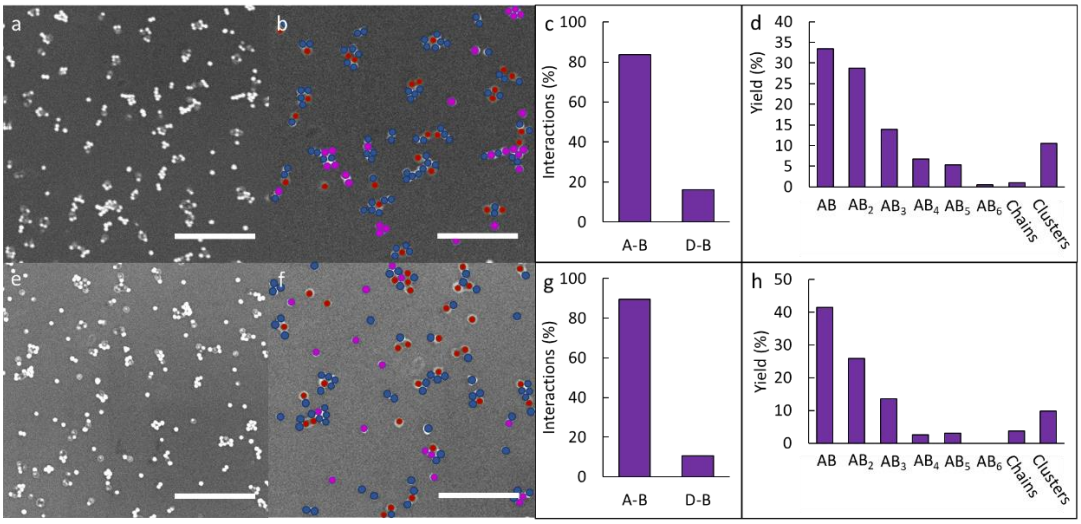

Figure 4.13 The self-assembly of **A2$_{20}$**, **B2**, and **D1** at a feeding ratio of 1:2:1. (a, e) SEM images of the assembly results in which the **B** and **D** particle sizes are (a) **B$_{30}$** and **D$_{40}$** and (b) **B$_{40}$** and **D$_{30}$**. (b, f) Labeled zoomed-in SEM image. The labeled particles are **B** (blue), **A** (red), and **D** (purple). (c, g) Plots showing the particle–particle interactions between the **B** particles and the **A** and **D** particles. (d, h) Plots showing the population statistics of the assemblies. The scale bars are 500 nm in (a, e) and 400 nm in (b, f).

4.3.5 Addition of Guest-Modified Particles to Assembled Solutions

To study the competitive self-assembly mechanism further, we were curious to see if the assemblies were reversible after the initial assembly. Specifically, we wanted to determine if adding a more favorable host-modified particle would result in structural changes to the assemblies. To test this idea, we initially assembled **M1$_{30}$** and **B1$_{20}$** particles together. We then added the **A** particle solution to the pre-

assembled **M** and **B** particles, followed by dialysis to remove DMF and imaged the resultant structures using SEM (Figure 4.14).

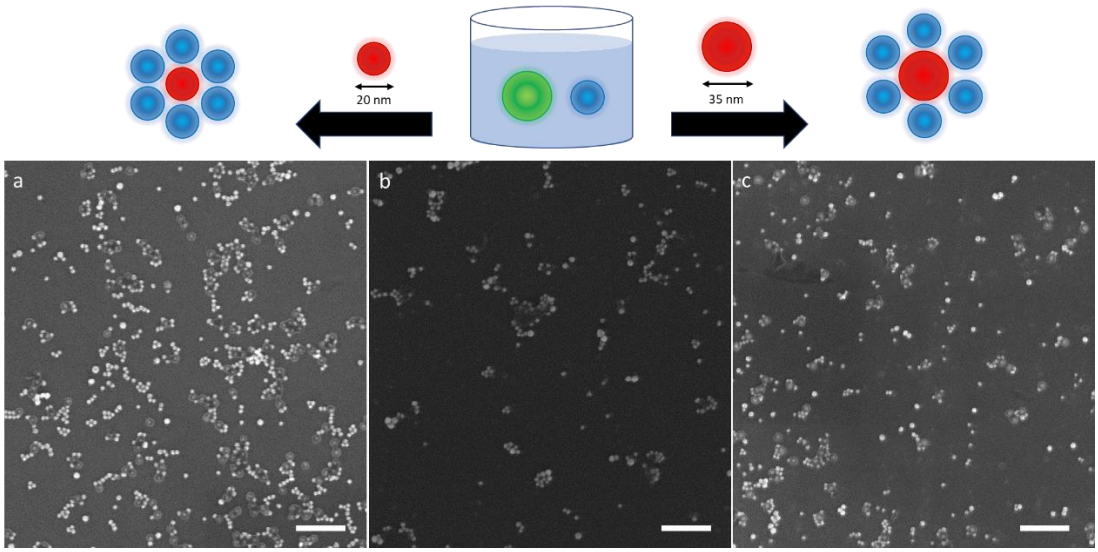

Figure 4.14 The self-assembly of **B1**$_{20}$ and **M1**$_{30}$ followed by assembly with **A2**. (a-c) Representative SEM images of the nanostructures in which the added guest particles were (a) **A2**$_{20}$ and (c) **A2**$_{35}$. (b) A control without **A2** particles. The scale bars are 400 nm.

As shown in Figure 4.14, regardless of the size of the **A** particle added, we observed interactions between the **A** and **B** particles. **A**–**B** interactions accounted for over 85% of all host–guest particle interactions in both samples. There are still signs of assembly between the **B** and **M** particles; however, most of the obtained structures follow the results expected based on the sizes of the **A** and **B** particles. For example, we observed sunflower and branched chain formation, which is consistent with particle A being the same size (Figure 4.14a) or larger (Figure 4.14c) than particle **B**. This result is advantageous, as it suggests we can initiate a morphological change via the addition of competitive host or guest particles.

4.4 Conclusion

In this Chapter, I demonstrated the reversibility of the particle self-assembly method introduced in Chapter 3. Additionally, I demonstrated the selectivity of the host–guest-functionalized particle interactions via the addition of competitive guests. As previously described, the particle self-assembly was driven by host–guest interactions between the complementary polymer brushes, as the guest moieties were destabilized under aqueous conditions. These interactions resulted in defined nanostructures that were achieved via fine tuning of the particle feeding ratio, particle sizes, and BCP lengths. Disassembly of these structures was achieved via the addition of free β-CD into the system. Particles could then be reassembled upon removal of the free β-CD moieties. However, this process could not be repeated more than once, so improvement is needed. Selectivity of the particle interactions was studied by assembling the host-modified **B** particles in solution with multiple different guest-modified particles. Analysis of the resultant structures makes it clear that the **B** particles preferentially interacted with the **A** particles, regardless of the particle size, the particle feeding ratio, or the identity of the competitive guest moiety. The observed structures aligned well with the results in Chapter 3, regarding particle-size effects. This selectivity leads to increased control over the directional interactions between particles and can allow us to target specific nanostructures and interactions in complex environments. Overall, reversibility over the particle assemblies along with selectivity over the particle interactions could greatly expand the use of these materials in applications such as sensing and optoelectronics.

Chapter 5: Conclusions and Future Work

5.1 Conclusions

The objective of this dissertation was to design robust methods to assemble block-copolymer-tethered inorganic NPs into water-stable, colloidal nanostructures with defined valences. I achieved this goal using two different assembly methods. The first method used complementary, acid–base-functionalized BCP-tethered NPs to drive the assembly. The neutralization of the reactive acid and base moieties drove the particle assembly to produce a range of supracolloids with defined valences in high yields. These products consisted of alternating $\mathbf{(AB)_n}$ chains and various $\mathbf{AB_n}$ structures (n = 1-6). The valence of the supracolloids was tuned by varying the size of the NPs, as well as length and composition of BCP tethers. Furthermore, the supracolloids exhibited enhanced stability when transferred to water, due to the amphiphilic nature of the BCP tethers in which the inner hydrophobic BCP core was shielded by the outer hydrophilic block.

The second method used complementary, host–guest-functionalized block-copolymer-tethered NPs to drive the assembly. When exposed to water, the host and guest moieties formed host–guest inclusion complexes, which drove the particle assembly to produce a range of supracolloids with defined valences in high yields. Similar to our acid–base assembly, our host–guest driven assembly resulted in various $\mathbf{AB_n}$ structures and nanochains. However, we only observed these structures when the diameter of particle **A** was smaller than or equal to the diameter of particle **B**. When the diameter of particle **A** was larger than the diameter of particle **B**, we

observed the formation of branched chains and sunflower-type structures. This phenomenon is attributed to the larger number of guest moieties on the larger **A** particles, which are better stabilized upon the addition of a greater number of **B** particles. This result was further confirmed when studying the effect of polymer length on particle **A** in which the number of sunflower petals increased with increasing polymer length.

Finally, we demonstrated the reversibility of this second assembly method by exposing our assembled nanostructures to competitive free host molecules. Upon addition of the free host molecules, we observed a blue-shift in the absorption spectra, which is indicative of particle disassembly. Upon removal of the free host, the spectra again red-shifted, indicating that the particles had reassembled. We also demonstrated the strength of the particle interactions by assembling our **A** and **B** particles together in the presence of another guest particle. We showed that the **B** particles preferentially assembled with the **A** particles, regardless of the identity of the other guest particle. Furthermore, the resulting nanostructures matched the expected outcomes based on the difference in particle size. The stability of these structures in water along with their reversibility makes these structures ideal candidates in cellular uptake studies in which these nanostructures can potentially be used as nano-sensors.

5.2 Future Work

5.2.1 Studying the Effects of pH and Salt

As established in Chapter 2, we demonstrated the self-assembly of BCP-tethered NPs via acid–base neutralization into water-stable supracolloids. Based on the work of Nie and co-workers, the addition of acid and base will influence the

residual acid and base moieties within the polymer brushes.[172,173] To explore this approach, the hierarchal assembly of **AB$_2$** trimers into ribbons, chains, and network structures was demonstrated by assembling the trimers at the interface between THF and water. The pH was varied and was found to impact the resulting assemblies; however, the use of interfacial self-assembly was required, as the **AB$_2$** trimers were not stable in water.[173] Thus, it would be interesting to explore the effect of pH on supracolloids that are water stable. Additionally, we can study the effect of adding salt to the assembly solutions, as salt can screen the charges in solution, which may result in different assembly behaviors.

We can also explore changing the composition of the block copolymers that were used to modify the NPs. Using the block copolymers in Chapter 3 as inspiration, it may be possible to employ DMA instead of St as the co-monomer in the inner BCP blocks. The addition of DMA would result in block copolymers that are more hydrophilic, which would allow us to assemble the BCP-tethered NPs directly in water rather than in THF. The ability to assemble these NP building blocks in water would allow for greater ease in studying pH and salt effects, as we would not be limited by solubility. Furthermore, we would be able to study these pH and salt effects on the initial assemblies.

5.2.2 Stimulus-Responsive Self-Assembly

Although this work has demonstrated the reversibility of host–guest-mediated self-assembly, it would be better to demonstrate cycling of the assembly. One method to achieve this would be to use hosts or guests with stronger binding affinities to either the β-CD or Ada, such as lithocholic acid or cucurbiturils.[213,214] It would also

be advantageous to design a reversible assembly that could be initiated via temperature, light, or an external field. These three methods are particularly useful, as they do not require changes to the surrounding medium or adding solvent or acid/base, which may destabilize the system, to reassemble the nanostructures. It may be possible to achieve these goals by changing the BCP brush or the inorganic NP core. For example, azobenzene in its *trans* state is known to form inclusion complexes with β-CD. Upon irradiation with UV light, the azobenzene isomerizes to its *cis* state, which weakens the host–guest interactions, leading to disassembly of the complex, until the azobenzene isomerizes back to the *trans* state.[212] This assembly pathway could be implemented as an alternative to the β-CD-driven mechanism. Furthermore, as shown in previous work by Yi *et al*, it is possible to exchange one of the complementary Au NP building blocks for an Fe_3O_4 NP building block.[172,173] Using Fe_3O_4 NPs would allow us to study how these structures behave when exposed to magnetic fields and could lead to interesting hierarchal assembly pathways that could be disassembled once the applied magnetic field was removed.

5.2.3 Additional Host–Guest Candidates

To continue studying host–guest-mediated self-assembly, it is important to expand the library of host–guest interactions. For example, α and γ-CD also exhibit host–guest interactions with different guest moieties, which could be interesting to explore in self-sorting applications. As shown by Harada and co-workers, hydrogels modified with α, β, and γ-CD formed stable gel–gel interactions with hydrogels containing their complementary guest moieties.[181] These gels were also self-sorting with the host gels only forming stable interactions with their complementary guest

gels even when exposed to different host and guest gels. This same concept could be explored further on the nanoscale, as demonstrated in Chapter 4. Implementation of additional host and guest moieties would allow for better understanding of the assembly mechanism and may facilitate the use of these nanostructures as nanosensors. Furthermore, we can begin to imagine these assembled nanostructures as molecules that we can manipulate in a manner similar to how small molecules react in solution. A schematic demonstrating this concept is shown in Figure 5.1.

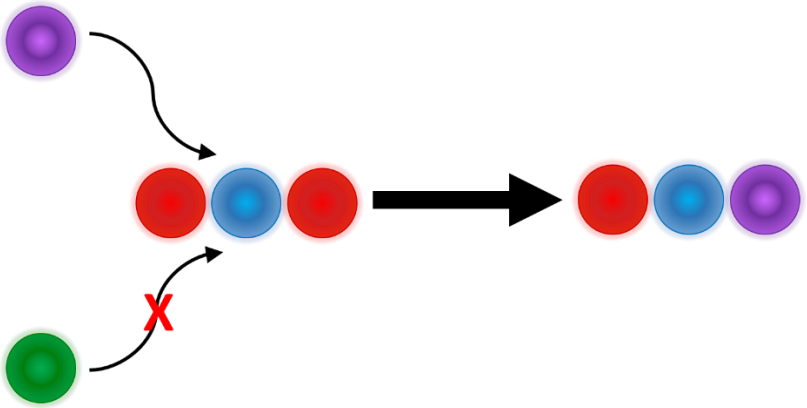

Figure 5.1 Schematic showing the selective displacement reaction of functionalized particles. Each type of particle is represented by a different color. Here, the purple particles demonstrate a higher selectivity for the blue particles than the red particles do, resulting in displacement of the red particle. Meanwhile, the red particles show a higher selectivity for blue particles than the green particles do, resulting in no reaction.

Chapter 6: Supporting Information

6.1 Chapter 2 Experimental

6.1.1 Polymer and Particle Characterization

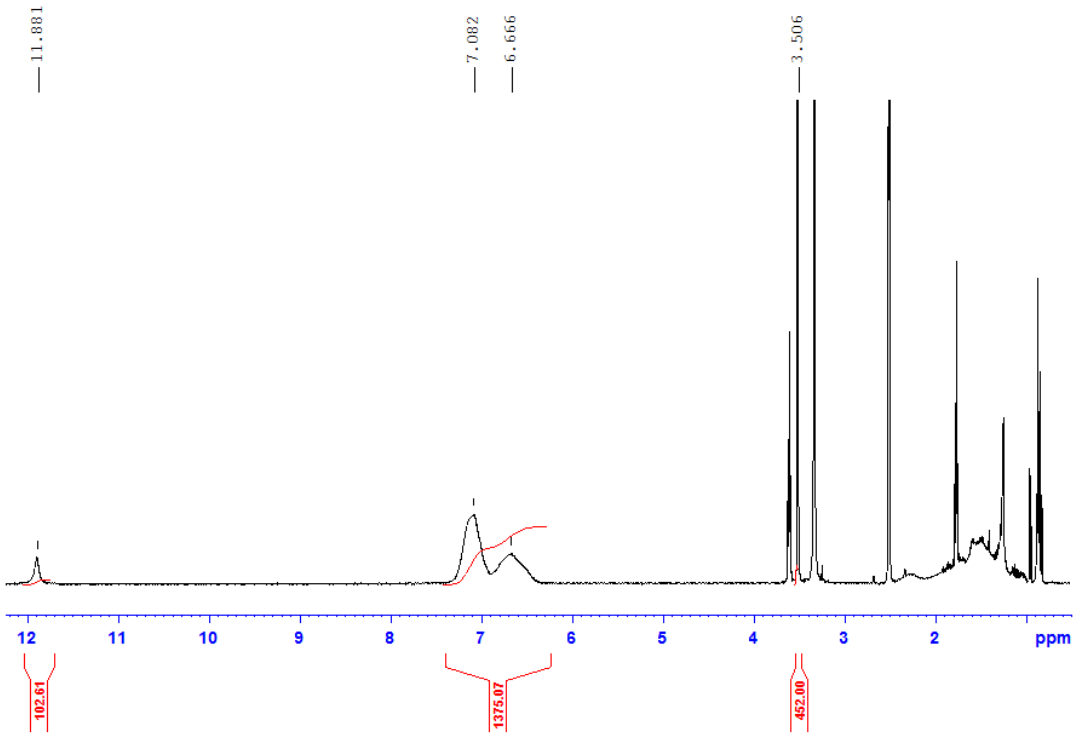

Figure 6.1 ^{1}H NMR spectrum (400 MHz, RT, DMSO-*d*6) of PEO_{113}-*b*-P(AA_{102}-*r*-St_{275})$_{254}$-SH.

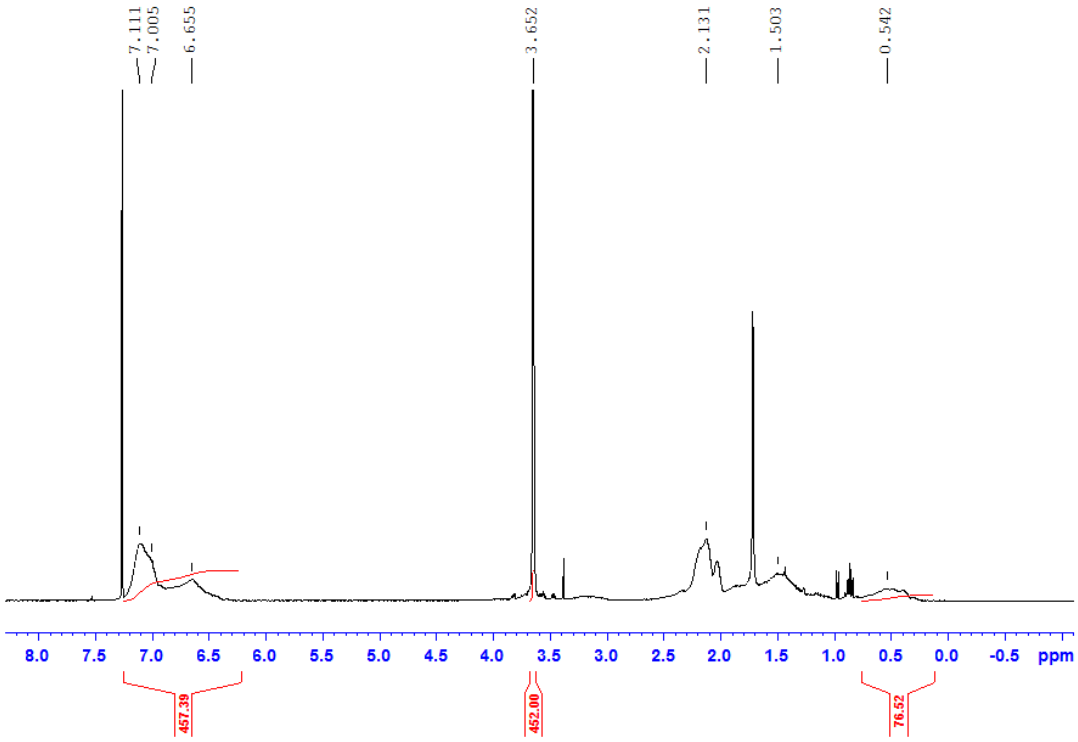

Figure 6.2 ^{1}H NMR spectrum (400 MHz, RT, $CDCl_3$) of PEO_{113}-*b*-P(DMAEMA$_{25}$-*r*-St$_{91}$)$_{116}$-SH.

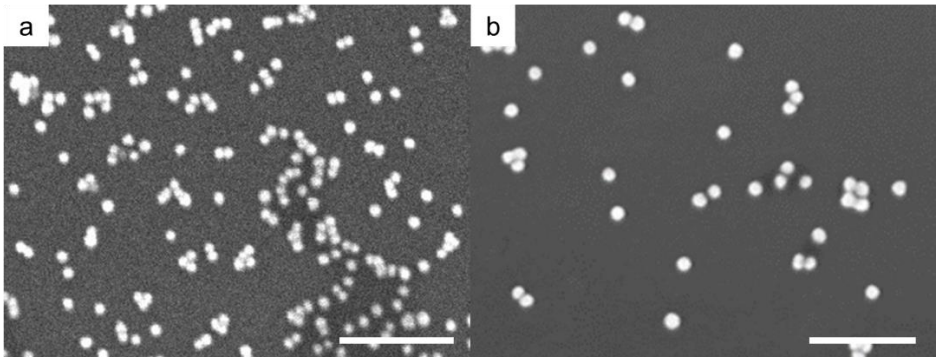

Figure 6.3 Representative SEM images of synthesized Au NPs. Au NPs are (a) 20.7 (± 1.8) nm diameter and (b) 34.9 (±3.0) nm diameter. The scale bars are 200 nm.

6.1.2 HINP Self-Assembly

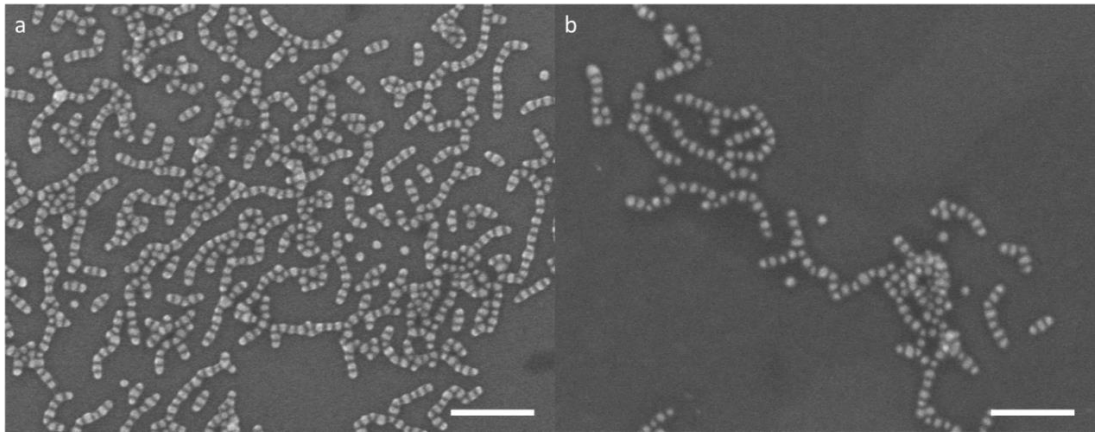

Figure 6.4 Representative SEM images of nanochains formed from the self-assembly of $\mathbf{A1}_{25}$ and $\mathbf{B1}_{35}$. The particle feeding ratio of **B**:**A** ~0.9:1. The scale bars are 200 nm.

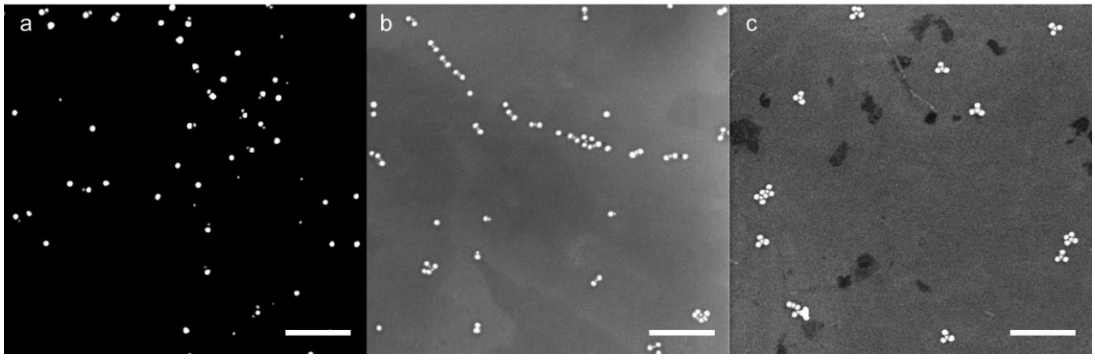

Figure 6.5 Large-area SEM images of nanostructures formed from the self-assembly of $\mathbf{A}_{20}$ and $\mathbf{B}_{35}$. The predominant nanostructures are (a) **AB**, (b) $\mathbf{AB}_2$, and (c) $\mathbf{AB}_3$. BCP combinations were (a) **A1**:**D2**, (b) **A1**:**D1**, and (c) **A4**:**D3**. The scale bars are 400 nm.

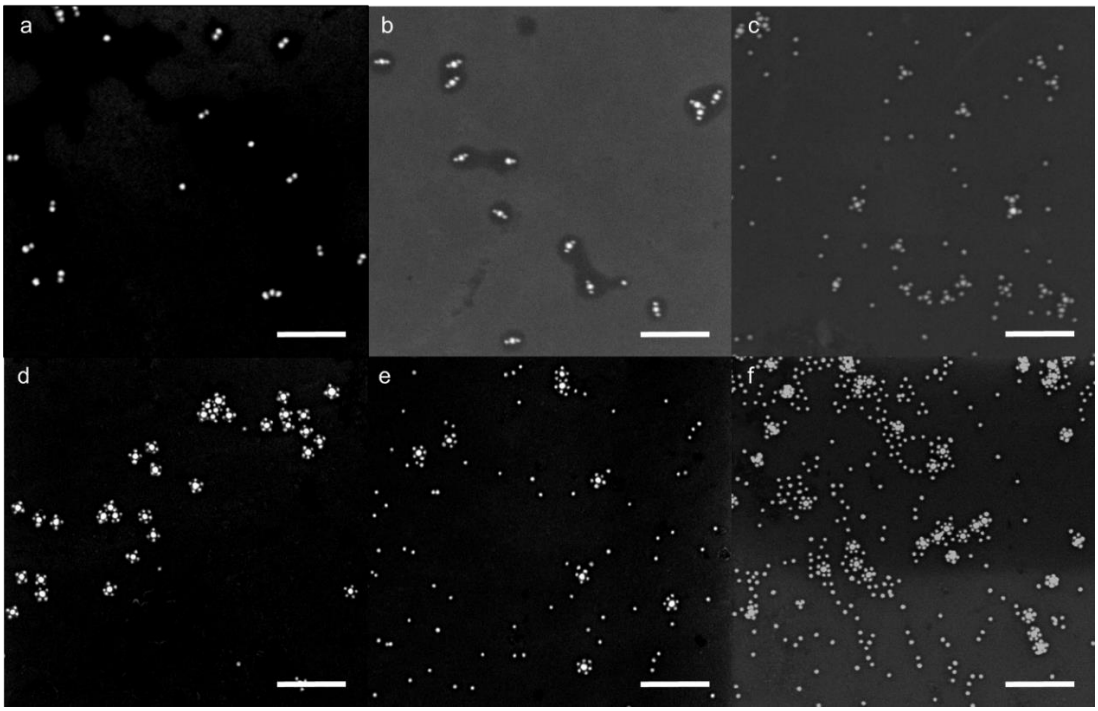

Figure 6.6 Large-area SEM images of nanostructures formed from the self-assembly of $\mathbf{A_{35}}$ and $\mathbf{B_{20}}$. The predominant nanostructures are (a) **AB**, (b) $\mathbf{AB_2}$, (c) $\mathbf{AB_3}$, (d) $\mathbf{AB_4}$, (e) $\mathbf{AB_5}$, and (f) $\mathbf{AB_6}$. BCP combinations were (a) **A1**:**D2**, (b) **A1**:**D1**, (c) **A1**:**D1**, (d) **A1**:**D2**, (e) **A2**:**D2**, and (f) **A2**:**D2**. The scale bars are 300 nm.

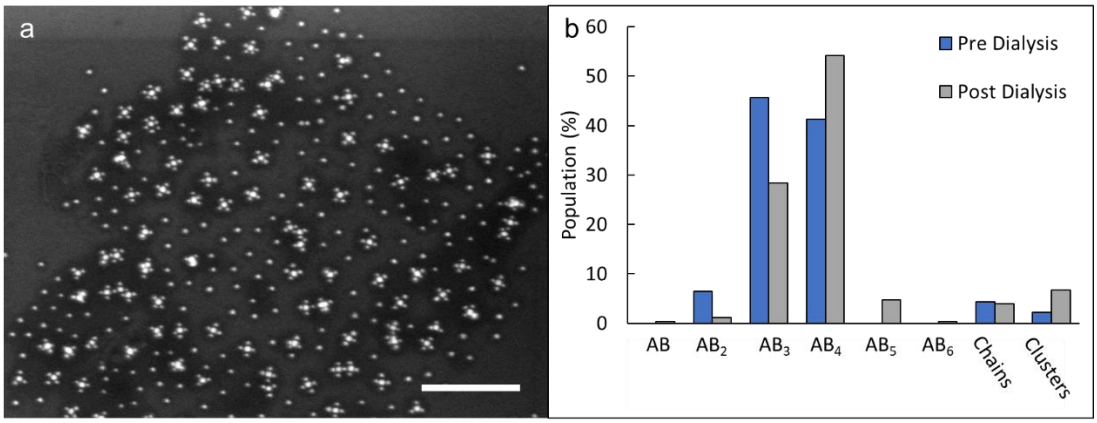

Figure 6.7 $\mathbf{AB_3}$ and $\mathbf{AB_4}$ structures composed of $\mathbf{A4_{35}}$ and $\mathbf{B3_{20}}$ particles after dialysis. (a) Large area SEM image after dialysis. (b) Population statistics plot showing the nanostructure populations before (blue) and after (grey) dialysis. The scale bar is 500 nm.

6.2 Chapter 3 Experimental

6.2.1 Synthesis

1-adamantylmethyl methacrylate (AdMA)

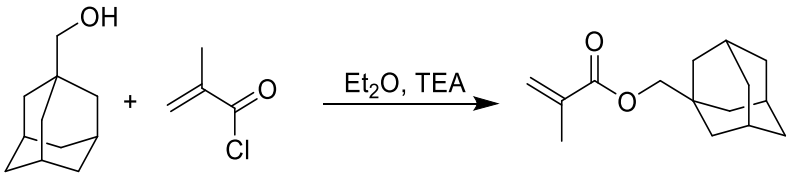

AdMA was synthesized via a Steglich esterification of 1-Adamantanemethanol and methacryloyl chloride in diethyl ether under the presence of TEA. Diethyl ether (50 mL), 1-adamantanemethanol (7.8598 g, 0.047 mol), and of anhydrous TEA (5.70 mL, 0.041 mol) were added to a 250-mL beaker. The roundbottom was fit with a dropping funnel and purged with nitrogen for 30 min. The solution was placed in an ice and salt bath. Methacryloyl chloride (5.20 mL, 0.053 mol) and diethyl ether (25 mL) were added to the dropping funnel. The methacryloyl chloride solution was then added dropwise over 30 min, and the reaction was allowed to stir for 2 h at -20 °C and for 12 h at RT. The organic layer of the solution was collected and washed three times with water. The organic layer was then dried with anhydrous sodium sulfate, and the diethyl ether was removed under reduced pressure. The crude product was collected and run through a silica column with a mobile phase of 19:1 hexanes:ethyl acetate to yield 7.7327 g (70%) of pure 1-adamantylmethyl methacrylate. The final product was collected and stored in a freezer until needed. ^{1}H NMR (400 MHz, $CDCl_3$); δ = 6.12 (s, 1H), 5.56-5.55 (s, 1H), 3.75 (s, 2H), 2.00, (t, 3H), 1.97 (s, 3H), 1.76-1.65 (t, 6H), 1.58-1.57 (d, 6H).

Mono-6-tosyl-β-cyclodextrin

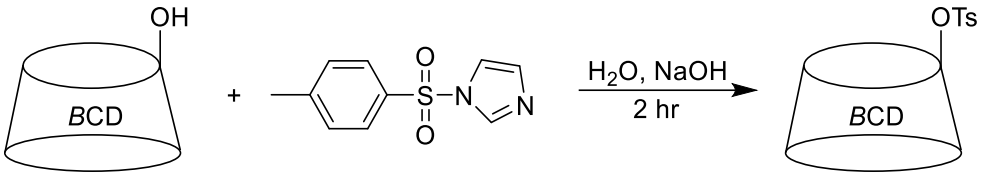

Mono-6-tosyl-β-cyclodextrin was synthesized based on a previously reported procedure.[215] β-CD (10.0004 g, 8.8 mmol) and distilled water (225 mL) were added to a 500 mL roundbottom flask. The solution was stirred at 60 °C until the β-CD was completely dissolved. The solution was then allowed to return to RT. Meanwhile, 1-(p-tosyl)-imidazole (7.7501 g, 34.9 mmol) was ground into a fine powder using a mortar and pestle. The tosyl-imidazole was then added to the β-cyclodextrin solution under stirring, and the solution was stirred vigorously for 2 h under air. After 20 min, an aqueous solution of sodium hydroxide (12.50 mL, 9.0 M) was added. After 2 h, ammonium chloride (12.0011 g, 0.22 mol) was added to quench the reaction, and the solution was stirred until all the solids were completely dissolved. The solution was then concentrated down to about 100 mL by blowing air on the solution overnight. The solution was then filtered, and the white solid was collected and washed twice with ice-cold water and once with acetone. The solid was dried overnight under vacuum at RT, yielding 5.3014 g (47%) of mono-6-tosyl-β-cyclodextrin. ^{1}H NMR (400 MHz, DMSO-*d*6) was consistent with the reported literature; however, minor impurities appear at δ = 7.1 and 7.7. These peaks are consistent with di-tosylation of the β-CD and are not expected to impact further reactions.[215]

Mono-6-azido-β-cyclodextrin

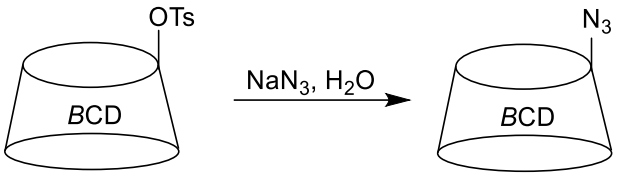

Mono-6-azido-β-cyclodextrin was synthesized based on a previously reported procedure.[216] Mono-6-tosyl-β-cyclodextrin (5.0003 g, 3.9 mmol), sodium azide (4.9899 g, 76.8 mmol), and distilled water (500 mL) were added to a 1 L roundbottom flask. The roundbottom was equipped with a condenser, and the solution was refluxed overnight. The solution was then concentrated to about 25 mL using a rotary evaporator. Subsequently, 1,1,2,2-tetrachloroethane (5.00 mL, 47.4 mmol) was added to the concentrated solution, and the solution was allowed to stir at RT for 30 min. The solution was then centrifuged at 5,000 rpm for 10 min, and the precipitate was collected. The solid was recrystallized in hot water and was dried overnight under vacuum at RT, yielding 3.9276 g (87%) of pure mono-6-azido-β-cyclodextrin. ^{1}H NMR (400 MHz, DMSO-*d*6) was consistent with the reported literature.[216]

6.2.2 Precursor and Polymer Characterization

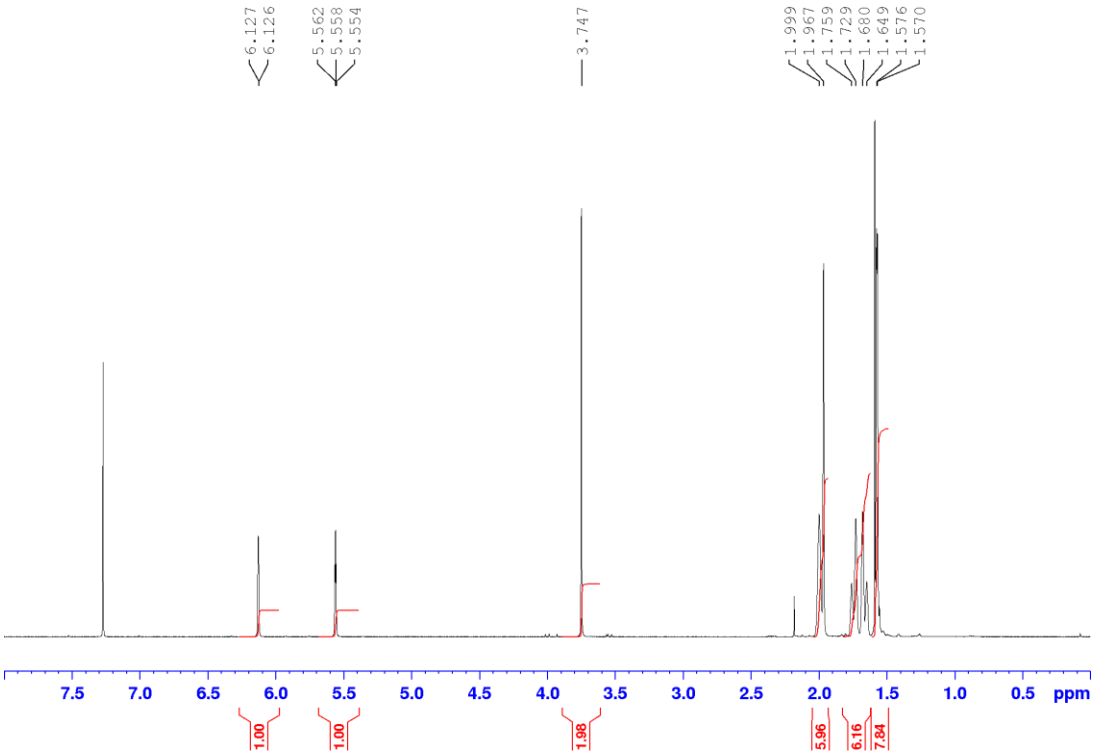

Figure 6.8 ^{1}H NMR (400 MHz, RT, $CDCl_3$) of 1-adamantylmethyl methacrylate.

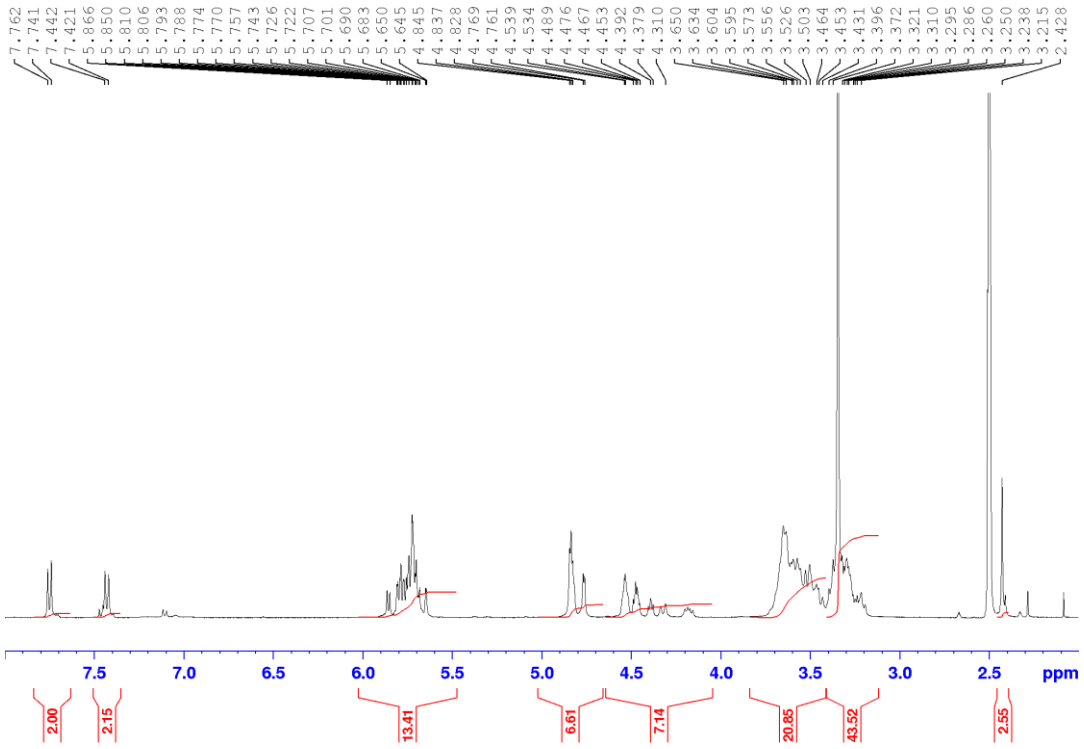

Figure 6.9 ^{1}H NMR (400 MHz, RT, DMSO-*d*6) of mono-6-tosyl-β-cyclodextrin.

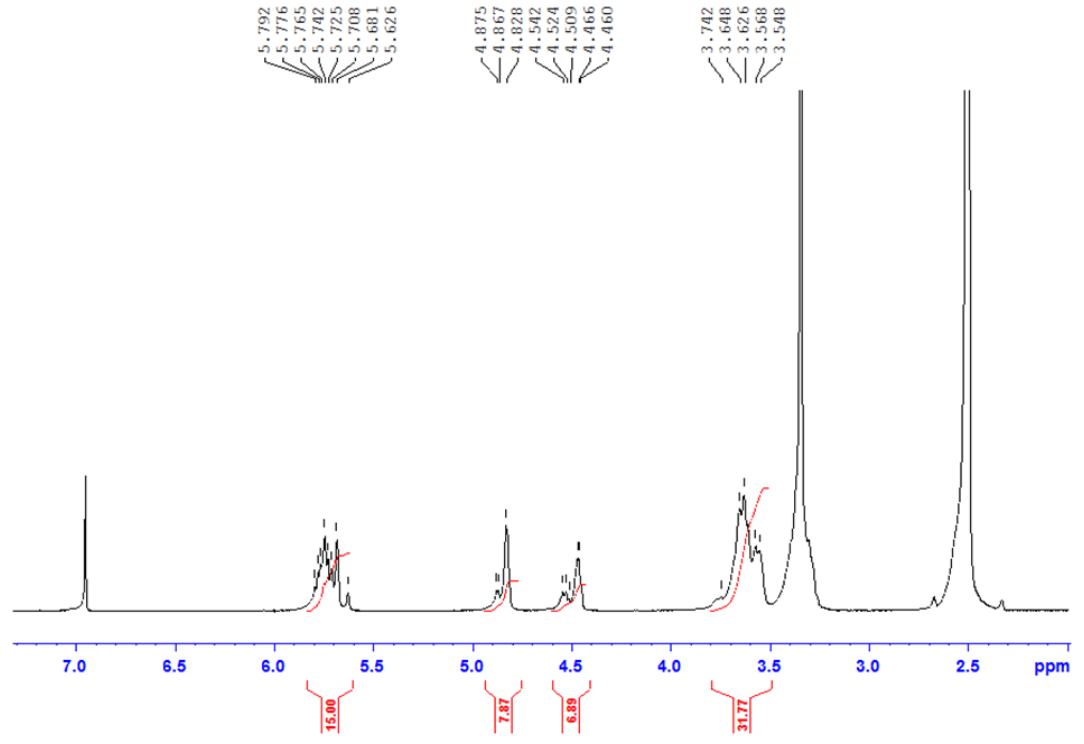

Figure 6.10 ^{1}H NMR (400 MHz, RT, DMSO-*d*6) of N_3-β-cyclodextrin.

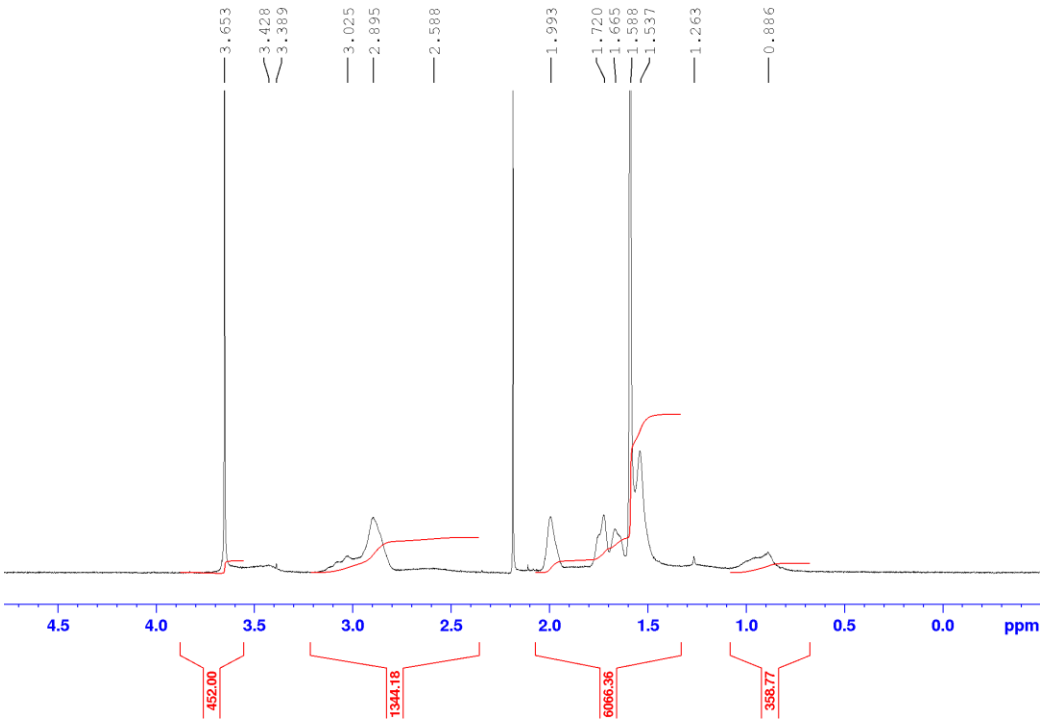

Figure 6.11 ^{1}H NMR (400 MHz, RT, $CDCl_3$) of PEO_{113}-*b*-P(DMA_{120}-*r*-$AdMA_{224}$)$_{344}$-SH.

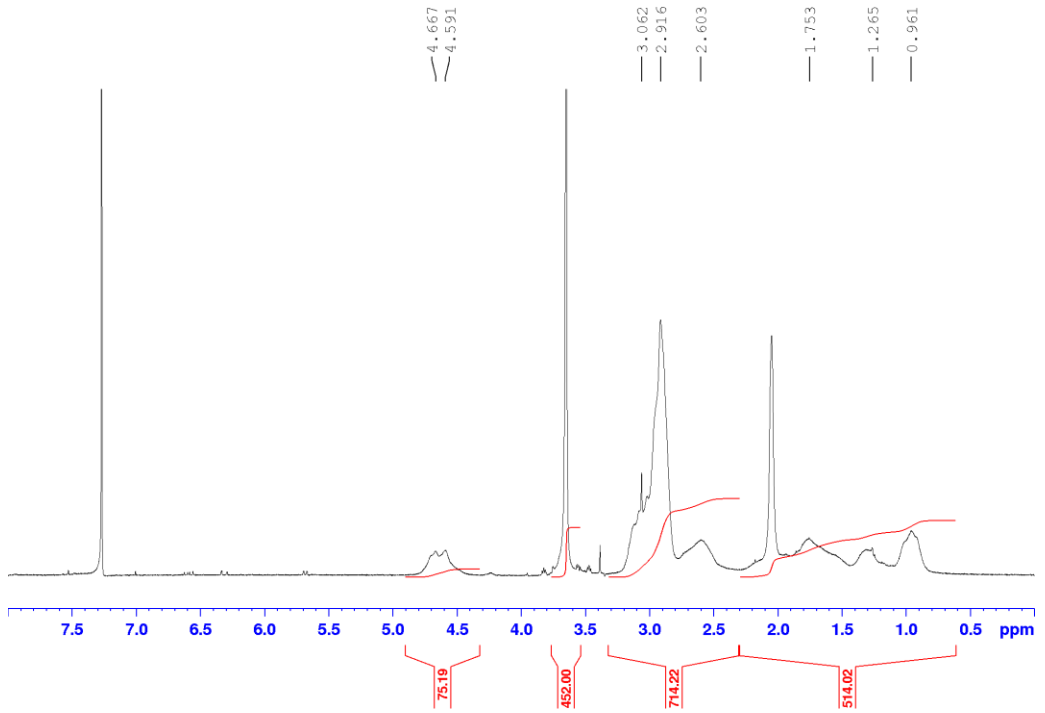

Figure 6.12 ^{1}H NMR (400 MHz, RT, $CDCl_3$) of PEO_{113}-*b*-P(DMA_{119}-*r*-$PgMA_{38}$)$_{157}$-SH.

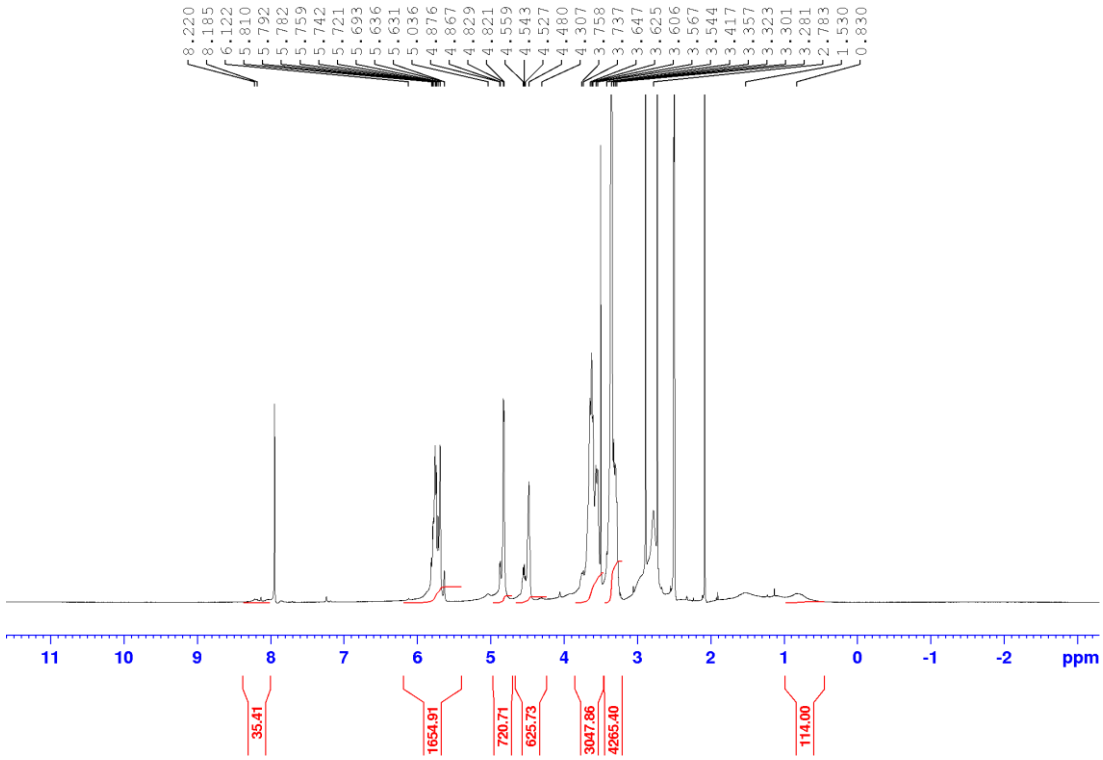

Figure 6.13 ^{1}H NMR (400 MHz, RT, DMSO-*d*6) of PEO_{113}-*b*-P(DMA_{119}-*r*-β-$CDMA_{38}$)$_{157}$-SH.

6.2.3 HINP Self-Assembly

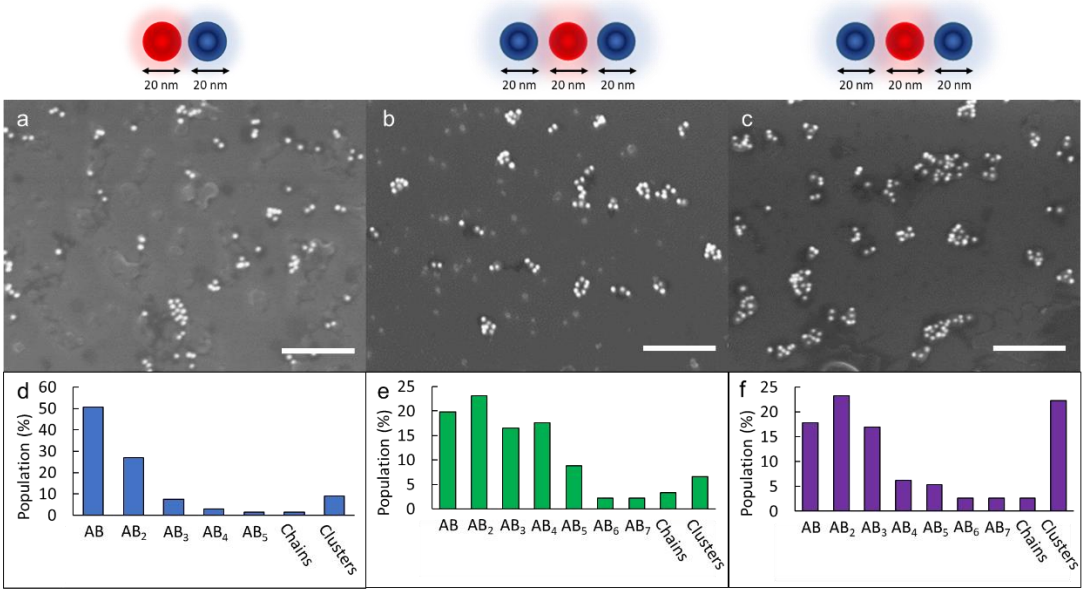

Figure 6.14 The self-assembly of **A1**$_{20}$ and **B3**$_{20}$ into various nanostructures. (a-c) Representative SEM images of the assembled nanostructures with an increasing feeding ratio of **B**:**A**. The feeding ratios are (a) 1:1, (b) 2:1, and (c) 3:1. (d-f) Population statistics plots showing the nanostructure populations. The scale bars are 300 nm.

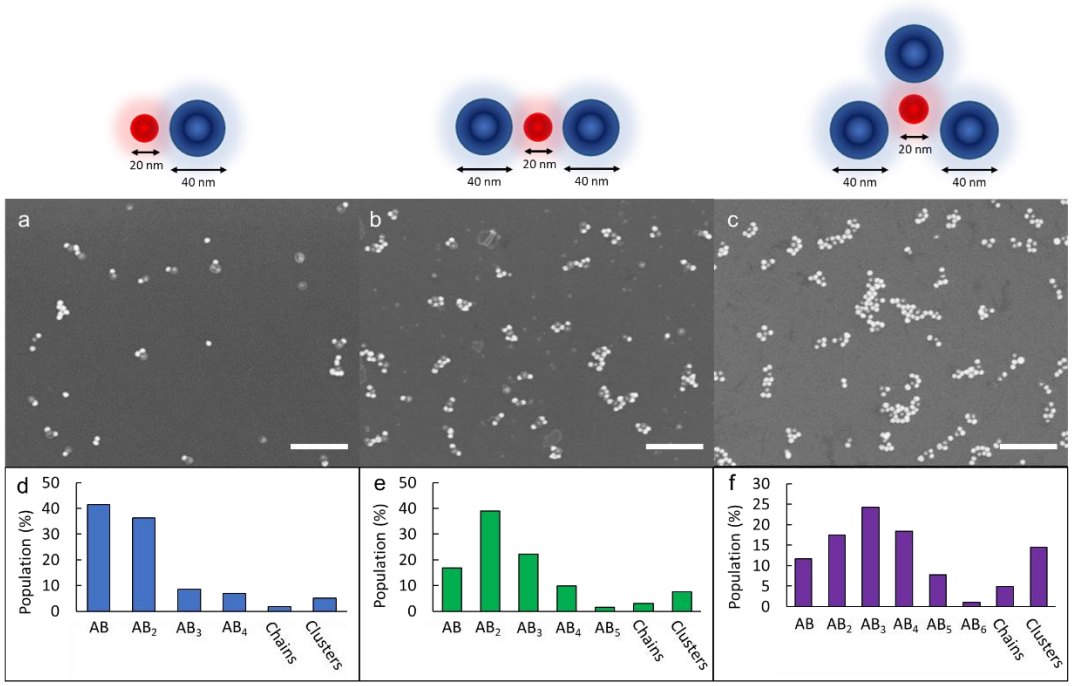

Figure 6.15 The self-assembly of **A1**$_{20}$ and **B3**$_{40}$ into various nanostructures. (a-c) Representative SEM images of the assembled nanostructures with an increasing feeding ratio of **B**:**A**. The feeding ratios are (a) 1:1, (b) 2:1, and (c) 3:1. (a-c) Representative SEM images. (d-f) Population statistics plots showing the nanostructure populations. The scale bars are 300 nm.

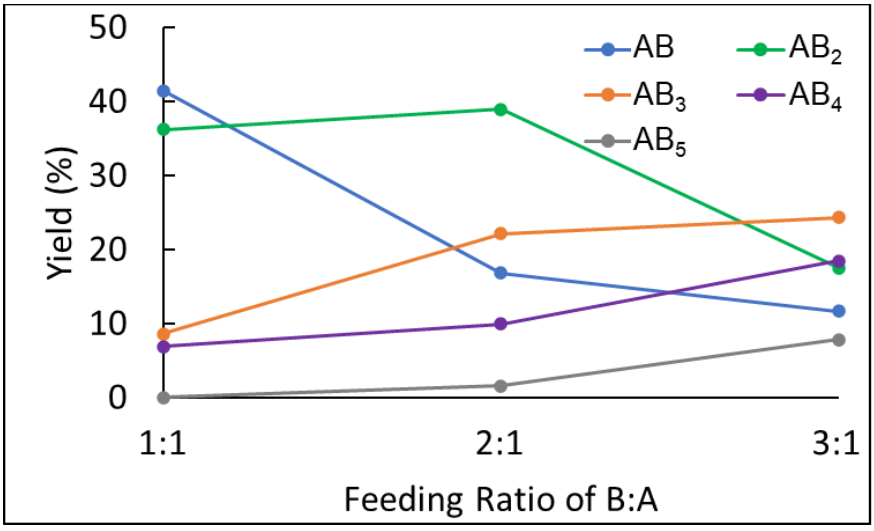

Figure 6.16 The change in nanostructure populations as a function of the feeding ratio of **B3**$_{40}$:**A1**$_{20}$.

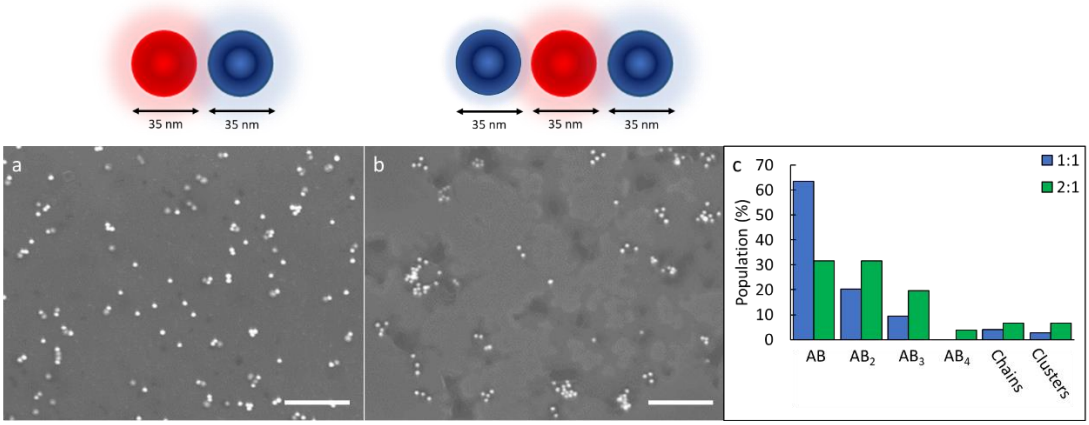

Figure 6.17 The self-assembly of **A1**$_{35}$ and **B3**$_{35}$ into various nanostructures. The assembled structures are (a) **AB** dimers and (b) **AB**$_2$ trimers. (a, b) Representative SEM images. (c) Population statistics plot showing the nanostructure populations. The scale bars are 500 nm.

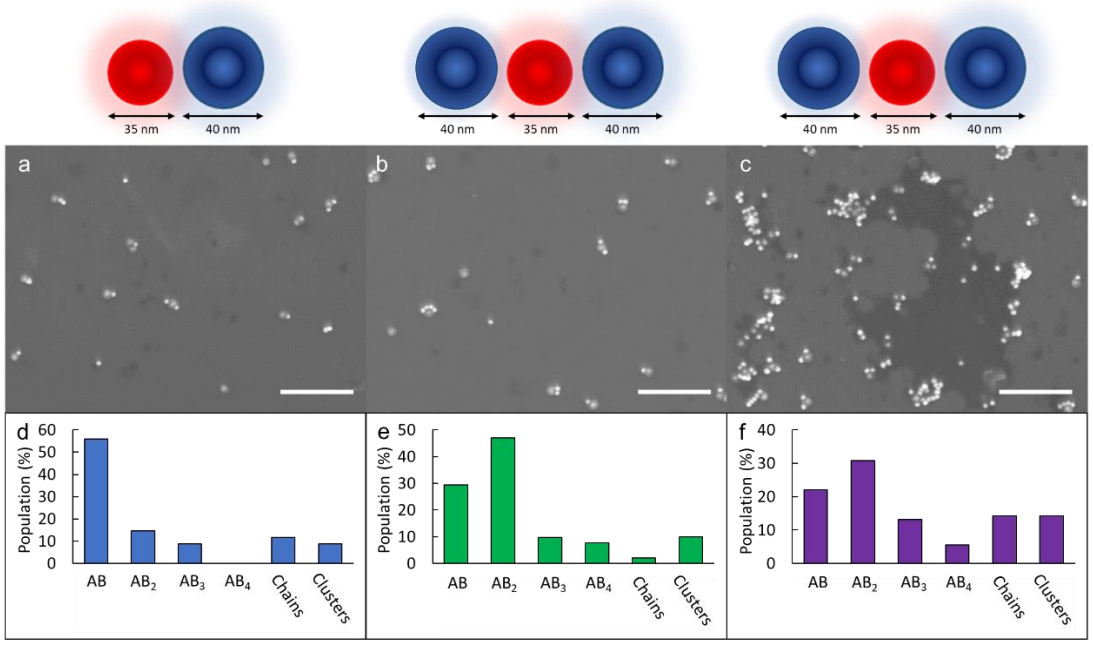

Figure 6.18 The self-assembly of **A1**$_{20}$ and **B3**$_{40}$ into various nanostructures. (a-c) Representative SEM images of the assembled nanostructures with an increasing feeding ratio of **B**:**A**. The feeding ratios are (a) 1:1, (b) 2:1, (c) and 3:1. (d-f) Population statistics plots showing the nanostructure populations. The scale bars are 500 nm.

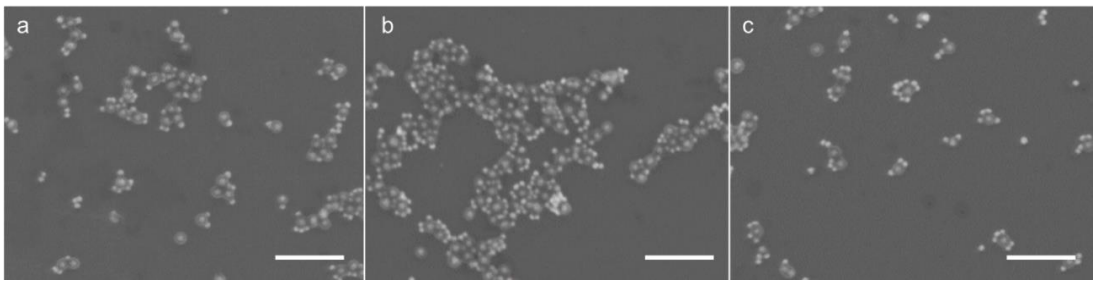

Figure 6.19 The self-assembly of **A1**$_{40}$ and **B3**$_{20}$ into various nanostructures. (a-c) Representative SEM images of assembled nanostructures with an increasing feeding ratio of **B**:**A**. The feeding ratios are (a) 1:1, (b) 2:1, and (c) 3:1. The scale bars are 300 nm.

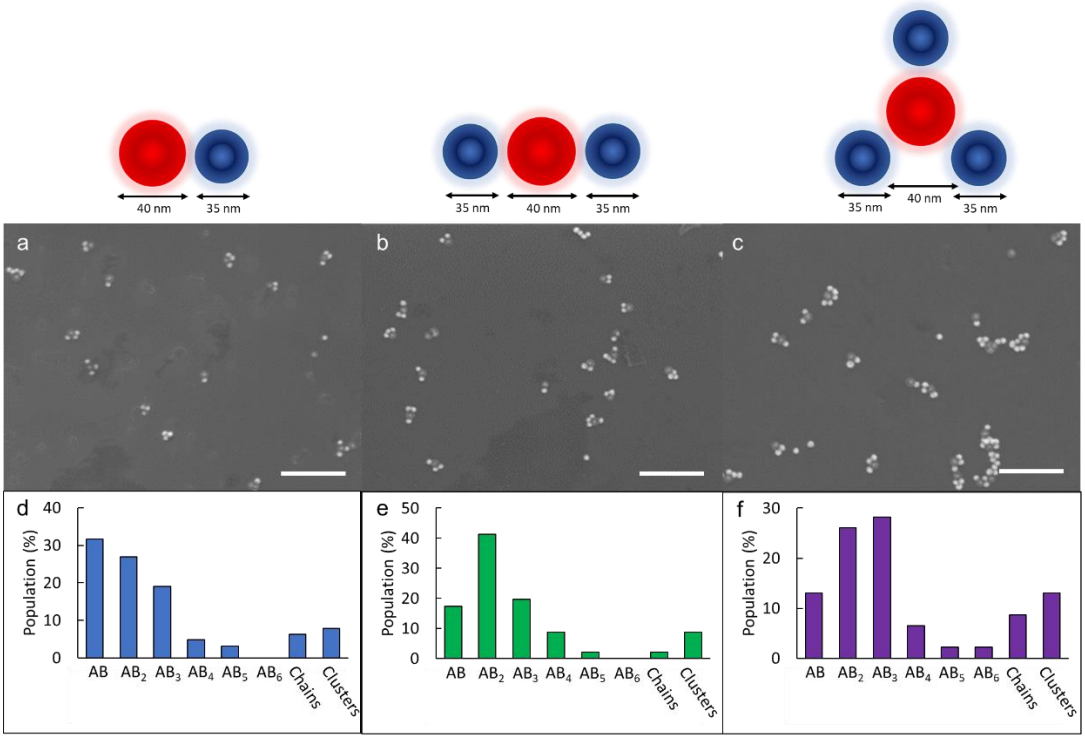

Figure 6.20 The self-assembly of **A1**$_{40}$ and **B3**$_{35}$ into various nanostructures. (a-c) Representative SEM images of the assembled nanostructures with an increasing feeding ratio of **B**:**A**. The feeding ratios are (a) 1:1, (b) 2:1, and (c) 3:1. (d-f) Population statistics plots showing the nanostructure populations. The scale bars are 500 nm.

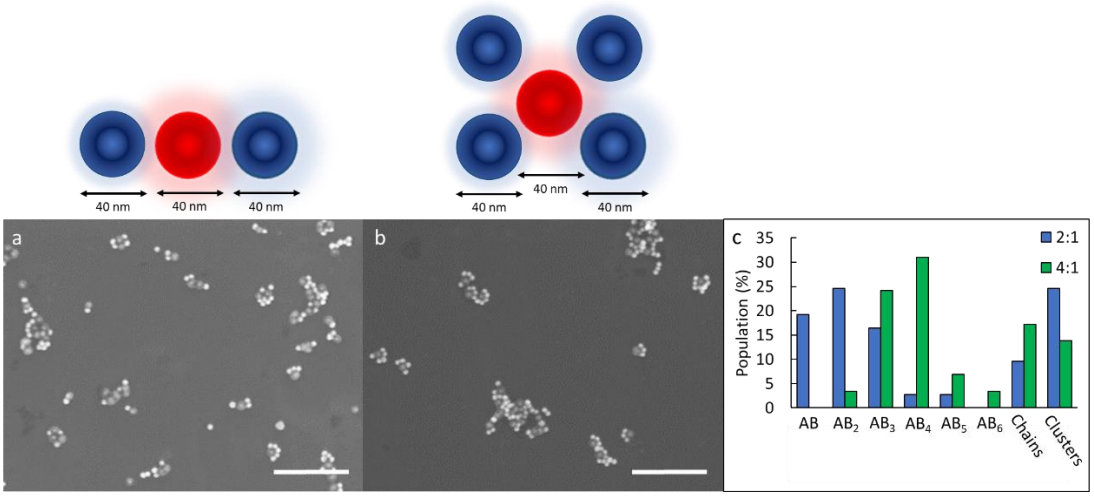

Figure 6.21 The self-assembly of **A1$_{40}$** and **B3$_{40}$** into various nanostructures. The assembled structures are (a) **AB$_2$** trimers and (b) **AB$_4$** pentamers. (a, b) Representative SEM images. (c) Population statistics plot showing the nanostructure populations. The scale bars are 400 nm.

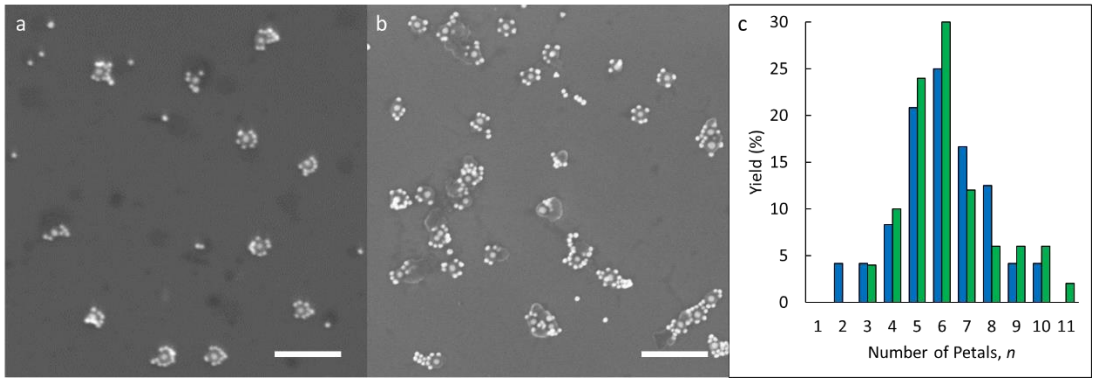

Figure 6.22 The self-assembly of **A1$_{35}$** and **B$_{20}$** into sunflower nanostructures. (a, b) Representative SEM images, in which the host particles are (a) **B3$_{20}$**, and (b) **B4$_{20}$**. (c) Plot showing the distribution of the number of petals per sunflower structure in which the number of petals is representative of the number of **B** particles per **A** particle. The scale bars are 400 nm.

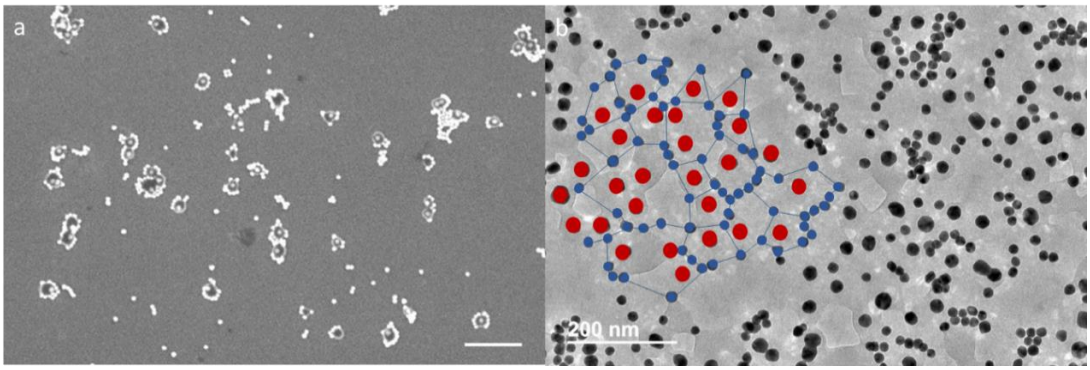

Figure 6.23 The self-assembly of **A2$_{35}$** and **B3$_{20}$** into sunflower nanostructures. (a) Representative SEM image, and (b) representative TEM image. The red and blue spheres represent **A2$_{35}$** and **B3$_{20}$** particles, respectively. The blue lines represent the boundaries of the nanostructures. The scale bars are 300 nm in (a) and 200 nm in (b).

6.3 Chapter 4 Experimental

6.3.1 Synthesis

3,3-dimethyl-1-butyl methacrylate (DMBMA)

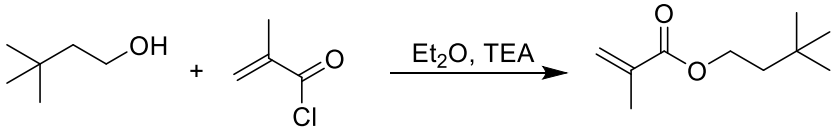

DMBMA was synthesized via a Steglich esterification of 3,3-dimethyl-1-butanol and methacryloyl chloride in diethyl ether in the presence of TEA. In a 250 mL roundbottom flask, we added diethyl ether (50 mL), 3,3-dimethyl-1-butanol (1.0233 g, 0.01 mol), and anhydrous TEA (5.70 mL, 0.041 mol). The roundbottom was fitted with a dropping funnel. The solution was purged with nitrogen for 30 min and placed in an ice and salt bath. Methacryloyl chloride (5.20 mL, 0.053 mol) and diethyl ether (25 mL) were added to the dropping funnel. The methacryloyl chloride solution was then added dropwise over 30 min, and the reaction was allowed to run for 2 h at -20 °C and 12 h at RT. The organic layer of the solution was removed using a separatory

funnel and was then washed three times with water. The organic layer was then dried with anhydrous sodium sulfate and concentrated under reduced pressure to remove the diethyl ether. The crude product was run through a silica column with a mobile phase of 6:1 hexanes:ethyl acetate. The final product was collected using a rotary evaporator to remove the remaining solvent, yielding 1.4783 g (86%) of pure 3,3-dimethyl-1-butyl methacrylate. The monomer was stored in a freezer until needed. ^{1}H NMR (400 MHz, $CDCl_3$) δ = 6.07 (s, 1H), 5.52 (s, 1H), 4.21-4.17 (t, 2H), 1.92, (s, 3H), 1.61-1.57 (t, 2H), 0.94 (s, 9H).

6.3.2 Precursor and Polymer Characterization

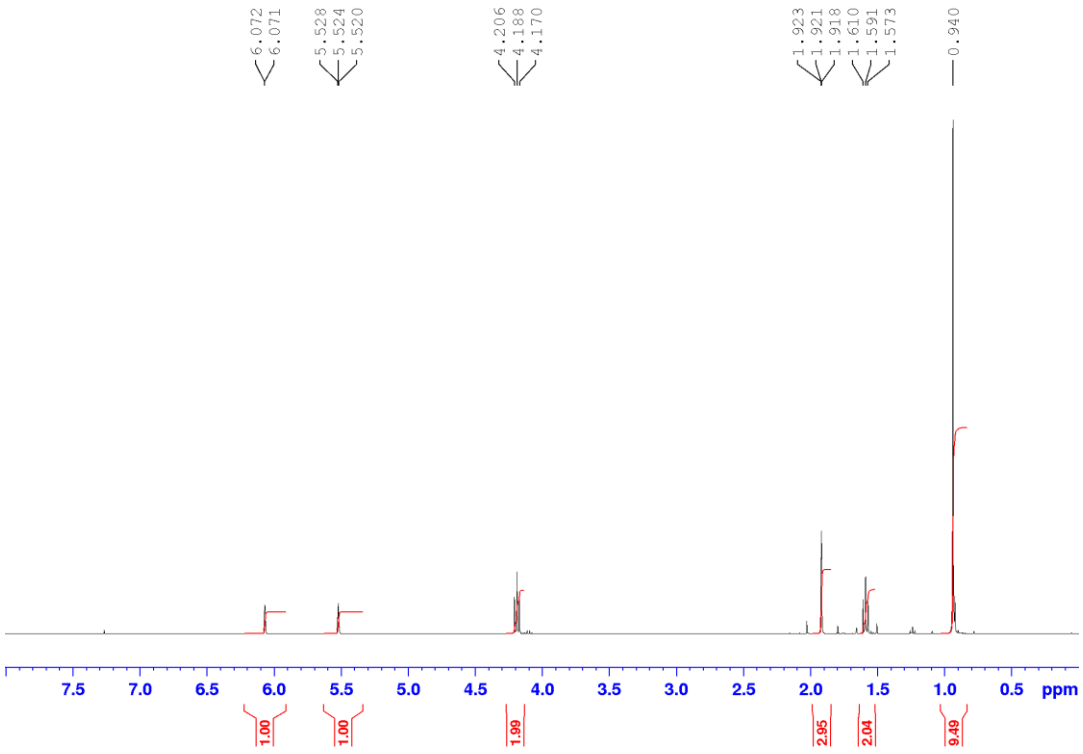

Figure 6.24 ^{1}H NMR (400 MHz, RT, $CDCl_3$) of 2,2-dimethyl-butyl-methacrylate.

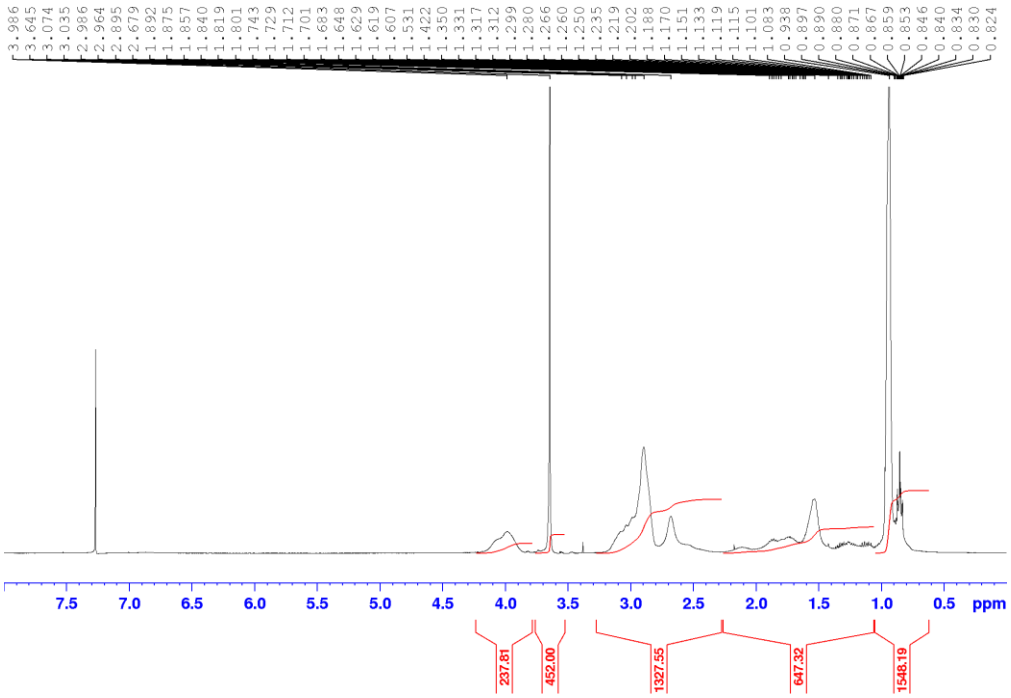

Figure 6.25 ^{1}H NMR (400 MHz, RT, $CDCl_3$) of PEO_{113}-*b*-P($DMBMA_{117}$-*r*-DMA_{221})$_{338}$-SH.

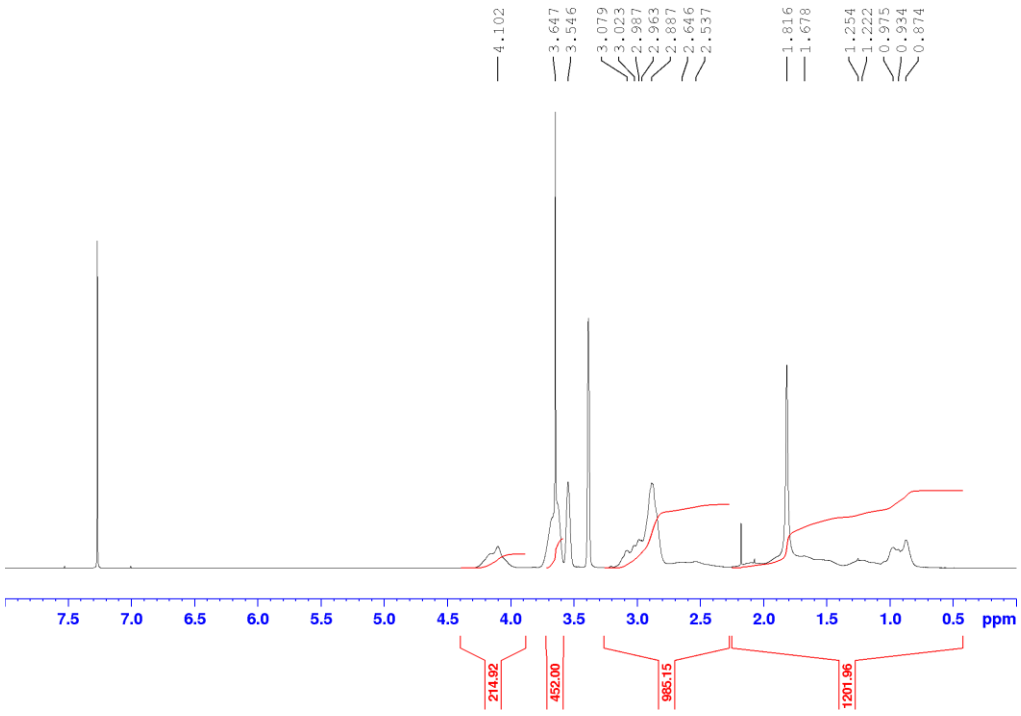

Figure 6.26 ^{1}H NMR (400 MHz, RT, $CDCl_3$) of PEO_{113}-*b*-P(MeO_2MA_{107}-*r*-DMA_{164})$_{271}$-SH.

6.3.3 HINP Self-Assembly

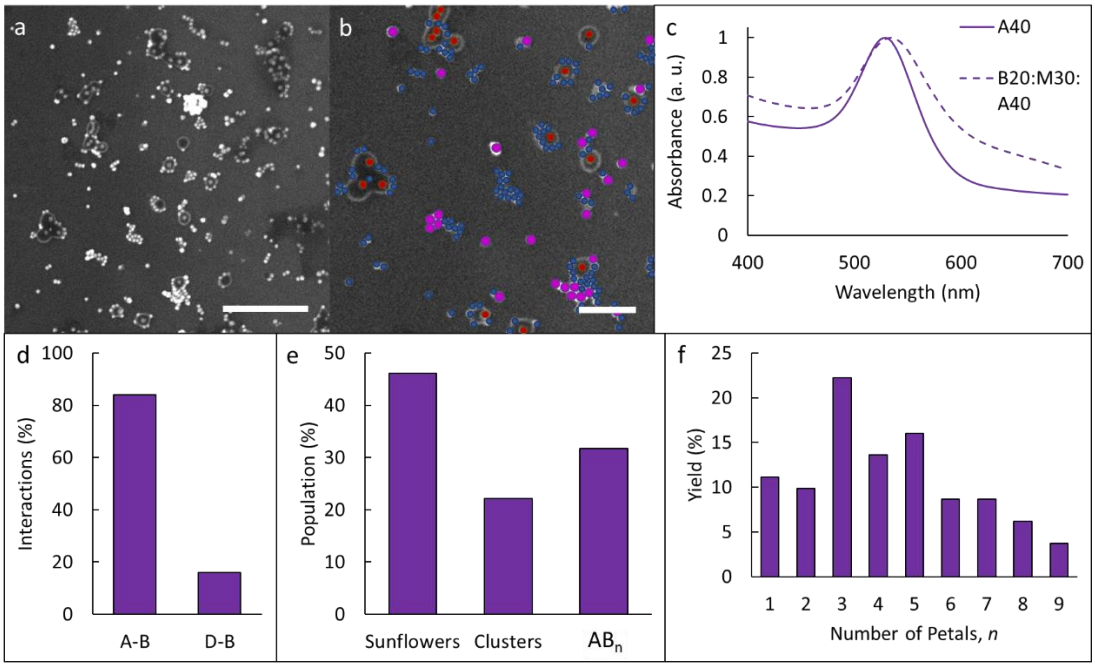

Figure 6.27 The self-assembly of **B2**$_{20}$, **A2**$_{40}$, and **D1**$_{30}$ at a feeding ratio of 2:1:1. (a) SEM image of the assembly structures. (b) Labeled zoomed-in SEM image. The labeled particles are **B2**$_{20}$ (blue), **A2**$_{40}$ (red), and **D1**$_{30}$ (purple). (c) UV-vis absorption spectrum of **A2**$_{40}$ particles (solid) and the assembled particles (dashed). (d) Plot showing the particle–particle interactions between the **B2**$_{20}$ particles and the **A2**$_{40}$ and **D1**$_{30}$ particles. (e) Population statistics of the nanostructures. (f) Plot showing the distribution of the number of petals per sunflower structure, in which the number of petals is representative of the number of **B** particles per **A** particle. The scale bars are 500 nm in (a) and 200 nm in (b).

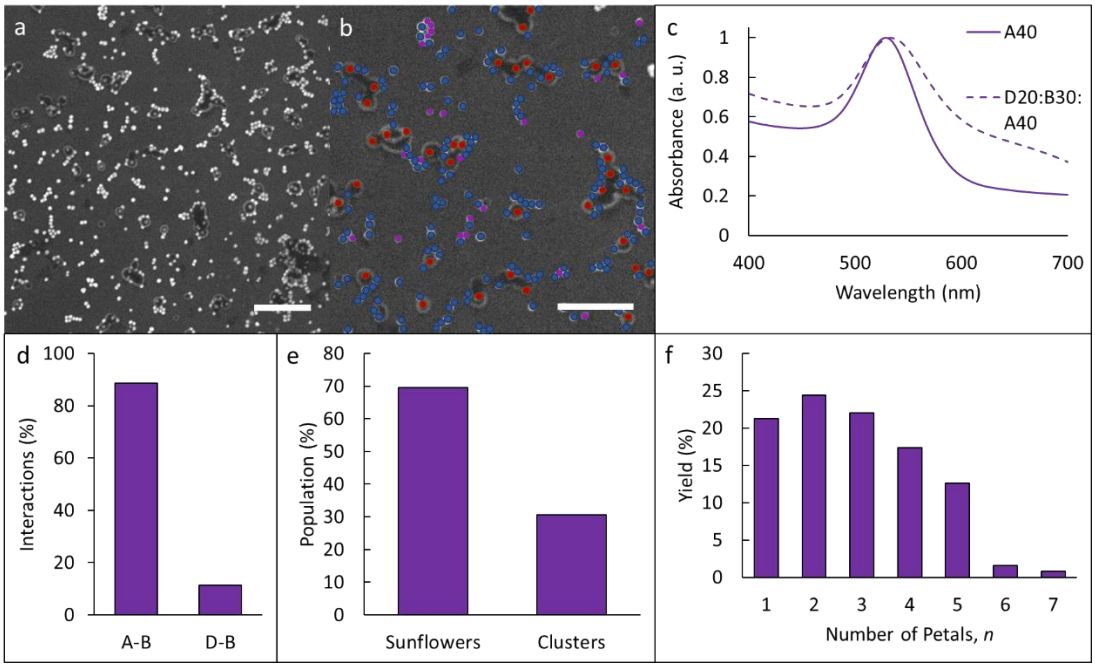

Figure 6.28 The self-assembly of **B2**$_{30}$, **A2**$_{40}$, and **D1**$_{20}$ at a feeding ratio of 2:1:1. (a) SEM image of the assembly structures. (b) Labeled zoomed-in SEM image. The labeled particles are **B2**$_{30}$ (blue), **A2**$_{40}$ (red), and **D1**$_{20}$ (purple). (c) UV-vis absorption spectrum of **A2**$_{40}$ particles (solid) and the assembled particles (dashed). (d) Plot showing the particle–particle interactions between the **B2**$_{30}$ particles and the **A2**$_{40}$ and **D1**$_{20}$ particles. (e) Population statistics of the nanostructures. (f) Plot showing the distribution of the number of petals per sunflower structure in which the number of petals is representative of the number of **B** particles per **A** particle. The scale bars are 800 nm in (a) and 400 nm in (b).

List of My Publications

(1) Lin, X. Y.; Ye, S. S.; Kong, C. C.; Webb, K.; Yi, C. L.; Zhang, S. Y.; Zhang, Q.; Fourkas, J. T.; Nie, Z. H. Polymeric Ligand-Mediated Regioselective Bonding of Plasmonic Nanoplates and Nanospheres. *J. Am. Chem. Soc.* **2020,** *142*, 17282–17286.

(2) Yang, Y; Pei, H. W.; Chen, G. D.; Webb, K.; Martinez-Miranda, L. J.; Lloyd, I. K.; Lu, Z. Y.; Liu, K.; Nie, Z. H. Phase Behaviors of Colloidal Analogues of Bent-Core Liquid Crystals. *Sci. Adv.* **2018**, *4*, 8829.

(3) Yang, Y.; Webb, K.; Liu, Y. J.; Liu, K.; Nie, Z. H. (2017). Synthesis, Self-Assembly, and Applications of Amphiphilic Janus and Triblock Janus Nanoparticle Analogs: Synthesis, Self-Assembly, and Applications; World Scientific, **2017**; pp 233-275. DOI:10.1142/9781786343130_0006.

(4) Yi, C. L.; Zhang, S. Y.; Webb, K. T.; Nie, Z. H. Anisotropic Self-assembly of Hairy Inorganic Nanoparticles. *Acc. Chem. Res*. **2017**, *50*, 12-21.

Bibliography

(1) Yadav, S.; Sharma, A. K.; Kumar, P. Nanoscale Self-Assembly for Therapeutic Drug Delivery. *Front. Bioeng. Biotechnol*. **2020**, *8*, 127.

(2) Yi, C. L.; Zhang, S. Y.; Webb, K. T.; Nie, Z. H. Anisotropic Self-Assembly of Hairy Inorganic Nanoparticles. *Acc. Chem. Res*. **2017**, *50*, 12-21.

(3) Yi, C. L.; Yang, Y. Q.; Liu, B.; He, J.; Nie, Z. H. Polymer-Guided Assembly of Inorganic Nanoparticles. *Chem. Soc. Rev*. **2020**, *49*, 465-508.

(4) Yang, K. K.; Zhang, S. Y.; He, J.; Nie, Z. H. Polymers and Inorganic Nanoparticles: A Winning Combination Towards Assembled Nanostructures for Cancer Imaging and Therapy. *Nano Today* **2021**, *36*, 101046.

(5) Klajn, R.; Bishop, K. J. M.; Grzybowski, B. A. Light-Controlled Self-Assembly of Reversible and Irreversible Nanoparticle Suprastructures. *PNAS* **2007**, *104*, 10305-10309.

(6) Kundu, P. K.; Samanta, D.; Leizrowice, R.; Margulis, B.; Zhao, H.; Borner, M.; Udayabhaskararao, T.; Manna, D.; Klajn, R. Light-Controlled Self-Assembly of Non-Photoresponsive Nanoparticles. *Nat. Chem*. **2015**, *7*, 646-652.

(7) He, H.; Ostwaldt, J.; Hirschhauser, C.; Schmuck, C.; Niemeyer, J. Dual pH-Induced Reversible Self-Assembly of Gold Nanoparticles by Surface Functionalization with Zwitterionic Ligands. *Small* **2020**, *16*, 2001044.

(8) Fan, C. F.; Bian, T.; Shang, L.; Shi, R.; Wu, L. Z.; Tung, C. H.; Zhang, T. R. pH-Responsive Reversible Self-Assembly of Gold Nanoparticles into Nanovesicles. *Nanoscale* **2016**, *8*, 3923-3925.

(9) Gerstner, D.; Kraus, T. Rapid Nanoparticle Self-Assembly at Elevated Temperatures. *Nanoscale* **2018**, *10*, 8009-8013.

(10) Chovnik, O.; Balgley, R.; Goldman, J. R.; Klajn, R. Dynamically Self-Assembling Carriers Enable Guiding of Diamagnetic Particles by Weak Magnets. *J. Am. Chem. Soc*. **2012**, *134*, 19564-19567.

(11) Quan, Z. W.; Xu, H. W.; Wang, C. Y.; Wen, X. D.; Wang, Y. X.; Zhu, J. L.; Li, R. P.; Sheehan, C. J.; Wang, Z. W.; Smilgies, D. M.; Luo, Z. P.; Fang, J. Y. Solvent-Mediated Self-Assembly of Nanocube Superlattices. *J. Am. Chem. Soc*. **2014**, *136*, 1352-1359.

(12) Nie, Z. H.; Fava, D.; Kumacheva, E.; Zhou, S.; Walker, G. C.; Rubinstein, M. Self-Assembly of Metal–Polymer Analogues of Amphiphilic Triblock Copolymers. *Nat. Mater*. **2007**, *6*, 609-614.

(13) Iqbal, M. Z.; Ali, I.; Khan, W. S.; Kong, X. D.; Dempsey, E. Reversible Self-Assembly of Gold Nanoparticles in Response to External Stimuli. *Materials & Design* **2021**, *205*, 109694.

(14) Zhang, L.; Dai, L. W.; Rong, Y.; Liu, Z. Z.; Tong, D. Y.; Huang, Y. J.; Chen, T. Light-Triggered Reversible Self-Assembly of Gold Nanoparticle Oligomers for Tunable SERS. *Langmuir* **2015**, *31*, 1164-1171.

(15) Wei, Y. H.; Han, S. B.; Kim, J.; Soh, S. L.; Grzybowski, B. A. Photoswitchable Catalysis Mediated by Dynamic Aggregation of Nanoparticles. *J. Am. Chem. Soc*. **2010**, *132*, 11018-11020.

(16) Si, S.; Raula, M.; Paira, T. K.; Mandal, T. K. Reversible Self-Assembly of Carboxylated Peptide-Functionalized Gold Nanoparticles Driven by Metal-Ion Coordination. *ChemPhysChem* **2008**, *9*, 1578-1584.

(17) Kalsan, A. M.; Fialkowski, M.; Paszewski, M.; Smoukov, S. K.; Bishop, K. J. M.; Grzybowski, B. A. Electrostatic Self-Assembly of Binary Nanoparticle Crystals with a Diamond-Like Lattice. *Science* **2006**, *312*, 420-424.

(18) Bian, T.; Gardin, A.; Gemen, J.; Houben, L.; Perego, C.; Lee, B. D.; Elad, N.; Chu, Z. L.; Pavan, G. M.; Klajn, R. Electrostatic Co-Assembly of Nanoparticles with Oppositely Charged Small Molecules into Static and Dynamic Superstructures. *Nat. Chem*. **2021**, *13*, 940-949.

(19) Lin, G. H.; Chee, S. W.; Raj, S.; Kral, P.; Mirsaidov, U. Linker-Mediated Self-Assembly Dynamics of Charged Nanoparticles. *ACS Nano* **2016**, *10*, 7443-7450.

(20) Shiraishi, Y.; Shirakawa, E.; Tanaka, K.; Sakamoto, H.; Ichikawa, S.; Hirai, T. Spiropyran-Modified Gold Nanoparticles: Reversible Size Control of Aggregates by UV and Visible Light Irradiations. *ACS Appl. Mater. Interfaces* **2014**, *6*, 7554-7562.

(21) Chen, Q.; Yan, J.; Zhang, J.; Bae, S. C.; Granick, S. Janus and Multiblock Colloidal Particles. *Langmuir* **2012**, *28*, 13555-13561.

(22) Chen, Q.; Bae, S. C.; Granick, S. Staged Self-Assembly of Colloidal Metastructures. *J. Am. Chem. Soc*. **2012**, *134*, 11080-11083.

(23) Chen, Q.; Bae, S. C.; Granick, S. Directed Self-Assembly of a Colloidal Kagome Lattice. *Nature* **2011**, *469*, 381-384.

(24) Yubo, W.; Quinsaat, J. E. Q.; Ono, T.; Maeki, M.; Tokeshi, M.; Isono, T.; Tajima, K.; Satoh, T.; Sato, S. I.; Miura, Y.; Yamamoto, T. Enhanced Dispersion Stability of Gold Nanoparticles by the Physisorption of Cyclic Poly(ethylene glycol). *Nat. Commun*. **2020**, *11*, 6089.

(25) Yang, K. K.; Liu, Y. J.; Liu, Y.; Zhang, Q.; Kong, C. C.; Yi. C. L.; Zhou, Z. J.; Wang, Z. T.; Zhang, G. F.; Zhang, Y.; Khashab, N. M.; Chen, X. Y.; Nie, Z. H. Cooperative Assembly of Magneto-Nanovesicles with Tunable Wall Thickness and Permeability for MRI-Guided Drug Delivery. *J. Am. Chem. Soc*. **2018**, *140*, 4666-4677.

(26) Abed, A.; Derakhshan, M.; Karimi, M.; Shirazinia, M.; Mahjoubin-Tehran, M.; Homayonfal, M.; Hamblin, M. R.; Mirzaei, S. A.; Soleimanpour, H.; Dehghani, S.; Dehkordi, F. F.; Mirzaei, H. Platinum Nanoparticles in Biomedicine: Preparation, Anti-Cancer Activity, and Drug Delivery Vehicles. *Front. Pharmacol*. **2022**, *13*, 797804.

(27) Xie, P.; Wang, Y. S.; Wei, D. S.; Zhang, L. P.; Zhang, B.; Xiao, H. H.; Song, H. Q.; Mao, X. Z. Nanoparticle-based Drug Delivery Systems with Platinum Drugs for Overcoming Cancer Drug Resistance. *J. Mater. Chem. B* **2021**, *9*, 5173–5194.

(28) Gu, T. X; Wang, Y.; Lu, Y. H.; Cheng, L.; Feng, L. Z.; Zhang, H.; Li, X.; Han, G. R.; Liu, Z. Platinum Nanoparticles to Enable Electrodynamic Therapy for Effective Cancer Treatment. *Adv. Mater*. **2019**, *31*, 1806803.

(29) Mastronardi, V.; Magliocca, E.; Gullon S. J.; Brescia, R.; Pompa, P. P.; Miller, T. S.; Moglianetti, M. Ultrasmall, Coating-Free, Pyramidal Platinum Nanoparticles for High Stability Fuel Cell Oxygen Reduction. *ACS Appl. Mater. Interfaces* **2022**, *14*, 36570-36581.

(30) Xiao, F.; Wang, Y.; Xu, G. L.; Yang, F.; Zhu, S. Q.; Sun, C. J.; Cui, Y. D.; Xu, Z. W.; Zhao, Q. L.; Jang, J. H.; Qiu, X. Y.; Liu, E.; Drisdell, W. S.; Wei, Z. D.; Gu, M.; Amine, K.; Shao, M. H. Fe–N–C Boosts the Stability of Supported Platinum Nanoparticles for Fuel Cells. *J. Am. Chem. Soc*. **2022**, *144*, 20372-20384.

(31) Wang. L.; Liu, Y. J.; He, J.; Hourwitz, M. J.; Yang, Y. L.; Fourkas, J. T.; Han, X. J.; Nie, Z. H. Continuous Microfluidic Self-Assembly of Hybrid Janus-Like Vesicular Motors: Autonomous Propulsion and Controlled Release. *Small* **2015**, *11*, 3762-3767.

(32) Willets, K. A.; Van Duyne, R. P. Localized Surface Plasmon Resonance Spectroscopy and Sensing. *Annu. Rev. Phys. Chem*. **2007**, *58*, 267–297.

(33) Pellas, V.; Hu, D.; Mazouzi, Y.; Mimoun, Y.; Blanchard, J.; Guibert, C.; Salmain, M.; Boujday, S. Gold Nanorods for LSPR Biosensing: Synthesis, Coating by Silica, and Bioanalytical Applications. *Biosensors* **2020**, *10*, 146.

(34) Sherry, L. J.; Jin, R. C.; Mirkin, C. A.; Schatz, G. C.; Van Duyne, R. P. Localized Surface Plasmon Resonance Spectroscopy of Single Silver Triangular Nanoprisms. *Nano Lett*. **2006**, *6*, 2060-2065.

(35) Huang, X. L.; Liu, Y. J; Barr, J.; Song, J.; He, Z. M.; Wang, Y. M.; Nie, Z. H.; Xiong, Y. H.; Chen, X. Y. Controllable Self-Assembled Plasmonic Vesicle-Based Three-Dimensional SERS Platform for Picomolar Detection of Hydrophobic Contaminants. *Nanoscale* **2018**, *10*, 13202-13211.

(36) Liu, Y. J.; He, J.; Yang, K. K.; Yi, C. L.; Liu, Y.; Nie, L. M.; Khashab, N. M.; Chen, X. Y.; Nie, Z. H. Folding Up of Gold Nanoparticle Strings into Plasmonic Vesicles for Enhanced Photoacoustic Imaging. *Angew. Chem. Int. Ed*. **2015**, *54* 15916-15920.

(37) Song, K.; Huang, P.; Yi, C. L.; Ning, B.; Hu, S.; Nie, L. M.; Chen, X. Y.; Nie, Z. H. Colorimetric and Photoacoustic Imaging for Latent Fingerprints Visualization. *ACS Nano* **2015**, *9*, 12344-12348.

(38) Narayanan, R.; El-Sayed, M. A. Shape-Dependent Catalytic Activity of Platinum Nanoparticles in Colloidal Solution. *Nano Lett.* **2004**, *4*, 1343-1348.

(39) Zhao, D. W.; Yu, M. Y.; Zheng, L. L.; Li, M.; Dai, S. J.; Chen, D. C.; Lee, T. C.; Yun, D. Q. Enhanced Efficiency and Stability of Planar Perovskite Solar Cells Using a Dual Electron Transport Layer of Gold Nanoparticles Embedded in Anatase TiO_2 Films. *ACS Appl. Energy Mater*. **2020**, *3*, 9568-9575.

(40) Yang, K. K.; Liu, Y. J.; Wang, Y.; Ren, Q. L.; Guo, H. Y.; Matson, J. B.; Chen, X. Y.; Nie, Z. H. Enzyme-induced in Vivo Assembly of Gold Nanoparticles for Imaging-Guided Synergistic Chemo-Photothermal Therapy of Tumor. *Biomaterials* **2019**, *223*, 119460.

(41) Zheng, D.; Yang, K. K; Nie, Z. H. Engineering Heterogeneity of Precision Nanoparticles for Biomedical Delivery and Therapy. *View* **2021**, *2*, 20200067.

(42) Liu, Y. J; Yin, J. J.; Nie, Z. H. Harnessing the Collective Properties of Nanoparticle Ensembles for Cancer Theranostics. *Nano Research* **2014**, *7*, 1719-1730.

(43) Tang, Y.; Ji, Y. J.; Yi, C. L.; Cheng, D.; Wang, B.; Fu, Y.; Xu, Y. F.; Qian, X. H.; Choonara, Y. E.; Pillay, V.; Zhu, W. P.; Liu, Y. N.; Nie, Z. H. Self-Accelerating H_2O_2-Responsive Plasmonic Nanovesicles for Synergistic Chemo/Starving Therapy of Tumors. *Theranostics* **2020**, *10*, 8691-8704.

(44) Dukes, D.; Li, Y.; Lewis, S.; Benicewicz, B.; Schadler, L.; Kumar, S. K. Conformational Transitions of Spherical Polymer Brushes: Synthesis, Characterization, and Theory. *Macromolecules* **2010**, *43*, 1564-1570.

(45) Diez-Pascual. A. M. Surface Engineering of Nanomaterials with Polymers, Biomolecules, and Small Ligands for Nanomedicine. *Materials* **2022**, *15*, 3251.

(46) Perez Cardenas, M. T.; Kong, C. C.; He, J.; Litvin, S.; Meyerson, M. L.; Nie, Z. H. Immobilized Seed-Mediated Growth of Two-Dimensional Array of Metallic Nanocrystals with Asymmetric Shapes. *ACS Nano* **2018**, *12*, 1107-1119.

(47) Lin, X. Y.; Liu, Y. J.; Lin, M. H; Zhang, Q.; Nie, Z. H. Synthesis of Circular and Triangular Gold Nanorings with Tunable Optical Properties. *Chem. Commun.* **2017**, *53*, 10765-10767.

(48) Moffitt, M. G. Self-Assembly of Polymer Brush-Functionalized Inorganic Nanoparticles: From Hairy Balls to Smart Molecular Mimics. *J. Phys. Chem. Lett*. **2013**, *4*, 3654-3666.

(49) Choueiri, R. M.; Galati, E.; Therien-Aubin, H.; Klinkova, A.; Larin, E. M.; Querejeta-Fernandez, A.; Han, L.; Xin, H. L.; Gang, O.; Zhulina, E. B.; Rubinstein, M.; Kumacheva, E. Surface Patterning of Nanoparticles with Polymer Patches. *Nature* **2016**, *538*, 79-83.

(50) Galati, E.; Tebbe, M.; Querejeta-Fernandez, A.; Xin, H. L.; Gang, O.; Zhulina, E. B.; Kumacheva, E. Shape-Specific Patterning of Polymer-Functionalized Nanoparticles. *ACS Nano* **2017**, *11*, 4995-5002.

(51) Song, J. B.; Cheng, L.; Liu, A. P.; Yin, J.; Kuang, M.; Duan, H. W. Plasmonic Vesicles of Amphiphilic Gold Nanocrystals: Self-Assembly and External-Stimuli-Triggered Destruction. *J. Am. Chem. Soc.* **2011**, *133*, 10760-10763.

(52) Hu, J. M.; Wu, T.; Zhang, G. Y.; Liu, S. Y. Efficient Synthesis of Single Gold Nanoparticle Hybrid Amphiphilic Triblock Copolymers and Their Controlled Self-Assembly. *J. Am. Chem. Soc.* **2012**, *134*, 7624-7627.

(53) Song, J. B.; Pu, L.; Zhou, J. J.; Duan, B.; Duan, H. W. Biodegradable Theranostic Plasmonic Vesicles of Amphiphilic Gold Nanorods. *ACS Nano* **2013**, *7*, 9947-9960.

(54) He, J.; Liu, Y. J.; Babu, T.; Wei, Z. J.; Nie, Z. H. Self-Assembly of Inorganic Nanoparticle Vesicles and Tubules Driven by Tethered Linear Block Copolymers. *J. Am. Chem. Soc.* **2012**, *134*, 11342-11345.

(55) He, J.; Huang, X. L.; Li, Y. C.; Liu, Y. J.; Babu, T.; Aronova, M. A.; Wang, S. J.; Lu, Z. Y.; Chen, X. Y.; Nie, Z. H. Self-Assembly of Amphiphilic Plasmonic Micelle-Like Nanoparticles in Selective Solvents. *J. Am. Chem. Soc.* **2013**, *135*, 7974-7984.

(56) Zhao, B.; Zhu, L. Mixed Polymer Brush-Grafted Particles: A New Class of Environmentally Responsive Nanostructured Materials. *Macromolecules* **2009**, *42*, 9369-9383.

(57) Li, M.; Pester, C. W. Mixed Polymer Brushes for "Smart" Surfaces. *Polymers* **2020**, *12*, 1553.

(58) Tang, S.; Lo, T. Y.; Horton, J. M.; Bao, C. H.; Tang, P.; Qiu, F.; Ho, R. M.; Zhao, B.; Zhu, L. Direct Visualization of Three-Dimensional Morphology in Hierarchically Self-Assembled Mixed Poly(tert-butyl acrylate)/Polystyrene Brush-Grafted Silica Nanoparticles. *Macromolecules* **2013**, *46*, 6575-6584.

(59) Bao, C. H.; Tang, S.; Wright, R. A. E.; Tang, P.; Qiu, F.; Zhu, L.; Zhao, B. Effect of Molecular Weight on Lateral Microphase Separation of Mixed Homopolymer Brushes Grafted on Silica Particles. *Macromolecules* **2014**, *47*, 6824-6835.

(60) Fox, T. L.; Tang, S.; Horton, J. M.; Holdaway, H. A.; Zhao, B.; Zhu, L.; Stewart, P. L. In Situ Characterization of Binary Mixed Polymer Brush-Grafted Silica Nanoparticles in Aqueous and Organic Solvents by Cryo-Electron Tomography. *Langmuir* **2015**, *31*, 8680-8688.

(61) Tang, S.; Fox, T. L.; Lo, T. Y.; Horton, J. M.; Ho, R. M.; Zhao, B.; Stewart, P. L.; Zhu, L. Environmentally Responsive Self-Assembly of Mixed Poly(tert-butyl acrylate)–polystyrene Brush-Grafted Silica Nanoparticles in Selective Polymer Matrices. *Soft Matter* **2015**, *11*, 5501-5512.

(62) Galati, E.; Tao, H.; Tebbe, M.; Ansari, R.; Rubinstein, M.; Zhulina, E. B.; Kumacheva, E. Helicoidal Patterning of Nanorods with Polymer Ligands. *Angew. Chem. Int. Ed*. **2019**, *59*, 3123-3127.

(63) Rossner, C.; Zhulina, E. B.; Kumacheva, E. Staged Surface Patterning and Self-Assembly of Nanoparticles Functionalized with End-Grafted Block Copolymer Ligands. *Angew. Chem. Int. Ed*. **2019**, *58*, 9269-9274.

(64) Yu, L. X.; Shi, R.; Qian, H. J.; Lu, Z. Y. Versatile Fabrication of Patchy Nanoparticles via Patterning of Grafted Diblock Copolymers on NP Surface. *Phys. Chem. Chem. Phys*. **2019**, *21*, 1417-1427.

(65) Zhou, Y.; Ma, X. D.; Zhang, L. S.; Lin, J. P. Directed Assembly of Functionalized Nanoparticles with Amphiphilic Diblock Copolymers. *Phys. Chem. Chem. Phys*. **2017**, *19*, 18757-18766.

(66) Gong, M. Q.; Yu, Q. Y.; Wang, C. L.; Wang, R. Simulating Surface Patterning of Nanoparticles by Polymers via Dissipative Particle Dynamics Method. *Langmuir* **2019**, *35*, 5534-5540.

(67) Wang, D. Y.; Mohwald, H. Template-Directed Colloidal Self-Assembly - The Route to 'Top-Down' Nanochemical Engineering. *J. Mater. Chem*. **2004**, *14*, 459-468.

(68) Kinge, S.; Crego-Calama, M.; Reinhoudt, D. N. Self-Assembling Nanoparticles at Surfaces and Interfaces. *ChemPhysChem* **2008**, *9*, 20-42.

(69) Hanske, C.; Hill, E. H.; Vila-Liarte, D.; Gonzalez-Rubio, G.; Matricardi, C.; Mihi, A.; Liz-Marzan, L. M. Solvent-Assisted Self-Assembly of Gold Nanorods into Hierarchically Organized Plasmonic Mesostructures. *ACS Appl.Mater. Interfaces* **2019**, *11*, 11763-11771.

(70) Hamon, C.; Novikov, S.; Scarabelli, L.; Basabe-Desmonts, L.; Liz-Marzan, L. M. Hierarchical Self-Assembly of Gold Nanoparticles into Patterned Plasmonic Nanostructures. *ACS Nano* **2014**, *8*, 10694-10703.

(71) Zhang, R.; Lee, B. J.; Stafford, C. M.; Douglas, J. F.; Dobrynin, A. V.; Bockstaller, M. R.; Karim, A. Entropy-Driven Segregation of Polymer-Grafted Nanoparticles Under Confinement. *PNAS* **2017**, *114*, 2462-2467.

(72) Flauraud, V.; Mastrangeli, M.; Bernasconi, G. D.; Butet, J.; Alexander, D. T. L.; Shahrabi, E.; Martin, O. J. F.; Brugger, J. Nanoscale Topographical Control of Capillary Assembly of Nanoparticles. *Nat. Nanotechnol*. **2017**, *12*, 73-80.

(73) Liang, R. J.; Xu, J. P.; Deng, R. H.; Wang, K.; Liu, S. Q.; Li, J. Y.; Zhu, J. T. Assembly of Polymer-Tethered Gold Nanoparticles under Cylindrical Confinement. *ACS Macro Lett.* **2014**, *3*, 486-490.

(74) Wang, K.; Jin, S. M.; Xu, J. P.; Liang, R. J.; Shezad, K.; Xue, Z. G.; Xie, X. L.; Lee, E.; Zhu, J. T. Electric-Field-Assisted Assembly of Polymer-Tethered Gold Nanorods in Cylindrical Nanopores. *ACS Nano* **2016**, *10*, 4954-4960.

(75) Correa-Duarte, M. A.; Perez-Juste, J.; Sanchez-Iglesias, A.; Giersig, M.; Liz-Marzan, L. M. Aligning Au Nanorods by Using Carbon Nanotubes as Templates. *Angew. Chem. Int. Ed*. **2005**, *44*, 4375-4378.

(76) Wang, P. P.; Qiao, Q.; Zhu, Y. M.; Ouyang, M. Colloidal Binary Supracrystals with Tunable Structural Lattices. *J. Am. Chem. Soc*. **2018**, *140*, 9095-9098.

(77) Deng, R. H.; Liang, F. X.; Qu, X. Z.; Wang, Q.; Zhu, J. T.; Yang, Z. Z. Diblock Copolymer Based Janus Nanoparticles. *Macromolecules* **2015**, *48*, 750-755.

(78) Deng, R. H.; Li, H.; Liang, F. X.; Zhu, J. T.; Li, B. H.; Xie, X. L.; Yang, Z. Z. Soft Colloidal Molecules with Tunable Geometry by 3D Confined Assembly of Block Copolymers. *Macromolecules* **2015**, *48*, 5855-5860.

(79) Yan, N.; Zhang, Y.; He, Y.; Zhu, Y. T.; Jiang, W. Controllable Location of Inorganic Nanoparticles on Block Copolymer Self-Assembled Scaffolds by Tailoring the Entropy and Enthalpy Contributions. *Macromolecules* **2017**, *50*, 6771-6778.

(80) Yang, Y.; Wang, Y. L.; Jin, S. M.; Xu, J. P.; Hou, Z. Y.; Ren, J. L.; Wang, K.; Lee, E.; Zhang, L. B.; Zhang, Y. F.; Zhu, J. T. 3D Confined Assembly of Polymer-Tethered Gold Nanoparticles into Size-Segregated Structures. *Mater. Chem. Front*. **2019**, *3*, 209-215.

(81) Leibler, L. Theory of Microphase Separation in Block Copolymers. *Macromolecules* **1980**, *13*, 1602-1617.

(82) Matsen, M. W.; Bates, F. S. Unifying Weak- and Strong-Segregation Block Copolymer Theories. *Macromolecules* **1996**, *29*, 1091-1098.

(83) Forster, S.; Antonietti, M. Amphiphilic Block Copolymers in Structure-Controlled Nanomaterial Hybrids. *Adv. Mater.* **1998**, *10*, 195-217.

(84) Kim, H. C.; Park, S. M.; Hinsberg, W. D. Block Copolymer Based Nanostructures: Materials, Processes, and Applications to Electronics. *Chem. Rev*. **2010**, *110*, 146-177.

(85) Tan, K. W.; Jung, B. K.; Werner, J. G.; Rhoades, E. R.; Thompson, M. O.; Wiesner, U. Transient Laser Heating Induced Hierarchical Porous Structures from Block Copolymer–Directed Self-Assembly. *Science* **2015**, *349*, 54-58.

(86) Sai, H.; Tan, K. W.; Hur, K.; Asenath-Smith, E.; Hovden, R.; Jiang, Y.; Riccio, M.; Muller, D. A.; Elser, V.; Estroff, L. A.; Gruner, S. M.; Wiesner, U. Hierarchical Porous Polymer Scaffolds from Block Copolymers. *Science* **2013**, *341*, 530-534.

(87) Cowman, C. D.; Padgett, E.; Tan, K. W.; Hovden, R.; Gu, Y. B.; Andrejevic, N.; Muller, D.; Coates, G. W.; Wiesner, U. Multicomponent Nanomaterials with Complex Networked Architectures from Orthogonal Degradation and Binary Metal Backfilling in ABC Triblock Terpolymers. *J. Am. Chem. Soc*. **2015**, *137*, 6026-6033.

(88) Fogg, D. E.; Radzilowski, L. H.; Dabbousi, B. O.; Schrock, R. R.; Thomas, E. L.; Bawendi, M. G. Fabrication of Quantum Dot-Polymer Composites: Semiconductor Nanoclusters in Dual-Function Polymer Matrices with Electron-Transporting and Cluster-Passivating Properties. *Macromolecules* **1997**, *30*, 8433-8439.

(89) Tsutsumi, K.; Funaki, Y.; Hirokawa, Y.; Hashimoto, T. Selective Incorporation of Palladium Nanoparticles into Microphase-Separated Domains of Poly(2-vinylpyridine)-block-polyisoprene. *Langmuir* **1999**, *15*, 5200-5203.

(90) Li, Q. F.; He. J. B.; Glogowski, E.; Li, X. F.; Wang, J.; Emrick, T.; Russell, T. P. Responsive Assemblies: Gold Nanoparticles with Mixed Ligands in Microphase Separated Block Copolymers. *Adv. Mater*. **2008**, *20*, 1462-1466.

(91) Thompson, R. B.; Ginzburg, V. V.; Matsen, M. W.; Balazs, A. C. Predicting the Mesophases of Copolymer-Nanoparticle Composites. *Science* **2001**, *292*, 2469-2472.

(92) Kang, H.; Detcheverry, F. A.; Mangham, A. N.; Stoykovich, M. P.; Daoulas, K. C.; Hamers, R. J.; Muller, M.; de Pablo, J. J.; Nealey, P. F. Hierarchical Assembly of Nanoparticle Superstructures from Block Copolymer-Nanoparticle Composites. *Phys. Rev. Lett*. **2008**, *100*, 148303.

(93) Lee, J. Y.; Thompson, R. B.; Jasnow, D.; Balazs, A. C. Entropically Driven Formation of Hierarchically Ordered Nanocomposites. *Phys. Rev. Lett*. **2002**, *89*, 1555031.

(94) Kim, B. J.; Fredrickson, G. H.; Kramer, E. J. Effect of Polymer Ligand Molecular Weight on Polymer-Coated Nanoparticle Location in Block Copolymers. *Macromolecules* **2008**, *41*, 436-447.

(95) Lin, Y.; Daga, V. K.; Anderson, E. R.; Gido, S. P.; Watkins, J. J. Nanoparticle-Driven Assembly of Block Copolymers: A Simple Route to Ordered Hybrid Materials. *J. Am. Chem. Soc.* **2011**, *133*, 6513-6516.

(96) Lin, Y.; Boker, A.; He, J. B.; Sill, K.; Xiang, H. Q.; Abetz, C.; Li, X. F.; Wang, J.; Emrick, T.; Long, S.; Wang, Q.; Balazs, A.; Russell, T. P. Self-Directed Self-Assembly of Nanoparticle/Copolymer Mixtures. *Nature* **2005**, *434*, 55-59.

(97) Kao, J.; Thorkelsson, K.; Bai, P.; Zhang, Z.; Sun, C.; Xu, T. Rapid Fabrication of Hierarchically Structured Supramolecular Nanocomposite Thin Films in One Minute. *Nat. Commun*. **2014**, *5*, 4053.

(98) Kao, J.; Bai, P.; Lucas, J. M.; Alivisatos, A. P.; Xu, T. Size-Dependent Assemblies of Nanoparticle Mixtures in Thin Films. *J. Am. Chem. Soc*. **2013**, *135*, 1680-1683.

(99) Chiu, J. J.; Kim, B. J.; Kramer, E. J.; Pine, D. J. Control of Nanoparticle Location in Block Copolymers. *J. Am. Chem. Soc*. **2005**, *127*, 5036-5037.

(100) Nepal, D.; Onses, M. S.; Park, K. W.; Jespersen, M.; Thode, C. J.; Nealey, P. F.; Vaia, R. A. Control over Position, Orientation, and Spacing of Arrays of Gold Nanorods Using Chemically Nanopatterned Surfaces and Tailored Particle–Particle–Surface Interactions. *ACS Nano* **2012**, *6*, 5693-5701.

(101) Nakano, T.; Kawaguchi, D.; Matsushita, Y. Anisotropic Self-Assembly of Gold Nanoparticle Grafted with Polyisoprene and Polystyrene Having Symmetric Polymer Composition. *J. Am. Chem. Soc*. **2013**, *135*, 6798-6801.

(102) Gao, B.; Arya, G.; Tao, A. R. Self-Orienting Nanocubes for the Assembly of Plasmonic Nanojunctions. *Nat. Nanotechnol*. **2012**, *7*, 433-437.

(103) Gao, B.; Alvi, Y.; Li, V.; Tao, A. R. Polymer-Directed Assembly of Colloidal Nanoparticle Heterojunctions. *CrystEngComm*. **2014**, *16*, 9434-9440.

(104) Gao, B.; Alvi, Y.; Rosen, D.; Lav, M.; Tao, A. R. Designer Nanojunctions: Orienting Shaped Nanoparticles within Polymer Thin-Film Nanocomposites. *Chem. Commun*. **2013**, *49*, 4382-4384.

(105) Jiang, G. Q.; Hore, M. J. A.; Gam, S.; Composto, R. J. Gold Nanorods Dispersed in Homopolymer Films: Optical Properties Controlled by Self-Assembly and Percolation of Nanorods. *ACS Nano* **2012**, *6*, 1578-1588.

(106) Liu, Y.; Rafailovich, H.; Sokolov, J.; Schwarz, A.; Zhong, X.; Eisenberg, A.; Kramer, E. J.; Sauer, B. B.; Satija, S. Wetting Behavior of Homopolymer Films on Chemically Similar Block Copolymer Surfaces. *Phys. Rev. Lett*. **1994**, *73*, 440-443.

(107) Kumar, S. K.; Jouault, N.; Benicewicz, B.; Neely, T. Nanocomposites with Polymer Grafted Nanoparticles. *Macromolecules* **2013**, *46*, 3199-3214.

(108) Akcora, P.; Liu, H. J.; Kumar, S. K.; Moll, J.; Li, Y.; Benicewicz, B. C.; Schadler, L. S.; Acehan, D.; Panagiotopoulis, A. Z.; Pryamitsyn, V.; Ganesan, V.; Ilavsky, J.; Thiyagarajan, P.; Colby, R. H.; Douglas, J. F. Anisotropic Self-Assembly of Spherical Polymer-Grafted Nanoparticles. *Nature Mater*. **2009**, *8*, 354-359.

(109) Meng, D.; Kumar, S. K.; Lane, J. M. D.; Grest, G. S. Effective Interactions Between Grafted Nanoparticles in a Polymer Matrix. *Soft Matter* **2012**, *8*, 5002-5010.

(110) Li, W. K.; Liu, S. Q.; Deng, R. H.; Wang, J. Y.; Nie, Z. H.; Zhu, J. T. A Simple Route to Improve Inorganic Nanoparticles Loading Efficiency in Block Copolymer Micelles. *Macromolecules* **2013**, *46*, 2282-2291.

(111) Li, W. K.; Liu, S. Q.; Deng, R. H.; Zhu, J. T. Encapsulation of Nanoparticles in Block Copolymer Micellar Aggregates by Directed Supramolecular Assembly. *Angew. Chem. Int. Ed*. **2011**, *50*, 5865-5868.

(112) Li, W. K.; Zhang, P.; Dai, M.; He, J.; Babu, T.; Xu, Y. L.; Deng, R. H.; Liang, R. J.; Lu, M. H.; Nie, Z. H.; Zhu, J. T. Ordering of Gold Nanorods in Confined Spaces by Directed Assembly. *Macromolecules* **2013**, *46*, 2241-2248.

(113) Li, W. K.; Wang, K.; Zhang, P.; He, J.; Xu, S. Y.; Liao, Y. G.; Zhu, J. T.; Xie, X. L.; Nie, Z. H. Self-Assembly of Shaped Nanoparticles into Free-Standing 2D and 3D Superlattices. *Small* **2016**, *12*, 499-505.

(114) Sanwaria, S.; Horechyy, A.; Wolf, D.; Chu, C. Y.; Chen, H. L.; Formanek, P.; Stamm, M.; Srivastava, R.; Nandan, B. Helical Packing of Nanoparticles Confined in Cylindrical Domains of a Self-Assembled Block Copolymer Structure. *Angew. Chem. Int. Ed*. **2014**, *53*, 9090-9093.

(115) Pickett, G. T.; Gross, M.; Okuyama, H. Spontaneous Chirality in Simple Systems. *Phys. Rev. Lett.* **2000**, *85*, 3652.

(116) Khanal, B. P.; Zubarev, E. R. Rings of Nanorods. *Angew. Chem. Int. Ed*. **2007**, *46*, 2195-2198.

(117) Maillard, M.; Motte, L.; Ngo, A. T.; Pileni, M. P. Rings and Hexagons Made of Nanocrystals: A Marangoni Effect. *J. Phys. Chem. B* **2000**, *104*, 11871-11877.

(118) Ohara, P. C.; Heath, J. R.; Gelbart, W. M. Self-Assembly of Submicrometer Rings of Particles from Solutions of Nanoparticles. *Angew. Chem. Int. Ed*. **1997**, *36*, 1078-1080.

(119) Bunz. U. H. F. Breath Figures as a Dynamic Templating Method for Polymers and Nanomaterials. *Adv. Mater*. **2006**, *18*, 973-989.

(120) Si, K. J.; Sikdar, D.; Chen, Y.; Eftekhari, F.; Xu, Z. Q.; Tang, Y.; Xiong, W.; Guo, P. Z.; Zhang, S.; Lu, Y. R.; Bao, Q. L.; Zhu, W. R.; Premaratne, M.; Cheng, W. L. Giant Plasmene Nanosheets, Nanoribbons, and Origami. *ACS Nano* **2014**, *8*, 11086-11093.

(121) Dong, D.; Yap, L. W.; Smilgies, D. M.; Si, K. J.; Shi, Q. Q.; Cheng, W. L. Two-Dimensional Gold Trisoctahedron Nanoparticle Superlattice Sheets: Self-Assembly, Characterization and Immunosensing Applications. *Nanoscale* **2018**, *10*, 5065-5071.

(122) Rao, S. Y.; Si, K. J.; Yap. L. M.; Xiang, Y.; Cheng, W. L. Free-Standing Bilayered Nanoparticle Superlattice Nanosheets with Asymmetric Ionic Transport Behaviors. *ACS Nano* **2015**, *9*, 11218-11224.

(123) Ohno, K.; Morinaga, T.; Takeno, S.; Tsujii, Y.; Fukuda, T. Suspensions of Silica Particles Grafted with Concentrated Polymer Brush: Effects of Graft Chain Length on Brush Layer Thickness and Colloidal Crystallization. *Macromolecules* **2007**, *40*, 9143-9150.

(124) Ye, X. C.; Zhu, C. H.; Ercius, P.; Raja, S. N.; He, B.; Jones, M. R.; Hauwiller, M. R.; Liu, Y.; Xu, T.; Alivisatos, A. P. Structural Diversity in Binary Superlattices Self-Assembled from Polymer-Grafted Nanocrystals. *Nat. Commun*. **2015**, *6*, 10052.

(125) Gu. X. W.; Ye, X. C.; Koshy, D. M.; Vachhani, S.; Hosemann, P.; Alivisatos, A. P. Tolerance to Structural Disorder and Tunable Mechanical Behavior in Self-Assembled Superlattices of Polymer-Grafted Nanocrystals. *PNAS* **2017**, *114*, 2836-2841.

(126) Pickering, S. U. CXCVI.-Emulsions. *J. Chem. Soc., Trans*. **1907**, *91*, 2001-2021.

(127) Ramsden, W. Separation of Solids in the Surface-Layers of Solutions and 'Suspensions' (Observations on Surface-Membranes, Bubbles, Emulsions, and Mechanical Coagulation).-Preliminary Account. *Proceedings of the Royal Society of London*. **1903**, *72*, 156-164.

(128) de Carvalho-Guimaraes, F. B.; Correa, K. L.; de Souza, T. P.; Amado, J. R. R.; Ribeiro-Costa, R. M.; Silva-Junior, J. O. C. A Review of Pickering Emulsions: Perspectives and Applications. *Pharmaceuticals* **2022**, *15*, 1413.

(129) Pieranski, P. Two-Dimensional Interfacial Colloidal Crystals. *Phys. Rev. Lett*. **1980**, *45*, 569.

(130) Lin, Y.; Skaff, H.; Emrick, T.; Dinsmore, A. D.; Russell, T. P. Nanoparticle Assembly and Transport at Liquid-Liquid Interfaces. *Science* **2003**, *299*, 226-229.

(131) Scanlon, M. D.; Smirnov, E.; Stockmann, T. J.; Peljo, P. Gold Nanofilms at Liquid–Liquid Interfaces: An Emerging Platform for Redox Electrocatalysis, Nanoplasmonic Sensors, and Electrovariable Optics. *Chem. Rev*. **2018**, *118*, 3722-3751.

(132) Ding, T.; Rudrum, A. W.; Herrmann, L. O.; Turek, V.; Baumberg, J. J. Polymer-Assisted Self-Assembly of Gold Nanoparticle Monolayers and Their Dynamical Switching. *Nanoscale* **2016**, *8*, 15864-15869.

(133) Chen, L. B.; Zukoski, C. F.; Ackerson, B. J.; Hanley, H. J. M.; Straty, G. C.; Barker, J.; Glinka, C. J. Structural Changes and Orientational Order in a Sheared Colloidal Suspension. *Phys. Rev. Lett.* **1992**, *69*, 688-691.

(134) Wang, L.; Wang, J. Y. Self-assembly of Colloids Based on Microfluidics. *Nanoscale* **2019**, *11*, 16708-16722.

(135) Zhang, J.; Coulston, R. J.; Jones, S. T.; Geng, J.; Scherman, O. A.; Abell, C. One-Step Fabrication of Supramolecular Microcapsules from Microfluidic Droplets. *Science* **2012**, *335*, 690-694.

(136) Liu, J.; Lan, Y.; Yu, Z.; Tan, C. S. Y.; Parker, R. M.; Abell, C.; Scherman, O. A. Cucurbit[n]uril-Based Microcapsules Self-Assembled within Microfluidic Droplets: A Versatile Approach for Supramolecular Architectures and Materials. *Acc. Chem. Res*. **2017**, *50*, 208-217.

(137) Min, Y. J.; Akbulut, M.; Kristiansen, K.; Golan, Y.; Israelachvili, J. The Role of Interparticle and External Forces in Nanoparticle Assembly. *Nat. Mater*. **2008**, *7*, 527-538.

(138) Sacanna, S.; Pine, D. J. Shape-Anisotropic Colloids: Building Blocks for Complex Assemblies. *Curr. Opin. Colloid Interface Sci*. **2011**, *16*, 96–105.

(139) Glotzer, S. C.; Solomon, M. J. Anisotropy of Building Blocks and Their Assembly into Complex Structures. *Nat. Mater*. **2007**, *6*, 557-562.

(140) Zhang, Z.; Horsch, M. A.; Lamm, M. H.; Glotzer, S. C. Tethered Nano Building Blocks: Toward a Conceptual Framework for Nanoparticle Self-Assembly. *Nano. Lett*. **2003**, *3*, 1341-1346.

(141) Walker, D. A.; Leitsch, E. K.; Nap, R. J.; Szleifer, I.; Grzybowski, B. A. Geometric Curvature Controls the Chemical Patchiness and Self-Assembly of Nanoparticles. *Nat. Nanotechnol*. **2013**, *8*, 676-681.

(142) Kim, A.; Vo, T.; An, H.; Banerjee, P.; Yao, L. H.; Zhou, S.; Kim, C.; Milliron, D. J.; Glotzer, S. C.; Chen, Q. Symmetry-Breaking in Patch Formation on Triangular Gold Nanoparticles by Asymmetric Polymer Grafting. *Nat. Commun*. **2022**, *13*, 6774.

(143) Zubarev, E. R.; Xu, J.; Sayyad, A.; Gibson, J. D. Amphiphilicity-Driven Organization of Nanoparticles into Discrete Assemblies. *J. Am. Chem. Soc*. **2006**, *128*, 15098-15099.

(144) Guo, Y. Y.; Harirchian-Saei, S.; Izumi, C. M. S.; Moffit, M. G. Block Copolymer Mimetic Self-Assembly of Inorganic Nanoparticles. *ACS Nano* **2011**, *5*, 3309-3318.

(145) Coleman, B. R.; Moffit, M. G. Amphiphilic Inorganic Nanoparticles with Mixed Polymer Brush Layers of Variable Composition: Bridging the Paradigms of Block Copolymer and Nanoparticle Self-Assembly. *Chem. Mater*. **2018**, *30*, 2474-2482.

(146) Klinkova, A.; Therien-Aubin, H.; Ahmed, A.; Nykypanchuk, D.; Choueiri, R. M.; Gagnon, B.; Muntyanu, A.; Gang, O.; Walker, G. C.; Kumacheva, E. Structural and Optical Properties of Self-Assembled Chains of Plasmonic Nanocubes. *Nano Lett*. **2014**, *14*, 6314-6321.

(147) Song, J. B.; Fang, Z.; Wang, C. X.; Zhou, J. J.; Duan, B.; Pu, L.; Duan, H. W. Photolabile Plasmonic Vesicles Assembled from Amphiphilic Gold Nanoparticles for Remote-Controlled Traceable Drug Delivery. *Nanoscale* **2013**, *5*, 5816-5824.

(148) Cheng, L.; Song, J. B.; Yin, J.; Duan, H. W. Self-Assembled Plasmonic Dimers of Amphiphilic Gold Nanocrystals. *J. Phys. Chem. Lett*. **2011**, *2*, 2258-2262.

(149) Grzelczak, M.; Sanchez-Iglesias, A.; Mezerji, H. H.; Bals, S.; Perez- Juste, J.; Liz-Marzan, L. M. Steric Hindrance Induces Crosslike Self-Assembly of Gold Nanodumbbells. *Nano. Lett*. **2012**, *12*, 4380-4384.

(150) Song, J. B.; Wu, B.H.; Zhou, Z. J.; Zhu, G. Z.; Liu, Y. J.; Yang, Z.; Lin, L. S.; Yu, G. C.; Zhang, F. W.; Zhang, G. F.; Duan, H. W.; Stucky, G. D.; Chen, X. Y. Double-Layered Plasmonic–Magnetic Vesicles by Self-Assembly of Janus Amphiphilic Gold–Iron(II,III) Oxide Nanoparticles. *Angew. Chem. Int. Ed*., **2017**, *56*, 8110-8114.

(151) Nie, Z. H.; Fava, D.; Rubinstein, M.; Kumacheva, E. "Supramolecular" Assembly of Gold Nanorods End-Terminated with Polymer "Pom-Poms": Effect of Pom-Pom Structure on the Association Modes. *J. Am. Chem. Soc*. **2018**, *130*, 3683-3689.

(152) Liu, K.; Nie, Z. H.; Zhao, N.; Li, W.; Rubinstein, M.; Kumacheva, E. Step-Growth Polymerization of Inorganic Nanoparticles. *Science* **2010**, *329*, 197-200.

(153) Liu, K.; Resetco, C.; Kumacheva, E. Salt-Mediated Kinetics of the Self-Assembly of Gold Nanorods End-Tethered with Polymer Ligands. *Nanoscale* **2012**, *4*, 6574-6580.

(154) Lukach, A.; Liu, K.; Therien-Aubin, H.; Kumacheva, E. Controlling the Degree of Polymerization, Bond Lengths, and Bond Angles of Plasmonic Polymers. *J. Am. Chem. Soc*. **2012**, *134*, 18853-18859.

(155) Liu, K.; Ahmed, A.; Chung, S. Y.; Sugikawa, K.; Wu, G. X.; Nie, Z. H.; Gordon, R.; Kumacheva, E. In Situ Plasmonic Counter for Polymerization of Chains of Gold Nanorods in Solution. *ACS Nano* **2013**, *7*, 5901-5910.

(156) Klinkova, A.; Therien-Aubin, H.; Choueiri, R. M.; Rubinstein, M.; Kumacheva, E. Colloidal Analogs of Molecular Chain Stoppers. *Proc. Natl. Acad. Sci. U. S. A.* **2013**, *110*, 18775-18779.

(157) Pavlopoulos, N. G.; Dubose, J. T.; Hartnett, E. D.; Char, K.; Pyun, J. Colloidal Random Terpolymers: Controlling Reactivity Ratios of Colloidal Comonomers via Metal Tipping. *ACS Macro. Lett*. **2016**, *5*, 950-954.

(158) Hill, L. J.; Richey, N. E.; Sung, Y.; Dirlam, P. T.; Griebel, J. J.; Lavoie-Higgins, E.; Shim, I. B.; Pinna, N.; Willinger, M. G.; Vogel, W.; Benkoski, J. J.; Char, K.; Pyun, J. Colloidal Polymers from Dipolar Assembly of Cobalt-Tipped CdSe@CdS Nanorods. *ACS Nano* **2014**, *8*, 3272-3284.

(159) Dong, W. H.; Yang, Z. M.; He, J.; Kong, C. C.; Nie, Z. H. Vesicular Self-Assembly of Copolymer-Grafted Nanoparticles with Anisotropic Shapes. *Soft Matter* **2023**, *19*, 634-639.

(160) Nie, Z. H.; Xu, S. Q.; Seo, M. S.; Lewis, P. C.; Kumacheva, E. Polymer Particles with Various Shapes and Morphologies Produced in Continuous Microfluidic Reactors. *J. Am. Chem. Soc.* **2005**, *127*, 8058-8063.

(161) He, J.; Wang, L.; Wei, Z. J.; Yang, Y. L.; Wang, C. Y.; Han, X. J.; Nie, Z. H. Vesicular Self-Assembly of Colloidal Amphiphiles in Microfluidics. *ACS Appl. Mater. Interfaces* **2013**, *5*, 9746-9751.

(162) He, J.; Wei, Z. J.; Wang, L.; Tomova, Z.; Babu, T.; Wang, C. Y.; Han, X. J.; Fourkas, J. T.; Nie, Z. H. Hydrodynamically Driven Self-Assembly of Giant Vesicles of Metal Nanoparticles for Remote-Controlled Release. *Angew. Chem. Int. Ed*. **2013**, *52*, 2463-2468.

(163) Roger, W. B.; Shih, W. M.; Manoharan, V. N. Using DNA to Program the Self-Assembly of Colloidal Nanoparticles and Microparticles. *Nat. Rev. Mater*. **2016**, *1*, 16008.

(164) Lalander, C. H.; Zheng, Y. H.; Dhuey, S.; Cabrini, S.; Bach, U. DNA-Directed Self-Assembly of Gold Nanoparticles onto Nanopatterned Surfaces: Controlled Placement of Individual Nanoparticles into Regular Arrays. *ACS Nano* **2010**, *4*, 6153-6161.

(165) Lermusiaux, L.; Funston, A. M. Plasmonic Isomers via DNA-Based Self-Assembly of Gold Nanoparticles. *Nanoscale* **2018**, *10*, 19557-19567.

(166) Thacker, V. V.; Herrmann, L. O.; Sigle, D. O.; Zhang, T.; Liedl, T.; Baumberg, J. J.; Keyser, U. F. DNA Origami Based Assembly of Gold Nanoparticle Dimers for Surface-Enhanced Raman Scattering. *Nat. Commun*. **2014**, *5*, 3448.

(167) Schreiber, R.; Luong, N.; Fan, Z. Y.; Kuzyk, A.; Nickels, P. C.; Zhang, T.; Smith, D. M.; Yurke, B.; Kuang, W.; Govorov, A. O.; Liedl, T. Chiral Plasmonic DNA Nanostructures with Switchable Circular Dichroism. *Nat. Commun*. **2013**, *4*, 2948.

(168) Li, N.; Wu, F.; Han, Z. H.; Wang, X. F.; Liu, Y.; Yi, C. L.; Ye, S. S.; Lu, G. W.; Yu, L.; Nie, Z. H.; Ding, B. Q. Shape Complementarity Modulated Self Assembly of Nanoring and Nanosphere Hetero-Nanostructures. *J. Am. Chem. Soc*. **2020**, *142*, 11680-11684.

(169) Hung, A. M.; Micheel, C. M.; Bozano, L. D.; Osterbur, L. W.; Wallraff, G. M.; Cha, J. N. Large-Area Spatially Ordered Arrays of Gold Nanoparticles Directed by Lithographically Confined DNA Origami. *Nat. Nanotechnol*. **2010**, *5*, 121-126.

(170) Edwardson, T. G. W.; Lau, K. L.; Bousmail, D.; Serpell, C. J.; Sleiman, H. F. Transfer of Molecular Recognition Information from DNA Nanostructures to Gold Nanoparticles. *Nat. Chem*. **2016**, *8*, 162-170.

(171) Lu, F.; Yager, K. G.; Zhang, Y.; Xin, H.; Gang, O. Superlattices Assembled Through Shape-Induced Directional Binding. *Nat. Commun*. **2015**, *6*, 6912.

(172) Yi, C. L.; Yang, Y. Q.; Nie, Z. H. Alternating Copolymerization of Inorganic Nanoparticles. *J. Am. Chem. Soc*. **2019**, *141*, 7917-7925.

(173) Yi, C. L.; Liu, H.; Zhang, S. Y.; Yang, Y. Q.; Zhang, Y.; Lu, Z. Y.; Kumacheva, E.; Nie, Z. H. Self-Limiting Directional Nanoparticle Bonding Governed by Reaction Stoichiometry. *Science* **2020**, *369*, 1369-1374.

(174) Lin, X. Y.; Ye, S. S.; Kong, C. C.; Webb, K.; Yi, C. L.; Zhang, S. Y.; Zhang, Q.; Fourkas, J. T.; Nie, Z. H. Polymeric Ligand-Mediated Regioselective Bonding of Plasmonic Nanoplates and Nanospheres. *J. Am. Chem. Soc*. **2020**, *142*, 17282-17286.

(175) Dong, W. H.; Zhang, Y.; Yi, C. L.; Chang, J. J.; Ye, S. S.; Nie, Z. H. Halogen Bonding-Driven Reversible Self-Assembly of Plasmonic Colloidal Molecules. *ACS Nano* **2023**, *17*, 3047-3054.

(176) Frens, G. Controlled Nucleation for the Regulation of the Particle Size in Monodisperse Gold Solutions. *Nat. Phys. Sci*. **1973**, *241*, 20-22.

(177) Xie, S. W.; Ren, B. P.; Gong, G.; Zhang, D.; Chen, Y.; Xu, L. J.; Zhang, C. F.; Xu, J. X.; Zheng, J. Lanthanide-Doped Upconversion Nanoparticle-Cross-Linked Double-Network Hydrogels with Strong Bulk/Interfacial Toughness and Tunable Full-Color Fluorescence for Bioimaging and Biosensing. *ACS Appl. Nano Mater*. **2020**, *3*, 2774-2786.

(178) Li, H. H.; Wei, R. Y.; Yan, G. H.; Sun, J.; Li, C. J.; Wang, H. F.; Shi, L.; Capobianco, J. A.; Sun, L. N. Smart Self-Assembled Nanosystem Based on Water-Soluble Pillararene and Rare-Earth-Doped Upconversion Nanoparticles for pH-Responsive Drug Delivery. *ACS Appl. Mater. Interfaces* **2018**, *10*, 4910-4920.

(179) Zhang, Q.; Sun, S. Q.; Wang, Z.; Li, J. B.; Xie, Y.; Shi, L.; Sun, L. N. Dandelion-Inspired Hierarchical Upconversion Nanoplatform for Synergistic Chemo-Photodynamic Therapy In Vitro. *ACS Appl. Bio Mater*. **2020**, *3*, 6015-6024.

(180) Dong, L.; Zhang, P.; Liu, X. J.; Deng, R. P.; Du, K.; Feng, J.; Zhang, H. J. Renal Clearable Bi–Bi_2S_3 Heterostructure Nanoparticles for Targeting Cancer Theranostics. *ACS Appl. Mater. Interfaces* **2019**, *11*, 7774-7781.

(181) Harada, A.; Kobayashi, R.; Takashima, Y.; Hashidzume, A.; Yamaguchi, H. Macroscopic Self-Assembly Through Molecular Recognition. *Nat. Chem*. **2011**, *3*, 34-37.

(182) Harada, A.; Takashima, Y.; Nakahata, M. Supramolecular Polymeric Materials via Cyclodextrin–Guest Interactions. *Acc. Chem. Res*. **2014**, *47*, 2128-2140.

(183) Yamaguchi, H.; Kobayashi, Y.; Kobayashi, R.; Takashima, Y.; Hashidzume, Y.; Harada, A. Photoswitchable Gel Assembly Based on Molecular Recognition. *Nat. Commun*. **2012**, *3*, 603.

(184) Nakahata, M.; Takashima, Y.; Harada, A. Redox-Responsive Macroscopic Gel Assembly Based on Discrete Dual Interactions. *Angew. Chem. Int. Ed*. **2014**, *53*, 3617-3621.

(185) Zheng, Y.; Hashidzume, Y.; Harada, A. pH-Responsive Self-Assembly by Molecular Recognition on a Macroscopic Scale. *Macromol. Rapid Commun*. **2013**, *34*, 1062-1066.

(186) Zheng, Y.; Hashidzume, Y.; Takashima, Y.; Yamaguchi, H.; Harada, A. Temperature-Sensitive Macroscopic Assembly Based on Molecular Recognition. *ACS Macro. Lett*. **2012**, *1*, 1083-1085.

(187) Zhang, J. Y.; Santos, P. J.; Gabrys, P. A.; Lee, S.; Liu, C.; Macfarlane, R. J. Self-Assembling Nanocomposite Tectons. *J. Am. Chem. Soc*. **2016**, *138*, 16228-16231.

(188) Wang, Y. P.; Santos, P. J.; Kubiak, J. M.; Guo, X. H.; Lee, M. S.; Macfarlane, R. J. Multistimuli Responsive Nanocomposite Tectons for Pathway Dependent Self-Assembly and Acceleration of Covalent Bond Formation. *J. Am. Chem. Soc*. **2019**, *141*, 13234-13243.

(189) Santos, P. J.; Cheung, T. C.; Macfarlane, R. J. Assembling Ordered Crystals with Disperse Building Blocks. *Nano Lett*. **2019**, *19*, 5774-5780.

(190) Santos, P. J.; Cao, Z.; Zhang, J. Y.; Alexander-Katz, A.; Macfarlane, R. J. Dictating Nanoparticle Assembly via Systems-Level Control of Molecular Multivalency. *J. Am. Chem. Soc*. **2019**, *141*, 14624-14632.

(191) Santos, P. J.; Gabrys, P. A.; Zornberg, L. Z.; Lee, M. S.; Macfarlane, R. J. Macroscopic Materials Assembled from Nanoparticle Superlattices. *Nature* **2021**, *591*, 586-591.

(192) Lee, M. S.; Alexander-Katz, A.; Macfarlane, R. J. Macroscopic Materials Assembled from Nanoparticle Superlattices. *Small* **2021**, *17*, 2102107.

(193) Dhulipala, S.; Yee, D. W.; Zhou, Z.; Sun, R.; Andrade, J. E.; Macfarlane, R. J.; Portela, C. M. Tunable Mechanical Response of Self-Assembled Nanoparticle Superlattices. *Nano Lett*. **2023**, *23*, 5155-5163.

(194) Yee, D. W.; Lee, M. S.; An, J.; Macfarlane, R. J. Reversible Diffusionless Phase Transitions in 3D Nanoparticle Superlattices. *J. Am. Chem. Soc*. **2023**, *145*, 6051-6056.

(195) de Jong, M. R.; Huskens, J.; Reinhoudt, D. N. Influencing the Binding Selectivity of Self-Assembled Cyclodextrin Monolayers on Gold through Their Architecture. *Chem. Eur. J*. **2001**, *7*, 4164-4170.

(196) Huskens, J.; Deij, M. A.; Reinhoudt, D. N. Attachment of Molecules at a Molecular Printboard by Multiple Host-Guest Interactions. *Angew. Chem. Int. Ed*. **2002**, *41*, 4467-4471.

(197) Auletta, T.; Dordi, B.; Mulder, A.; Sartori, A.; Onclin, S.; Bruinink, C. M.; Peter, M.; Nijhuis, C. A.; Beijleveld, H.; Schonherr, H.; Vancso, G. J.; Casnati, A.; Ungaro, R.; Ravoo, B. J.; Huskens, J.; Reinhoudt, D. N. Writing Patterns of Molecules on Molecular Printboards. *Angew. Chem. Int. Ed*. **2004**, *43*, 369-373.

(198) Wankar, J.; Kotla, N. G.; Gera, S.; Rasala, S.; Pandit, A.; Rochev, Y. A. Recent Advances in Host–Guest Self-Assembled Cyclodextrin Carriers: Implications for Responsive Drug Delivery and Biomedical Engineering. *Adv. Funct. Mater*. **2020**, *30*, 1909049.

(199) Cengiz, B.; Gevrek, T. N.; Chambre, L.; Sanyal, A. Self-Assembly of Cyclodextrin-Coated Nanoparticles: Fabrication of Functional Nanostructures for Sensing and Delivery. *Molecules* **2023**, *28*, 1076.

(200) Munteanu, M.; Choi, S. W.; Ritter, H. Cyclodextrin Methacrylate via Microwave-Assisted Click Reaction. *Macromolecules* **2008**, *41*, 9619-9623.

(201) Wang, C.; Shi, W. Q.; Zhang, W.; Zhang, X. Force Spectroscopy Study on Poly(acrylamide) Derivatives: Effects of Substitutes and Buffers on Single-Chain Elasticity. *Nano Lett*. **2002**, *2*, 1169-1172.

(202) Mark, J. E. Physical Properties of Polymers Handbook, Second ed.; Springer, **2007**.

(203) Jones, E. R.; Mykhaylyk, O. O.; Semsarilar, M.; Boerakker, M.; Wyman, P.; Armes, S. P. How Do Spherical Diblock Copolymer Nanoparticles Grow during RAFT Alcoholic Dispersion Polymerization?. *Macromolecules* **2016**, *49*, 172-181.

(204) Lamar, C.; Liu, Y. J.; Yi, C. L.; Nie, Z. H. Entropy-Driven Segregation and Budding in Hybrid Vesicles of Binary Nanoparticle Amphiphiles. *Giant* **2020**, *1*, 100010.

(205) Huebner, D.; Rossner, C.; Vana, P. Light-Induced Self-Assembly of Gold Nanoparticles with a Photoresponsive Polymer Shell. *Polymer* **2016**, *107*, 503-508.

(206) Qian, X. M.; Li, J.; Nie, S. M. Stimuli-Responsive SERS Nanoparticles: Conformational Control of Plasmonic Coupling and Surface Raman Enhancement. *J. Am. Chem. Soc*. **2009**, *131*, 7540-7541.

(207) Torii, Y.; Sugimura. N.; Mitomo, H.; Niikura, K.; Ijiro, K. pH-Responsive Coassembly of Oligo(ethylene glycol)-Coated Gold Nanoparticles with External Anionic Polymers via Hydrogen Bonding. *Langmuir* **2017**, *33*, 5537-5544.

(208) Durand-Gasselin, C.; Sanson, N.; Lequeux, N. Reversible Controlled Assembly of Thermosensitive Polymer-Coated Gold Nanoparticles. *Langmuir* **2011**, *27*, 12329-12335.

(209) Harada, A.; Adachi, H.; Kawaguchi, Y.; Kamachi, M. Recognition of Alkyl Groups on a Polymer Chain by Cyclodextrins. *Macromolecules* **1997**, *30*, 5181-5182.

(210) Harada, A.; Kamachi, M. Complex Formation between Poly(ethylene glycol) and α-Cyclodextrin. *Macromolecules* **1990**, *23*, 2823-2824.

(211) Harada, A.; Li, J.; Kamachi, M. Preparation and Properties of Inclusion Complexes of Polyethylene Glycol with α-Cyclodextrin. *Macromolecules* **1993**, *26*, 5698-5703.

(212) Rosales, A. M.; Rodell, C. B.; Chen, M. H.; Morrow, M. G.; Anseth, K. S.; Burdick, J. A. Reversible Control of Network Properties in Azobenzene-Containing Hyaluronic Acid-Based Hydrogels. *Bioconjugate Chem*. **2018**, *29*, 905-913.

(213) Yang, Z. W.; Breslow, R. Very Strong Binding of Lithocholic Acid to β-Cyclodextrin. *Tetrahedron Lett*. **1997**, *38*, 6171-6172.

(214) Moghaddam, S.; Yang, C.; Rekharsky, M.; Ko, Y. H.; Kim, K.; Inoue, Y.; Gilson, M. K. New Ultrahigh Affinity Host−Guest Complexes of Cucurbit[7]uril with Bicyclo[2.2.2]octane and Adamantane Guests: Thermodynamic Analysis and Evaluation of M2 Affinity Calculations. *J. Am. Chem. Soc*. **2011**, *133*, 3570-2581.

(215) Tan, T.; Ng, S. C.; Wang, Y.; Xiao, Y. Synthesis of Mono-6-tosyl-β-cyclodextrin, a Key Intermediate for the Functional Cyclodextrin Derivatives. *Protocol Exchange* **2011**.

(216) Tang, W.; Ng, S. C. Facile Synthesis of Mono-6-amino-6-deoxy-α-, β-, γ-cyclodextrin Hydrochlorides for Molecular Recognition, Chiral Separation and Drug Delivery. *Nat. Prot*. **2008**, *3*, 691-697.